Bioaéroelasticité d'aéronefs à voilure tournante par bond graphs

Georges Tod

ParisTech
INSTITUT DES SCIENCES ET TECHNOLOGIES
PARIS INSTITUTE OF TECHNOLOGY

ARTS ET MÉTIERS ParisTech

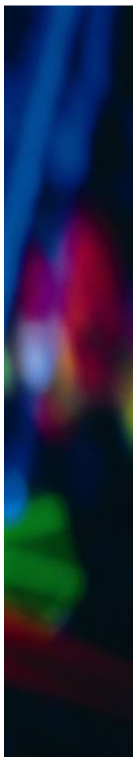

2015-ENAM-0042

École doctorale n° 432 : Sciences des Métiers de l'ingénieur

Doctorat ParisTech

T H È S E

pour obtenir le grade de docteur délivré par

l'École Nationale Supérieure d'Arts et Métiers

Spécialité "Automatique"

présentée et soutenue publiquement par

Georges TOD

14 décembre 2015

Bioaéroelasticité d'aéronefs à voilure tournante par bond graphs

Rotorcraft bioaeroelasticity using bond graphs

Directeur de thèse : **Pierre-Jean BARRE**
Co-encadrement de la thèse : **François MALBURET et Julien GOMAND**

Jury

Mme. Geneviève DAUPHIN-TANGUY, Professeur des universités, LAGIS, Ecole Centrale de Lille	Rapporteur
M. Pierangelo MASARATI, Professore associato, Politecnico di Milano	Rapporteur
M. André PREUMONT, Professeur ordinaire, ASL, Université Libre de Bruxelles	Président
M. Pierre-Jean BARRE, Professeur des universités, LSIS, Arts et Métiers ParisTech	Examinateur
M. François MALBURET, Maître de conférences, LSIS, Arts et Métiers ParisTech	Examinateur
M. Julien GOMAND, Maître de conférences, LSIS, Arts et Métiers ParisTech	Examinateur
Mme Marilena PAVEL, Associate professor, Delft University of Technology	Invitée

Arts et Métiers ParisTech – Campus d'Aix-en-Provence
Laboratoire des Sciences de l'Information et des Systèmes

T H È S E

Rotorcraft bioaeroelasticity using bond graphs

Georges Tod

Under the supervision of
François Malburet, Julien Gomand and Pierre-Jean Barre

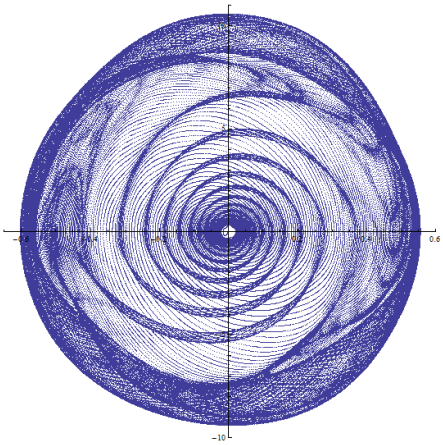

If a man is in need of rescue, an airplane can come in and throw flowers on him, and that's just about all. But a direct lift aircraft could come in and save his life.

Igor Sikorsky

Acknowledgements

Je remercie Pierre-Jean Barre pour tous les conseils et orientations que vous m'avez donnés. Un grand merci à François Malburet pour la passion transmise pour les voilures tournantes et la trajectoire de masses en rotation. Mais aussi pour la confiance que tu m'as accordée et surtout de m'avoir donné la chance de poursuivre dans cette voie ! Je remercie aussi Julien Gomand pour la précision et la justesse de ton regard et contributions.

Je remercie Geneviève Dauphin-Tanguy d'avoir accepté de rapporter mes travaux. Ringrazio Pierangelo Masarati per aver accettato di partecipare a questo lavoro. Je remercie André Preumont d'avoir accepté d'être le président du jury. A special thanks also to Marilena Pavel, with whom the discussions have always challenged my thoughts.

A tous ceux qui se perdent sur la route de la recherche scientifique ou pas, je conseillerai de lire « Le travail intellectuel » de Jean Guitton.

Et finalement je remercie également tous les personnels de l'Ecole Nationale Supérieure d'Arts et Métiers qui ont sans aucun doute contribué d'une manière ou d'une autre à ce travail. Je remercie la Fondation Airbus Group d'avoir financé ces travaux en nous laissant une liberté de recherche incroyable. Je remercie encore le système éducatif français, nos institutions sans lesquels ce travail n'aurait pu aboutir. Je n'oublie pas la planète Terre sans laquelle nous n'aurions pas eu les ressources pour produire, ou plutôt transformer, tout cela. Mais aussi le système solaire, la voie lactée, l'univers et tous les astéroïdes dont la masse et la trajectoire n'ont pas modifié le cours de la vie sur Terre pendant 3 ans.

Table of contents

List of figures

List of tables

Nomenclature

PIO	=	Pilot Induced Oscillations
PAO	=	Pilot Assisted Oscillations
RPC	=	Rotorcraft-Pilot Coupling
APC	=	Aircraft-Pilot Coupling
FCS	=	Flight Control System
AFCS	=	Automatic Flight Control System
SAS	=	Stability Augmentation System
BDFT	=	Biodynamic Feedthrough (rad/m.s^2)
CNS	=	Central Nervous System
BG	=	Bond graph
MBG	=	Multibond graph (vectorial BG)
ODE	=	Ordinary Differential Equation
DAE	=	Differential Algebraic Equation
CKC	=	Closed kinematic Chain
BDF	=	Backward Differentiation Formula
LTP	=	Linear Time Periodic
LTI	=	Linear Time Invariant
LCE	=	Lyapunov Characteristic Exponent
dof	=	degree of freedom
MGY	=	Multiport Gyrator Element
MTF	=	Multiport Gyrator Element
I	=	Inertial Element
C	=	Capacitive Element
R	=	Dissipative Element
MSe	=	Modulated Source of effort Element
MSf	=	Modulated Source of flow Element
0	=	junction, same effort, sum of flows
1	=	junction, same flow, sum of efforts

$(\mathbf{x}_0,\mathbf{y}_0,\mathbf{z}_0)$ = inertial reference frame
$(\mathbf{x}_3,\mathbf{y}_3,\mathbf{z}_3)$ = frame attached to the airframe
$(\mathbf{x}_4,\mathbf{y}_4,\mathbf{z}_4)$ = frame attached to the rotor hub
$(\mathbf{x}_{10},\mathbf{y}_{10},\mathbf{z}_{10})$ = frame attached to the arm
$(\mathbf{x}_{11},\mathbf{y}_{11},\mathbf{z}_{11})$ = frame attached to the cyclic lever
$(\mathbf{x}_{12},\mathbf{y}_{12},\mathbf{z}_{12})$ = frame attached to the forearm

$\mathbf{u} \wedge \mathbf{v}$ = Vectorial product between the vector $\boldsymbol{u}$ and the vector $\boldsymbol{v}$
$\mathbf{u}^i$ = Vector $\boldsymbol{u}$ expressed in the frame attached to the body i
$\|\mathbf{u}\|$ = Vector $\boldsymbol{u}$ norm
$\mathbf{M}^i_{P,\mathrm{a}\to\mathrm{b}}$ = Moment vector applied by body a on body b around the point P expressed in the frame attached to body i
$\mathbf{F}^i_{a\to\mathrm{b}}$ = Force vector applied by body a on body b expressed in the frame attached to body i
$\boldsymbol{\sigma}^i_{P,\mathrm{a/b}}$ = Angular momentum vector of body a with respect to body b around the point P expressed in the frame attached to body i
$\mathbf{V}^i_{P,\mathrm{a/b}}$ = Velocity vector of body a with respect to body b around the point P expressed in the frame attached to body i
$\boldsymbol{\Omega}^i_{\mathrm{a/b}}$ = Angular velocity vector of body a with respect to body b expressed in the frame attached to body i
$\mathbf{G}_i\mathbf{A}_i$ = Vector from the point A_i to the point G_i
$\mathbf{G}_i$ = Center of mass of body i
$\mathbf{I}_{G,i}$ = Inertia matrix of body i around its center of mass and principal axis
$\mathbf{M}_{a\to b}$ = Rotation matrix from frame attached to body a to frame attached to b

T = kinetic energy
V = potential energy
D = dissipative energy
Q = generalized forces
$\mathbf{q}$ = generalized coordinates vector
$\mathbf{x}$ = state vector

x	=	airframe lateral translation (m)
z	=	airframe vertical translation (m)
α_y	=	airframe roll angle (rad)
$\beta_i, \delta_i, \theta_i$	=	individual blade flap, lag and pitch angles (rad)
$\beta_0, \beta_{1c}, \beta_{1s}$	=	collective and cyclic blades flap angles (rad)
$\delta_0, \delta_{1c}, \delta_{1s}$	=	collective and cyclic blades lag angles (rad)
$\theta_0, \theta_{1c}, \theta_{1s}$	=	collective and cyclic blades pitch angles (rad)
b	=	main rotor number of blades
R	=	rotor radius (m)
e	=	blade root eccentricity (m)
γ	=	lock number
ρ	=	air density
c	=	profile chord (m)
Cl	=	lift coefficient
cl	=	lift coefficient derivative
Ω	=	main rotor angular velocity (rad/s)
β_{0ss}	=	steady-state coning angle (rad)
m_s	=	individual blade static moment at blade root (m.kg)
I_{bl}	=	individual blade inertia at blade root (m².kg)
M_{bl}	=	individual blade mass (kg)
k_δ	=	individual blade equivalent angular lag damper stiffness (N.m/rad)
c_δ	=	individual blade equivalent angular lag damper damping (N.m.s/rad)
ω_δ	=	lag motion natural frequency (Hz)
M_f	=	helicopter mass (kg)
I_{yy}	=	airframe roll inertia around its center of mass (m².kg)
h	=	rotor head height from airframe center of mass (m)
G	=	gearing ratio

a	=	muscular activation coefficient
a_0	=	initial muscular activation coefficient
k_p	=	muscle reflexive feedback gain on muscle length
k_v	=	muscle reflexive feedback gain on muscle contraction velocity
ω	=	pilot biodynamics resonant frequency (rad/s)
k	=	pilot biodynamics gain
ζ	=	pilot biodynamics damping (1/s)

Introduction

The present work is the result of the collaboration between *l'Ecole Nationale Supérieure d'Arts et Métiers* in Aix-en-Provence and the *Fondation Airbus Group* who founded together the industrial chair "Dynamics of Complex Mechanical Systems". The research was conducted at the LSIS Laboratory (Laboratoire des Sciences de l'Information et des Systèmes) and more precisely within the INSM team (Ingénierie Numérique des Systèmes Mécaniques - UMR CNRS n°7296).

Helicopters are being designed and built for a century now. The use of rotary wings to provide lift, propulsion and control give the advantage of being capable of hover flight even if the airframe velocity is null (Johnson, 1980). In places in which 'in plane' transportation using wheels reaches some limits, vertical and three dimensional space transportation becomes necessary. But in a competitive environment in which new flying concepts emerge faster and faster; from drones, jet packs, multirotor electric helicopters to hybrid airships, who knows if helicopters will still fulfill the mission at an acceptable cost? Are helicopter designs as we know them an endangered species? The Vertical advantage of Take-Off and Landing (VTOL) over fixed wing aircrafts has a cost; for instance a higher power is required for vertical flight. Furthermore, rotors are sources of vibration that generate alternative loads that degrade not only the comfort of passengers but also the lifetime of mechanical parts by fatigue resulting in higher maintenance costs.
To help design safer, greener[1], faster and economically sound machines, important research & development efforts are supported by manufacturers around the world. This work is an attempt to contribute in that direction by providing tools and methods to designers in the field of dynamics. **Chapter 1** of this manuscript introduces the context and a vision in terms of how tools and methods could look like in the future. This chapter also explains the main interest of using a modeling approach based on bond graphs. The chosen dynamic phenomenon of application involves *human-machine interactions* for which it seems that to improve the performance of helicopters, designers will need to take more disciplines into consideration such as *biodynamics*. In **chapter 2**, a helicopter *aeromechanical model* using bond graphs is developed. In **chapter 3**, a pilot *neuromusculoskeletal model* using bond graphs is developed. In **chapter 4**, both helicopter and pilot models are coupled and the resulting *bioaeroelastic* behavior in terms of stability is analyzed from a linear model. **Chapter 5** focuses on how to analyze the *stability of equilibriums* of dynamic systems directly from nonlinear models. The first blocks of a method based on *Chetaev functions* are proposed.

Each chapter starts with an extended abstract in French; it is then followed by the full story in English.

[1] In the sense of ecology, not color

Chapter 1
Aeroelastic Rotorcraft-Pilot Couplings

Résumé long du chapitre 1

Les concepteurs d'hélicoptères délivrent à leurs clients des machines capables de voler dans une certaine enveloppe de vol, dans laquelle sont données des limites en termes de vitesse, d'altitude et de température. En essayant de repousser ces limites, en améliorant les performances des appareils actuels, des phénomènes dynamiques peuvent apparaître, comme par exemple, ***la résonance sol****,* ***la résonance air*** (Krysinski & Malburet, 2011)*,* ***le flottement gyroscopique*** *ou* ***les oscillations induites/assistées par le pilote*** *(PIO/PAO),* (Pavel, et al., 2013)*. Ces travaux s'intéressent à cette dernière catégorie de phénomènes, récemment renommé par la communauté scientifique sous le nom de Couplages Pilote-Aéronef (en anglais,* ***Rotorcraft-Pilot Couplings (RPCs)****).*

Ce chapitre présente dans un premier temps le contexte industriel de la thèse. Un exemple très détaillé de RPC est présent dans la littérature ouverte. Il s'agit du cas d'un aéronef convertible, le V-22 des constructeurs Boeing et Bell, voir la Figure 1-1, pour lequel plusieurs modes incluant un mouvement de roulis à basses fréquences ont été ressentis par les pilotes lors d'essais. L'analyse de ces essais a mis en évidence, que le pilote participait involontairement à la déstabilisation de ces modes. En effet, les vibrations latérales du fuselage de l'appareil, dues au mouvement de roulis du fuselage, déplacent les membres du pilote, dont son bras droit, qui impose un mouvement au manche de roulis. Ces vibrations ont été mesurées à des fréquences supérieures aux fréquences de pilotage (~1Hz) et sont donc considérées comme involontaires. Une des solutions retenues a été dans ce cas, d'augmenter la masse du manche de commande du pilote, afin de diminuer l'amplitude des déplacements réinjectés. Augmenter la masse d'un élément sur une machine volante, est toujours pénalisant, et n'est pas toujours une solution acceptable.
Ce type de phénomène apparaît également sur des hélicoptères d'architecture conventionnelle, c'est-à-dire disposant d'un rotor principal et d'un rotor de queue, voir la Figure 1-3. Pour voler, l'hélicoptère doit générer une force qui s'oppose à son poids. Cette force de poussée, « thrust » voir Figure 1-4, est générée par les forces aérodynamiques qui s'appliquent sur les pales du rotor. La norme et la direction de cette force sont imposées par le pilote en modifiant le pas des pales :

- ***Soit collectivement****. Par l'intermédiaire du manche de pas collectif et la chaîne de commande (Figure 1-5), le pilote impose une translation aux plateaux suivant l'axe du mât rotor (swashplates de la Figure 1-4 (b)). Ceci modifie la norme du vecteur de « poussée ».*

- ***Soit de manière cyclique****. Par l'intermédiaire du manche de pas cyclique et la chaîne de commande, le pilote impose une orientation au plateau fixe*

> *(« swashplate », plateau inférieur sur la Figure 1-4 (b)). Etant donné que le rotor tourne, chaque rayon du plateau dit tournant (« swashplate », plateau supérieur sur la Figure 1-4 (b)) change d'orientation pendant chaque tour de rotor. Ceci permet de modifier l'orientation du vecteur de poussée.*

Une des particularités de ce type d'architecture d'aéronef est que le rotor principal exerce un couple sur le fuselage autour de l'axe de lacet (« yaw axis » sur la Figure 1-3). La solution la plus courante, afin de contrer ce couple, consiste à implanter un rotor sur la queue de l'appareil ; celui-ci génère une force, « tail force » sur la Figure 1-4, dont la norme est imposée par le pilote par l'intermédiaire des pédales à ses pieds, voir Figure 1-3. Cette brève explication montre au lecteur la difficulté que peut représenter le pilotage d'une telle machine : tous ses axes sont couplés. Autrement dit, chaque action sur un des manches ou pédales demandera une action corrective sur chacune des autres commandes, et ce de manière itérative jusqu'à converger vers une attitude acceptable de l'appareil.
La Figure 1-7 montre des mesures réalisées il y a quelques années lors de l'essai en vol d'un hélicoptère autour de l'aéroport de Marignane. Il s'agit de deux mesures, l'une de l'angle de roulis imposé au manche cyclique par le pilote et l'autre de l'angle de roulis de l'appareil. Sur cette figure, les commentaires des auteurs du rapport d'essai ont été reproduits en couleur orange. Ils attribuent l'amplification des oscillations en roulis du fuselage à une action du pilote. Encore une fois, ces actions (~3Hz) sont qualifiées d'involontaires car elles se produisent à des fréquences supérieures à celles du contrôle manuel d'un véhicule (~1Hz). Une discussion avec un pilote, sur Apache AH-64D de Boeing, de l'armée de l'air Royale des Pays-Bas, a confirmé que les pilotes peuvent ressentir des vibrations inhabituelles dans la cabine. De plus, ils sentent parfois qu'ils participent au phénomène, parce qu'ils tiennent trop fermement les manches de commandes. S'ils se retrouvent dans une situation où cela est possible, le relâchement des commandes permet au pilote d'atténuer l'amplitude des vibrations liées au phénomène. Mais cette solution est loin d'être acceptable.

Dans un deuxième temps, le contexte scientifique est progressivement introduit. Parmi les premiers travaux autour des phénomènes de couplages entre pilotes et aéronefs, on trouve ceux de (McRuer, 1995). *Ces travaux se concentrent surtout sur les phénomènes qui apparaissent sur les aéronefs à voilure fixe. Plus récemment, le projet de recherche européen Aristotel (2010-2013) a proposé de distinguer deux types de couplages entre pilote et aéronef à voilure tournante : les couplages dits « rigides » pour des oscillations inférieures à 1Hz et des couplages dits « aéroélastiques » pour des oscillations comprises entre 2 et 8Hz* (Pavel, et al., 2013). *Le terme aéroélastique qualifie la nature des forces en interactions : aérodynamiques, inertielles et élastiques (dues aux déformations). Comme suggéré dans* (Masarati & Quaranta, 2014) *, le terme* ***aéroélastique*** *peut être étendu à* ***bio-aéroélastique*** *lorsque les forces générées par le comportement biodynamique de l'humain doivent être prises en compte.*

Les aéronefs à voilure tournante sont connus pour avoir un niveau vibratoire plus important que les aéronefs à voilure fixe, ce qui fait des aéronefs à voilure

tournante des machines plus sensibles aux phénomènes aéroélastiques et donc aux couplages aéroélastiques entre pilote et aéronef (RPCs). Ces phénomènes ont un impact critique sur la sécurité parce qu'ils peuvent être à l'origine de cycles limites ou instabilités. Même si les RPCs ne sont pas toujours instables, les vibrations et cycles limites sont, inconfortables pour les passagers, et une source d'efforts alternatifs, qui fatiguent les matériaux des pièces de l'aéronef, et réduisent par conséquent ses performances.

Jusqu'à aujourd'hui, la plupart des efforts de recherches se sont concentrés sur la prédiction des RPCs aéroélastiques sur l'axe vertical des hélicoptères. Dans (Mayo, 1989)*, des expériences sur simulateurs ont permis d'identifier un modèle du comportement biodynamique du pilote sur la commande de pas collectif, qui agit sur l'axe vertical de l'hélicoptère. Celui-ci a été ensuite couplé à un modèle linéaire d'hélicoptère, sur son axe vertical, afin de simuler de potentiels RPCs aéroélastiques, et de concevoir un filtre ; celui-ci supprime des commandes du pilote sur une bande de fréquences et atténue le couplage pilote-aéronef. Dans* (Gennaretti, et al., 2013)*, des modèles d'hélicoptères bien plus détaillés sont proposés, afin d'étudier le phénomène toujours sur l'axe vertical de la machine. Dans* (Masarati & Quaranta, 2014)*, un modèle non linéaire, du comportement biodynamique du bras gauche du pilote, qui agit sur la commande de pas collectif, est obtenu en se basant sur des principes physiques. Il est ensuite couplé à un modèle d'hélicoptère. Cette approche constitue une des premières approches qui tente de prédire le comportement involontaire du pilote en utilisant des principes physiques.*

Ce comportement involontaire a été formalisé sous le nom de ***biodynamic feedthrough (BDFT)****. Une définition est donnée par* (Venrooij, 2014)*: « **il s'agit du transfert d'accélérations par le corps humain pendant l'exécution d'une tâche de contrôle manuel, qui engendre des forces involontaires qui s'appliquent sur le dispositif de commande, et qui peut éventuellement provoquer des mouvements involontaires du dispositif de commande** ». Cette définition, très générale permet d'imaginer que ce transfert peut se produire sur n'importe quel type de véhicule et pas uniquement des aéronefs.*

Il est reconnu dans (Walden, 2007) *que les phénomènes qui se produisent sur l'axe latéral des hélicoptères, ont tendance à être plus critiques que ceux sur son axe vertical. Dans* (Lantzsch, Hamers, & Wolfram, 2014)*, le développement d'un contrôleur est proposé afin de supprimer les oscillations en roulis (autour de 1.8Hz) lorsque la boucle de retour du système d'augmentation de la stabilité d'un hélicoptère H135 d'Airbus (anciennement Eurocopter EC135) est fermée. Une contribution à la compréhension du mécanisme physique entre les interactions d'un système de pilotage automatique (AFCS) et la dynamique latérale d'un hélicoptère est proposée dans* (Pavel & Padfield, 2008)*. En complément dans* (Pavel M. , 2010)*, les flux d'énergies relativement complexes sont révélés, entre les degrés de liberté de battement et de traînée des pales du rotor, le roulis du fuselage et un système de pilotage automatique (AFCS). Dans* (Muscarello, et al., 2015)*, un modèle aeroservoélastique (« servo », qui tient compte dans une certaine mesure de la dynamique des servocommandes) d'hélicoptère est couplé à des modèles de pilote, identifiés à l'aide d'un simulateur. Les prédictions numériques de couplages entre pilote et aéronefs sont ensuite comparées à des résultats d'essais dans des conditions similaires sur simulateur.*

Des conjectures intéressantes sont dégagées de cette étude : « les prédictions suggèrent que les RPCs sur les axes latéral et de roulis sont plus susceptibles d'apparaître sur les hélicoptères dont la technologie du rotor est de type souple dans le plan, et dont les modes de traînées du rotor dans le plan sont peu amortis, […], plus dangereux lorsque la vitesse de l'aéronef est élevée et lorsque les pilotes (leur comportement biodynamique) sont caractérisés par une fréquence propre proche de la fréquence du mode de traînée du rotor dans le plan ».
D'une manière générale, sur des hélicoptères conventionnels, les RPCs aéroélastiques dépendent des modes du rotor et du fuselage, de la phase de vol mais aussi d'un grand nombre de sous-systèmes : le système d'augmentation de la stabilité (SAS), le système de commande de vol (FCS), la chaîne de commande, la chaîne de transmission de puissance (moteur/boîte de vitesse), des actionneurs des plateaux fixe et tournant, etc. comme le montre la Figure 1-8. Il existe encore des concepts d'aéronefs à voilure tournante qui souffrent de RPCs ainsi que d'autres phénomènes dynamiques indésirables d'une manière générale. L'atténuation de ses phénomènes est généralement obtenue par des solutions développées après de nombreux essais en vol. Mais ce processus itératif représente un coût important. Dans certains cas, les phénomènes dynamiques comme les RPCs peuvent être mêmes destructifs, présentant alors un danger pour les pilotes, les passagers et la population.
Dès lors, il existe un intérêt important d'être capable de prédire des RPCs et tous phénomènes dynamiques indésirables le plus tôt possible dans le processus de conception des machines. Ceci permettrait de réduire le coût de réduction de l'impact de ces phénomènes par le développement de solutions de conception le plus tôt possible pendant le processus de conception. Les méthodes et outils idéaux devraient donner la possibilité au concepteur de modéliser un aéronef complet avec tous les sous-systèmes pertinents, qui interagiraient dans le cas d'un RPC, de telle façon, que la modélisation puisse être adaptée efficacement au problème d'étude. En termes de résolution physique, cela nécessiterait d'être capable de prendre en compte non seulement des modèles très détaillés d'aérodynamique instationnaire ; mais également l'interaction de ces forces, avec des pales déformables aux géométries complexes, composées de matériaux anisotropes ainsi que des couplages avec un fuselage déformable. En même temps, tous les comportements biophysiques et cognitifs du pilote pertinents devraient être pris en compte ; puis couplés avec le modèle décrit précédemment en tenant compte de la dynamique de la chaîne de commande et sa cinématique complexe. La méthode de modélisation devrait également être suffisamment flexible pour intégrer des éléments de contrôle actif, qui seront de plus en plus présent sur les futurs aéronefs.
« Les calculs dans le domaine des aéronefs à voilure tournante demandent la plus vaste intégration possible des disciplines, une des raisons pour laquelle les analyses globales sont difficiles » dit (Johnson, 2013). *De plus, les RPCs sont sensibles aux phases de vol des appareils. En conséquence, le modèle devrait être capable de représenter n'importe quelle phase de vol et devrait être validé expérimentalement.*
Finalement, des méthodes devraient permettre d'analyser le modèle mathématique non linéaire obtenu, dans le but d'être prédictif en terme d'efforts, de stabilité aéroélastique et de qualités de vol sur toute l'enveloppe de vol d'un aéronef, le tout avec un coût de calcul le plus faible possible. Ceci permettrait de mieux

comprendre les mécanismes physiques derrière de tels phénomènes dynamiques et de trouver des solutions efficaces aux RPCs.

Une fois le contexte décrit et l'idéal projeté, nous nous intéressons aux approches globales actuelles. Les constructeurs d'hélicoptères développent leurs propres outils de calculs pour mieux comprendre les phénomènes dynamiques qu'ils découvrent avec le temps. Ces outils de calcul aéromécanique comme CAMRAD ou HOST, (Johnson, 2013), *sont devenus de plus en plus détaillés en termes de physique et ont été traduits sous forme de code afin de pouvoir en automatiser leur utilisation. Avec le temps, ce code peut devenir difficile à comprendre et peut demander de plus en plus de temps pour être modifié ; il est donc de plus en plus coûteux de le conserver et de l'entretenir sous cette forme. Des approches développées par des universités ont également été entreprises, comme UMARC (University of Maryland, USA), MBDyn (Politecnico di Milano, Italie) et DYMORE (Georgia Institute of Technology, USA), voir également* (Johnson, 2013). *Cependant, il n'y a pas de consensus jusqu'à maintenant, dans la manière d'approcher la modélisation et la simulation du comportement de systèmes comme les aéronefs à voilure tournante.*
Parallèlement aux besoins de modélisation, un besoin d'égale importance est de savoir comment analyser de tels modèles, et plus particulièrement en termes de stabilité aéroélastique. Jusqu'à maintenant la plupart des analyses pratiquées dans la communauté des voilures tournantes sont des analyses basées sur des modèles linéaires. Néanmoins, comme décrit précédemment, l'utilisation entre autres de nouveaux matériaux et de géométries complexes de pales (Friedmann, 2004), *va entrainer un besoin croissant d'analyse de la stabilité à partir de modèles non linéaires. Des avancés récentes vont dans cette direction. Dans* (Tamer & Masarati, 2015) *et* (Wang, Shan, Bin, & Bauchau, 2015), *le calcul des Exposants Caractéristiques de Lyapunov (LCEs) est appliqué à l'étude de la stabilité aéroélastique de systèmes, et notamment d'hélicoptères, directement à partir de modèles non linéaires.*

Afin de formaliser le problème, la chaire industrielle « Dynamique des systèmes mécaniques complexes » (2010-2015) propose d'identifier les caractéristiques générales de ***systèmes complexes*** *tels que les hélicoptères :*

1. *Ils possèdent un* ***grand nombre de sous-systèmes*** *en interaction*
2. *Ils sont caractérisés par une forte* ***interaction Homme-Machine***
3. *Ce sont des systèmes* ***multiphysiques***
4. *Qui peuvent avoir des* ***comportements non linéaires*** *comme le développement de cycle limite*
5. *Et finalement ce sont des systèmes dont les équilibres sont* ***potentiellement instables***

Il est à noter que cette chaire industrielle est la première de l'Ecole d'Arts et Métiers ParisTech, et a été créée à Aix-en-Provence avec le soutien financier de la Fondation d'entreprise Airbus Group.
Concernant l'aspect scientifique, cette chaire étudie l'utilisation d'une approche complémentaire aux approches plus classique de la communauté « hélicoptère ».

C'est une approche énergétique par bond graphs (BGs), dont certains de ces intérêts sont rappelés ici. Les bond graphs sont des représentations graphiques de systèmes physiques dans lesquelles les sous-systèmes, représentés par des éléments énergétiques, échangent de la puissance à travers des ports (Dauphin-Tanguy, 2000), (Karnopp, Margolis, & Rosenberg, 2012), (Borutzky, 2009). *Etant donné que la puissance est le 'langage naturel de communication' entre tous les domaines de la physique, les BGs peuvent être vu comme un langage unifié lorsqu'il s'agit de représenter à la fois des comportements mécaniques, hydrauliques et électromagnétiques. Les BGs facilitent donc la modélisation de systèmes multiphysiques. De plus, une modélisation par BG est connue pour permettre une* ***approche structurelle de la modélisation*** (Chikhaoui, 2013). *On entend par approche structurelle que les frontières du système physique ainsi que les frontières de ses sous-systèmes apparaissent explicitement sur le bond graph du système en question. Cette caractéristique des BGs est également parfois qualifiée de* ***modulaire*** (Boudon, 2014) *; la Figure 1-9 illustre ce potentiel. Il est attendu de cette méthode qu'elle donne de la flexibilité dans la modélisation. Ce 'langage commun' pourrait également faciliter l'échange de modèles dans un contexte industriel afin par exemple d'améliorer la conception des interfaces entre les sous-systèmes d'un hélicoptère. On citera, par exemple, les échanges nécessaires entre les dynamiciens et automaticiens qui définissent les lois des systèmes de commande de vol et l'équipe qui s'intéressent aux qualités de vol,* (Chikhaoui, 2013). *Bien que les BGs aient été développés par Henri Paynter en 1961 au Massachusetts Institute of Technology, ses applications dans l'industrie aérospatiale ne sont pas encore répandues: ils ont par exemple été utilisés à la NASA par* (Montgomery & Granda, 2003) *pour obtenir un grand nombre de systèmes d'états qui modélisent un nombre important de configurations possibles du module Zvezda de la Station Spatiale Internationale.*

En revenant à l'approche de la chaire « Dynamique des systèmes mécaniques complexes », sa vision à long terme consiste à vouloir obtenir un modèle global énergétique de l'hélicoptère par l'assemblage des modèles énergétiques de ses sous-systèmes. On peut noter qu'il est déjà possible de retrouver dans la littérature, le sous-système de la chaîne de commande de vol (Martin, 2013), *le sous-système rotor-fuselage dans* (Chikhaoui, 2013) *et le présent mémoire, le sous-système de suspension d'un hélicoptère dans* (Boudon, 2014), *ainsi que le sous-système modélisant le comportement biodynamique du pilote, également dans le présent mémoire de thèse.*

De plus, les modèles deviennent réellement utiles lorsqu'ils peuvent être analysés à un coût acceptable. Dans le cas des RPCs aéroélastiques, le premier besoin est d'être capable d'évaluer les marges de stabilité d'un modèle d'aéronef paramétré par un jeu de variables de conception. Les instabilités qui peuvent apparaître sur un hélicoptère, comme la résonance sol, ou comme il sera démontré dans ce travail les RPCs aéroélastiques, sont des ***instabilités paramétriques*** (Krysinski & Malburet, 2011). *On ne pourra donc en aucun cas les identifier au niveau graphique d'un bond graph, comme suggéré par* (Zeid, 1989) *pour des systèmes et instabilités de nature plus simple. Néanmoins, au niveau graphique d'un BG, la mise en place des causalités (voir l'Appendix 1) permet d'obtenir les équations du système physique. Que ces équations soient obtenues analytiquement ou à l'aide d'un bond graph, le modèle mathématique de ces équations prend la forme d'un*

système d'équations différentielles algébriques (DAEs) (Borutzky, 2009), (Mantegazza & Masarati, 2012). *L'étude de la stabilité de l'équilibre d'un système décrit par un grand nombre de DAE non linéaire est encore une question ouverte.*

Ce dernier paragraphe, synthétise les problèmes qui sont traités dans ce travail et décrit le chemin suivi par chapitre afin de tenter d'y répondre. Dans le but de prédire l'émergence de phénomènes dynamiques, comme des instabilités bio-aéroélastique, sur des aéronefs à voilure tournante, le plus tôt possible dans le processus de conception, une approche énergétique par bond graph est utilisée afin de modéliser et simuler un système dynamique complexe. Les ***chapitres 2 et 3*** *illustrent la traduction de modèles tirés de la littérature en bond graph, d'un modèle aéromécanique d'hélicoptère ainsi que d'un modèle biodynamique de pilote d'hélicoptère. L'objectif du* ***chapitre 3*** *est de développer un modèle prédictif du comportement involontaire du pilote ou « biodynamic feedthrough » (BDFT) suivant l'axe latéral d'un cockpit. L'association des modèles de pilote et d'aéronef au* ***chapitre 4*** *afin de prédire des RPCs aéroélastiques sur les axes latéral et roulis d'un hélicoptère est considérée comme originale. Finalement, l'objectif de ces* ***chapitres 2,3 et 4*** *est d'illustrer comment l'approche par bond graph peut faciliter la modélisation de systèmes complexes. Une analyse de la stabilité au* ***chapitre 4*** *démontre la conjecture, issue de la littérature selon laquelle le mode régressif de traînée est le mode déstabilisé lors de RPCs aéroélastiques sur les axes latéral et de roulis. De plus, les résultats indiquent que le mode progressif de traînée peut également être déstabilisé.*
Finalement, le ***chapitre 5*** *pose les premières pierres d'une méthode, basée sur les fonctions de Chetaev, visant à analyser la perte de stabilité de l'équilibre d'un système dynamique, directement à partir de son modèle mathématique non linéaire à un coût de calcul potentiellement intéressant.*

Rotorcraft designers deliver to their customers a machine capable of flying inside a given flight envelope, which gives limits of speed, altitude and temperature as major constraints. However, when trying to push the limits of this envelop by improving the performance of actual designs, engineers might face the emergence of dynamic phenomena such as *ground resonance*, *air resonance* (Krysinski & Malburet, 2011), *whirl flutter*, or *pilot-induced/assisted oscillations* (PIO/PAO) (Pavel, et al., 2013). This work focuses on this last dynamic phenomenon involving a significant part of the human and the machine, recently renamed by the rotorcraft research community as *Rotorcraft-Pilot Couplings* (RPCs).

A well-documented illustration available in the open literature concerns the Boeing-Bell V-22 Osprey tiltrotor, see Figure 1-1, for which three unstable RPCs were found after flight testing in 1991 in (Parham, Popelka, Miller, & Froebel, 1991).

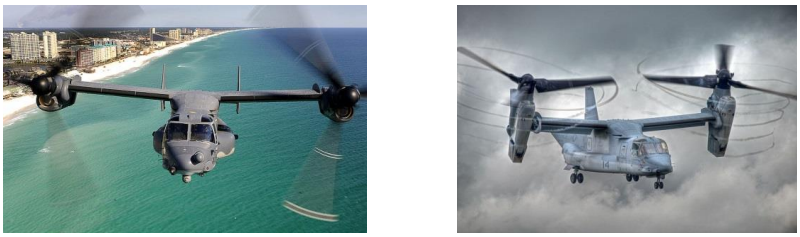

Figure 1-1. Tiltrotor Boeing-Bell V-22 in airplane and helicopter mode (photos: Julianne Showalter, Peter Gronemann)

Two lightly damped modes appeared while on the ground while the last one appeared during flight tests at high speed. The mechanism behind the first two modes was found to be due to a difference of thrust between the two rotors that was the result of an output of the flight control system due to the involuntary movement of the lateral lever by the pilot. These involuntary movements were explained to be induced by the lateral acceleration oscillation of the fuselage and were hardly controllable by the pilot. To increase the damping of the two first modes, the designers added extra mass to the cyclic lever; a reduction of the amplitude of the movements of the stick when the vibrations appeared was obtained. For the 3.4Hz mode, the implemented solution consisted in filtering the pilot's inputs around 3.4Hz using a *notch filter* implemented in the flight control system. While this solution revealed to work efficiently at this frequency[2], it could not have been implemented for the lower frequency modes, since around 1Hz it would filter voluntary and necessary inputs from the pilot for the manual control of the vehicle. Even if it cannot be explicitly correlated, an idea of the magnitude of roll oscillations during a 1991 flight test is illustrated on the video image captures of a duration of 10 seconds see Figure 1-2.

[2] Notch filters have the undesirable effect of adding time delays in the flight control system that need to be taken into account to avoid deteriorating the handling qualities of the aircraft

Figure 1-2. Roll oscillations during flight tests of Boeing-Bell V-22 tiltrotor from (DefenceVideos, 2013)

1.1. Context

1.1.1. Helicopter basics

An explanation of what are the controls a pilot has at disposal and how they act on a helicopter is proposed in the next paragraph, readers who are familiar with rotorcrafts should jump to the next section.
A helicopter has the capability to fly in any spatial direction and perform hover flight, thanks to a variable magnitude and orientation of the rotor thrust vector, see Figure 1-4.

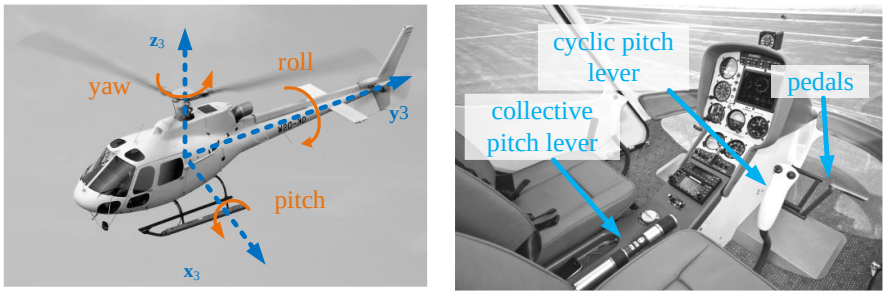

(a). axes definitions (b). cockpit

Figure 1-3. Helicopter and cockpit

The rotor thrust vector is the sum of the individual blade aerodynamic forces. So far, in actual technologies, the rotor angular velocity is maintained constant; as a result the variations of both magnitude and orientation of the thrust vector can only be obtained by modifying the pitch of the main rotor blades. This modification can be done,

- *Collectively*: constant individual blade pitch per rotor revolution. This is achieved by translating vertically the swashplates see (b) Figure 1-4. The norm of the thrust vector is modified by a constant collective blade pitch angle through the *collective pitch lever* see Figure 1-3.

- *Cyclically*: varying individual blade pitch per rotor revolution. This is achieved by changing the orientation of the swashplates see (b) Figure 1-4. For pitch and roll helicopter orientations, the pilot has to modify the *cyclic pitch lever* angles in one or a combination of the two directions Figure 1-3.

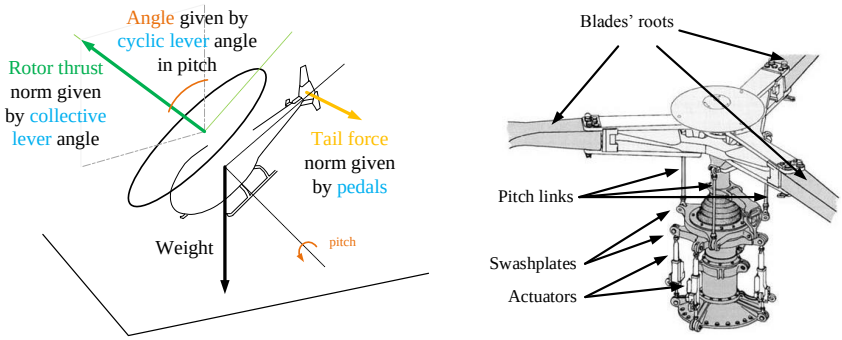

(a). vectorial thrust (b). rotor technology

Figure 1-4. Helicopter main rotor thrust vector and technology

On Figure 1-5, the links are detailed between the cyclic and collective levers to the control of the actuators that will impose the position and orientation of the main rotor swashplates (see (b) Figure 1-4).

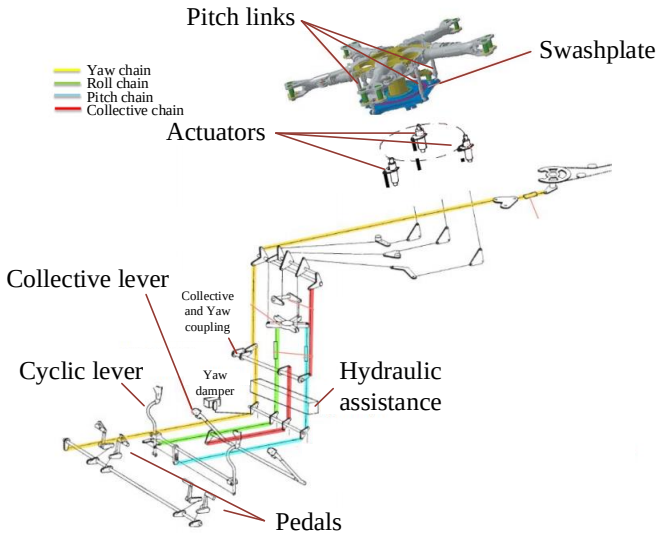

Figure 1-5. Helicopter main rotor flight controls technology from (Martin, 2013)

A particularity of conventional helicopter architectures is that a torque around the yaw axis is generated by the main rotor on the airframe. A tail rotor has to be implemented to counter act this torque thanks to the tail force vector see Figure 1-4. This force vector norm can be adjusted by the pilot thanks to the *pedals* see (b) Figure 1-3.
At this point, the reader should note that all the axis of the helicopter are coupled: a modification of any of the controls (*collective*, *cyclic*, *pedals*) will need an iterative corrective action on all of them. Behind the unique VTOL (Vertical Take-Off and Landing) and hover flight capabilities of helicopters, one can already have an idea of the complexity of the machine. Even if this investigation will focus on conventional helicopters, one should keep in mind the methods used in this work could still be applicable to other rotorcraft architectures such as Figure 1-6 examples.

(a). Sikorsky Aircraft – S-69 (1981)

(b). Airbus Helicopters X^3 (2010)

Figure 1-6. No tail rotor unconventional rotorcraft architectures (photos: Sergeant Lloyd H. Cole, Airbus Helicopters ©)

1.1.2. Bioaeroelasticity

Very practically, the Figure 1-7 shows unusual helicopter roll oscillations that appeared during a flight test many years ago around Marignane airport. The comments in orange were written down by the engineer that compiled the report. What can be seen is that during the flight both pilot and fuselage oscillations are unusually amplified to a certain point (orange arrows) before decreasing. The report states that the pilot inputs seem to be at the origin of the phenomena but that considering the frequency of the signal (>2Hz) it is too high to be a voluntary action of the pilot.

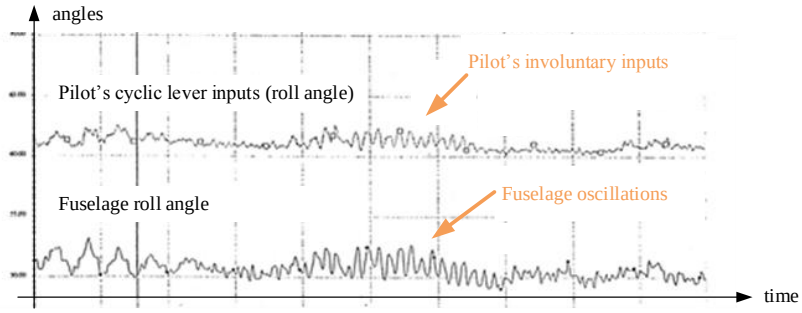

Figure 1-7. Roll oscillations measured during a flight test (Laffisse & Zoppitelli, 1993)

By discussing[3] with a Royal Netherlands Air force Boeing AH-64D Apache pilot, it appeared that sometimes pilots can feel unusual cockpit vibrations while piloting. In some cases they realize they are participating in the vibratory event by for example holding 'too tight' the controls. If they are in a situation in which they can, releasing the controls can help attenuating the phenomena; however this is far from being an acceptable solution.
The first investigations around these kind of phenomena, known as *Aircraft-Pilot Couplings* (APCs) are reported in the fixed wing aircraft industry, for which a general definition is proposed by (McRuer, 1995) these are "*inadvertent, sustained aircraft oscillations which are a consequence of an abnormal joint enterprise between the aircraft and the pilot"*. Recently, the Aristotel (2010-2013) European research project devoted to the investigation of RPCs has categorized the phenomenon into two categories depending on the frequency of the oscillations: 'rigid' below 1Hz and 'aeroelastic' ones between 2 and 8Hz (Pavel, et al., 2013). The term aeroelastic comes from the nature of the forces in interaction: aerodynamic, inertial and elastic[4] forces.

As suggested in (Masarati & Quaranta, 2014), the term *aeroelasticity* is extended to *bioaeroelasticity* when additional forces generated by human biodynamics need to be taken into account.

---

[3] This was possible during a stay at the Delft University of Technology in November 2015
[4] From flexible structures

Due to the harsher vibratory environment of rotorcraft compared to fixed wing aircrafts, rotorcraft designs are more sensitive to aeroelastic phenomena and therefore aeroelastic RPCs. These phenomena have a critical impact on safety since they can be at the origin of undesirable vibrations, limit cycle oscillations or instabilities. Even if RPCs are not always unstable, vibrations and limit cycle oscillations are uncomfortable for the passengers and a source of alternative loads that fatigue the materials and reduce the lifetime of aircrafts, limiting their performances.

So far, most research efforts have concentrated in the prediction of aeroelastic RPCs on the vertical axis of helicopters. In (Mayo, 1989), based on simulator experimental results a vertical pilot biodynamics model is proposed and then coupled to a high order linear helicopter model to simulate potential Pilot-Assisted Oscillations (PAOs) in the vertical axis of helicopters, and to design a filter of selected pilot's inputs capable of alleviating the phenomena. In (Gennaretti, et al., 2013), very detailed helicopter models are developed to predict vertical instabilities associated to PAOs/RPCs. In (Masarati & Quaranta, 2014), detailed nonlinear models of pilot's left arm acting on the collective lever and a helicopter model are coupled to investigate vertical PAOs. This approach constitutes one of the first attempts to predict the involuntary behavior of the pilot using physical principles.

This involuntary behavior has been formalized as quantity known as biodynamic feedthrough. A definition is proposed by (Venrooij, 2014): "*the transfer of accelerations through the human body during the execution of a manual control task, causing involuntary forces being applied to the control device, which may result in involuntary control device deflections*". One can immediately imagine this quantity might appear in any vehicle and not just aircrafts.

It is recognized in (Walden, 2007) that the lateral axis for PAOs tends to be more critical. In (Lantzsch, Hamers, & Wolfram, 2014), the development of a controller is reported to cancel the emergence of a roll oscillatory phenomenon (around 1.8 Hz) when closing the roll rate feedback of a stability augmentation system of an Airbus helicopter H135 (previously known as Eurocopter EC135). A contribution to understanding the physical mechanisms between the potential interactions of an automatic flight control system (AFCS) and lateral helicopter dynamics can be found in (Pavel & Padfield, 2008) and (Pavel M. , 2010), especially about the complex energy flows between blade flap, lag and the airframe roll motion in the presence of an AFCS.

In (Muscarello, et al., 2015), linear aeroservoelastic models were coupled to pilot biodynamic models derived from simulator experimental excitation and compared to flight simulator experimental trials. Interesting conjectures are drawn: "*predictions suggest that the roll/lateral PAO phenomena are more likely to occur on helicopters with soft in-plane rotors that have lightly damped in-plane rotor modes, more sensitive to time delay than gearing ratio with respect to the lateral cyclic control, more dangerous when the flight speed increases and more likely to occur with pilots that are characterized by a natural frequency of the biodynamic poles that is close to the lightly damped in-plane rotor mode*".

On conventional helicopters, aeroelastic RPCs depend on rotor-airframe modes, flight mechanics but also on many subsystems such as the stabilization augmentation system (SAS), flight control system (FCS), flight controls, engine/drive train dynamics and

swashplate actuators, see the potential frequencies of interferences of these subsystems see Figure 1-8 from (Serafini, 2008). Many rotorcraft designs and technologies still suffer from emerging RPCs and from undesirable dynamic phenomena in general. Their alleviation is usually achieved by developing solutions during extensive flight tests. But this process has an important cost and some of the dynamic phenomena such as RPCs might be destructive, presenting a danger for the pilots, passengers and population.

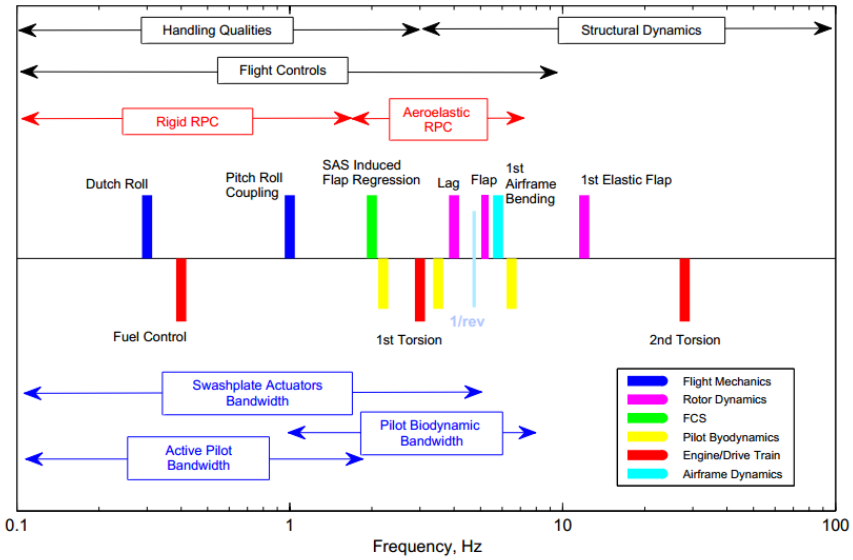

Figure 1-8. Characteristic frequencies[5] of conventional helicopter dynamics, from (Serafini, 2008)

1.2. Towards a global energetic approach of helicopters

There is a considerable interest in being capable of predicting RPCs and other dynamic phenomena as early as possible in the design process of new rotorcrafts to decrease the cost of alleviation of these phenomena thanks to early design modifications. The ideal methods and tools should give the ability to the designer to model the complete rotorcraft with all the relevant subsystems that may interact in RPCs in such a way that he can adapt as efficiently as possible the resolution of a model for a particular problem. In terms of physical resolution, this would imply being able to take into account highly detailed unsteady aerodynamic formulations. And especially their interactions with deformable rotor blades with complex geometries, made of anisotropic materials and a deformable airframe. At the same time, all the relevant biophysical and cognitive characteristics of the pilot should be also modeled

[5] The frequencies are positioned around 1/rev, which is the main rotor angular velocity

and coupled to the previous model by also taking into account the relevant dynamics of the actuation system and its complex kinematics. The modeling method should also be flexible enough to adapt the modeling to any other component and active controls since they will be implemented more in future rotorcrafts.
"Rotorcraft calculations demand the widest possible integration of disciplines, a fact that makes comprehensive analyses challenging", (Johnson, 2013).
Furthermore, RPCs are sensitive to the flight configuration. As a result, the model should have the capacity to represent any given flight configuration and should be validated with experimental results.
Finally, analysis methods should be found to give the possibility to analyze the highly nonlinear resultant mathematical model and be predictive in terms of loads, aeroelastic stability and handling qualities on the rotorcraft flying envelop at the lowest computational cost. It would allow rotorcraft designers to better understand the physical drivers hidden behind such phenomena and lead to solutions to alleviate RPCs.

1.2.1. Problem statement

Rotorcraft designers have been developing predictive numerical tools to better understand the dynamic phenomena they have been discovering through the years and tackle them as early as possible in the design process. The aeromechanical comprehensive tools they have been developing for many years, such as CAMRAD or HOST, (Johnson, 2013) have become more and more detailed in terms of physics and have been translated into code to automate their use. With the years the code might become more and more difficult to understand, more time consuming to modify and therefore more costly to maintain in its form. Academic approaches are also under development, UMARC (University of Maryland), MBDyn (Politecnico di Milano) and DYMORE (Georgia Institute of Technology), see (Johnson, 2013). There is however, no consensus so far, on the approach to model and simulate rotorcraft systems.
In parallel to the modeling capabilities, an important topic is how to analyze such models and in particular in terms of aeroelastic stability. So far most aeroelastic stability analysis in the rotorcraft community are performed using linear stability analysis. However as stated previously, with the implementation of for example new materials and complex blade geometries (Friedmann, 2004), the need to be capable of analyzing the aeroelastic stability of nonlinear models will become more and more important. Recent advances in the rotorcraft community have pushed in this direction; for instance in (Rezgui, Lowenberg, Jones, & Monteggia, 2014), numerical continuation and bifurcation analysis methods are proposed to predict nonlinear stability and have a better understanding of both local and global stability of helicopter systems. In (Tamer & Masarati, 2015) and (Wang, Shan, Bin, & Bauchau, 2015), Lyapunov Characteristic Exponents[6] (LCEs) are used in application to aeroelastic and rotorcraft systems problems to investigate their stability directly from nonlinear models.

[6] LCEs give a quantitative measure of the sensitivity of a dynamical system to initial conditions and are used to measure the chaotic behavior of dynamical systems

Finally, from the above rotorcraft industrial context, the problems that have been raised can be extended to the wide range of systems that can be defined as *complex systems* characterized as proposed by the Dynamics of Complex Mechanical Systems Chair[7] by,

1. A large number of subsystems
2. *Human-machine* interactions
3. Multiphysical
4. Which can exhibit nonlinear behavior such as limit cycle oscillations
5. And potentially unstable

1.2.2. The Dynamics of Complex Mechanical Systems Chair

Rather than trying to replace any existing approaches, the Dynamics of Complex Mechanical Systems Chair has been investigating a complementary approach, based on energetic methods and bond graphs[8] (BGs) in particular.
Bond graphs (BGs) are graphical representations of physical systems in which subsystems represented by energetic elements exchange power through power ports (Dauphin-Tanguy, 2000), (Karnopp, Margolis, & Rosenberg, 2012), (Borutzky, 2009). Since power is the 'natural communication language' between physical domains, BGs can be seen as a single language to represent mechanics, hydraulics, and electromagnetism. As a result, BGs facilitate the modeling of multiphysical systems.
In addition, a BG-based modeling approach is known to be a *structural modeling approach* (Chikhaoui, 2013); in the sense the physical system and subsystems structural frontiers appear explicitly on the bond graph of the system. In other words, the BG modeling approach could also be qualified of a *modular modeling approach* (Boudon, 2014). The Figure 1-9 gives an illustration. This method is expected to give modeling flexibility. This 'common language' could also facilitate model exchanges and therefore simulations in an industrial context to improve the design of interfaces between rotorcraft subsystems like those under the responsibility of dynamicists, flight control designers and handling qualities teams (Chikhaoui, 2013). While bond graphs where firstly developed by Henri Paynter at the Massachusetts Institute of Technology in 1961, its applications in the aerospace industry are not yet wide: it has been used for example at NASA by (Montgomery & Granda, 2003) for its efficiency to obtain a large set of state space systems when modeling the different dynamic configurations of the Zvezda module of the International Space Station (ISS).
With time one could imagine obtaining a global energetic model of helicopters by assembling literature subsystems models developed using energetic approaches such as the flight control subsystem (Martin, 2013), rotor-airframe subsystem (Chikhaoui,

[7] First industrial chair at the engineering school Arts et Metiers ParisTech, Aix-en-Provence, supported by the Fondation Airbus Group from 2010 to 2015.
[8] In the text, *vectorial bond graphs* or *multibond graphs* will be called for simplicity *bond graphs.* The quantities transported by a *vectorial bond* are vectors, of size 3 in this work, and 1 for *scalar bonds*.

2013) and this work, helicopter suspension subsystem (Boudon, 2014), pilot biodynamics subsystem (in this work), etc.

Models become truly useful because when they can be analyzed in a cost efficient way. In the case of aeroelastic RPCs, the first major need is to be able to deduce the impact of rotorcraft design parameters on its stability. Since the instabilities that might appear in rotorcraft systems such as *ground resonance* or as it will be shown in this work *aeroelastic RPCs* are *parametric instabilities* (Krysinski & Malburet, 2011), one cannot expect to be able to identify them at the level of the structure of a bond graph[9] as proposed for simpler systems in (Zeid, 1989). However, at the graphical level of the bond graph, the augmentation of causality see Appendix 1 allows to obtain the equations of the physical system. Whether obtained purely analytically or by bond graphs, the mathematical model of a multiphysical system takes the general form of a set of *differential-algebraic equations* (DAEs) (Borutzky, 2009), (Mantegazza & Masarati, 2012). The investigation of the stability of equilibrium of a large set of nonlinear DAEs is also an open question.

1.3. Proposal

In order to predict the proneness of rotorcrafts to dynamic phenomena such as bioaeroelastic instabilities as early as possible in their design process, the application of an energetic approach using bond graphs is investigated to model and simulate complex dynamic systems. **Chapters 2 and 3** illustrate how to translate existing literature aeromechanical models of helicopters and pilot biodynamics into bond graphs. Chapter 3 objective is to develop a predictive model of pilot biodynamic feedthrough (BDFT) on the lateral axis. The association of the models on **chapter 4** to predict aeroelastic RPCs in the lateral-roll axes of helicopters is considered original. In the end, these first chapters illustrate how the bond graph method can facilitate increasing the level of detail of a given model.
The results of chapter 4 enlighten how important is the role of the regressing lag mode as conjectured in literature in lateral-roll aeroelastic RPCs. In addition, the results show the advancing lag mode could also be destabilized by pilot involuntary behavior.

Finally on **chapter 5** the first blocks of a method based on Chetaev functions, which can also be energy-based functions, are proposed to analyze the stability of a dynamic system equilibrium, directly from its nonlinear mathematical model, at a potentially interesting computational cost.

[9] The graph level is parameter independent

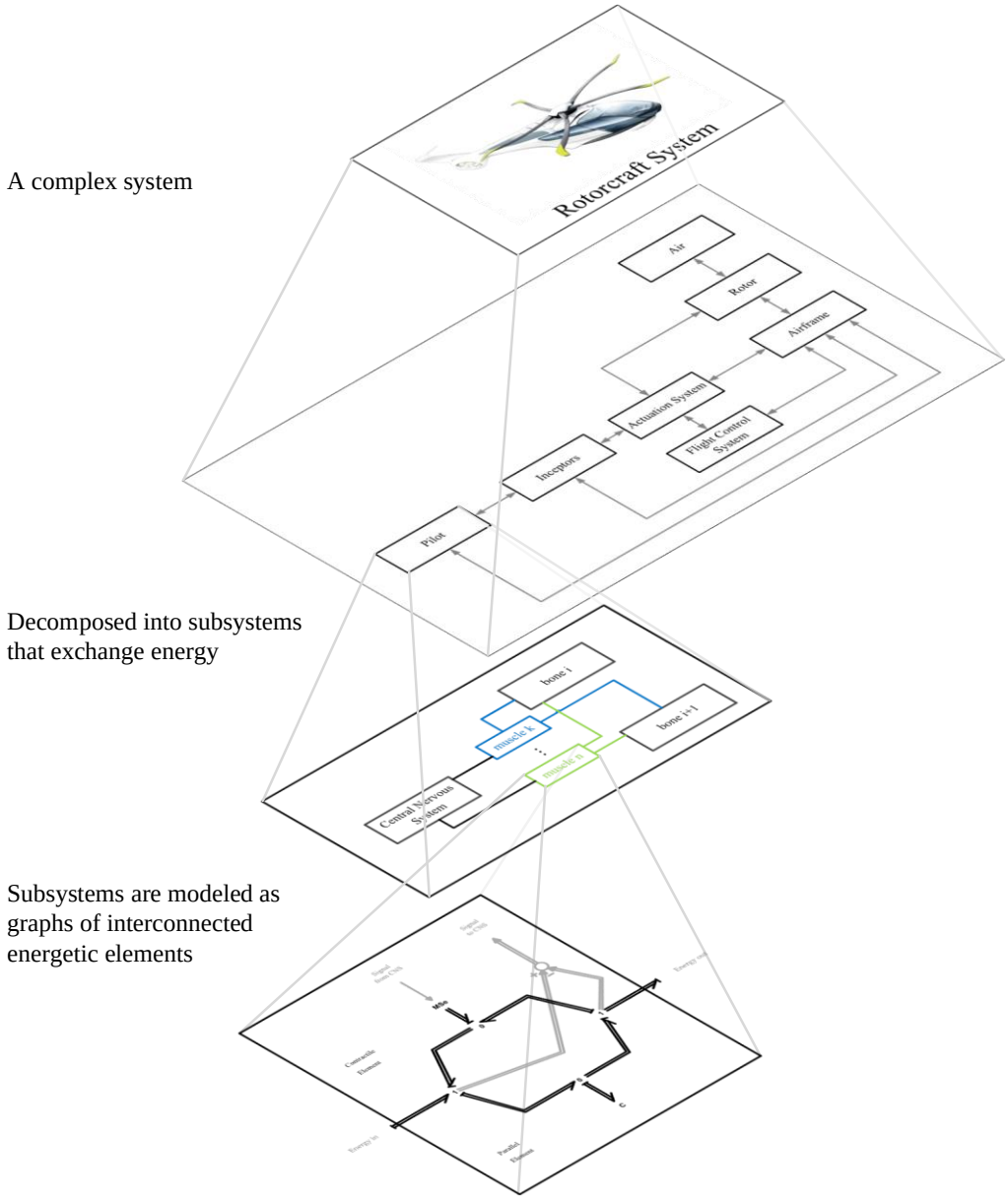

Figure 1-9. Bond graphs for a systems approach of modeling

Chapter 2
Rotorcraft aeromechanical system bond graph

Résumé long du chapitre 2

Dans ce chapitre, un modèle aéromécanique d'hélicoptère est développé et la forme de sa représentation bond graphs justifiée. Dans un deuxième temps, la validité du modèle est discutée.
Comme présenté dans le premier chapitre, les phénomènes de RPCs aéroélastiques se manifestent à des fréquences comprises entre 2 et 8Hz (Pavel, et al., 2013), (Muscarello, et al., 2015). *Le modèle développé doit donc être suffisamment représentatif du comportement de l'hélicoptère dans cette plage de basses fréquences. Le premier sous-système qui doit être modélisé, au cœur des comportements dynamiques les plus importants de l'hélicoptère, est le sous-système rotor-fuselage. Dans la plage de fréquences de notre intérêt, le fuselage comme les pales du rotor peuvent être considérés comme des solides rigides* (Bielawa, 2006). *En ce qui concerne les degrés de liberté du fuselage, celui-ci peut translater latéralement et verticalement ainsi que changer d'orientation autour de son axe de roulis, voir ces trois degrés de libertés sur la Figure 2-2. Chaque pale du rotor possède également trois degrés de libertés : battement (« flap »), traînée (« lag ») et pas (« pitch), voir la Figure 2-3. De plus, il est supposé que le rotor tourne à vitesse constante ; cette vitesse est notée tout au long du manuscrit Ω. Le type de rotor modélisé correspond à une technologie particulière qui est celle des rotors articulés, voir Figure 2-1. Pour ce type de rotor, un amortisseur, dit de « traînée » (« lag damper ») est installé entre le manchon en pied de pale et le moyeu du rotor, voir Figure 2-1, afin d'atténuer les phénomènes de résonance sol et air* (Krysinski & Malburet, 2011). *Les hypothèses de modélisation proposées ici sont classiques par rapport à ce que l'on peut retrouver dans la littérature et notamment dans* (Donham, 1969), (Takahashi & Friedmann, 1991) *et* (Krysinski & Malburet, 2011). *Afin d'obtenir les équations du mouvement, il est proposé, comme dans* (Chikhaoui, 2013)*, de les représenter à l'aide de bond graphs vectoriels, appelés également multibond graph (MBG). Il existe plusieurs alternatives pour obtenir les équations du mouvement. Il est choisi ici de s'appuyer sur une approche multicorps, particulièrement adaptée à la description de systèmes d'ingénierie. L'approche multicorps consiste à décomposer un système en corps rigides ou flexibles, reliés entre eux par des liaisons et sur lesquels peuvent s'appliquer des forces extérieures de nature quelconque* (Eberhard & Schiehlen, 2006). *Lorsqu'il est choisi de représenter un système mécanique de corps rigides, par une approche multicorps à l'aide des équations de Newton-Euler, à l'aide de coordonnées relatives, un intérêt des MBG apparait. En effet, la représentation en MBG de chacun de ces corps rigides possède une structure graphique identique. Ceci a été démontré pour la première fois dans* (Tiernego & Bos, 1985)*. L'intérêt d'avoir à disposition une structure graphique identifiée est que cela permet de construire le*

graphique d'un système mécanique constitué de plusieurs corps rigides sans avoir la nécessité d'écrire la moindre équation et de procéder par 'copier-coller' de cette fameuse structure, voir Figure 2-5. Cet intérêt a été exploité dans un grand nombre de domaines, et notamment afin de modéliser un robot à segments flexibles (Maschke, 1990)*, ou encore la marche humaine* (Hernani, Romero, & Jazmati, 2011) *et plus récemment dans notre laboratoire, en application aux hélicoptères, un système rotor-fuselage* (Chikhaoui, 2013) *et un système de suspension d'hélicoptère* (Boudon, 2014). *Etant donné que l'exploitation de la représentation MBG de corps rigides par les équations de Newton-Euler est utilisée dans tous les modèles développés dans ce manuscrit, qu'il s'agisse du couplage rotor-fuselage ou du modèle biomécanique du bras du pilote, il est proposé de redémontrer la forme de la structure du graph, présentée en Figure 2-5. Cette démonstration, voir les équations (1) à (16), n'utilise pas les notations proposées dans* (Tiernego & Bos, 1985)*, mais plutôt celles utilisées dans l'approche analytique de* (Lamoureux, 1992).

Avec cette approche, l'obtention des équations du mouvement d'un système complexe est facilitée. Néanmoins, comme souvent en mécanique, plus les équations son faciles à obtenir et plus le modèle mathématique associé est 'compliqué' : ici, non seulement des équations différentielles ordinaires (ODEs) apparaissent mais également des équations différentielles algébriques (DAEs). Ceci est dû à la redondance des coordonnées et aux contraintes entre corps. Sous la forme de DAEs, un système d'équations linéaires ne peut pas être représenté sous forme d'état d'une manière systématique, ce qui limite les possibilités d'analyse d'un tel système et de son utilisation dans une boucle de contrôle actif en temps réels. De plus, dans le cas général où les équations sont non linéaires, des stratégies particulières doivent être employées afin, soit de transformer les DAEs en ODEs, soit d'intégrer directement les DAEs à l'aide d'une méthode numérique adaptée, comme par exemple, Runge-Kutta implicite ou Backward Differences, voir (Cuadrado, Cardenal, & Bayo, 1997), (Pennestri & Vita, 2004), (Mantegazza & Masarati, 2012).

En ce qui concerne la représentation des liaisons entre corps, une librairie est proposée dans (Zeid & Chung, 1992) *et* (Favre, 1997). *Dans notre cas, les deux types de liaisons nécessaires sont les pivots et les rotules, voir Figure 2-6. Les différentes manières d'imposer des contraintes sont présentées Figure 2-7. Une contribution à la représentation en BG de l'enchaînement de trois liaisons pivots est notamment proposée. La structure du graph est présentée Figure 2-9. Celle-ci permet notamment de supprimer trois équations algébriques et donc de faciliter la résolution numérique du système d'équations par une intervention au niveau graphique. Ce type de liaison, avec un enchaînement de trois liaisons pivots est notamment utile lorsqu'il s'agit de représenter la liaison entre chaque pale et le moyeu d'un rotor articulé, voir Figure 2-1, Figure 2-3 et Figure 2-8.*

Une fois le modèle rotor-fuselage mis en place, les efforts extérieurs, et notamment, les efforts aérodynamiques qui s'appliquent sur les pales du rotor doivent être représentés. Ces efforts jouent un rôle central dans le comportement aéroélastique de l'hélicoptère. Etant donné la faible fréquence, à laquelle les phénomènes auxquels nous nous intéressons apparaissent, une hypothèse acceptable est de considérer ces efforts comme quasi-statique et s'appliquant sur une ligne portante le long de l'envergure d'une pale (Bielawa, 2006)*, voir Figure 2-10. De plus,*

comme justifié dans (Dryfoos, Kothmann, & Mayo, 1999), *la vitesse induite est négligée car sa dynamique est bien plus rapide que celle de notre intérêt. Le même article, précise qu'une approximation du nombre de Lock (définition autour de l'équation (29)) entre 60 et 70% de sa valeur totale permet d'en tenir compte d'une manière acceptable. Etant donné que les pales sont considérées comme rigides à basses fréquences, il n'est pas nécessaire de les discrétiser spatialement. Néanmoins, il est très souvent nécessaire de tenir compte de caractéristiques aérodynamiques différentes le long de l'envergure de la pale, notamment à cause du vrillage de celle-ci ou de leurs géométries spécifiques. Un modèle d'efforts aérodynamiques quasi-statiques s'adaptant aux caractéristiques aérodynamiques variables le long de l'envergure d'une pale est alors proposé, voir équations (23) à (35) et représentation BG Figure 2-11. Le modèle obtenu impose de discrétiser le champ des vitesses le long de l'envergure de la pale, raison pour laquelle la représentation en MBG est constituée de* ***n branches****. Ce modèle permet de plus, de tenir compte de l'éventuelle vitesse d'avancement de l'appareil sans avoir à modifier le graph. En effet, la vitesse des pales par rapport au référentiel galiléen est obtenue à partir de la représentation MBG des équations de Newton-Euler. Ce modèle est considéré comme une contribution.*

Une fois les modèles du sous-système rotor-fuselage et des efforts aérodynamiques assemblés, on obtient un modèle aéromécanique de l'hélicoptère par bond graph, voir Figure 2-15. A l'aide de ce modèle, il est théoriquement possible de simuler différentes phases de vol comme le vol stationnaire ou d'avancement. Afin de s'assurer de la validité du modèle, il serait nécessaire de comparer des résultats de simulation du modèle avec d'autres modèles eux-mêmes valides ou avec des résultats d'essais. Il est néanmoins presque aussi difficile d'apprendre le langage des bond graphs que d'avoir accès à un modèle valide ou des résultats d'essais dans la communauté des hélicoptéristes. En l'absence de ces informations, il est proposé de vérifier la cohérence du modèle aéromécanique proposé en trois étapes. La première étape consiste à vérifier le comportement du modèle d'efforts aérodynamiques. Pour cela, le comportement d'une pale en battement soumise à des efforts aérodynamiques est étudié. D'un côté, l'équation (36) représente l'équation linéaire en battement. De l'autre, le modèle aéromécanique développé précédemment est simplifié de la manière suivante : les degrés de liberté du fuselage sont supprimés ainsi que le degré de liberté en traînée de chaque pale. On obtient ainsi un rotor, constitué de 4 pales articulées en battement. Une excitation sinusoïdale en pas collectif variant de 0 à 12 Hz est appliquée aux deux modélisations (équation linéaire du battement d'une pale et modèle bond graph simplifié) et reportée sur la Figure 2-17. Afin de s'assurer, que plus le pas de discrétisation du champ des vitesses des pales par rapport au repère galiléen, est grand, plus les résultats convergent. On fait varier ce pas de discrétisation entre 5 et 20 éléments. La table 2 permet également de vérifier que l'effort de portance statique des deux modélisations de rotors sont proches, et de plus en plus proche avec l'augmentation du pas de discrétisation.

La deuxième étape de la validation est légèrement plus ambitieuse car elle vise la comparaison du modèle sur l'axe vertical de l'hélicoptère à des résultats d'essais au sol, Figure 2-18 et Figure 2-19. Le modèle précédent est réutilisé en libérant le degré de liberté vertical du fuselage. Un couple formé d'un ressort et d'un amortisseur linéaires en parallèle est introduit entre le fuselage et le sol,

représentant ainsi raideur et amortissement du train d'atterrissage. Dans l'expérience menée chez Airbus Helicopters, l'hélicoptère est posé au sol, son rotor tourne et il est demandé au pilote d'exercer une commande de pas collectif sinusoïdale d'amplitude constante et d'une fréquence variant entre environ 0 et 10 Hz. En parallèle, l'accélération verticale du fuselage est mesurée, voir Figure 2-18. Ensuite le rapport entre l'amplitude des accélérations du fuselage et de l'accélération du manche de pas collectif est tracé, voir Figure 2-19. La courbe rouge reproduisant les conditions de l'expérience. On peut voir que l'amplitude est étonnamment proche de ce qui a été mesuré expérimentalement, et que la fréquence du pic résonnant sur cet axe n'est décalée que d'un demi-hertz. Ces deux comparaisons permettent ainsi de valider le modèle aéromécanique proposé sur l'axe vertical de l'hélicoptère.

Un des intérêts majeurs de ce modèle est qu'il permet d'étudier le phénomène de RPC aéroélastique connu sous la terminologie anglaise de 'vertical collective bounce'. Ce phénomène est le résultat du couplage entre le mode vertical du fuselage posé sur son train, avec le mode collectif de battement des pales du rotor, ainsi qu'avec le mouvement du bras gauche du pilote, qui déplace le manche de pas collectif, sous l'effet des vibrations verticales du cockpit. Ce comportement bio-aéroélastique étant le plus étudié dans la littérature, (Mayo, 1989), (Masarati & Quaranta, 2014), (Muscarello, Quaranta, & Masarati, 2014) *et* (Orlita, 2015), *ce manuscrit se concentre de manière complémentaire sur le comportement bio-aéroélastique de l'hélicoptère sur ses axes latéral et de roulis.*

Ainsi, la dernière étape de validation du modèle, consiste à libérer deux degrés de liberté supplémentaires du fuselage : la translation suivant l'axe latéral et la rotation autour de l'axe de roulis. L'axe vertical du fuselage est libre, le train d'atterrissage n'est plus représenté, le pas collectif des pales à l'équilibre est constant et non nul, l'hélicoptère est en vol stationnaire. De plus, chaque pale possède un degré de liberté de plus : celui dit de « traînée », voir Figure 2-3. Malheureusement, aucun résultat d'essais n'était disponible afin de vérifier le comportement autour de cet axe. On peut néanmoins vérifier la cohérence physique du modèle que nous proposons vis-à-vis du principe de Hamilton. Pour cela, il est proposé de comparer le modèle BG avec un modèle obtenu à partir des mêmes hypothèses en utilisant les équations de Lagrange. Celui-ci est développé en Appendix 2. Ceci ne garantit pas la validité du modèle vis-à-vis de l'expérience, mais permet au moins de vérifier que les deux modèles respectent bien la même loi physique. Le modèle obtenu à partir des équations de Lagrange est linéarisé autour de la position d'équilibre, qui est un vol stationnaire. L'équation (A2.2) en Appendix 2 montre que l'axe vertical de l'appareil est, avec les hypothèses choisies ici, découplé des mouvements cycliques de l'appareil. Ceci ne serait certainement pas le cas si le rotor de queue avait été modélisé. Il est donc décidé de supprimer le degré de liberté du fuselage en translation sur son axe vertical. Des balayages d'amplitude constante à une fréquence variable entre 0 et 10 Hz sur le manche de pas cyclique sont effectués sur les deux modèles. Les résultats présentés en Figure 2-26 sont suffisamment satisfaisants pour pouvoir, dans le futur, les confronter à des résultats d'essais en vol.

In this chapter, first the development of a helicopter aeromechanical model using bond graphs is presented. Then its validity is discussed.

2.1. Rotor-airframe model using multibody dynamics

A central coupling to be modeled in rotorcraft dynamics is the rotor-airframe one. This coupling is at the heart of the most classic aeroelastic phenomenon in helicopters such as *ground resonance, air resonance* (Krysinski & Malburet, 2011). Many historical analytical models of this coupling can be found in literature in (Takahashi & Friedmann, 1991) and with a minimalistic number of degrees of freedom in (Krysinski & Malburet, 2011). To avoid these phenomena (Donham, 1969), (Krysinski & Malburet, 2011) a damper is introduced in articulated rotor systems around the lag axis between blades and hub to damp the amplitude of blade lag, see Figure 2-3, movement and position the frequency of its oscillations.

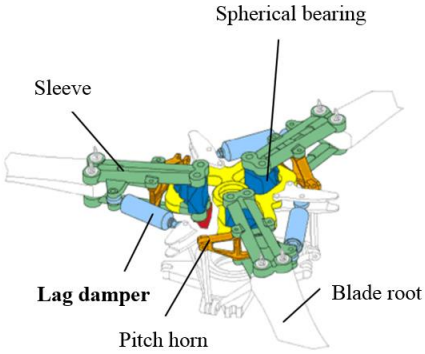

Figure 2-1. Articulated rotor technology

The design of this lag damper is a major concern for rotorcraft designers and it is chosen here to model it with linear characteristics. Since lateral-roll RPCs are known to appear at relatively low frequencies, between 2 and 8Hz (Pavel, et al., 2013), (Muscarello, et al., 2015) the blades and fuselages can be considered as rigid bodies. Modeling them as rigid bodies is an acceptable approximation (Bielawa, 2006) to capture the relevant dynamics at low frequencies, around 3Hz. The fuselage is given 3 degrees of freedom centered on its center of gravity: roll, lateral translation and vertical translation, see Figure 5. Choosing these degrees of freedom allows the center of gravity to have a planar movement, normal to $\mathbf{y}_3$ see Figure 2-2.

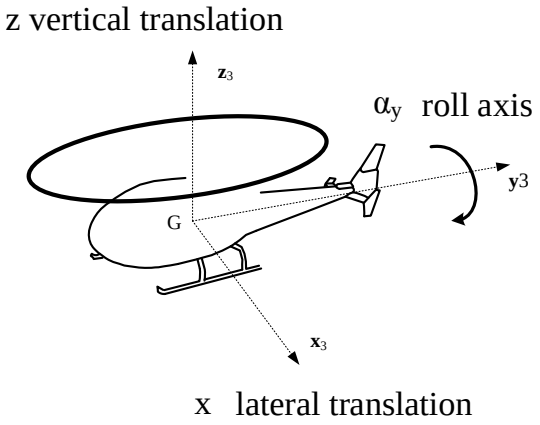

Figure 2-2. Airframe axis definitions

Each blade of the rotor is allowed to flap, lag and pitch see Figure 2-3. In (Pavel, et al., 2013) the flap-lag and blade torsion coupling is mentioned to be modeled when investigating high load maneuvers. It is important to mention too, that during the same high load factor maneuvers, hingeless soft-in plane rotors lag dampers lose their damping and stiffness characteristics decreasing the damping of the flap-lag coupling. In this approach the coupling with blade torsion is however neglected.

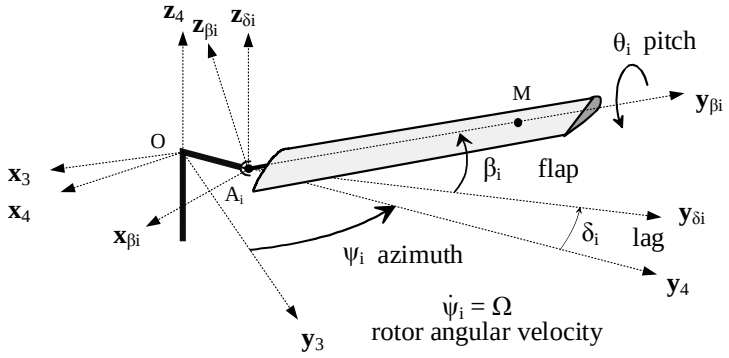

Figure 2-3. Rotor *i*th blade axis definitions

In this section, classic assumptions have been adopted for the mechanical part. In the next, the development of the bond graph to this modeling assumption is presented as well as the aerodynamic model.

2.1.1. Multibody dynamics and Newton-Euler equations in bond graphs

There are many alternatives to derive the equations of motion of systems based on Newton's laws, Hamilton's principle, from which Lagrange equations can be derived or d'Alembert's principle. While in Newton's laws quantities are expressed in terms of vectors (force, momentum, angular momentum) in Lagrangians dynamics the vector quantities are substituted by scalar quantities (energy and work). A major difference between the two formulations results in the choice of coordinates one can make. In the case of Lagrangian dynamics, generalized coordinates of the system are defined globally for the system and eliminate the interaction forces resulting from constraints between elementary parts of the system (Preumont, 2013). When applying Newton laws one has more freedom in the choice of coordinates: each elementary part of the system coordinates' can be chosen as dependent or independent from other elementary parts coordinates'.

Since our interest is on engineering systems, a natural way of describing them is by using multibody dynamics in which the physical system is replaced "*by rigid and or/flexible bodies, joints, gravity, springs, dampers and position and/or force actuators*" (Eberhard & Schiehlen, 2006). The constrained system is then disassembled as free body systems using an appropriate number of inertial, moving reference and body fixed frames for the mathematical description (Eberhard & Schiehlen, 2006). When it comes to the bond graph method a procedure is proposed in (Karnopp D. , 1977), (Favre, 1997) to obtain the bond graph of a multibody system using generalized coordinates. The main drawback of this procedure (Favre, 1997) is that it demands a priori derivation of equations by hand before obtaining the bond graph. Another approach, more systematic (Tiernego & Bos, 1985), (Favre, 1997) in the sense there is no need to identify generalized coordinates or derive a priori any equations by hand is first proposed by (Tiernego & Bos, 1985). It is based on the fact that, when representing a multibody system of rigid bodies using Newton-Euler equations using bond graphs, a pattern appears. It can therefore be reproduced, copied, connected without the need to derive any equation by hand. In this representation the coordinates are *relative* coordinates[10]. The application of this procedure has been used to investigate a flexible robot dynamics (Maschke, 1990), human gait modeling (Hernani, Romero, & Jazmati, 2011), and more recently in our laboratory on helicopter applications: a rotor-airframe system (Chikhaoui, 2013) and a helicopter suspension system (Boudon, 2014).

When modeled with such procedure, the equations of motion can be obtained relatively easily. However, as often in mechanics, the easier the equations of motion are obtained, the more complex the mathematical models are: not only Ordinary Differential Equations (ODE) appear but also Differential Algebraic Equations (DAEs). This is due to the redundancy of coordinates and the implementation of constraints. Under the form of DAEs, a set of linear equations cannot be set in a systematic manner into state-space form, drastically limiting the possibilities to analyze the model or use it in a closed loop for real time calculation. And when the equations are nonlinear, which is the case when dealing with large displacements and

[10] A discussion about the choice of coordinates is out of the scope of this work

complex engineering systems, special strategies have to be used to either transform the DAEs into ODEs or to directly integrate the DAEs with an adapted numerical method such as Backward Differences or Implicit Runge-Kutta, (Cuadrado, Cardenal, & Bayo, 1997), (Pennestri & Vita, 2004), (Mantegazza & Masarati, 2012).
Without being exhaustive about how to model any system using bond graphs for which one can find excellent explanations in (Karnopp, Margolis, & Rosenberg, 2012), (Borutzky, 2009), the modeling of a multibody system in a systematic way is presented following the approach of (Tiernego & Bos, 1985). Using a systematic approach has of course the advantage of being applicable to a large class of problems but the drawback of probably not being the most computationally efficient for a particular problem.

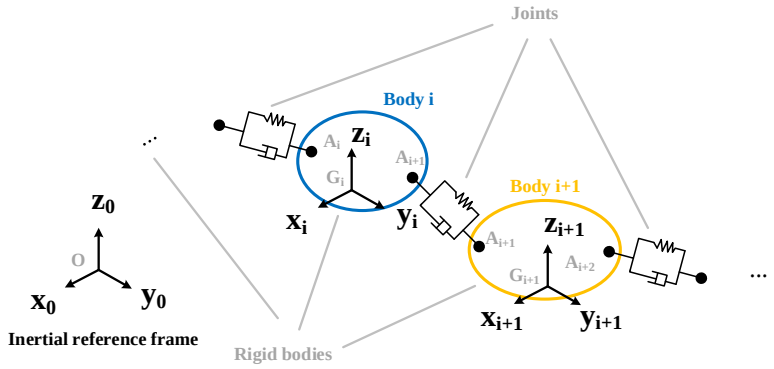

Figure 2-4. A multibody system

To simplify the resulting bond graph from the development of the equations of a multibody system and without loss of generality, one can see on Figure 2-4 that a reference frame has been associated to each rigid body which is chosen to be its principal reference frame and therefore attached to its center of mass.

Step by step, Newton-Euler equations are derived in such a way that efforts and flows of each power bond of the graph become recognizable on Figure 2-5. Let us first isolate the i^{th} body, by definition (Lamoureux, 1992),

$$\sum \mathbf{M}^{i}_{G_i,ext\to i} = \frac{d}{dt}^{0} \boldsymbol{\sigma}^{i}_{G_i,i/0} \tag{1}$$

$$\sum \mathbf{F}^{0}_{ext\to i} = m_i \frac{d}{dt}^{0} \mathbf{V}^{0}_{G_i,i/0} \tag{2}$$

Now by supposing the body is attached to two bodies, *i-1* and *i+1*, see Figure 2-4,

$$\sum \mathbf{M}^{i}_{G_i,ext\to i} = \mathbf{M}^{i}_{G_i,i-1\to i} + \mathbf{M}^{i}_{G_i,i+1\to i} \tag{3}$$

$$\sum \mathbf{F}^{0}_{ext\to i} = \mathbf{F}^{0}_{i-1\to i} + \mathbf{F}^{0}_{i+1\to i} \tag{4}$$

And decomposing the expressions of the moment of external forces in such a way that the attachment points appear[11],

$$\mathbf{M}^i_{G_i,i-1\to i} = \mathbf{M}^i_{A_i,i-1\to i} + \mathbf{G}_i\mathbf{A}_i{}^i \wedge \mathbf{F}^i_{i-1\to i} \tag{5}$$

$$\mathbf{M}^i_{G_i,i+1\to i} = \mathbf{M}^i_{A_{i+1},i+1\to i} + \mathbf{G}_i\mathbf{A}_{i+1}{}^i \wedge \mathbf{F}^i_{i+1\to i} \tag{6}$$

By calculating the total time derivative (in the inertial frame) of the angular momentum expressed in the reference frame of the body, two terms can be identified,

$$\begin{aligned}\frac{d}{dt}{}^0\,\boldsymbol{\sigma}^i_{G_i,i/0} &= \frac{d}{dt}{}^i\,\boldsymbol{\sigma}^i_{G_i,i/0} + \boldsymbol{\Omega}^i_{i/0} \wedge \boldsymbol{\sigma}^i_{G_i,i/0} \\ &= \frac{d}{dt}{}^i\,\mathbf{I}_{G,i}\boldsymbol{\Omega}^i_{i/0} + \boldsymbol{\Omega}^i_{i/0} \wedge \mathbf{I}_{G,i}\boldsymbol{\Omega}^i_{i/0} \\ &= \underbrace{\mathbf{I}_{G,i}\frac{d}{dt}{}^i\,\boldsymbol{\Omega}^i_{i/0}}_{\text{inertial element}} + \underbrace{\boldsymbol{\Omega}^i_{i/0} \wedge \mathbf{I}_{G,i}\boldsymbol{\Omega}^i_{i/0}}_{\substack{\text{Eulerian Junction Structure}\\ \text{MGY element}}}\end{aligned} \tag{7}$$

It should be noted that $\boldsymbol{I}_{G,i}$ is the inertia matrix of the body around the center of mass of the rigid body expressed in the reference frame of body *i*, that contains the principal axis of the body; the matrix is therefore diagonal.

$$\mathbf{I}_{G,i} = \begin{bmatrix} I_{1,i} & 0 & 0 \\ 0 & I_{2,i} & 0 \\ 0 & 0 & I_{3,i} \end{bmatrix}_{(G,x_i,y_i,z_i)} \tag{8}$$

Concerning the second term that appears, it contains the moments that are generated by gyroscopic effects. This term is responsible for potential precession and nutation motions and plays an important role in the stability of rotor blade and rotor-airframe systems (Bielawa, 2006). The term can be represented in multibond graphs with a modulated multiport gyrator element (MGY) (Borutzky, 2009), which is a power conserving transformation. These moments do not either provide or dissipate energy from the system but result from instantaneous energy transfers (Favre, 1997).

So far, all the efforts of the power junctions of the multibond graph of Figure 2-5 can be determined. In addition, the remaining flows can be determined by expressing the following kinematic relations,

$$\mathbf{V}^0_{A_i,i/0} = \mathbf{V}^0_{G_i,i/0} + \boldsymbol{\Omega}^0_{i/0} \wedge \mathbf{G}_i\mathbf{A}_i{}^0 \tag{9}$$

$$\mathbf{V}^0_{A_{i+1},i/0} = \mathbf{V}^0_{G_i,i/0} + \boldsymbol{\Omega}^0_{i/0} \wedge \mathbf{G}_i\mathbf{A}_{i+1}{}^0 \tag{10}$$

---

[11] More attachment points could be introduced by adding the necessary expressions as the ones above.

The vectorial products presented above are represented in multibond graphs by a transformation element (TF) that contains the following equation,

$$\begin{aligned}\boldsymbol{\Omega}_{i/0}^{i} \wedge \mathbf{G}_i \mathbf{A}_i^{\,i} &= \mathbf{u} \wedge \mathbf{v} \\ &= \begin{pmatrix} a \\ b \\ c \end{pmatrix} \wedge \begin{pmatrix} a' \\ b' \\ c' \end{pmatrix} \\ &= \underbrace{\begin{bmatrix} 0 & c' & -a' \\ -c' & 0 & b' \\ a' & -b' & 0 \end{bmatrix}}_{\mathbf{X}(\mathbf{G}_i \mathbf{A}_i^{\,i})} . \underbrace{\begin{pmatrix} a \\ b \\ c \end{pmatrix}}_{\boldsymbol{\Omega}_{i/0}^{i}}\end{aligned} \tag{11}$$

This leads to,

$$\begin{aligned}\begin{pmatrix} effort_{input} \\ flow_{output} \end{pmatrix} &= \begin{pmatrix} \mathbf{G}_i \mathbf{A}_i^{\,i} \wedge \mathbf{F}_{i-1\to i}^{i} \\ \boldsymbol{\Omega}_{i/0}^{i} \wedge \mathbf{G}_i \mathbf{A}_i^{\,i} \end{pmatrix} \\ &= \underbrace{\begin{bmatrix} 0 & \mathbf{X}(\mathbf{G}_i \mathbf{A}_i^{\,i})^T \\ \mathbf{X}(\mathbf{G}_i \mathbf{A}_i^{\,i}) & 0 \end{bmatrix}}_{\text{TF element}} . \underbrace{\begin{pmatrix} \boldsymbol{\Omega}_{i/0}^{i} \\ \mathbf{F}_{i-1\to i}^{i} \end{pmatrix}}_{\begin{pmatrix} flow_{input} \\ effort_{output} \end{pmatrix}}\end{aligned} \tag{12}$$

The projection from the i^{th} body frame to the inertial reference frame demands to multiply by the rotation matrix from the i^{th} reference to the inertial reference and that accounts for all the intermediary body rotations. For any vector $\mathbf{v}^0$ expressed in the inertial reference frame,

$$\mathbf{v}^0 = \mathbf{M}_{i\to 0} . \mathbf{v}^i \tag{13}$$

The expression of the, rotation matrix from the i^{th} reference to the inertial reference frame being,

$$\mathbf{M}_{i\to 0} = \mathbf{M}_{i\to i-1} \mathbf{M}_{i-1\to i-2} \ldots \mathbf{M}_{2\to 1} . \mathbf{M}_{1\to 0} \tag{14}$$

As a result this transformation is state dependent contrarily to the vectorial product presented before, but also power conservative (Karnopp, Margolis, & Rosenberg, 2012). The representation of this transformation using multibond graphs is the following multiport modulated transformer,

$$\begin{pmatrix} effort_{input} \\ flow_{output} \end{pmatrix} = \begin{pmatrix} \mathbf{F}^{i}_{i-1\to i} \\ \mathbf{\Omega}^{0}_{i/0} \end{pmatrix} = \underbrace{\begin{bmatrix} 0 & \mathbf{M}_{i\to 0}{}^{T} \\ \mathbf{M}_{i\to 0} & 0 \end{bmatrix}}_{\text{MTF element}} \cdot \underbrace{\begin{pmatrix} \mathbf{\Omega}^{i}_{i/0} \\ \mathbf{F}^{0}_{i-1\to i} \end{pmatrix}}_{\begin{pmatrix} flow_{input} \\ effort_{output} \end{pmatrix}} \tag{15}$$

Finally, in Figure 2-5, by multiplying each effort by each flow the power that is being transported by each bond can be expressed. What it is proposed on Figure 2-5 differs from (Tiernego & Bos, 1985) in the positioning of the modulated transformer elements: usually only one element is considered by positioning it just above the bottom one junction. This choice facilitates the implementation of additional external forces in the inertial reference which is critical is our application when implementing muscle forces see 3.3.

Furthermore, the sum of the integration of these quantities at the root of the two inertial elements gives the expression of the kinetic energy T_i that is stored in each rigid body at a time *t*, which is exactly what would be obtained analytically (Lamoureux, 1992) by definition of the kinetic energy of a rigid body in spatial motion,

$$T_i = \frac{1}{2} m_i \mathbf{V}^{0}_{G_i,i/0}{}^{T} . \mathbf{V}^{0}_{G_i,i/0} + \frac{1}{2} \mathbf{\Omega}^{i}_{i/0}{}^{T} . \mathbf{I}_{G,i} . \mathbf{\Omega}^{i}_{i/0} \tag{16}$$

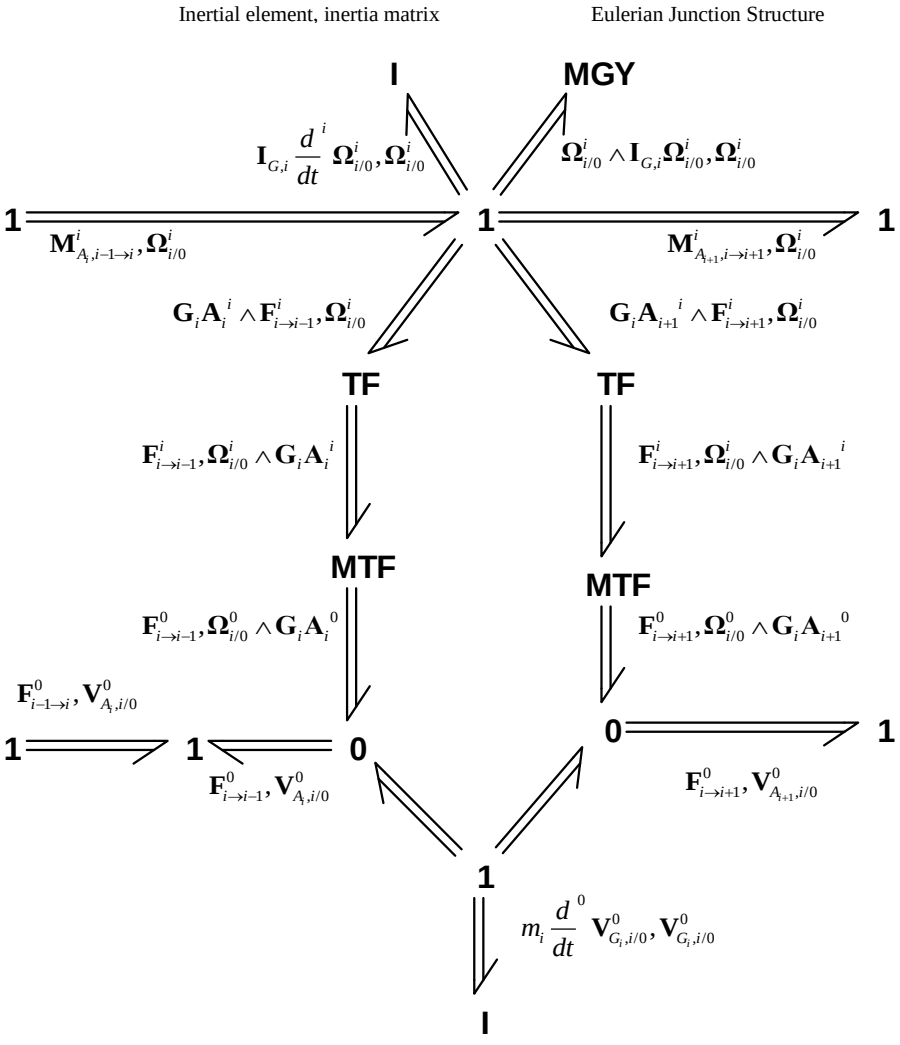

Figure 2-5. Multibond graph of the i^{th} rigid body spatial motion (effort, flow) at each bond

In order to constrain the motion between bodies, a library of joints using multibond graphs can be found in (Zeid & Chung, 1992) and (Favre, 1997). In this work, the modeling of the rotorcraft and pilot subsystems require to be able to model revolute and spherical joints. The modeling of these two joints is presented by illustrating the three main methods available in literature. On Figure 2-6, the structure of the joint between *i* and *i+1* bodies is presented; the power inputs of this graph are the power outputs of the graph on Figure 2-5.

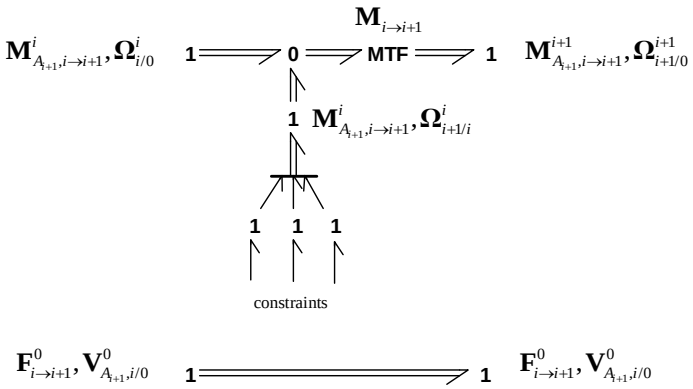

Figure 2-6. Multibond graph structure of a revolute or spherical joint

Revolute and spherical joints constrain all translational degrees of freedom, as a result the forces and velocities (in translation) that enter the joint are the same ones that leave the joint. In the upper part of the multibond graph on Figure 2-6 a zero junction is added to release the constraint on one angular velocity for a revolute joint or on three angular velocities for a spherical joint. In this last case, since no constraints would be enforced, the scalar bond graph one junctions would be just free. In the case of the revolute joint, the natural method to enforce two angular velocity constraints (e.g. around $\mathbf{X}_i$ and $\mathbf{Y}_i$) is to use null sources of flow, see case (a) of Figure 2-7. The consequence of this choice is that automatically after attributing causality (see Appendix 1), the inertial element that stores energy in rotation motion in body *i+1* will be in derivative causality (Van Dijk & Breedveld, 1991), (Tod, Malburet, Gomand, & Barre, 2013), which means that the underlying mathematical model becomes a Differential Algebraic Equations (DAE). Numerical simulations of the model can still be performed with adapted numerical methods (Van Dijk & Breedveld, 1991). Two methods have been proposed (Van Dijk & Breedveld, 1991) to remove derivative causalities that can be applied to joints. The first one consists in replacing the null sources of flow by high stiffnesses and dampers, sometimes called parasitic elements (Van Dijk & Breedveld, 1991). This method removes the derivative causality on inertial elements but the underlying mathematical model will be 'stiff' Ordinary Differential Equations (Van Dijk & Breedveld, 1991) and also has the disadvantage to introduce new state variables and therefore new modes that will perturb the analysis of the system. In addition, there is no systematic method to choose the value of stiffness and damping of these elements; however identified to actual components physical stiffness & damping characteristics. The last method consists in enforcing constraints by Lagrange multipliers (Borutzky, 2009), (Van Dijk &

Breedveld, 1991), which removes the derivative causality but the underlying mathematical model is this time composed of DAEs of index[12] 2 (Van Dijk & Breedveld, 1991), (Borutzky, 2009).

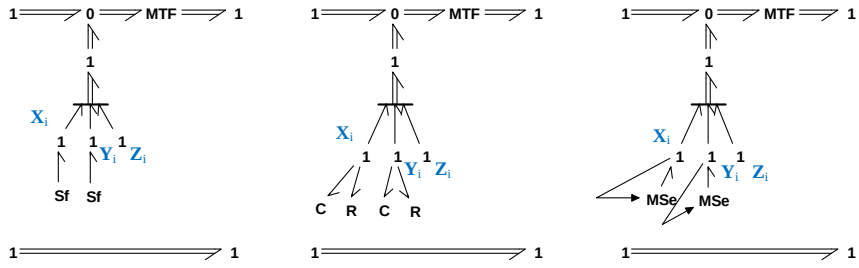

(a). null velocities constraint (b). parasitic elements (c). Lagrange multipliers

Figure 2-7. Three methods to implement joint constraints

A comparison between the three methods and others is proposed on a simple physical system in (Van Dijk & Breedveld, 1991) and the conclusion is that even if the three implementations can be solved by a BDF numerical method, the Lagrange multiplier method *"results are less accurate and the computational effort is higher in comparison to the case where causal paths between inertia ports are accepted and a DAE system of index 1 is solved*" (Borutzky, 2009) about (Van Dijk & Breedveld, 1991).

This section has discussed on how to model a multibody system of rigid bodies using Newton-Euler equations in bond graphs and how to implement constraints using joints. Finally it was shown how the implementation of constraints in joints might lead to a specific mathematical model which is in the general case a DAE system of varying index.

In our application the previously presented modeling method is applied to model the rotor-airframe system which consists in one rigid body for the fuselage and four rigid bodies for the rotor blades. A revolute joint between the airframe and the hub is implemented. Each blade is then attached to the hub through the concatenation of three revolute joints in the following order: first for the lag motion, then flap and finally pitch, see Figure 2-3. A contribution to the modeling of this concatenation is proposed, in the next paragraph that suppresses equation constraints at the graphical level.

[12] Index: number of times the constraint equation has to be differentiated to obtain a system of ODEs (Van Dijk & Breedveld, Simulation of system models containing zero-order causal paths—I. Classification of zero-order causal paths, 1991)

2.1.2. Joint between blade and hub for lag-flap-pitch motions

The proposed representation could be classified with the classic methods of reduction of equations of motion such as transformation of inertial bond graph elements (Van Dijk & Breedveld, 1991), (Borutzky, 2009). This representation has been presented at the iNacomm 2013 conference at the Indian Institute of Technology, Roorkee, see (Tod, Malburet, Gomand, & Barre, 2013).

By attaching the reference frame 4 to the hub, see Figure 2-8 and Figure 2-3, each blade angular velocity is defined as follows,

$$\boldsymbol{\Omega}_{blade/hub} = \dot{\delta}\mathbf{z}_4 + \dot{\beta}\mathbf{x}_\delta + \dot{\theta}\mathbf{y}_\beta \tag{17}$$

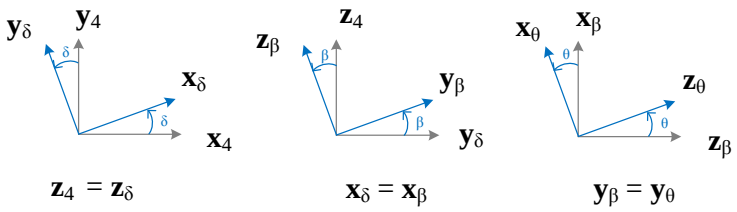

Figure 2-8. Individual blade angle definitions

On Figure 2-9, the concatenation of three revolute joints that represent equation (17) are presented with a 'classic' structure (a) and the proposed structure without the inclusion of any null sources of flow to relax causality (Tod, Malburet, Gomand, & Barre, 2013).

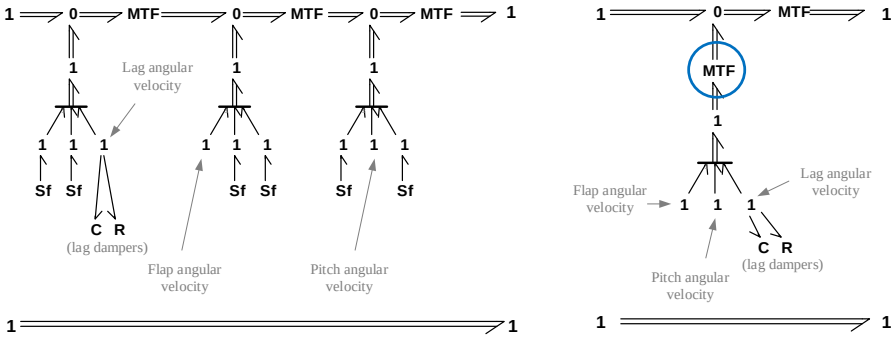

(a). Classic structure (b) Proposed

Figure 2-9. Concatenation of three revolute joints proposal

The use of the proposed structure demands to introduce a modulated multiport transformer element (circled in blue on Figure 2-9) which contains a matrix that has to be derived by projecting all the vectors of the equation (17) in the reference frame 4 (hub). It leads to the matrix below, which is a rotation matrix from a non-orthogonal frame to an orthogonal one,

$$\mathbf{M}_{x_\delta, y_\beta, z_4 \to hub} = \begin{bmatrix} \cos\delta & -\cos\beta\sin\delta & 0 \\ \sin\delta & \cos\beta\cos\delta & 0 \\ 0 & \sin\beta & 1 \end{bmatrix} \tag{18}$$

$$\mathbf{\Omega}^{hub}_{blade/hub} = \mathbf{M}_{x_\delta, y_\beta, z_4 \to hub} \begin{pmatrix} \dot{\beta} \\ \dot{\theta} \\ \dot{\delta} \end{pmatrix} \tag{19}$$

$$\mathbf{MTF} = \begin{bmatrix} 0 & \mathbf{M}_{x_\delta, y_\beta, z_4 \to hub}{}^{T} \\ \mathbf{M}_{x_\delta, y_\beta, z_4 \to hub} & 0 \end{bmatrix} \tag{20}$$

It has been verified analytically in (Tod, Malburet, Gomand, & Barre, 2013) that the proposed structure is also dynamically equivalent to the classic one and illustrated by the simulation of an inertial navigation system. In that example, the proposal allowed to obtain to an ODE system of equations of motion instead of a DAE system improving the computational efficiency. It should be noticed that the proposed rotation matrix is not always invertible for particular angles but that this could be overcome by redeveloping the idea using other definitions for the angles such as quaternions. In our application, angles will not vary more than +/-10° for which this matrix is not singular. Finally the kinematic relation at the zero junction of the proposed joint is simply,

$$\mathbf{\Omega}^{hub}_{hub/0} + \mathbf{\Omega}^{hub}_{blade/hub} = \mathbf{\Omega}^{hub}_{blade/0} \tag{21}$$

As a result the non-circled modulated multiport transformer element of the proposal in Figure 2-9 transforms vectors from the hub reference frame to the blade reference frame,

$$\mathbf{MTF} = \begin{bmatrix} 0 & \mathbf{M}_{hub \to blade}{}^{T} \\ \mathbf{M}_{hub \to blade} & 0 \end{bmatrix} \tag{22}$$

With,

$$\mathbf{M}_{hub\to blade} = \mathbf{M}_{R_\beta \to blade}.\mathbf{M}_{R_\delta \to R_\beta}.\mathbf{M}_{hub\to R_\delta}$$

$$= \begin{bmatrix} \cos\theta & 0 & \sin\theta \\ 0 & 1 & 0 \\ -\sin\theta & 0 & \cos\theta \end{bmatrix}^T . \begin{bmatrix} 1 & 0 & 0 \\ 0 & \cos\beta & -\sin\beta \\ 0 & \sin\beta & \cos\beta \end{bmatrix}^T . \begin{bmatrix} \cos\delta & -\sin\delta & 0 \\ \sin\delta & \cos\delta & 0 \\ 0 & 0 & 1 \end{bmatrix}^T$$

2.1.3. Quasi-steady aerodynamic forces

The previous sections have justified the modeling of the rotor-airframe system. In this section, the modeling of quasi-steady aerodynamic forces applied to each rotor blade is proposed.

Aerodynamic forces play a fundamental role; however their modeling is an ongoing research challenge by itself. More sophisticated approaches include unsteady aerodynamics, stall and free wake geometry models. The aerodynamic forces can be considered in a first approach in the investigation of low frequency phenomena by considering the lifting-line theory with quasi-steady aerodynamics (Bielawa, 2006). In (Dryfoos, Kothmann, & Mayo, 1999) inflow velocity is neglected since the inflow dynamics are expected to be generally faster than the dynamics of interest. In the same paper it is argued that it can be reasonably well approximated by replacing the Lock number with the reduced Lock number: usually between 60 to 70% of the actual Lock number.

Since the bodies represented before are considered as rigid for the dynamics of our interest, there is no need to any spatial discretization in the modeling. However, if flexible bodies where to be modeled, a spatial discretization would have been necessary for which bond graph representations exist (Borutzky, 2009). When modeling a blade, it can be necessary also to take into account for the variable characteristics (such as lift coefficient) of blade sections along their spans. In this case, a discretization of the velocity field along the blade span is necessary. The proposed modeling serves this potential need and has also the advantage leaving the possibility to represent not only hover flight but also forward flight configurations without any aerodynamic model modification.

By considering the point M of a blade section, the local lift force $\mathbf{dF}_{air\rightarrow blade}$, blade pitch angle θ_i, and section incidence angle i, inflow angle Φ and velocity $\mathbf{v}_{air/blade}$ see Figure 2-10.

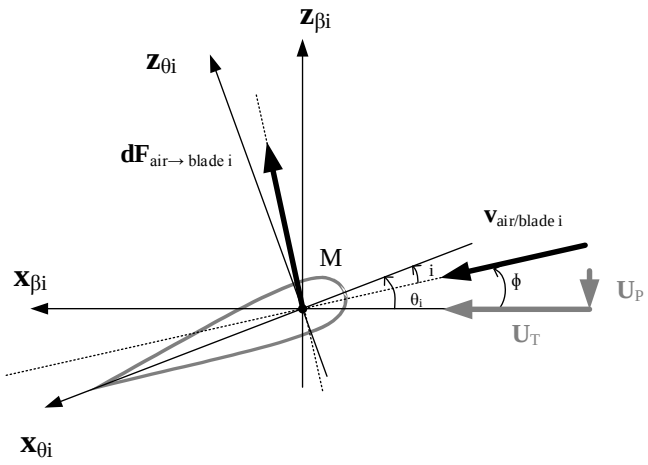

Figure 2-10. Quasi-steady aerodynamics model – per section

The expression of the local lift force is,

$$dF_{air\rightarrow blade} = \frac{1}{2}\rho c C_L \mathbf{v}^2_{air\rightarrow blade} dr \tag{23}$$

Where without considering the inflow velocity and no airframe advancing velocity,

$$\begin{aligned} \mathbf{v}_{air/blade} &= \mathbf{v}_{air/0} - \mathbf{v}_{blade/0} \\ &\quad =0 \\ &= \mathbf{U}_P + \mathbf{U}_T \\ &\approx \mathbf{U}_T \end{aligned} \tag{24}$$

Therefore,

$$\begin{aligned} \mathbf{U}_P &= -\mathbf{v}_{blade/0}.\mathbf{x}_\beta \\ \mathbf{U}_T &= -\mathbf{v}_{blade/0}.\mathbf{z}_\beta \end{aligned} \tag{25}$$

And assuming small incidence angles and small pitch angles,

$$\begin{aligned} i &= \theta - \phi = \theta - \arctan\frac{U_P}{U_T} \\ &\approx \theta - \frac{U_P}{U_T} \end{aligned} \tag{26}$$

The lift coefficient can then be expressed by,

$$C_L = \frac{\partial C_L}{\partial i}.i \approx c_l.i \tag{27}$$

Which leads to the following aerodynamic force expression,

$$dF_{air\to blade} = \frac{1}{2}\rho c c_l \left(\theta {U_T}^2 - U_P U_T\right) dr \tag{28}$$

And by introducing the Lock number γ, which represents the ratio between aerodynamic and inertia forces,

$$\gamma = \rho \frac{c.c_l}{I_{bl}} R^4 \tag{29}$$

$$dF_{air\to blade} = \frac{\gamma I_{bl}}{2R^4}\left(\theta {U_T}^2 - U_P U_T\right) dr \tag{30}$$

The expression of the lift force on the blade would be,

$$F_{air\to blade} = \int_0^R dF_{air\to blade} \tag{31}$$

The integral can then be approximated using the rectangle method,

$$\int_0^R dF_{air\to blade} = \lim_{n\to+\infty} \frac{R}{n} \sum_{k=0}^{n-1} \frac{dF_{air\to blade}}{dr}(k) \tag{32}$$

This finally becomes, for *n* large enough,

$$\int_0^R dF_{air\to blade} \approx \frac{R}{n} \sum_{k=0}^{n-1} \frac{dF_{air\to blade}}{dr}(k) \tag{33}$$

With,

$$\frac{dF_{air\to blade}}{dr}(k) = \frac{\gamma(k) I_{bl}}{2R^4}\left(\theta U_T(k)^2 - U_P(k) U_T(k)\right) \tag{34}$$

Finally, the moment of the forces can be expressed analytically at the blade root A,

$$\int_0^R \mathbf{AM} \wedge \mathbf{dF}_{air\to blade} \approx \frac{R}{n} \sum_{k=0}^{n-1} \mathbf{AM}_k \wedge \frac{d\mathbf{F}_{air\to blade}}{dr}(k) \tag{35}$$

By the way the multibond graph of a rigid body was generated, see Figure 2-5, the previous moment has to be expressed not at the blade root A but around the center of mass of the blade. This leads to a multibond graph representation that has *n* branches for which only the k^{th} one has been represented; the two horizontal bonds, see Figure 2-11, transport the power input from the blade multibond graph, see Figure 2-5.

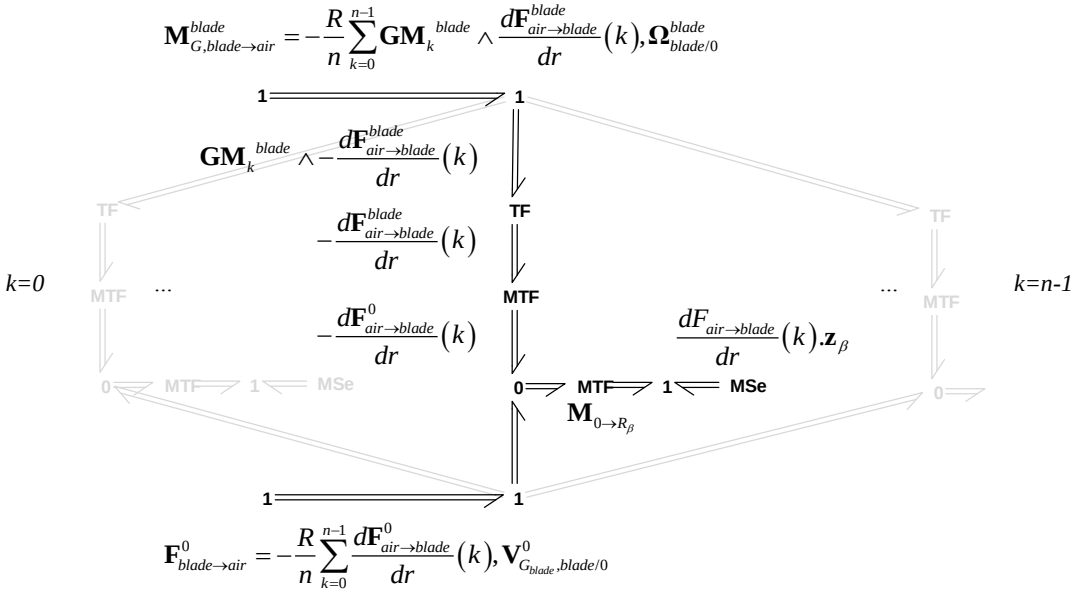

Figure 2-11. A flexible model to represent quasi-steady aerodynamic forces by spatial discretization of the blade velocity field along its span

2.2. Aeromechanical model validity

In this section, the validity of the rotorcraft model constructed previously is discussed in three steps. First, a rotor, with flapping blades including aerodynamic forces, attached to the ground is verified against the classic flapping equation (36). Then this rotor is attached to a rigid body fuselage with one vertical degree of freedom and compared with an identification experiment lead at Airbus Helicopters. Finally, the lateral and roll degrees of freedom of the fuselage are released as well as the lag degree of freedom of each blade and compared to an equivalent model developed using Lagrange equations.
A general overview of the complete model is presented on Figure 2-15. The rotor subsystem contains the blades rigid bodies as well as the joints that constrain them to the hub, Figure 2-9. The model is implemented in a software that is able to represent both bond and multibond graphs such as 20-sim®.
The last point of importance in rotorcraft dynamics is the flight configuration. As a matter of fact, the flight configuration determines not only the equilibrium position around which dynamic phenomena may appear but it has also an impact on the system characteristics. For example, an important role is played by the aerodynamic damping in rotor stability; during forward flight the speed of advancing blades will be higher than retreating ones, leading to more aerodynamic damping on advancing blades; this is not the case in hover flight. Linearity around hover flight is justified by (Aponso, Johnston, Johnson, & Magdaleno, 1994), in which a helicopter dynamics linear model is developed and compared to flight tests of Sikorsky's CH-53E in hover; the results show a good agreement between the model and the tests for a range of frequencies between 1 and 10Hz.

The ground subsystem is a joint between the airframe and the inertial reference frame in which the first to the sixth degrees of freedom of the airframe can be blocked or released see Figure 2-12 by implementing constraints as explained in previous sections.

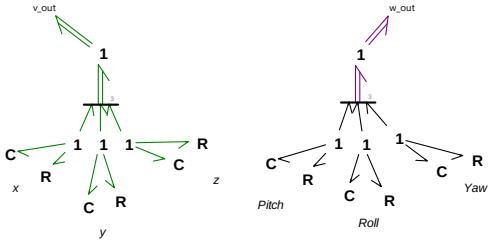

Figure 2-12. Ground subsystem

The engine subsystem contains only a source of flow that feeds the rotor angular velocity into the $\mathbf{z}_3$ axis (on Figure 2-3) of the revolute joint. The hub subsystem, Figure 2-13 has the multibond graph structure of rigid body in spatial motion described in Figure 2-5 from which inertial elements have been removed, since its mass and inertia are neglected; the dynamics of the hub and mast are therefore

neglected but it could be interesting to include them in a more detailed study. It leaves to this structure mainly a kinematic role. The four branches to the right correspond to the power transmission bonds to the blades.

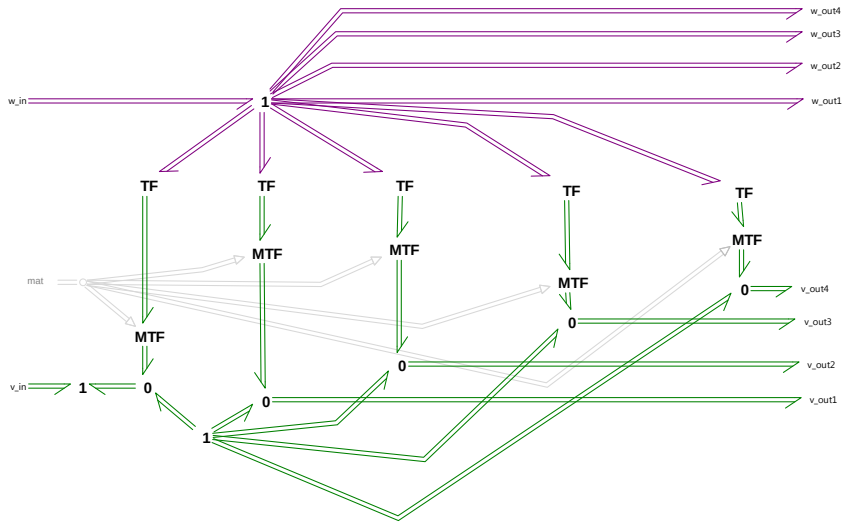

Figure 2-13. Hub subsystem and power outputs to blades

Concerning the controls subsystem, it has the structure presented on Figure 2-14, where all the gray elements are information bonds as they would appear in the software interface where the graph has been implemented and not transmit any power. The expression of the pitch transmitted to each blade via the bond graph sources of flow is also detailed on Figure 2-14.

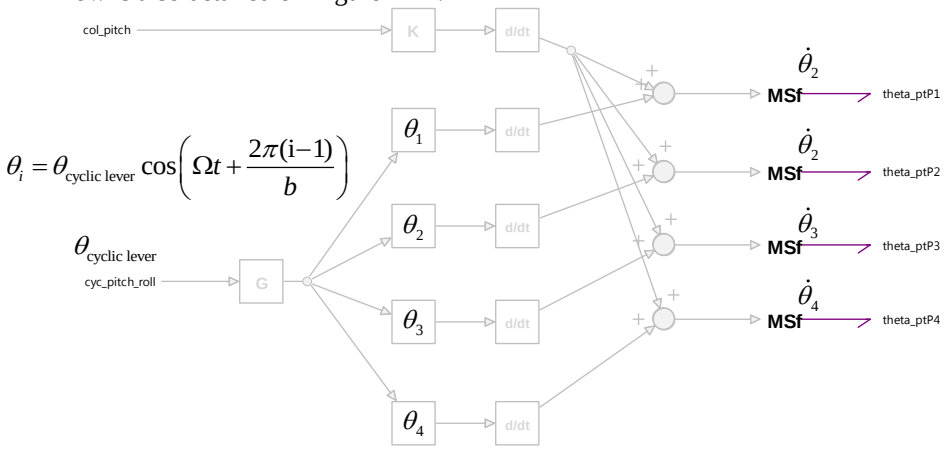

Figure 2-14. Controls subsystem

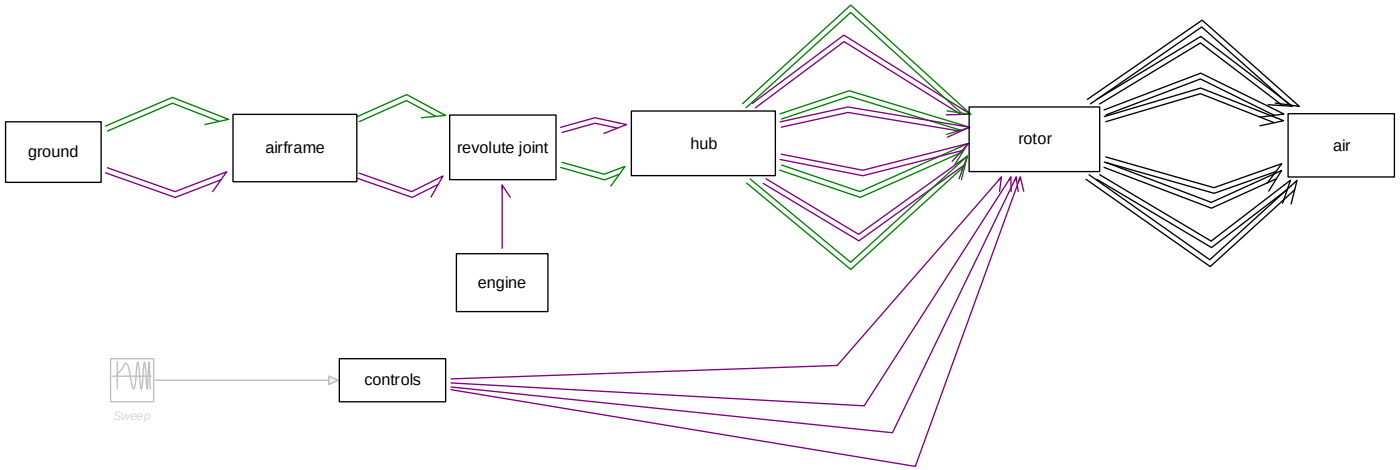

Figure 2-15. Rotorcraft system model using bond graphs

2.2.1. Rotor flapping dynamics

A very first step prior to the validation of the model is to verify whether the proposed aerodynamic forces model converges when the number of blade sections is higher. Very pragmatically, the model is proposed to be compared to the very classic flap equation of a rigid blade (Krysinski & Malburet, 2011),

$$I_{bl}\ddot{\beta}_i + \frac{I_{bl}\gamma\Omega}{8}\dot{\beta}_i + (I_{bl} + em_s)\Omega^2\beta_i = \frac{I_{bl}\gamma\Omega}{8}\theta_i \tag{36}$$

Where it can be seen that *e*, the blade hinge eccentricity, see Figure 2-3, shifts the flapping natural frequency from being the rotor angular velocity. Furthermore, the second term, which corresponds to a damping term takes its origin from aerodynamic forces, see equation (30). The right member of the equation contains the first part of aerodynamic forces which are proportional the blade pitch angle. This equation can be represented in a very compact form in a bond graph, Figure 2-16, that it is implemented next to the model Figure 2-15 for a comparative identification by numerical simulations under the same conditions.

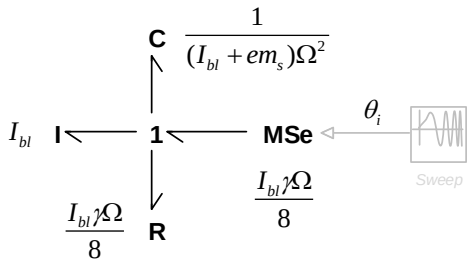

Figure 2-16. Flapping equation using bond graphs

Table 1. Rotor data

Rotor		
Number of blades	b	4
Radius	R (m)	7.5
Blade root eccentricity	e (m)	0.3
Lock number	γ	9
Angular velocity	Ω (rad/s)	29
Individual blade		
Static moment	m_s (m.kg)	390
Inertia	I_{bl} (m².kg)	1953

The isolation of the rotor multibody model is obtained by blocking the airframe degrees of freedom and blade lag motion. The forced flapping response of a blade is simulated numerically by sweeping the collective lever angle from 0 to 12 Hz and the results in the time domain are then plotted in the frequency domain using a discrete

Fourier transform, Figure 2-17. With this figure, it can be verified that the proposed modeling of quasi-steady aerodynamics converges with the increase of the number of elements and that it also converges to the linear equation especially below and after the natural flapping frequency.

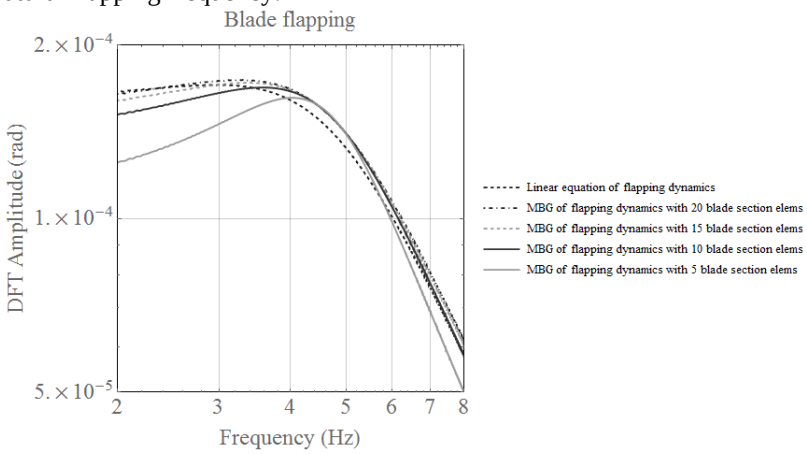

Figure 2-17. Identification of blade flapping response to collective pitch inputs

Around the natural frequency, the damping difference is due to a different approximation between the two models: in the multibond graph model there is no linearization on the calculation of the inflow angle Φ, see Figure 2-10 and equation (26). This is possible in the bond graph model because the velocities of the blade are available very naturally in the graph – however this is not a bond graph property and could have also been done from analytical equations solved numerically.

Table 2. Rotor static lift force numerical simulation from the bond graph model

$$F_{\text{static lift from rotor}} = b\int_{r=e}^{r=R} \frac{\gamma I_{bl}}{2R^4}\theta_i.\left(e\Omega + r\Omega cos(\beta_{0ss})\right)^2.dr$$

After numerical application, F=25 772 N

# of blade sections	Force(N)	Difference
20	22 200	13.8%
15	21 600	16.2%
10	20 550	20.3%
5	17 400	32.5%

In the end, from Table 2, it appears that the rotor static lift force converges when the number of blade sections is higher. The flapping dynamic behavior also converges with the number of elements, see Figure 2-17. Even if this verification might seem basic, it allows to verify that the 80 multi bonds of the aerodynamic model are well connected and paves the road towards more complex verifications.

2.2.2. Vertical dynamics validity on the ground

In this section, the previous model is modified: the vertical degree of freedom of the airframe is released. Then, pilot and flight control system dynamics models are inserted. A collective pitch sweep is used as an input and the behavior of the airframe is identified. This numerical experiment was compared (Orlita, 2015) to a real ground test performed at Airbus Helicopters.
The experiment performed at Airbus Helicopters on an actual helicopter. It consisted in measuring the vertical absolute accelerations of two components: the airframe and the collective lever, see Figure 2-18.

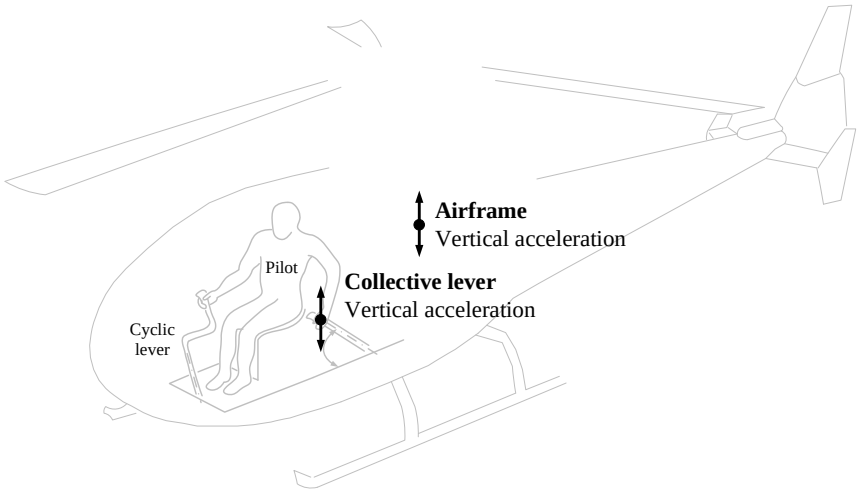

Figure 2-18. Acceleration measurements on the vertical axis during ground testing

The rotor angular velocity was close to nominal speed allowing the blades to flap as described in the previous section. In order to excite the system, the pilot was asked to apply a voluntary motion on the collective lever between 2 and 5Hz. The identification results of the collective lever to fuselage absolute accelerations are plotted in the frequency domain on Figure 2-19 (dashed green). A resonant frequency between 2 and 3Hz appears corresponding to the vertical mode of coupled rotor-airframe system while on the ground. The model proposed in Figure 2-15 of the previous section has been modified by closing the loop between the airframe and rotor collective pitch inputs see Figure 2-21 with a pilot and collective control subsystem. This subsystem contains a pilot model which is known in literature as Mayo's model (Mayo, 1989), that is the result of identifications of pilot behavior performed on one of Sikorsky's motion based simulators. It has been widely used in literature to investigate the vertical collective bounce phenomenon.

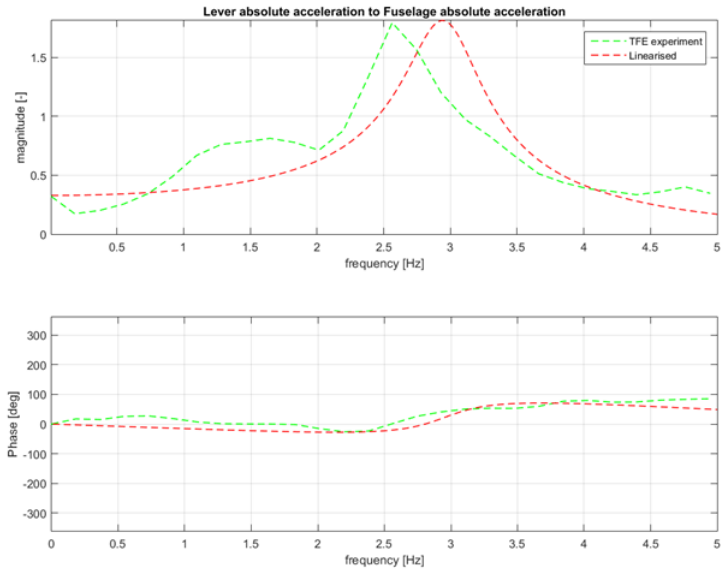

Figure 2-19. Experiment and numerical identification results of helicopter[13] vertical dynamics

The control subsystem of Figure 2-14 is replaced by the one on Figure 2-20. It contains both the pilot transfer function and a transfer function associated to the dynamics of vertical the flight control system. The resulting model has allowed obtaining the red dashed transfer function between the lever and airframe absolute accelerations on Figure 2-19.

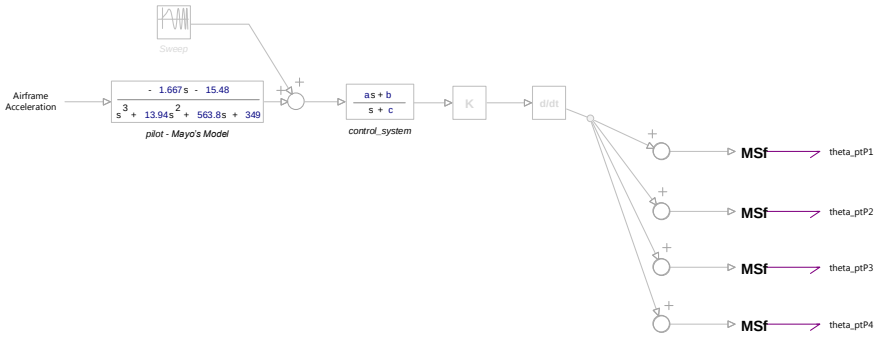

Figure 2-20. Pilot and control system subsystem model

[13] Without any scientific impact on the explanations, magnitudes have been intentionally deformed from actual measurements; helicopter details are intentionally not provided

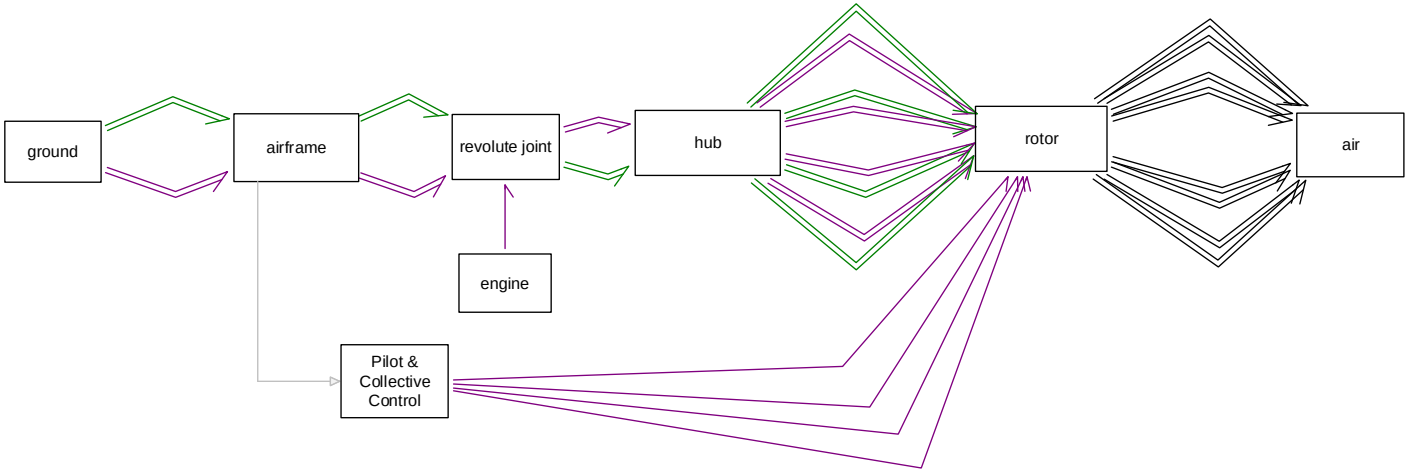

Figure 2-21. Closing the loop with pilot and collective control models for experimental confrontation

The model correlation with the experiment is quite satisfactory. Sensitivity analysis on pilot model parameters has shown this transfer function is pilot independent. Therefore it allows identifying the vehicle dynamics on the vertical direction.
The complete resulting bioaeroelastic model could help performing parametric sweeps of design variables of a given helicopter to investigate its proneness to 'vertical collective bounce', (Mayo, 1989), (Masarati & Quaranta, 2014), (Muscarello, Quaranta, & Masarati, 2014), (Orlita, 2015). However, it is preferred to focus on lateral-roll axes phenomena since less investigations are available in open literature.

2.2.3. Lateral/roll dynamics validity of the model around hover

In the two previous sections, the model has been 'downgraded' to verify the flapping dynamics of the rotor alone and illustrating how the aerodynamic model performs. Secondly the airframe was released on its vertical axis only and compared to an experiment performed on a real helicopter at Airbus Helicopters flight testing facility in which the results are quite encouraging. Ideally, the remaining axis of the model that have not been verified, namely lateral and roll dynamics of the helicopter should be compared to flight tests. However, being able to find flight test results can be as challenging as learning the bond graph language. As a result, a model has been developed using Lagrange equations based on the same hypothesis, see Rotor-airframe model using multibody dynamics section, Figure 2-2. Airframe axis definitions and Figure 2-3. Rotor i^{th} blade axis definitions. Both the bond graph multibody model and the analytical model developed using Lagrange equations can be derived from Hamilton's principle; as a result by verifying that both models match is expected to be a mutual verification of their physical validity. Of course this verification does not replace necessary experimental validations to be done in the future.

The principal steps of the development of the model using Lagrange equations are described so the hypothesis can be reviewed and the state-space resulting system is presented in Appendix 2. In this section the main focus will be on the modal analysis and time simulations of the resulting system and how it was compared with the bond graph model. The equations of motion are first linearized around hover flight, at this stage the resulting system is time-periodic and the multiblade coordinate transformation (Appendix 2) is used to obtain a time-invariant system that is put into state-space form Appendix 2.

A set of parameters is fixed for the helicopter and the pilot, see Table 3. These parameters correspond to a medium weight helicopter; the individual blade lag motion natural frequency ω_δ is inferior to the rotor angular velocity,

$$\omega_\delta = \sqrt{\frac{k_\delta}{I_{bl}}} = 1.53\ Hz\ \left(\approx 0.33\Omega\right)$$

The positioning of ω_δ corresponds to a soft-in-plane rotor technology ($\omega_\delta < \Omega$) and has lightly damped in-plane rotor modes see Figure 2-22.

Table 3. Helicopter data

Main rotor		
Number of blades	b	4
Radius	R (m)	7.5
Blade root eccentricity	e (m)	0.3
Lock number	γ	9
Angular velocity	Ω (rad/s)	29
Steady-state coning angle	β_{0ss} (rad)	0.0175
Individual blade		
Static moment	m_s (m.kg)	360
Inertia	I_{bl} (m².kg)	1728
Mass	M_{bl} (kg)	100
Equivalent angular lag damper stiffness	k_δ (N.m/rad)	160000
Equivalent angular lag damper damping	c_δ (N.m.s/rad)	3000
Airframe		
Mass	M_f (kg)	7500
Roll inertia around center of mass	I_{yy} (kg)	10000
Rotor head height from center of mass	h (m)	2
Cyclic blade pitch/lever roll angle		
Gearing ratio	G	0.1

A modal analysis of the system is conducted and shows the classic repartition of regressing, advancing lag and flap modes in the complex plane, see Figure 2-22, as it can be found in literature (Takahashi & Friedmann, 1991).

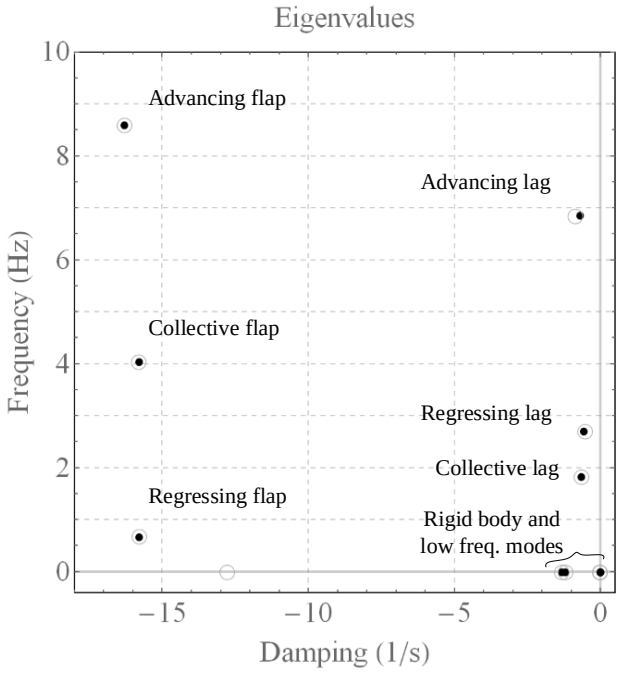

Figure 2-22. Eigenvalues without (•) and with (○) extra stiffness and damping terms

A pure lateral static mode appears in the system as unstable. This mode is not physical, it appears due to the reductive modeling hypothesis; at low frequencies, one would expect *Dutch roll* eventually, see Figure 1-8. In order to perform a time simulation of the system of equations resulting from the nonlinear bond graph model, this mode has to become stable. Very interestingly, this mode disappears once the pilot model will be included.

To stabilize the mode, stiffness and damping terms are added to the lateral and roll degrees of freedom ($kp_x=0.1N/m$, $kd_x=1.10^5N.s/m$, $kp_{\alpha y}=0.10.1N.m/rad$, $kd_{\alpha y}=0.1$ *N.m.s/rad*) in both analytical and bond graph model resulting in the modal analysis of empty circle on Figure 2-22 and on stabilization of the lateral airframe static mode see Figure 2-23.

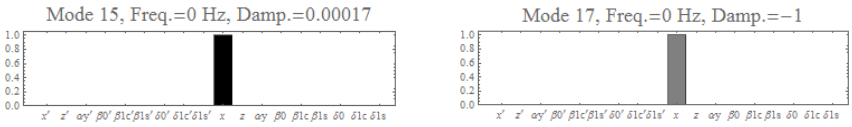

(a). without, unstable mode (a). with, stable mode

Figure 2-23. Lateral airframe static mode shape without and with extra stiffness and damping terms

It should be noticed that most modes are not affected by this additional terms, see Appendix 3.

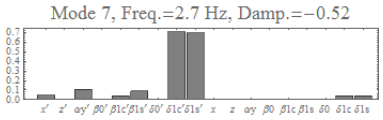

(a). regressing lag mode

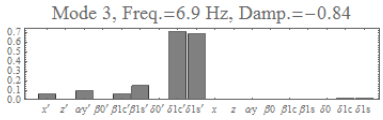

(a). advancing lag mode

Figure 2-24. Weakly damped modes

The linear equations of motion are presented on Appendix 2: a closer look at the equation on the vertical axis, see (A2.2), shows that with the chosen hypothesis the vertical motion is uncoupled from flapping and lagging cyclic motion. It is therefore chosen to block the vertical axis translation of the airframe on the bond graph. Once this is done, the forced response of the stable system Figure 2-15 to swept inputs of roll cyclic pitch inputs Figure 2-25 is simulated from both bond graph and analytical models.

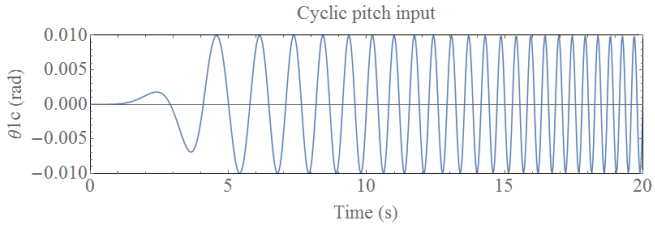

Figure 2-25. Roll cyclic pitch input sweep between 0 and 10 Hz in 100s (only first 20s plotted)

On Figure 2-26, the first two columns are the time simulation results from respectively linear and nonlinear (from the bond graph Figure 2-15) models. The last column presents discrete Fourier transforms of the first two columns results. For every state variable of that figure, the two peaks of both regressing and advancing lag modes are recognizable, see Figure 2-24. The scale is the same for all plots shows pretty good agreement, except at very low frequencies for the flapping response and in between peaks for the lateral airframe velocity; it is invoked here that it comes from a difference in the aerodynamic model using bond graphs that does not approximate the computation of the angle of attack see equation (26). It is interesting to remark that once the pilot model will be included, the parasitic elements that have been introduced here are not needed anymore to obtain a stable system that can be simulated numerically.

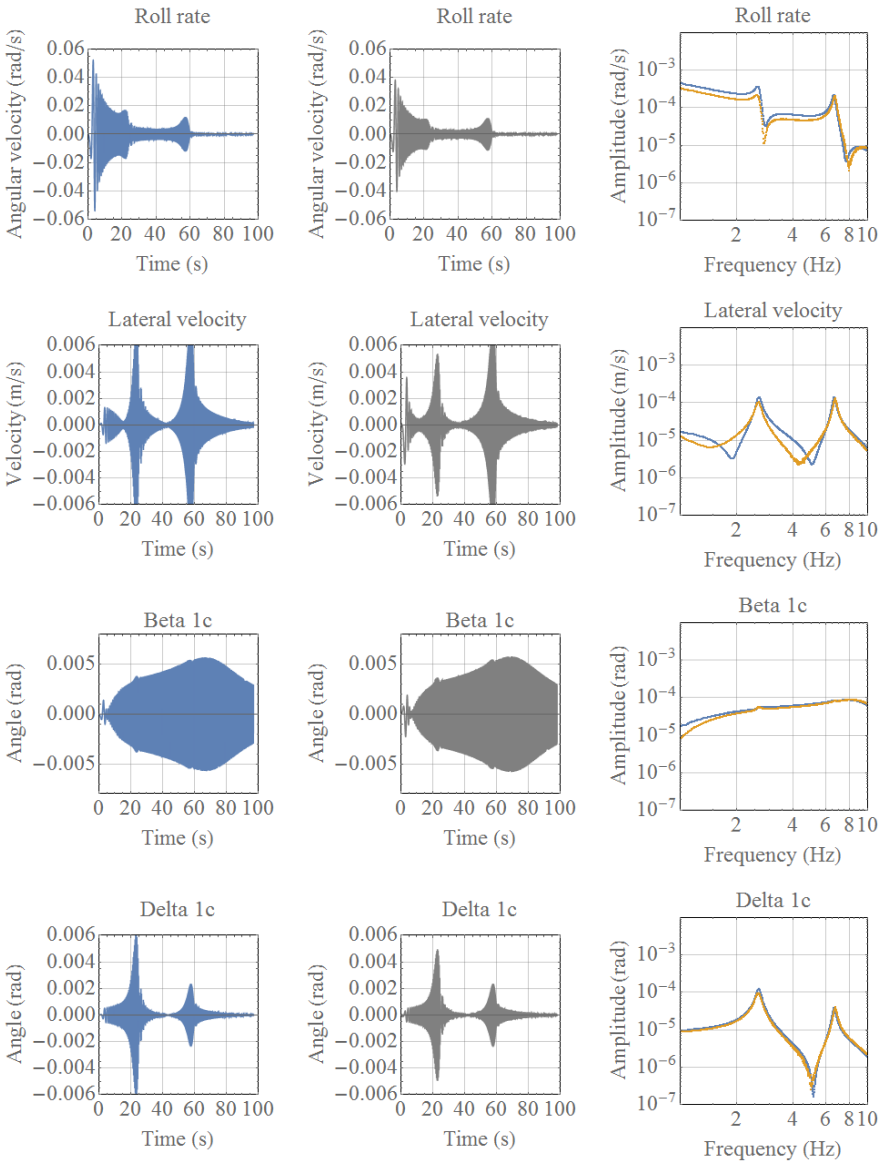

(a) Analytical

(b) Bond graph

(c) Analytical (blue)
Bond graph (orange)

Time simulations

Discrete Fourier Transforms

Figure 2-26. Identification of analytical and bond graph models forced responses of a helicopter around hover

2.3. Conclusion

In this chapter, the development of an aeromechanical rotor-airframe model is proposed to be representative of the real physical system at low frequencies. The quasi-steady aerodynamics forces graph is considered to be an original contribution. It both allows to take into account for variable aerodynamic properties along its span and can be used without any modification to represent hover or forward flight configurations. The model behavior has been compared to ground test results on the vertical axis for which it seems to be representative enough of what has been measured. On the lateral-roll axes of the airframe, the model has not been compared to flight tests since no data was available in the open literature. However, it has been compared to a linear model of the same assumptions but using Lagrange equations for which the agreement seems between the two is satisfactory.

The proposed model needs to be compared to flight tests to be considered as valid in the future. One of the first improvements that will need to be done on the modeling hypothesis concerns the necessity to take into account rotor inflow velocity in the aerodynamic model. The implementation of unsteady aerodynamic models should also be investigated. However, it should be kept in mind that bond graphs represent naturally *differential equations* and not *partial differential equations*. If the need is such, a more adapted energetic method could be used such as *Port-Hamiltonian Systems*, an evolution of bond graphs (Schaft, 2006).

Concerning the method, using the multibody system approach in bond graphs has of course the advantage of being applicable to a large class of problems but the drawback of probably not being the most computationally efficient for a particular problem. In fact, when modeled with such procedure, the equations of motion can be obtained relatively easily. However, as often in mechanics, the easier the equations of motion are obtained, the more complex the mathematical models are: not only Ordinary Differential Equations (ODEs) appear but also Differential Algebraic Equations (DAEs).

It has also been illustrated that in order to limit the number of DAEs, it is possible to act at the graphical level. In this work, most constraints were implemented using parasitic elements. It is a systematic method that can be used at the graphical level to remove the derivative causality on inertial elements of rigid bodies to limit the number of DAEs but the underlying mathematical model will after that include ‘stiff’ ODEs; it also has the disadvantage to introduce new state variables and therefore new modes that will perturb the analysis of the system.

When modeling the joint between each blade and hub of an articulated rotor, an original bond graph representation is proposed to avoid using parasitic elements or Lagrange multipliers. It consists in a local reduction of the equations that can be implemented at the graphical level in every system where three revolute joints need to be concatenated. The proposed representation could be classified with the classic methods of reduction of equations of motion such as transformation of inertial bond graph elements.

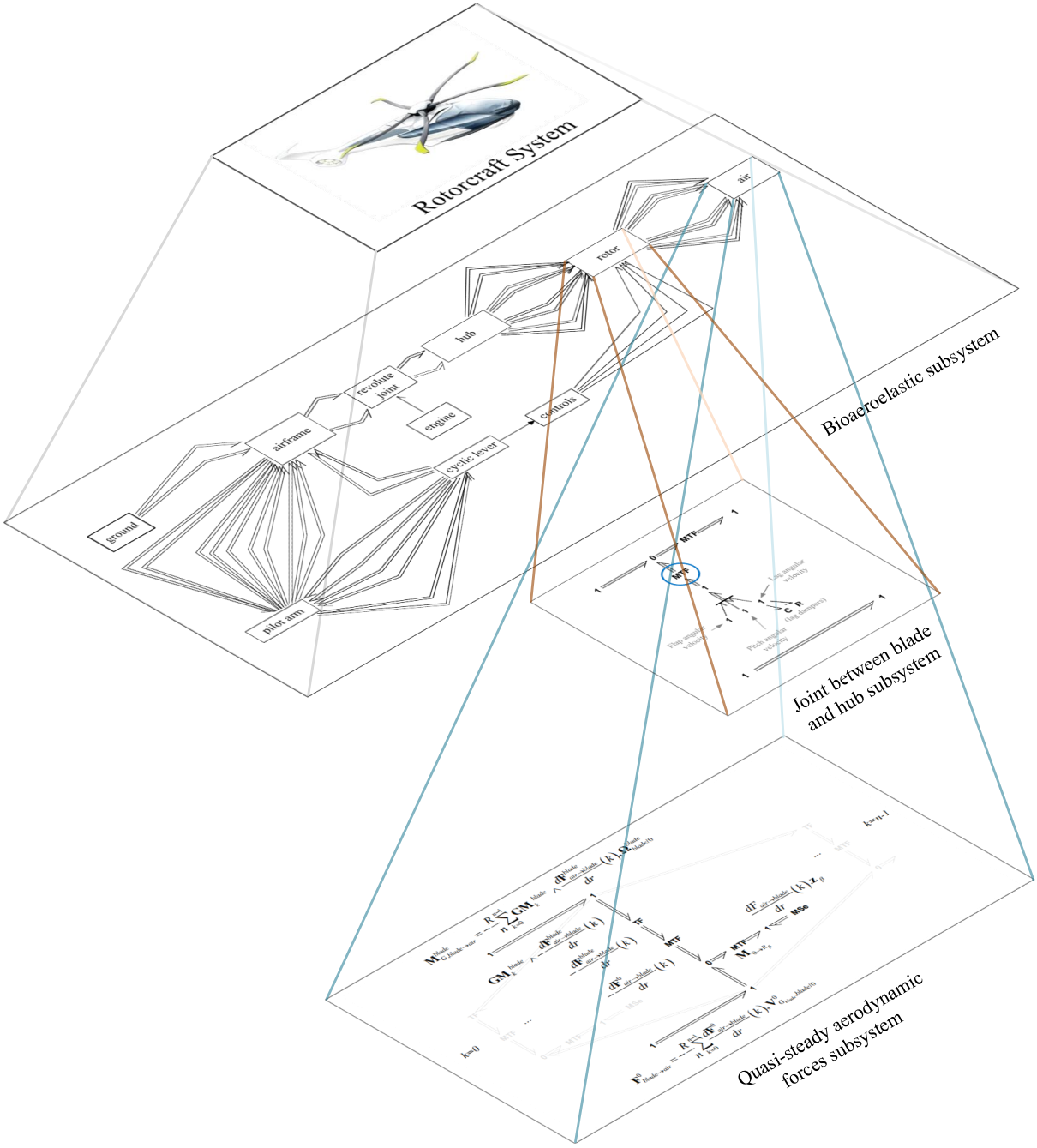

Figure 2-27. Chapter 2 main modeling blocks contribution to the global modeling approach

Chapter 3
Pilot neuromusculoskeletal system bond graph

Résumé long du chapitre 3

Dans le chapitre précédent, un modèle aéromécanique d'hélicoptère a été développé. Dans ce chapitre, un modèle neuro-musculo-squelettique du bras droit du pilote est développé. Le caractère prédictif du modèle est discuté en le comparant à des résultats expérimentaux disponibles dans la littérature.
Une revue des modèles de pilotes d'aéronef à voilure fixe est proposée dans (McRuer & Jex, 1967) *; celle-ci conduit McRuer à développer pendant des années son travail sur les interactions homme-machine dont un aperçu est donné dans* (McRuer, 1980)*. Concentré sur les oscillations induites par les pilotes d'aéronefs,* (McRuer, 1995) *distingue trois comportements principaux chez les pilotes qui sont : le suivi de trajectoire, la compensation et l'anticipation. Le comportement compensatoire, peut-être visualisé, en imaginant, par exemple, l'attitude d'un pilote d'hélicoptère pendant un ravitaillement air-air en carburant. Le comportement d'anticipation correspond lui aux actions prises par le pilote par anticipation du comportement dynamique de la machine qu'il contrôle et en se basant sur son expérience. Dans* (Lone & Cooke, 2010) *et* (Lone & Cooke, 2014)*, une vision du pilote plutôt du point de vue de l'ingénieur est proposée. En effet, les auteurs décomposent les modèles de pilote en trois catégories : sensorielle (capteurs), de contrôle (lois de commande) et biomécanique (actionneurs), voir la Figure 3-1. Des combinaisons de ces différents modèles permettent d'étudier les oscillations induites par le pilote (PIO) et assistées par le pilote (PAO). Si l'on se restreint aux PAOs,* (McRuer, 1995) *dresse une liste d'incidents survenus sur des avions comme le YF-12 de Lockheed ou le F-111 de General Dynamics. Sur les avions de chasse, le phénomène le plus étudié dans la littérature ouverte est probablement le PAO connu sous le nom de « roll rachet »*. (Hess, 1998) *et* (Höhne, 2000) *décrivent le phénomène comme « des oscillations indésirables et imprévues à haute fréquence sur l'axe de roulis d'avions de chasse de haute performance qui apparaissent lors de manœuvres rapides en roulis »*. (Höhne, 2000) *déclare qu'il est désormais accepté, que le phénomène de « roll rachet » est influencé par le système neuromusculaire des pilotes. Dans ses travaux, il propose un modèle biomécanique du pilote couplé à un modèle d'aéronef afin d'étudier le phénomène et grâce auquel il arrive à reproduire numériquement un incident survenu sur un F16 du constructeur General Dynamics. Ce phénomène est aussi reporté pour être survenu sur un Eurofighter Typhoon,* (Lone & Cooke, 2014)*. Dans la communauté des aéronefs à voilure tournante, une revue d'incidents survenue dans la US Navy et le corps des Marines est rapporté dans* (Walden, 2007)*. On y trouve un grand nombre d'appareils touchés par le phénomène de PAO ou RPC aéroélastique.* (Walden, 2007) *cite un exemple aux conséquences impressionnantes à propos de l'hélicoptère CH-53 Super Stallion du constructeur Sikorsky, voir Figure 3-2.*

Walden rapporte qu'un véhicule militaire qui était transporté à l'aide d'une élingue par l'hélicoptère a dû être largué pendant le vol à cause de l'émergence très violente du phénomène de 'vertical collective bounce'. Afin de mieux comprendre le problème, (Mayo, 1989) *propose le premier modèle à être utilisé dans l'industrie et représentant la biodynamique d'un pilote d'hélicoptère. Ce modèle linéaire, voir Figure 3-3, a été obtenu par identification à partir d'expériences menées dans le simulateur de vol du constructeur Sikorsky. L'expérience consistait à enregistrer le mouvement du manche de pas collectif imposé par un pilote alors que la plateforme du simulateur oscillait verticalement de manière forcée à des fréquences entre 1 et 5 Hz. Ceci a permis d'obtenir la transmissibilité du pilote selon leurs morphologies : mésomorphe ou ectomorphe. Comme nous l'avons déjà précisé en introduction, ce comportement de la part du pilote est un comportement au-dessus des fréquences de contrôle manuel d'un véhicule. Par conséquent, il est considéré comme un comportement involontaire du pilote. De plus, il est facile d'imaginer que ce type de comportement peut apparaître sur d'autres types de véhicules que des aéronefs. La fonction qui caractérise ce comportement a été formalisée par* (Venrooij, 2014) *sous le nom de* ***« biodynamic feedthrough » (BDFT)*** *et il l'a défini comme « **le transfert d'accélérations par le corps humain pendant l'exécution d'une tâche de contrôle manuel, qui engendre des forces involontaires qui s'appliquent sur le dispositif de commande, et qui peut éventuellement provoquer des mouvements involontaires du dispositif de commande** ». Les expériences de* (Mayo, 1989) *montrent Figure 3-3 que le BDFT est variable en fonction des pilotes, de par leur morphologie. Mais le BDFT est également variable chez un même pilote ; en effet les pilotes adaptent leurs actions et donc leur 'corps' en fonction des tâches qui leurs sont demandées d'effectuer, de leur charge de travail et de leur état de fatigue* (Venrooij, 2014). *En effet, lors d'expériences menées sur le simulateur de vol Simona de l'université technologique de Delft (TU Delft), par Venrooij, il a été demandé à chaque pilote d'effectuer trois types de tâches différentes alors que la plateforme du simulateur vibrait dans le but de mesurer leur BDFT. L'objectif derrière la demande d'effectuer des tâches différentes étaient de forcer chaque pilote à réadapter son système neuromusculaire à chaque tâche. Les résultats sont présentés sur la Figure 3-4 sur les axes latéral, longitudinal et vertical de l'hélicoptère. Il apparaît assez clairement que le BDFT dépend de la tâche effectuée par chaque pilote. Une des conclusions principales de* (Venrooij, 2014) *est que la fréquence de résonance du BDFT est la plus haute lorsque la tâche demandée au pilote le force à devenir plus 'raide' lorsqu'il agit sur les commandes. Des conclusions similaires sont rapportées dans* (Lone & Cooke, 2014) *qui précisent que ce type de comportements peut être atteint lors de situations d'urgence notamment. Dès lors, il apparaît nécessaire de pouvoir représenter l'adaptation du système neuromusculaire d'un pilote. Deux types d'approches ont été identifiés dans la littérature afin de modéliser le comportement biodynamique des pilotes. La première consiste à identifier la réponse du corps humain à des accélérations dans le domaine fréquentiel à partir d'expériences* (Mayo, 1989), (Venrooij, et al., 2011) *et* (Muscarello, et al., 2015). *La deuxième approche consiste à tenter de prédire le BDFT en déduisant les mouvements en se basant sur des principes physiques, par exemple en utilisant une approche multicorps afin de modéliser le squelette humain sur lequel on superpose des modèles dynamiques de*

muscles ainsi que, dans une certaine mesure, du système nerveux central (Masarati & Quaranta, 2014). *C'est la voie ouverte par ces travaux, basée sur des principes physiques, que nous prenons afin d'obtenir un modèle prédictif dans un grand nombre de mises en situations virtuelles. L'état de l'art des modèles dits « neuro-musculo-squelettique » est très vaste dans le domaine de la biomécanique, on peut citer notamment* (Maurel, 1999), (Pandy, 2001), (Garner & Pandy, 2001), (Lee & Terzopoulos, 2006), (Pennestri, Stefanelli, Valentini, & Vita, 2007), (Erdemir, McLean, Herzog, & van den Bogert, 2007), (Hernani, Romero, & Jazmati, 2011) *ou encore* (Masarati & Quaranta, 2014). *Ce type de modèles, basés sur des principes physiques, peut être appliqué à l'étude d'un nombre de situations virtuelles bien plus vastes et dans un nombre de domaine bien plus important que les modèles obtenus par identification, valables eux, uniquement dans les conditions expérimentales à partir desquelles ils ont été obtenus.*

Il n'y a pas, à l'heure actuelle, de consensus sur comment prédire le BDFT par le calcul à partir d'un modèle neuro-musculo-squelettique. Il est proposé ici de développer un tel modèle, du bras droit du pilote à partir de modèles existants dans la littérature et notamment à partir des travaux répertoriés dans le paragraphe précédent. Le modèle proposé est néanmoins original pour deux raisons. La première est qu'il est développé à l'aide de bond graphs ; il existe des modèles multicorps squelettiques en bond graphs, mais pas de modèle neuro –musculo-squelettique. La deuxième raison est qu'il est capable de tenir compte de mouvements spatiaux du squelette. Ceci est nécessaire dans notre application, puisque nous souhaitons être capable de calculer les mouvements sur l'axe latéral d'un cockpit d'hélicoptère. Le modèle proposé ici contient 16 muscles et le bras est décomposé en 2 os : un ensemble radius et cubitus d'une part et l'humérus d'autre part, voir Figure 3-7 et la Table 4, ainsi que Appendix 4 pour les données et définitions des repères.

Si l'on considère le système bras et manche de pas cyclique, ceux-ci sont attachés à un même solide : le fuselage. Par conséquent, le système est cinématiquement bouclé, voir Figure 3-8. Le modèle mathématique derrière un tel système peut-être difficile à résoudre numériquement. Une méthode connue sous le nom des « perturbations singulières » (Zeid & Overholt, 1995), (Boudon, 2014) *permet de transformer le modèle mathématique afin de faciliter sa résolution numérique. La méthode consiste à 'assouplir' au moins une contrainte de la boucle cinématique au niveau d'une liaison par l'ajout d'éléments de raideur (C) et de dissipation (R) linéaires. Il est choisi dans ce cas d'application, d'assouplir la contrainte au niveau de la liaison pivot entre le manche de pas cyclique et le fuselage, voir Figure 3-9. Cette méthode possède l'avantage d'être systématique et peut-être implémentée directement au niveau graphique d'un bond graph. Afin que le modèle reste physiquement valide, le choix des valeurs des éléments (C) et (R) peut se faire en identifiant la raideur et l'amortissement de la liaison du système physique. La méthode a le désavantage d'introduire de nouvelles variables d'état et donc de venir potentiellement perturber l'analyse du système par la prise en compte de modes indésirables.*

Le modèle squelettique est un modèle multicorps sur lequel il est nécessaire de superposer les muscles. Parmi les modèles comportementaux des muscles, on trouve le plus classique qui est le modèle de Hill, voir (Zajac, 1988), *tenant compte de l'activation musculaire voir* (Pennestri, Stefanelli, Valentini, & Vita, 2007). *Ce*

dernier est traduit ici en bond graphs, équations (37) à (54) et permet d'aboutir à la structure graphique d'un muscle voir, Figure 3-12. Sur cette même figure, on voit apparaître en gris, des signaux qui vont vers et viennent du système nerveux central (CNS). Physiologiquement parlant, des 'capteurs' placés sur les fibres musculaires envoient une information sur l'état d'élongation des fibres en question ; c'est ainsi que le corps humain peut réguler la contraction ou la décontraction des muscles pour réaliser un mouvement ou maintenir une posture donnée. En effet, une posture peut être maintenue avec différents niveaux d'activations musculaires. Afin de mieux comprendre ceci, on peut s'imaginer avec un verre à la main ; il est possible de tenir ce verre plus ou moins fermement. Cette fermeté donne une idée du niveau d'activation musculaire : plus le verre est tenu fermement, plus l'activation est élevée. Ceci est formalisé mathématiquement par la quantité a, qui module la force produite par un muscle, voir équation (39) et Figure 3-10. De plus, on peut voir que la force musculaire, comme prévue par le modèle de Hill dépend de l'élongation du muscle (fonctions f_1 et f_3) et de sa vitesse d'élongation (fonction f_2). Un modèle quasi-statique du système nerveux central est également reproduit, (Lee & Terzopoulos, 2006), *afin de représenter le contrôle par le CNS, des forces musculaires. Cette modélisation consiste à ajouter le terme Δa à l'activation musculaire initiale a_0, voir l'équation (56). Deux coefficients apparaissent, k_p et k_v qui permettent de paramétrer l'état plus ou moins 'raide' du système neuromusculaire.*

Le modèle neuro-musculo-squelettique ainsi obtenu possède plus de muscles (16) que de degrés de liberté (9). Le système est donc sur-actionné ; mathématiquement le système possède plus d'inconnues que d'équations. En l'état, le système d'équations ne possède aucune, ou une infinité de solutions, (Pandy, 2001), (Erdemir, McLean, Herzog, & van den Bogert, 2007). *Afin de lever le problème d'indétermination, un principe physique supplémentaire est en général pris en compte. Par exemple, on peut postuler, afin de réaliser un mouvement ou de maintenir une posture donnée, que le corps humain minimise l'énergie consommée, appelée coût métabolique, par ses muscles,* (Erdemir, McLean, Herzog, & van den Bogert, 2007). *A partir de la modélisation précédente nous avons accès au travail mécanique fournit par chaque muscle, voir équation (55). Cette quantité ne représente pas tout à fait le coût métabolique ; en effet, lorsqu'un muscle travaille il dissipe une quantité d'énergie non négligeable sous forme de chaleur. Néanmoins, il est assumé qu'il est acceptable de minimiser le travail des muscles lorsque l'on cherche à minimiser le coût métabolique. La minimisation du travail des forces des muscles est prise en compte afin d'obtenir les coefficients d'activation musculaire initiaux a_0 des muscles. Pour cela, le modèle neuro-musculo-squelettique est implémenté dans le logiciel 20-sim ® et couplé au logiciel Matlab ® afin de pouvoir utiliser un algorithme d'optimisation, voir* Figure 3-15. *Le modèle est simulé au voisinage de l'équilibre, manche de pas cyclique droit, c'est-à-dire lorsque le pilote maintien cette posture. En paramétrant comme conditions initiales un angle de manche de pas cyclique légèrement décalé de sa valeur à l'équilibre et des coefficients a_0 nuls, on obtient un résultat de simulation de la réponse libre du système ; en quelques secondes, les oscillations s'atténuent et le système atteint l'équilibre. Cette opération donne une première valeur à la fonction coût qui est par la suite envoyée à la fonction d'optimisation, sous Matlab*

®, *qui propose un nouvel ensemble de coefficients d'activations musculaires. Par itération, on obtient un jeu de coefficients optimaux.*

La dernière étape de ce chapitre consiste à discuter de la validité du modèle. Il est proposé de reproduire les expériences réalisées sur le simulateur Simona de l'université technologique de Delft et dont les résultats ont été présentés Figure 3-4*. Dans ces expériences, il est demandé à chaque pilote d'effectuer 3 tâches différentes dans le cockpit alors que celui-ci vibre. Les vibrations qui nous intéressent sont notamment celles sur l'axe latéral de l'hélicoptère. La première tâche qui est demandée d'effectuer à chaque pilote est une tâche dite de « position » : le pilote doit par des mouvements de manche placer un curseur dans une cible qui se déplace sur l'écran du simulateur. La deuxième tâche est dite de « force » : le pilote doit chercher d'abord à contrer les forces qu'il ressent au manche avant de chercher à positionner le curseur sur la cible. La dernière tâche dite « relax » consiste à maintenir le manche dans sa position initiale en gardant un état des muscles proches de l'état initial sans forcément cherche à positionner le curseur dans la cible. Les résultats* Figure 3-4 *montrent que le BDFT dépend de la tâche qu'un pilote doit effectuer et donc de l'état de son système neuromusculaire ; le pilote semble notamment plus 'raide' lors des tâches du type « position ». Afin de pouvoir reproduire différents types d'état du système neuromusculaire par la simulation du modèle proposé, nous avons introduit le modèle quasi-statique du système nerveux central qui est paramétré par deux coefficients k_p et k_v,* (Stroeve, 1999), (Masarati & Quaranta, 2014). *Il n'y a pas de consensus dans la littérature sur la valeur à donner à ses coefficients selon la tâche que l'on demande d'effectuer à un pilote. Dans les présents travaux nous ne faisons varier que k_p, qui correspond au gain de la boucle de contrôle du coefficient d'activation musculaire pour la partie qui dépend de l'élongation d'un muscle. Ici un seul coefficient paramètre tous les muscles. De plus, on se permet de modifier la raideur et l'amortissement de deux articulations du modèle de bras, au niveau de l'épaule et du poignet. Ceci est fait par l'intermédiaire d'un coefficient multiplicateur des valeurs nominales de raideur et d'amortissement noté α.*
En se fixant des valeurs de k_p et α qui imposent un état neuromusculaire donné, on peut par l'opération d'optimisation décrite précédemment calculer les coefficients d'activation musculaire optimisés pour l'état neuromusculaire donné. Les résultats sont présentés Figure 3-16*. A partir de ces résultats, deux des jeux de paramètres sont choisis et une simulation, de la réponse forcée du bras pilote sur le manche de pas cyclique est menée pour des excitations en accélération latérale du cockpit d'amplitude constante et de fréquence variable entre 0.8 et 8 Hz. Une approximation des moindres carrées des résultats est effectuée et les résultats sont tracés sur la* Figure 3-17*, puis superposés aux résultats expérimentaux de* (Venrooij, et al., 2011). *La correspondance des résultats est très encourageante, les tâches de « force » et de « position » ont été reproduites par le calcul numérique. Il reste néanmoins encore des points d'amélioration. Le premier concerne la modification du paramètre α, qui paramètre la raideur et l'amortissement du bras aux interfaces. Il serait intéressant de voir si ce coefficient peut être remplacé par la modélisation d'un nombre encore plus important de muscles aux interfaces, comme par exemple le muscle deltoïde de l'épaule, voir* Figure 3-21*. Un dernier*

point qui n'a pas été abordé est que lorsque le coefficient k_p=1.25, le modèle présente un comportement non linéaire très fort à basse fréquence, voir le spectrogramme Figure 3-20 *: des harmoniques apparaissent et leur amplitude est importante. Les résultats de simulation de BDFT présentés* Figure 3-17 *et par les résultats expérimentaux de la littérature ne représentent donc qu'une partie de la réponse biodynamique du pilote : celle aux fréquences d'excitations.*

In addition to the rotorcraft model presented in the previous section, the development of a pilot model is presented in this section. The objective of this model is to be able to predict pilot's involuntary behavior known as *biodynamic feedthrough* (BDFT) on the lateral axis of a helicopter cockpit. The model is in the last section confronted to literature flight simulator experiment results.

3.1. State-of-the art

An early review of pilot models is proposed in (McRuer & Jex, 1967); it lead McRuer to extensive work around human dynamics in man-machine systems in (McRuer, Human dynamics in man-machine systems, 1980). Mainly concentrated on aircraft pilot induced oscillations, (McRuer, 1995) distinguishes three main pilot behavioral descriptions which are trajectory following, compensation and precognitive. The compensation behavior could be imagined as the one an aircraft or helicopter pilot would have during an air to air refueling operation. It usually demands fast and short term actions from the pilot. The precognitive behavior concerns anticipative actions based on experience taken by the pilot to make the aircraft reach a desired state. In (Lone & Cooke, 2010), (Lone & Cooke, 2014) review pilot modeling techniques and propose to represent such behavior by discretizing the pilot models into three model categories: sensory models, control models, and biomechanical models see Figure 3-1. The human sensory models represent the dynamics between the inputs of visual cues (through the primary flight display, out of the window cues), the proprioception (cyclic lever see Figure 2, collective lever and pedals positions) and finally the vestibular system (sensing body motion - inner ear) and outputs that are communicated to higher brain functions for processing. Once the brain has processed the information, it sends a decision, also influenced by experience and skills, to the 'actuation system' of the human body, its neuromuscular system.

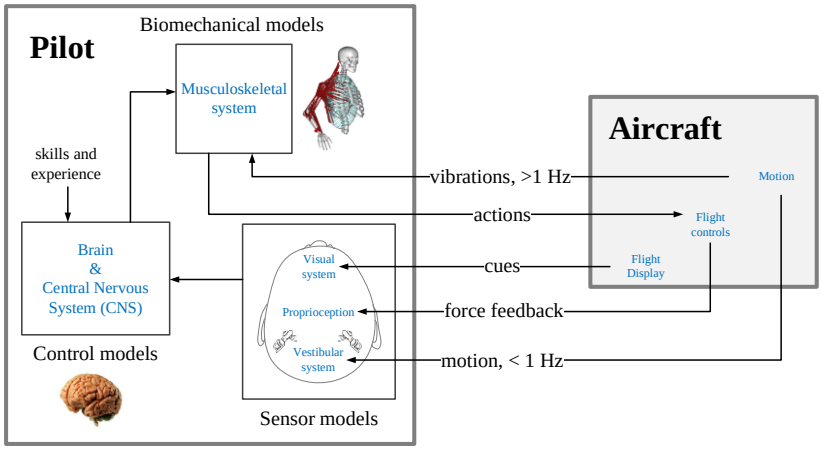

Figure 3-1. Pilot submodels in human-aircraft systems, adapted from (Lone & Cooke, 2014)

This thesis focuses on the pilot interaction with higher frequency helicopters modes also known as aeroelastic RPCs or pilot assisted oscillations (PAOs). A list of incidents is reported in (McRuer, 1995), in which aircrafts such as Lockheed YF-12 or General Dynamics F-111 have been involved in a PAO. Perhaps the most studied phenomena in the open literature concerning aircrafts is the 'roll ratchet' phenomena (Hess, 1998), which is "*an unwanted and inadvertent high frequency oscillation in the roll axis encountered in high performance fighter aircraft during rapid roll maneuvers*" (Höhne, 2000). The same author points out that "*it is widely accepted that roll ratchet is influenced by the pilot's neuromuscular system*" and proposes a biomechanical model of the pilot coupled to an aircraft model to investigate the phenomena. It successfully reproduced the incident on General Dynamics F16. This phenomena is also known to have appeared on Eurofighter Typhoon (Lone & Cooke, 2014).

In the rotorcraft community, an extensive list of incidents associated to rotorcraft PAOs in the US Navy and Marine Corps is presented by (Walden, 2007). Tiltrotor designs such as the Boeing-Bell V-22 Osprey were very sensitive to PAOs, for which three unstable aeroelastic RPCs in its lateral axis were found after flight testing in (Parham, Popelka, Miller, & Froebel, 1991). The first two modes appeared while on the ground while the last one appeared in the air at high speed. The mechanism behind the first two modes was found to be due to a difference of thrust between the two rotors that was the result of an output of the flight control system due to the involuntary movement of the lateral lever by the pilot. A PAO tendency of conventional helicopters that has been widely studied in the community is the 'vertical collective bounce phenomena' for which Sikorsky's CH-53 Super Stallion was prone when transporting a slung load see Figure 3-2. It is reported in (Walden, 2007) that the load at the end of the cable, a light armored vehicle had once during an incident to be jettisoned.

Figure 3-2. Sikorsky CH-53E Super Stallion with external slung load

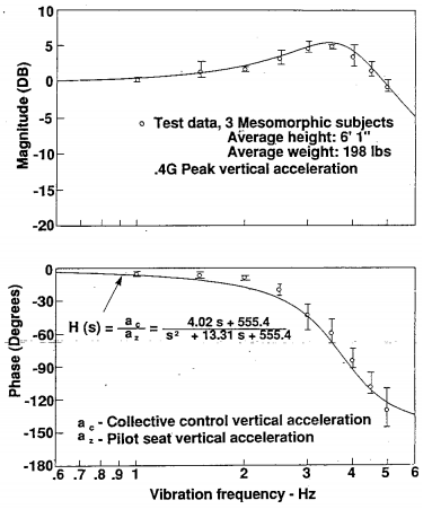

Figure 3-3. Pilot transmissibility experiment from (Mayo, 1989)

In order to better understand the problem and design a solution, (Mayo, 1989) proposed one of the first pilot biodynamics model to be used in industry. This model was obtained by identifications from experiments conducted on one of Sikorsky's motion-based simulators. The experiment consisted in recording pilot's collective stick motion while vertical sinusoidal commands were applied to the simulator platform at discrete frequencies ranging from 1 to 5 Hz (see Figure 3-3). It allowed to obtain the transmissibility of different pilots based on their body shapes: mesomorph or ectomorph. This behavior represents an involuntary behavior of the pilots that arises at higher frequencies than those of manual control, in the present example around 3Hz. This behavior is not restricted to aircrafts or rotorcrafts but can appear in any man-machine system and it is usually called *biodynamic feedthrough* (BDFT). A framework to measure BDFT and its definition proposed by (Venrooij, 2014): "*the transfer of accelerations through the human body during the execution of a manual control task, causing involuntary forces being applied to the control device, which may result in involuntary control device deflections*". BDFT therefore explains that when a pilot is engaged in a manual control task under vehicle accelerations, these vibrations can cause involuntary limb motions leading to involuntary control inputs. The experiments presented by (Mayo, 1989) on Figure 3-3 show that BDFT varies between different subjects. Furthermore it is known that pilots adapt their response and therefore their bodies to task instruction, workload and fatigue (Venrooij, 2014). In that same work, BDFT responses of humans were measured when asked to perform different control tasks. The objective of asking one subject to perform different tasks is to force him to adapt his body and therefore his neuromuscular system to the task. The results are presented on Figure 3-4 for the lateral, longitudinal and vertical helicopter axis translations and show that BDFT is also task dependent. These experimental results from (Venrooij, 2014) were obtained on TU Delft's experimental motion based simulator, for which the subjects were asked to perform three tasks. A position task (PT) with the instruction to minimize the stick position, a force task (FT)

with the instruction to minimize the force applied to the stick and finally a relax task (RT) with the instruction to relax the arm.

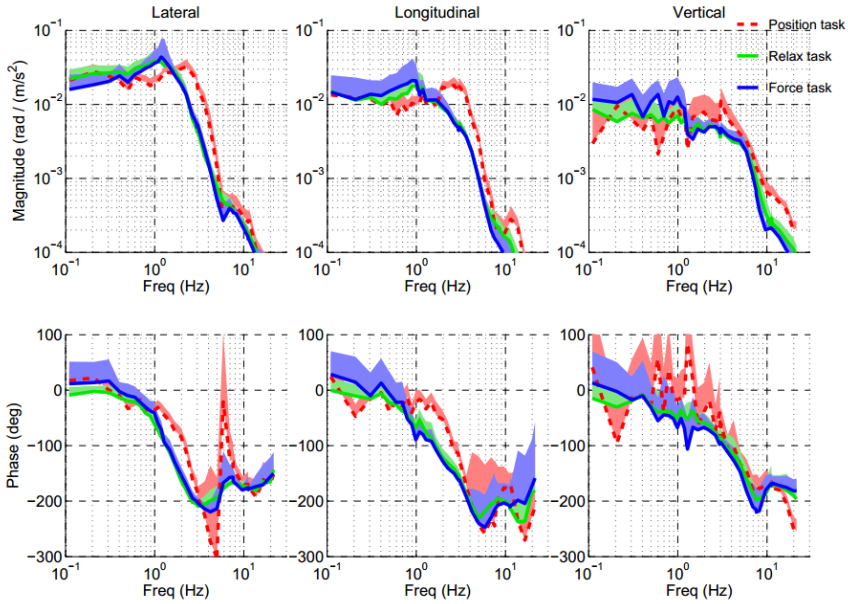

Figure 3-4. Biodynamic feedthrough task dependency, helicopter flight simulator experiments, from (Venrooij, 2014)

From the frequency responses of Figure 3-4, it appears that for position tasks (PT) the resonant peak of BDFT is higher. The conclusions drawn in (Venrooij, 2014) are that the position task is the one that requires the higher stiffness adaption of the neuromuscular system. Similar conclusions are reported in (Lone & Cooke, 2014) and especially that the body 'stiffens' during urgent tracking tasks.

As a result, the main relevant behavior to model BDFT is the neuromuscular system adaption of the pilot. When modeling pilot biodynamics, two approaches can be identified. The first one consists in identifying the human body response in the frequency domain to fuselage accelerations from experiments (Mayo, 1989), (Venrooij, et al., 2011) and (Muscarello, et al., 2015) to name a few. The second approach consists in trying to predict biodynamic feedthrough by deducing the motion based on physical principles using for example a multibody approach to capture the skeletal motion superposed to dynamic models of the muscles and central nervous system control (Masarati & Quaranta, 2014).

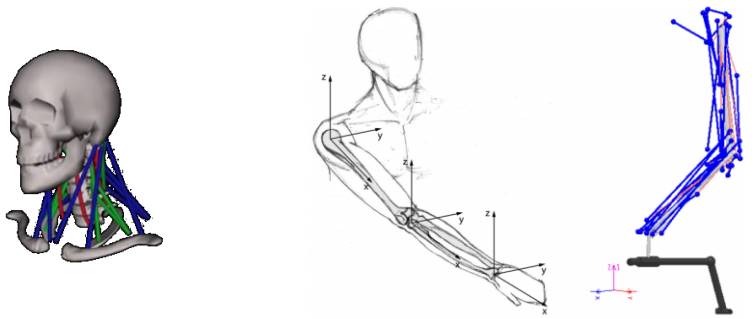

(a) Head-neck, from (Lee & Terzopoulos, 2006)

(b) Upper limb and helicopter collective lever from (Masarati & Quaranta, 2014)

Figure 3-5. Virtual human neuromusculoskeletal models

Early works in virtual human modeling and simulation can be found in (Maurel, 1999), in which even the modeling of soft tissues like skin is proposed. A skeletal model using a multibody approach using multibond graphs is proposed in (Martinez, Vera, & Félez, 1997). A formalization of the problem of the computation of human movement when excitation and the activation dynamics of muscles are taken into account is proposed in (Pandy, 2001) and (Pandy & Barr, 2003). A detailed upper limb musculoskeletal model is proposed in (Garner & Pandy, 2001), the positioning of muscle attachment points is particularly clear. In (Lee & Terzopoulos, 2006), a human head-neck biomechanical model is proposed. On top of the model, a multiple level neuromuscular control model is proposed; machine learning techniques are employed to train the neural networks of the controller to generate movements of the human head and face, see Figure 3-5. The impact and need to model control to obtain realistic arm impedance is discussed in (Stroeve, 1999) for which "*arm impedance is the resultant of passive dynamics of the arm, intrinsic impedance of activated muscles and reflexive contributions*". Usually, in these models known as "neuromusculoskeletal" represent to a certain extent the behavior of the three subsystems, skeleton, muscles and their control thanks to the central nervous system. However, these models of the human body are limited, since they do not take into account for example, muscle volume, or make the hypothesis that muscle forces are exerted along straight lines. These two hypothesis are not obvious to justify see Figure 3-6; more precise geometric reconstructions of muscles are proposed in (Ng-Thow-Hing, 2001) are muscle forces are exerted on more complex paths. These kind of physical details come at a higher computational cost.

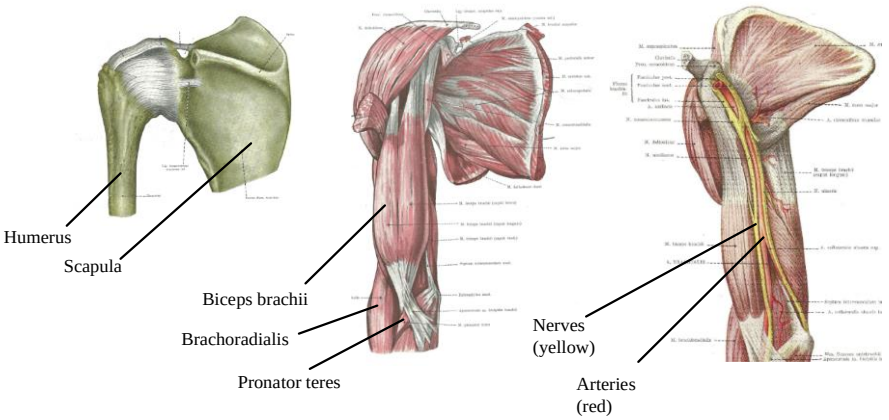

(a) Skeleton (b) Muscles (c) Nerves

Figure 3-6. Partial physiology drawings of the shoulder from (Kiss & Szentágothai, 1966)

In (Pennestri, Stefanelli, Valentini, & Vita, 2007) the mathematical model of a virtual musculoskeletal model that takes into account muscular activation dynamics of the upper limb is detailed in a reproducible way. These two models have been applied in (Masarati & Quaranta, 2014) to model the right arm of a helicopter pilot in order to compute a helicopter pilot BDFT in its vertical axis.

To synthetize, identification model approaches lead to black box models, which are usually linear and easy to be integrated by third parties in vehicle model analysis. However, they have a limited validity to the experiment in which they were identified. While approaches based on physical principles allow testing many more virtual situations. These more complex models could also have wider applications by contributing to the development of model-based estimation of muscle forces for clinical applications because they can provide "*insight into neural control and tissue loading and can thus contribute to improved diagnosis and management of both neurological and orthopedic conditions*" (Erdemir, McLean, Herzog, & van den Bogert, 2007).

Ideally, the prediction of biodynamic feedthrough would be a major contribution to improve rotorcraft designs. More precisely the prediction of envelops of BDFT that would represent the population of pilot involuntary behaviors in any flight configuration would be of interest. It could help, as early as possible in the design, to optimize the choice of design parameters and improve the design of the flight control system for a better robustness to PAOs.

3.2. Proposal

However, there has not yet been a consensus on how to model a human arm to compute biodynamic feedthrough as measured in experiments. The model proposed in this chapter is a combination of the models proposed in (Lee & Terzopoulos, 2006), (Pennestri, Stefanelli, Valentini, & Vita, 2007) and (Masarati & Quaranta, 2014). Its

originality is twofold, firstly the model is developed using bond graphs and secondly it is applied to the prediction of BDFT on the lateral axis of a conventional helicopter. While computing the left arm of a helicopter pilot movement that controls the collective lever, requires only representing a planar movement of the arm. In the present case of the right arm of the pilot, where he controls the cyclic lever, the arm movement is not planar anymore but spatial and the muscular repartition more asymmetrical; the resulting motion is therefore more complex. In the next sections the computation prediction of biodynamic feedthrough is described and then compared to literature experiments.

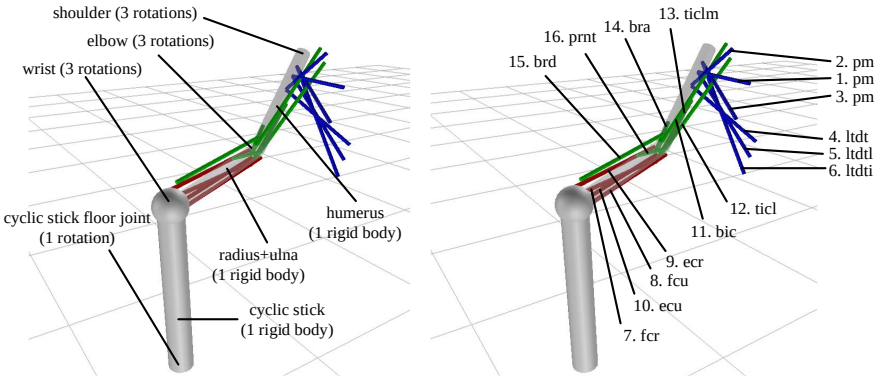

(a) Multibody system (b) Muscular system

Figure 3-7. Pilot's left upper limb neuromusculoskeletal system model proposal

Table 4. Muscle number and name of the proposed model

Muscle #	Abbrev	Name
between humerus and shoulder		
1	pm	pectoralis major (stern)
2	pm	pectoralis major (clav)
3	pm	pectoralis major (ribs)
4	ltdt	latissimus dorsi (thoracic)
5	ltdtl	latissimus dorsi (lumbar)
6	ltdti	latissimus dorsi (iliac)
between humerus and hand		
7	fcr	flexor carpi radialis
8	fcu	flexor carpi ulnaris
9	ecr	extensor carpi radialis
10	ecu	extensor carpi ulnaris

between radius and shoulder		
11	bic	biceps brachii caput l/b
between ulna and shoulder		
12	ticl	triceps brachii caput longus
between humerus and ulna		
13	ticlm	triceps brachii caput l/m
14	bra	brachialis
between humerus and radius		
15	brd	brachoradialis
16	prnt	pronator teres

3.3. Upper limb skeleton subsystem and closed kinematic loops

In the upper limb model developed in this work the forearm is considered to be directly attached to the cyclic stick, subtracting the presence of the hand. The arm is attached through the shoulder directly to the airframe, neglecting the motion of any supplementary limb. All the articulations are considered to be spherical joints and represent wrist, elbow and shoulder, see Figure 3-7. Each one of these joints degree of freedom contains stiffness and damping characteristics that are obtained from literature experimental identifications (Mattaboni, Fumagalli, Quaranta, & al., 2009). All the parameters and axes definitions of both *arm and cyclic lever* are presented on Appendix 4.The human forearm skeleton contains radius and ulna bones but it has been simplified to a single rigid body representing the characteristics of both bones. The humerus is also considered as a rigid body leading to a skeletal model of 2 rigid bodies and 9 degrees of freedom. The multibody model is developed using the approach presented in the previous chapter. When this skeleton subsystem is not attached to the cyclic stick it can be seen as a chain of bodies see Figure 3-8. However, once it is attached to the cyclic stick, both cyclic stick and arm are attached to the rotorcraft airframe leading to a multibody system that contains a closed kinematic chain (CKC) or loop on Figure 3-8. The computation of numerical solutions of multibody systems with a (CKC) is challenging because the topological loop (Figure 3-8) leads to equations of motion in the form of DAEs of a higher index[14] than 2, usually 3, see (Dabney, 2002) .

[14] Index: number of times the constraint equation has to be differentiated to obtain a system of ODEs (Van Dijk & Breedveld, Simulation of system models containing zero-order causal paths—I. Classification of zero-order causal paths, 1991)

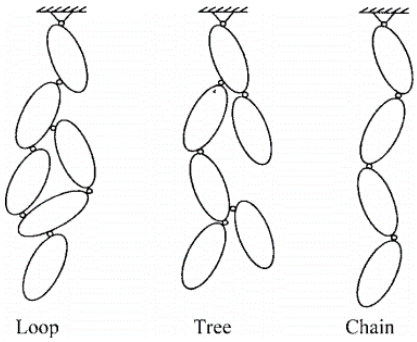

Figure 3-8. Topology of multibody systems from (Eberhard & Schiehlen, 2006)

While this higher index DAEs can be theoretically solved numerically, most numerical methods implemented in commercial software might not be able to solve them. Many methods exist to circumvent the problem based on the manipulation of equations (Boudon, 2014). Another approach, known as the singular perturbation method (Zeid & Overholt, Singularly Perturbed Formulation: Explicit Modeling Of Multibody Systems, 1995), (Boudon, 2014) consists in reworking the hypothesis of the system model at the physical level. This approach is chosen in this work since it can be controlled at the bond graph level in a systematic way. The approach consists in breaking the kinematic loop constraint by replacing at least one rigid constraint of the loop with a stiff compliance and a damping term; the index of the DAE is reduced but a 'stiff' ordinary differential equation is added to the system that can be efficiently solved numerically in 20-sim® using the integrated Backward Differentiation Formula (BDF) method. In our application, this approach is implemented by breaking the rigid translation velocity constraint of the revolute joint between the cyclic stick and the airframe at the bond graph level see, Figure 3-9.

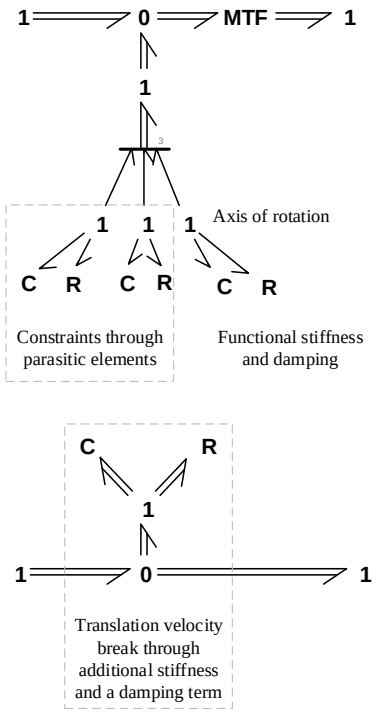

Figure 3-9. 'Breaking' the translation velocity constraint of a revolute joint

This method has the disadvantage, as already stated in the previous chapter, of introducing new state variables and therefore new modes that will perturb the analysis of the system. In addition, there is no systematic method to choose the value of stiffness and damping of these elements. The advantage of this method is that it can be implemented at a physical level in a systematic way by the modeler whether analytically or at the bond graph level.

3.4. Hill-type muscle forces subsystem

The human upper limb contains more than 60 muscles but in this first approach only 16 will be represented, see Figure 3-7 and Table 4. Prior to further complexification, experimental confrontation of the actual model is needed to verify muscles forces and kinematic predictions. Once the skeletal model is in place, muscles can be superposed to the multibody system. In this section, a bond graph representation of a Hill-type muscle (Zajac, 1988) as developed analytically in (Pennestri, Stefanelli, Valentini, & Vita, 2007) is proposed. In (Wojcik, 2003), a Hill-type muscle is represented using bond graphs by a source of effort; however neither the explicit expression of the force and the computation of activation dynamics are presented, making it impossible to be used. The particularity of the model proposed in this section is that it allows taking into account spatial motion of the skeleton which is essential in our application. As

described in (Pennestri, Stefanelli, Valentini, & Vita, 2007), Hill-type muscle force models can be decomposed into an active and a passive component,

$$F_{muscle} = F_a + F_p \tag{37}$$

The active component generates a force that depends on the muscle length, its contraction velocity and its muscular activation function *a(t)* "*which assumes a value between 0 and 1 (0 for not-activated and 1 for fully activated muscle)*" (Pennestri, Stefanelli, Valentini, & Vita, 2007). The passive component depends on the muscle length only.
Nondimensional muscle length *x* and muscle contraction velocity *v* are defined as,

$$x = \frac{l(t)}{l_0} \text{ and } v = \frac{\dot{l}(t)}{v_{\max}} \tag{38}$$

Where v_{max} is the maximum contraction velocity chosen as muscle independent and to be equal to 2.5 m/s (Pennestri, Stefanelli, Valentini, & Vita, 2007). By introducing, the maximal muscle force scalar f_0, the functions f_1 and f_3 that depend on muscle length *l(t)*, and f_2 that takes into account muscle forces that vary with muscle length, muscle stretching velocity and their activation the muscle force is expressed as,

$$F_{muscle} = f_0 \left(f_1(x) f_2(v) a + f_3(x) \right) \tag{39}$$

Where each function is,

$$\begin{aligned} f_1(x) &= e^{-40(x-0.95)^4+(x-0.95)^2} \\ f_2(v) &= 1.6\left(1 - e^{-1.1/(1-v)^4+0.1/(1-v)^2}\right) \\ f_3(x) &= 1.3\arctan\left(0.1\left(x-0.22\right)^{10}\right) \end{aligned} \tag{40}$$

On Figure 3-10, the nondimensional muscle force is plotted for a fully activated and not-activated muscle; in this last case, the purely elastic characteristic of the muscle can be observed.

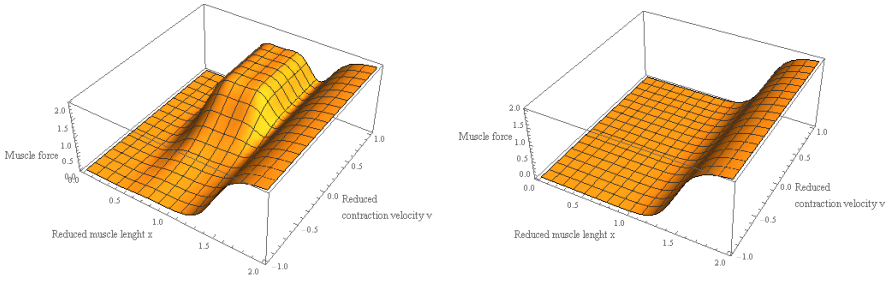

(a) Fully activated muscle, *a=1* (b) Not-activated muscle, *a=0*

Figure 3-10. Muscle force length and velocity relationships
$f_1(x)f_2(v)a+f_3(x)$

In application to the representation of the first muscle of the proposed model in this work, which is *pectoralis major*, see Figure 3-7, the bond graph representation of a muscle derivation is developed below. First let us define the muscle force line of action,

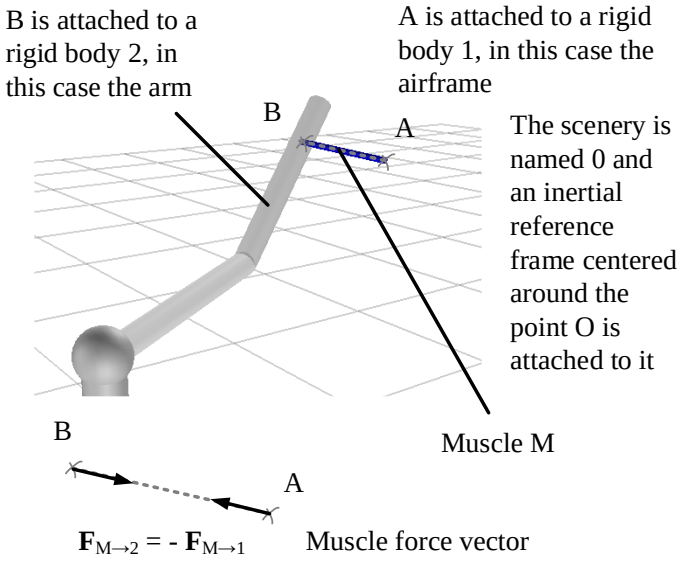

Figure 3-11. Muscle force vector definition between two rigid bodies in spatial motion

Since the muscle force vector norm depends on muscle length *l(t)* and stretch velocity (total time derivative of *l(t)*), these two quantities need to be expressed in a bond graph exploitable way,

$$l(t) = \|\mathbf{AB}(t)\| \tag{41}$$

$$\begin{aligned}\mathbf{AB} &= \mathbf{AO} + \mathbf{OB} \\ &= -\int\left(\frac{d}{dt}^{0}\mathbf{OA}\right)dt + \int\left(\frac{d}{dt}^{0}\mathbf{OB}\right)dt\end{aligned} \tag{42}$$

The above total time derivatives in the inertial reference frame are introduced to let appear the velocities of the points A and B with respect to the inertial reference frame. By definition,

$$\frac{d}{dt}^{0}\mathbf{OA} = \mathbf{V}_{A,1/0} \tag{43}$$

$$\frac{d}{dt}^{0}\mathbf{OB} = \mathbf{V}_{B,2/0} \tag{44}$$

These velocities are bond graph flows that naturally appear in the multibond graph representation of a rigid body, see Figure 2-5 and the explanations associated in that section. The muscle length can therefore be expressed,

$$l(t) = \left\|\int\left(\mathbf{V}_{B,2/0} - \mathbf{V}_{A,1/0}\right)dt\right\| \tag{45}$$

By previous definitions, Figure 3-11 and knowing that f_0, f_1, f_2 and f_3 are positive definite functions,

$$\mathbf{F}^{0}_{M\to 2} = -f_0\left(f_1 f_2 a + f_3\right)\frac{\mathbf{AB}^{0}(t)}{\left\|\mathbf{AB}^{0}(t)\right\|} \tag{46}$$

The equations at the zero junctions of the multibond graph structure proposed on Figure 3-12 which is quite similar to the classic Hill-type schematic muscle structure leads to,

$$\mathbf{F}^{0}_{M\to 2} = \mathbf{F}^{0}_{PE} + \mathbf{F}^{0}_{CE} \tag{47}$$

With the expressions of the contractile and parallel element forces as functions of their incoming bond flows,

$$\begin{aligned}\mathbf{F}^{0}_{CE} &= -f_0 f_1 f_2 a\frac{\mathbf{AB}^{0}(t)}{\left\|\mathbf{AB}^{0}(t)\right\|} \\ &= -f_0 f_1 f_2 a\frac{\int\left(\mathbf{V}^{0}_{B,2/0} - \mathbf{V}^{0}_{A,1/0}\right)dt}{\left\|\int\left(\mathbf{V}^{0}_{B,2/0} - \mathbf{V}^{0}_{A,1/0}\right)dt\right\|}\end{aligned} \tag{48}$$

$$\begin{aligned}\mathbf{F}^{0}_{PE} &= -f_0 f_3\frac{\mathbf{AB}^{0}(t)}{\left\|\mathbf{AB}^{0}(t)\right\|} \\ &= -f_0 f_3\frac{\int\left(\mathbf{V}^{0}_{B,2/0} - \mathbf{V}^{0}_{A,1/0}\right)dt}{\left\|\int\left(\mathbf{V}^{0}_{B,2/0} - \mathbf{V}^{0}_{A,1/0}\right)dt\right\|}\end{aligned} \tag{49}$$

In order to be able to say that the parallel element of the muscle is a C element, and that it is energy conservative, it has to verify the *Maxwell reciprocity condition* (Borutzky, 2009). By using standard, bond graph definitions, a C element storage element is defined by the function[15] $\boldsymbol{\Phi}_C$ relating the effort vector $\boldsymbol{e}$ to the generalized displacement vector $\boldsymbol{q}$,

$$\mathbf{e}(t) = \boldsymbol{\Phi}_C^{-1}(\mathbf{q}(t)) \tag{50}$$

The *Maxwell's reciprocity condition* implies that for $i \neq j$,

$$\frac{\partial e_i}{\partial q_j} = \frac{\partial e_j}{\partial q_i} \tag{51}$$

In our case the generalized displacement vector can be expressed by,

$$\mathbf{q}(t) = \int flow.dt = \int \left(\mathbf{V}_{B,2/0}^0 - \mathbf{V}_{A,1/0}^0 \right) dt = \mathbf{AB}^0(t) \tag{52}$$

Therefore the inverse of the function Φ_C can be expressed as,

$$\boldsymbol{\Phi}_C^{-1}(\mathbf{q}) = \frac{f_0 \cdot f_3\left(\frac{\sqrt{\mathbf{q}^T.\mathbf{q}}}{l_0} \right)}{\sqrt{\mathbf{q}^T.\mathbf{q}}} \mathbf{q} \tag{53}$$

Finally one can verify with the help of a formal computation software such as Mathematica® that for $i \neq j$, the equality below is verified and that the parallel element behavior of the muscle can be modeled as a bond graph C element,

$$\frac{\partial}{\partial q_j}\left(\frac{f_0 \cdot f_3\left(\frac{\sqrt{\mathbf{q}^T.\mathbf{q}}}{l_0} \right)}{\sqrt{\mathbf{q}^T.\mathbf{q}}} q_i \right) = \frac{\partial}{\partial q_i}\left(\frac{f_0 \cdot f_3\left(\frac{\sqrt{\mathbf{q}^T.\mathbf{q}}}{l_0} \right)}{\sqrt{\mathbf{q}^T.\mathbf{q}}} q_j \right) \tag{54}$$

[15] Mechanically speaking, modeling a spring with a linear constant stiffness characteristic k would simply lead to $\Phi_C^{-1}(q) = k$, such that the spring force equal to $\Phi_C^{-1}(q).q$

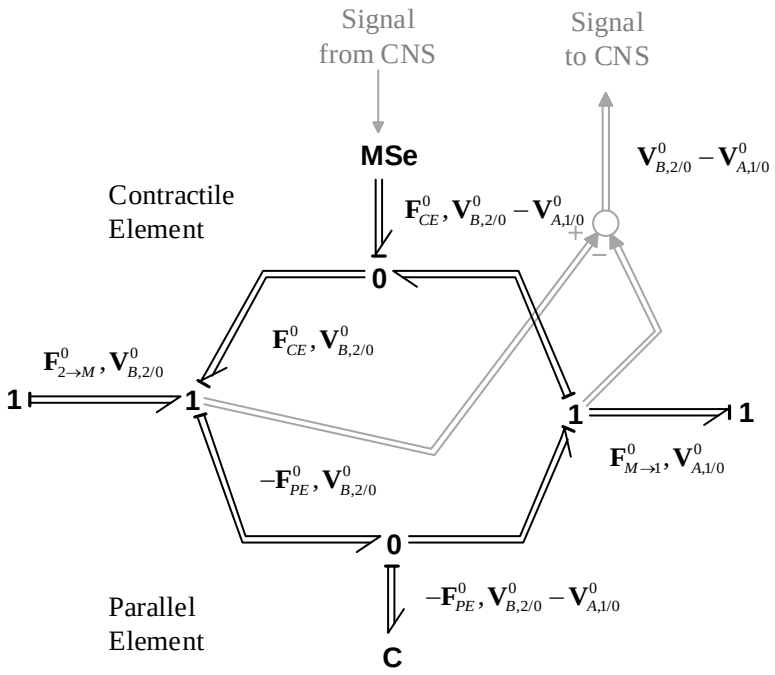

Figure 3-12. Hill-type muscle structure proposal using multibond graphs

In terms of energy, the total work that muscle forces input in the system can be computed by summing the energy at the root of the modulated source of effort (MSe) and the capacitance (C). Each muscle force work expression is given by,

$$W_{muscle} = \int \left(\mathbf{F}^0_{CE} - \mathbf{F}^0_{PE}\right).\left(\mathbf{V}^0_{B,2/0} - \mathbf{V}^0_{A,1/0}\right) dt \tag{55}$$

Since human body motion can only be achieved by the power given by muscle forces, this quantity represents the energetic cost for the organism to generate the motion. However this quantity represents only a part of the energy cost for our body to move, because in the process, muscles also heat. Summing all the energetic costs for the body to generate motion leads to what is called metabolic cost. The dissipation of energy due to heating is not negligible (Schiehlen, 2006). However, our interest in metabolic cost will be to minimize it rather than trying to obtain realistic values of it. As a result, it is reasonable to think that minimizing metabolic cost is equivalent to minimizing W_{muscle}.

3.5. Central nervous system (CNS) control subsystem

In addition to the musculoskeletal system, the reflex control of the muscles by the central nervous system is taken into account. The reflex control model proposed in (Lee & Terzopoulos, 2006), (Masarati & Quaranta, 2014) reproduce the variation of muscular activation Δa that depends on the muscle length and the muscle contraction velocity. This section model is the one that has been developed in (Lee & Terzopoulos, 2006) as part of the neural control system of a neck face model 'to synthesize a variety of autonomous movements for the behavioral animation of the human head and face', see Figure 3-13.

Figure 3-13. Neuromuscular control of the neck from (Lee & Terzopoulos, 2006)

The variation of muscular activation Δa is due to the feedback control that is represented in gray on Figure 3-12 such that,

$$a = a_0 + \Delta a \tag{56}$$

Where a_0 is an initial muscle activation coefficient and Δa is a quasi-steady variation around it such that, by introducing the muscle reflexive feedback gain on muscle length k_p; and the reflexive feedback gain on muscle contraction velocity k_v,

$$\Delta a = k_p.x + k_v.v \tag{57}$$

In addition a function is defined such that if $a_0+k_px+k_vv<0$ then $a=0$ and if $a_0+k_px+k_vv>1$ then $a=1$. In this way, a can only take a value between 0 and 1, respecting the definition of activation given previously.

3.6. Minimizing metabolic cost to compute muscular activation coefficients

The human musculoskeletal system possesses more muscles than degrees of freedom; as a result it is over actuated. And since each muscle force depends on its activation, the over actuation leads to a mathematical indeterminacy (Pandy, 2001), (Erdemir, McLean, Herzog, & van den Bogert, 2007): there are more unknowns than equations and the problem has an infinity number of solutions. However when a human tries to grab an object with his arms, it seems he always find one similar solution to go from your initial arm position to the 'object grabbed' position. After experimental work,

scientists have hypothesized that the human body tries to minimize its energy consumption or metabolic cost during walking (Zarrugh, Todd, & Ralston, 1974), it is also proposed to be a principle governing neuronal biophysics in (Hasenstaub, Otte, Callaway, & Sejnowski, 2010). The addition of this principle of minimization of metabolic cost allows solving the indeterminacy and computing muscle activation coefficients (Erdemir, McLean, Herzog, & van den Bogert, 2007). This is not the only way of solving the indeterminacy problem; another very popular minimization is the one of muscle stress (Erdemir, McLean, Herzog, & van den Bogert, 2007). The same work proposes a review of the different techniques that can be employed to compute muscle forces or muscle excitations see Figure 3-14.

In A, the objective is to obtain the equivalent muscle forces that need to appear in the musculoskeletal model to match with joint torques that are the output of experimental kinematic measures through an inverse dynamics model; "*muscle forces are iteratively updated by an optimization scheme until the objective function J (e.g. total muscle stress) is minimized and equality constraints between experimental joint torques and muscular moments are satisfied*" (Erdemir, McLean, Herzog, & van den Bogert, 2007). In B, the objective is to obtain muscular excitations. In the previous section, the notion of muscle activation has been introduced, however "*muscles cannot be activated or relaxed instantaneously*" (Pandy, 2001). A time delay appears between muscle excitation and muscle activation due to the chemical process between the two events. As a result, this dynamic might be represented (Pandy, 2001).

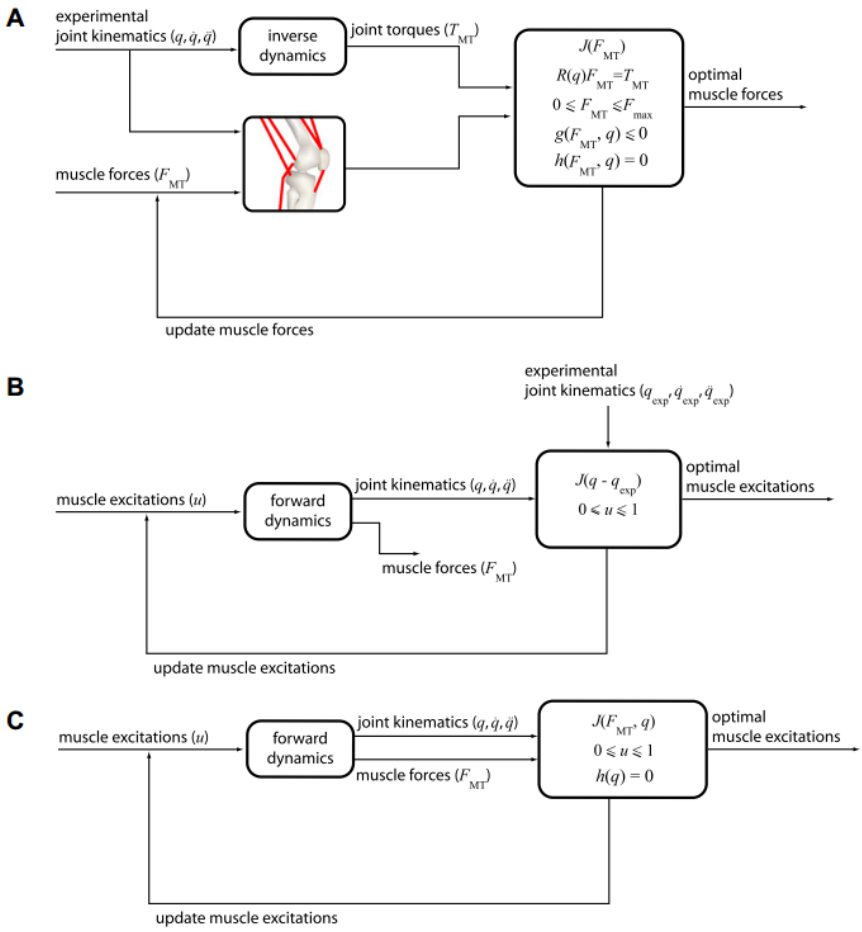

Figure 3-14. Model-based estimation of forces or excitations from (Erdemir, McLean, Herzog, & van den Bogert, 2007)

In this work, this time delay has not been taken into account; the C approach of Figure 3-14 is applied, see Figure 3-15.

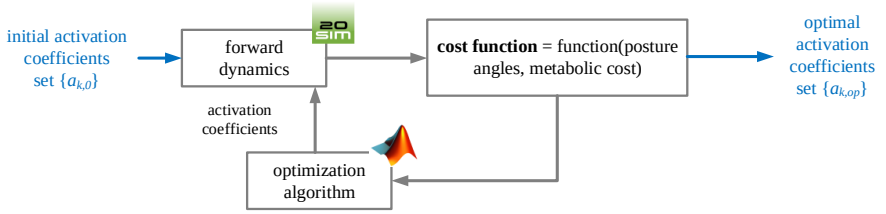

Figure 3-15. Applying a forward dynamics approach to determine muscular activation coefficients

It consists in determining optimal activation coefficients for a given posture and reflex control setting by minimizing a cost function that depends both on the upper limb bone angles and metabolic as proposed in (Brouwn, 2000). In that work the following cost function *J* is proposed,

$$J = \int_0^t \left\{ q.\left[x(t) - x_d(\mathrm{t}) \right]^2 + p.u^2(t) \right\} dt \tag{58}$$

Where x is the vector of positions, x_d is the vector of desired equilibrium or posture and u the control signal. The metabolic energy consumption is modeled by u^2. In this case, p and q weighing factors parameter the strategy adaption of the central nervous system to achieve an objective (Brouwn, 2000). In our work, the weighing factors are set to 1, not to privilege any strategy, and the metabolic energy consumption is replaced by the muscles forces work that can be naturally computed from the bond graph, see equation (55) and the paragraph associated. The cost function J becomes therefore,

$$J = \int_0^t \left\{ \left[x(t) - x_d \right]^2 + \left(\sum_i W_{muscle\ i}(t) \right)^2 \right\} dt \tag{59}$$

In this work, see Figure 3-15, the optimization function that is used is *fminsearch* from Matlab®, to find the minimum of unconstrained multivariable nonlinear functions using a derivative-free method. Since the muscular activation coefficients need to be constrained between 0 and 1, the absolute value of the sinus of the results proposed by Matlab® are the muscular activation coefficients that are sent for simulation to the bond graph physical model implemented in 20-sim®. More efficient and adapted optimization functions could be used, for example by providing also the derivative of the cost function, but out of the scope of this work.

3.7. Biodynamical model validity

In the previous section an upper limb neuromusculoskeletal model was developed with the objective of predicting numerically the biodynamic feedthrough (BDFT) of a helicopter pilot on its lateral axis.

As a remainder of the beginning of the chapter, in (Venrooij, et al., 2011) BDFT measures on helicopter flight simulators lateral axis are presented. In that experiment, BDFT of different subjects were measured when asked to perform different control tasks. The objective of asking one subject to perform different tasks is to force him to adapt his body and therefore his neuromuscular system to the task. The results are presented on Figure 3-4 for the lateral, longitudinal and vertical helicopter axis translations and show that BDFT is also task dependent. The subjects were asked to perform three tasks. A position task (PT) with the instruction to minimize the position of the stick, a force task (FT) with the instruction to minimize the force applied to the stick and finally a relax task (RT) with the instruction to relax the arm. Trying to characterize the arm response can be interpreted as trying to characterize its impedance. In (Stroeve, 1999) for which "*arm impedance is the resultant of passive dynamics of the arm, intrinsic impedance of activated muscles and reflexive contributions*".

In order to reproduce a given task, which is conjectured to correspond to a neuromuscular system set, the variation of two parameters is discussed in the next paragraphs, which are the reflexive feedback gain on muscle length *kp* and a multiplication coefficient on wrist and elbow passive stiffness and damping characteristics denoted α. Once these two parameters are chosen, the forward dynamics approach described in previous sections is launched to obtain optimal muscular activation coefficients. The results are presented on Figure 3-16 where *kp* and α are gradually increased. It does not to be a consensus in literature on which parameters should be varied to parameter a given neuromuscular set.

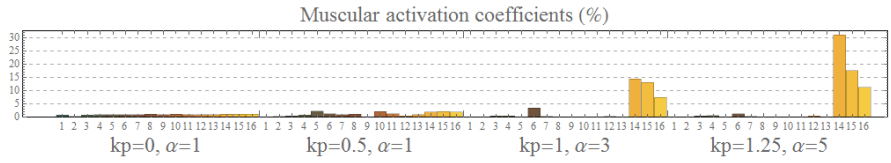

Figure 3-16. Arm muscular activation coefficients computation for each one of the 16 muscles

Interestingly, the optimization converges to the need for the upper limb of the pilot model to activate more importantly muscles 14, 15 and 16 which correspond to *brachialis* (30%), *brachoradialis* (20%) and *pronator teres* (10%). These three muscles connect the humerus to the ulna and radius, see Figure 3-6 and Figure 3-7. In other words for given variations of position and velocity between the forearm and the arm of the pilot, these muscles produce higher forces when increasing reflexive feedback *kp* and passive characteristics of wrist and elbow joints coefficient α.

The obtained muscle activation coefficients for different setups of the pilot neuromuscular system are conjectured to represent pilot task variability. For each task

or neuromuscular system setup, the next step of the numerical experiment consists in computing the lateral BDFT; which is the cyclic stick lever angle divided by the imposed sinusoidal airframe accelerations on its lateral axis that vary from 0.8 to 8 Hz. On Figure 3-17, the results of two simulations are presented for two sets of parameters for α and *kp*. On Figure 3-18, the numerical experiment described above is performed also without the pilot; the result in gray points shows simply the behavior of a second order mass-spring system that corresponds to the oscillations of the cyclic stick with no pilot action. The inclusion of the pilot in the system modifies the shape of this behavior as it can be seen on Figure 3-18.

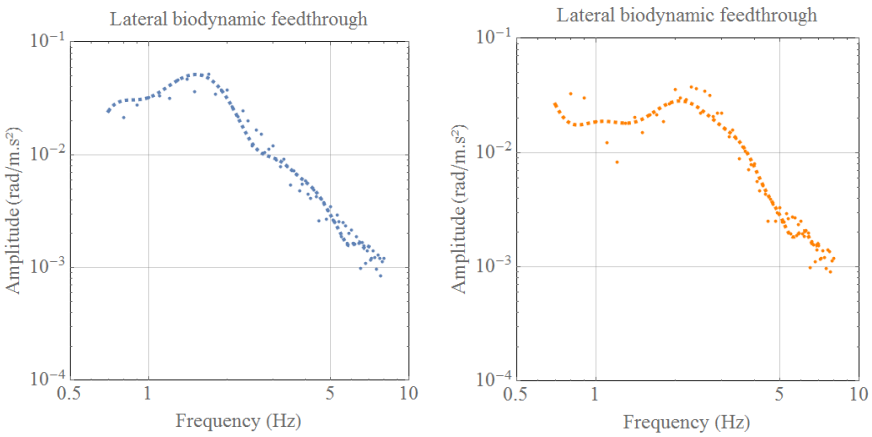

(a) kp=0, α=1, least square approximation

(b) kp=1.25, α=5, least square approximation

Figure 3-17. BDFT Numerical simulation results

The increase of α from 1 to 5 shifts the resonant frequency and decreases the amplitude of BDFT at this same frequency. This is understandable since, increasing α is equivalent to an increase of wrist and shoulder stiffness, which at constant mass and inertia leads to a higher resonant frequency. The increase of α also leads to an increase of wrist and shoulder local damping moments for which the decrease of amplitude of BDFT can be explained. The impact of modifying *kp*, which parameters the reflexive muscle length feedback coefficient of the activation has especially an impact at lower frequencies, below 1 Hz where harmonics appear with high gains see Figure 3-20. The increase in reflexive feedback also impacts the shape of BDFT around the resonant frequency see (b) Figure 3-17.

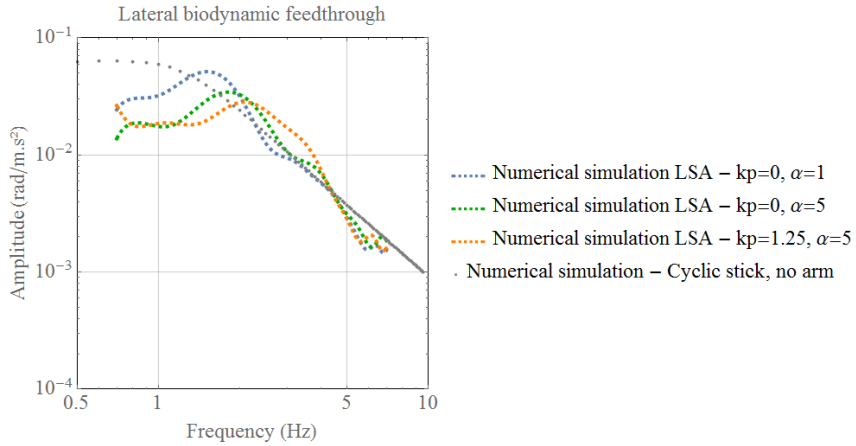

Figure 3-18. BDFT Numerical simulations evolution with and without pilot

On Figure 3-19 (a), the proposed set of parameters leads to a BDFT resonant frequency that is higher from what has been found in the experiment. This is not surprising when taking into account that the pilot model parameters of mass, inertia, stiffness and damping characteristics come from subject identification experiments that are not related with this BDFT experimental measures. On Figure 3-19 (b), the increase of *kp* has allowed to maintain a high amount of gain at lower frequencies than resonant frequency which seems to correspond to what has been observed during the experiment.

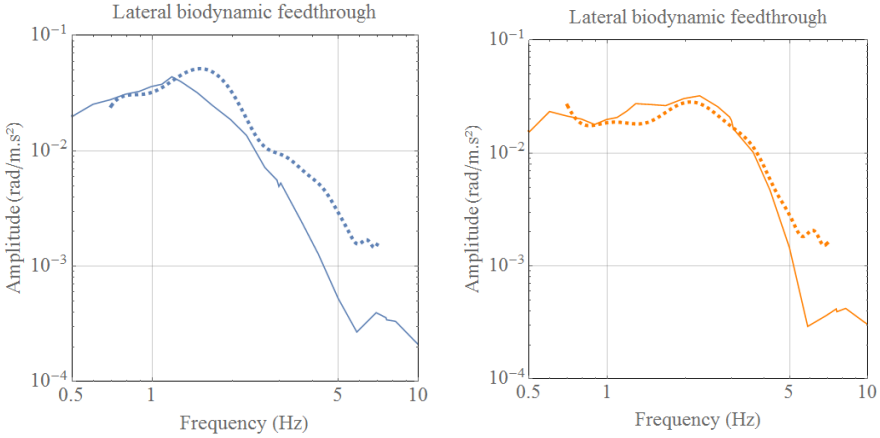

(a) experimental force task (FT) (–) simulation *kp*=0, *α*=1 (--)

(b) experimental position task (PT) (–) simulation *kp*=1.25, *α*=5 (--)

Figure 3-19. BDFT experimental results from (Venrooij, et al., 2011) vs. numerical simulation results

Finally the comparison presented on Figure 3-19 is encouraging. However, in general, additional experiments are needed to identify consistent pilot model parameters of mass, inertia, stiffness and damping characteristics of the upper limb with the subjects that actually were in the cockpit of the flight simulator experiment. In terms of BDFT identification, Figure 3-17 (a) and (b) are sections of Figure 3-20. For the (b), the model is clearly nonlinear see the peaks on (b) Figure 3-20.

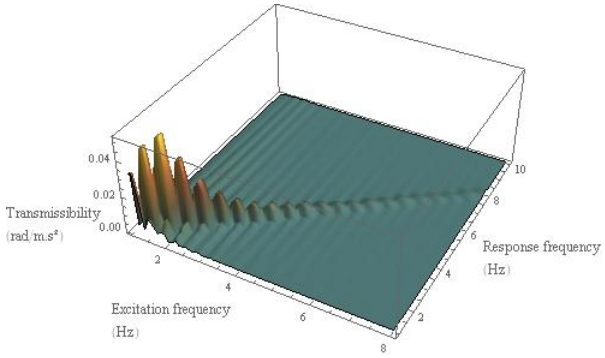

(a) kp=0, α=1

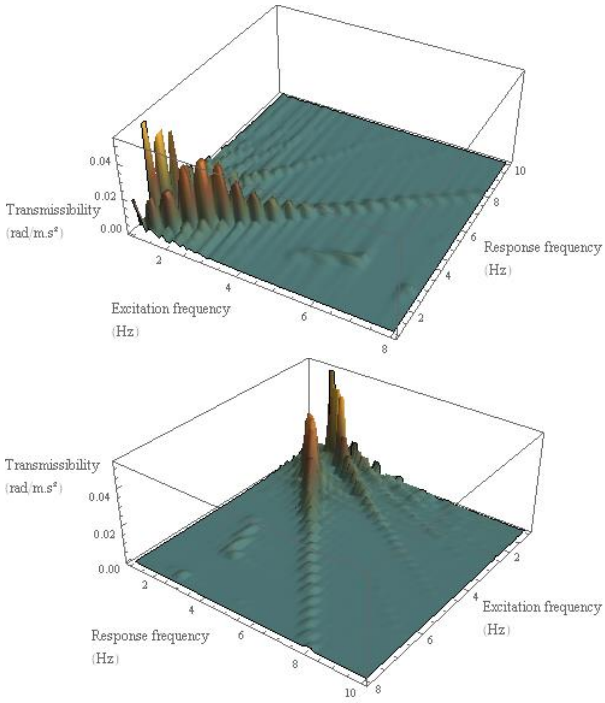

(b) kp=1.25, α=5 (two different views)

Figure 3-20. Numerical simulation, BDFT Spectrograms

The hypothesis of taking the BDFT as a section at those low frequencies seems to be very reductive. This could be addressed, by comparing complete BDFT spectrograms and not just sections from both simulation and experiment. In addition, the modelling of the interfaces at the level of the wrist and the shoulder needs probably to be more detailed since the muscular activation of the muscles around these zones seem extremely low. In particular the deltoid muscle has not been modeled, see Figure 3-21. Once this is done, it would be interesting to see if α coefficient still plays a significant role in the shift of BDFT resonant frequency.

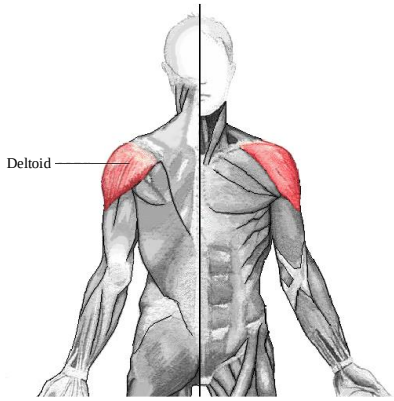

Figure 3-21. Deltoid muscle position

3.8. Conclusion

In this chapter a pilot model has been developed. It consists in a neuromusculoskeletal model of pilot's left upper limb. The individual subsystems that compose this model have been taken from literature. However, multibond graph representations are proposed for the first time to model individual muscles that produce force between bones that have spatial motion. This model is applied on the first time for the prediction of BDFT on the lateral axis of a helicopter.

It is known that the computation of the motion of human movement or posture leads to a mathematical indeterminacy because the human body possesses less degrees of freedoms than muscles that act as actuators that can only contract. It has been pointed out as proposed in literature, that the addition of an energetic principle can solve the indeterminacy problem. It consists in postulating that the human body minimizes metabolic cost during motion. From a computational point of view an optimization algorithm is used to minimize muscle forces work which can be computed naturally by the energetic representation given by bond graphs. This allows to obtain the muscular activation coefficients around several neuromuscular settings.

The system represented in this chapter has also the particularity of being closed, kinematically speaking. The simulation of such systems is challenging; the singular perturbation method can be locally applied at the graphical level in a systematic manner to reduce the index of the DAEs prior to a resolution with a commercial

solver. This method has however the disadvantage of introducing new state variables and therefore new modes that will perturb the analysis of the system.

Finally numerical simulations are performed to compute pilot's biodynamic feedthrough (BDFT). The results are quite encouraging and allow to find similar qualitatively similar gain values to literature experiments. The task dependency of helicopter pilots BDFT can be predicted to a certain extent. As a manner of fact, an iterative procedure has allowed to find a set of parameters that have a physical meaning to reproduce what has been seen in experiments.

In the short term, the model prediction in terms of kinematics should be compared to other literature models and supplementary experiments. In the long term, the next step would be to find an explicit mathematical relation between task and neuromuscular system parameters. This would allow obtaining a useful quantity for rotorcraft designers which would be BDFT maximal envelops rather than precise BDFT pilot behaviors.

In synthesis, the reader should remember the BDFT of a given human being depends on the settings of his neuromuscular system; for example whether he/she is stressed or not.

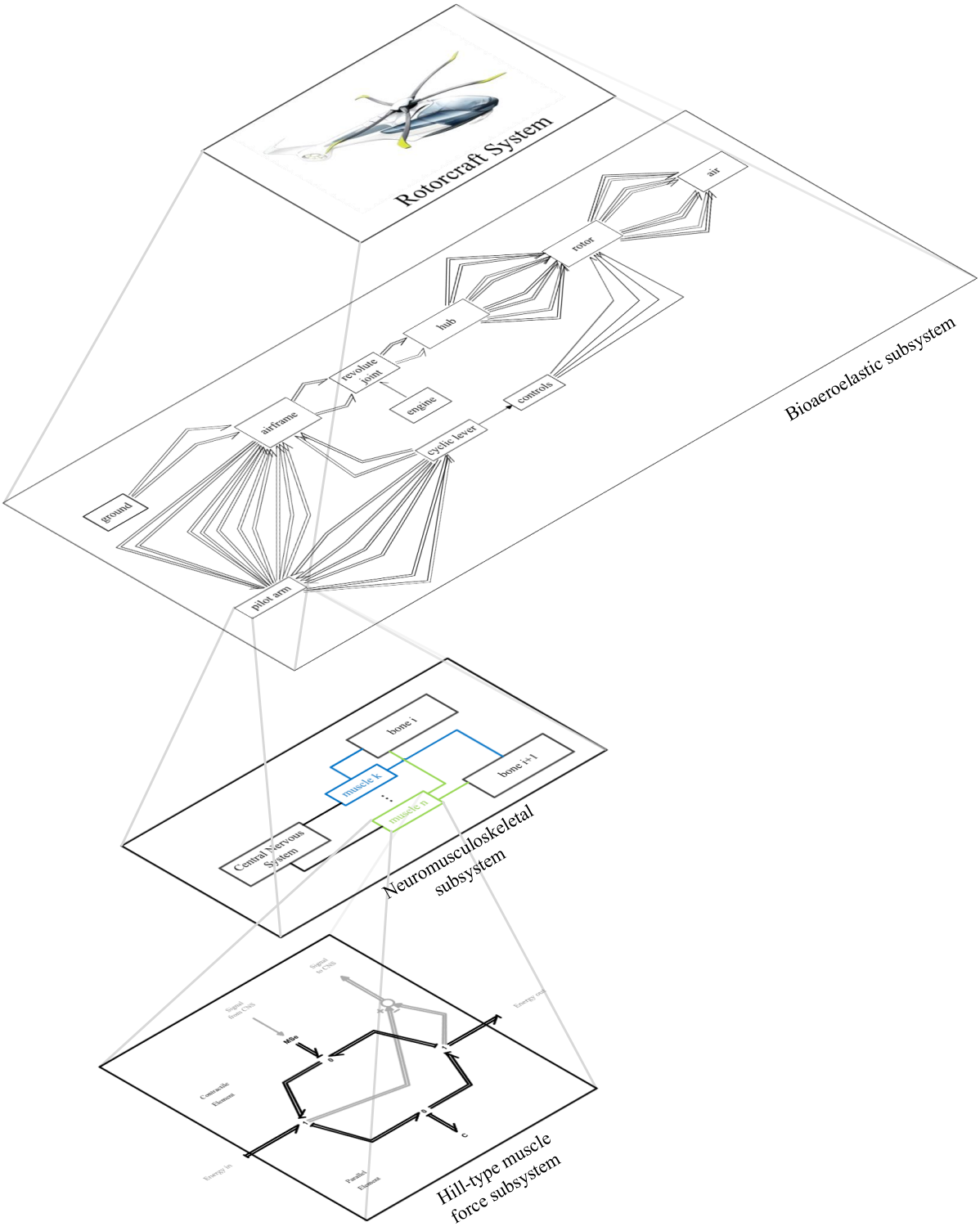

Figure 3-22. Chapter 3 main modeling blocks contribution to the global modeling approach

Chapter 4
Bioaeroelastic linear stability analysis and nonlinear time simulations

Résumé du chapitre 4

Le premier objectif de ce chapitre est d'illustrer comment les modèles de véhicule et de pilote développés dans les deux chapitres précédents peuvent être assemblés afin d'obtenir le comportement bio-aéroélastique du système global. Il est notamment montré, par comparaison entre l'espace Cartésien, voir Figure 4-1, et « l'espace » des bond graphs, voir Figure 4-2, comment ces deux espaces partagent des frontières communes explicites, faisant du bond graph une approche de modélisation dite « structurelle ».
Dans un deuxième temps, une analyse linéaire de la stabilité est menée sur les axes latéral et de roulis d'un modèle bio-aéroélastique d'hélicoptère en vol stationnaire. Cette analyse révèle que les modes qui peuvent potentiellement être déstabilisés sont les modes dits de « traînées » de rotors articulés. La déstabilisation du mode régressif de « trainée » par le comportement biodynamique est conjecturée dans (Muscarello, et al., 2015)*. Le modèle présenté ici appui cette conclusion, voir Figure 4-5. De plus, l'analyse révèle que le mode progressif de « traînée » peut également être déstabilisé par le pilote ; une expérience est néanmoins nécessaire afin de confirmer ou d'infirmer cette analyse. En parallèle, des résultats de simulations dans le domaine temporel, obtenus à partir du modèle bio-aéroélastique non linéaire en bond graphs, sous 20-sim ®, de la réponse libre du système sont présentés, voir Figure 4-7. Dans les cas choisis, on peut observer que selon l'état neuromusculaire du pilote, celui-ci peut participer à la déstabilisation de l'hélicoptère à des fréquences au voisinage de $\Omega-\omega_\delta$ ($\approx$ 3 Hz) ou $\Omega+\omega_\delta$ ($\approx$ 7 Hz). Il faut toutefois tempérer les conclusions en tenant compte des hypothèses fortes qui ont été faites, notamment en ce qui concerne le modèle aérodynamique qui n'est que quasi-statique et le modèle de comportement de pilote qui est approximé au comportement d'un système du second-ordre. Dans tous les cas, des résultats d'essais en vol semblent nécessaires pour pouvoir avancer.*

The first objective of this chapter is to describe how the vehicle and pilot bond graph models developed in the previous chapters can be assembled to represent the bioaeroelastic behavior of the global system. Secondly, a linear stability analysis on the lateral-roll axis of a helicopter is performed, revealing the modes that can be eventually destabilized; finally time simulations are performed from the nonlinear model and seem to be in agreement with the linear model conclusions and give an appreciation of what could be observed in the Cartesian space when this phenomenon occurs.

4.1. Pilot-vehicle system bond graph

4.1.1. Bond graphs for a structural modeling approach

From the bond graph models of both helicopter and pilot developed in the previous chapters, one can assemble them into one graph as illustrated on Figure 4-2. In the Cartesian space this is equivalent to what can be seen on Figure 4-1, where the point P_1 is the center of the spherical joint between the pilot's arm and the cockpit of the helicopter. The points P_2 to P_9 are attachment points of muscles between the pilot and the cockpit. The implicit assumption made here is that the pilot's torso cannot move in the seat and the seat cannot move either with respect to the cockpit.
Interestingly, one can see the points that appear in the physical space are materialized at the bond graph level see Figure 4-1 and Figure 4-2. The frontiers of the system's subsystems are explicitly represented, and the physical quantity that is exchanged between them is power. This is why the bond graph method is said to be *structural* (Chikhaoui, 2013)*;* in other words, the global bond graph of a complex system can be decomposed into sub graphs that have the same frontiers as the physical subsystems.

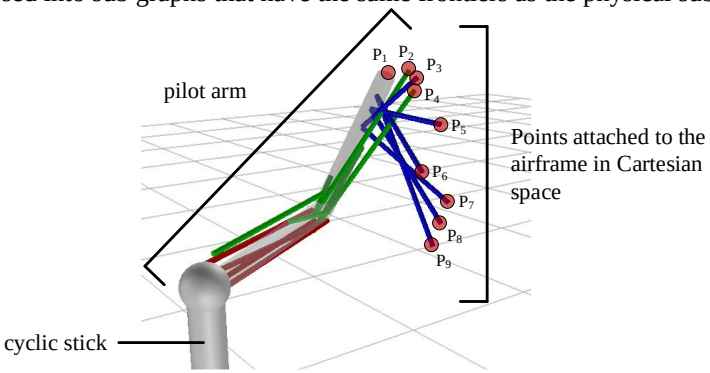

Figure 4-1. Attachment points of the pilot arm model on the airframe

The power exchanged between the pilot arm and the helicopter airframe through the point P_1 is the result of the product of both static and kinematic screws[16],

[16] *Torseur* in French

$$P_{P_1} = \mathbf{F}_{0\to arm}.\mathbf{V}_{P_1,arm/0} + \mathbf{M}_{P_1,0/arm}.\boldsymbol{\Omega}_{arm/0} \tag{60}$$

The green and purple arrows behind P_1 on Figure 4-2 respectively transport the force-velocity and the angular velocity-moment products.
For the rest of the points P_i of Figure 4-1 for *i* between 2 and 9, the power exchanged expression is,

$$P_{P_i} = \mathbf{F}_{Muscle\ i\to airframe}.\mathbf{V}_{P_i,airframe/0} \tag{61}$$

This quantity is materialized on the graph Figure 4-2 by the green arrow behind each P_i point (for *i* between 2 and 9).

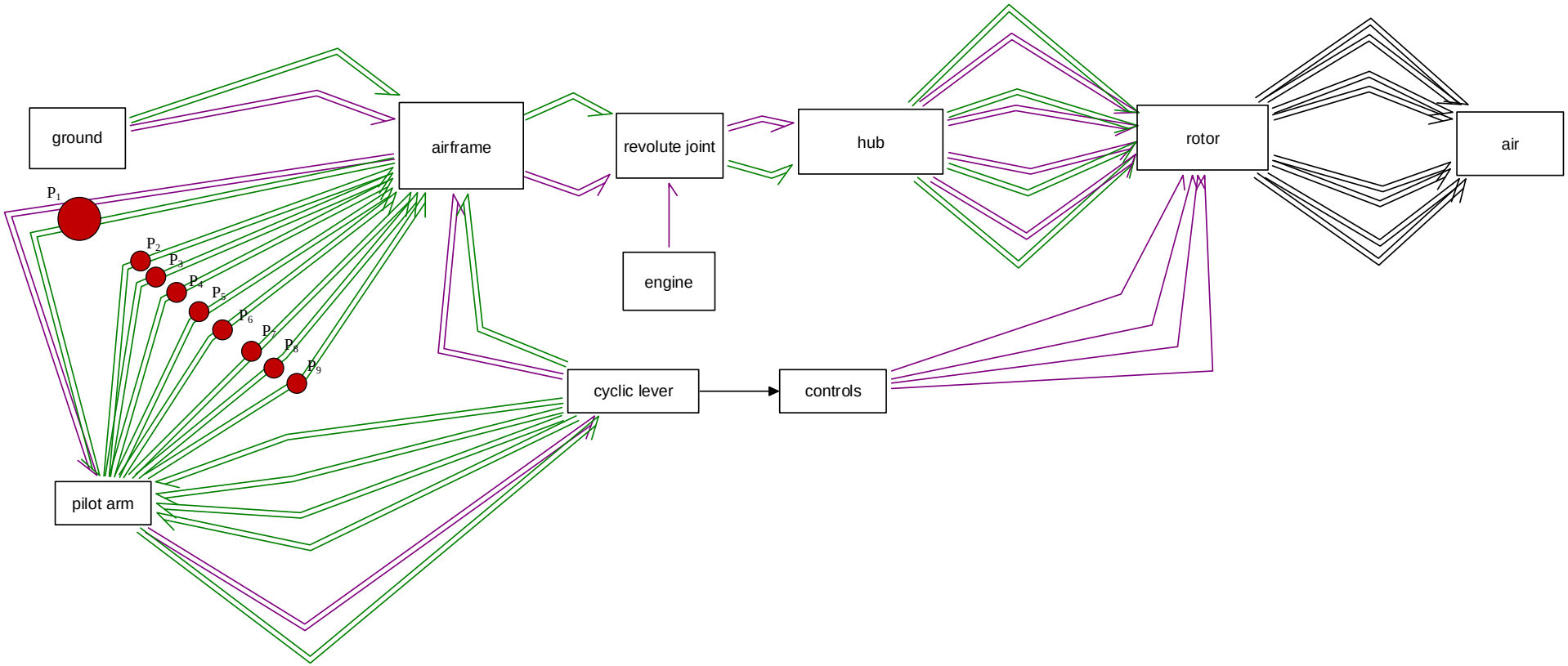

Figure 4-2. Rotorcraft bioaeroelastic system model using bond graphs

4.1.2. Pilot biodynamics model order reduction

The pilot biodynamics model developed in the previous chapter can be used in several manners. The first one consists in directly analyzing the resulting bioaeroelastic model developed previously for which several flight conditions and cabin configurations could be virtually simulated and explored. A second approach, consists in coupling a given vehicle model with a pilot model obtained by identification from experimental results or numerical simulation results, see Figure 4-4.
In order to see how the involuntary pilot behavior can affect the stability of a helicopter on its lateral-roll axis, it is proposed to use the second approach and to perform a sweep of potential pilot neuromuscular system's behaviors for a given helicopter. Furthermore, in order to be able to use powerful stability analysis tools such as Lyapunov's indirect method (eigenvalue analysis of dynamic system's state space matrix) and Campbell diagrams[17], the pilot model is proposed to be reduced to a second order model, as follows,

$$bdft(s) = \frac{\theta_{lat}}{\ddot{x}} \approx \frac{k.\omega^2}{\omega^2 + 2.\zeta.\omega.s + s^2} \tag{62}$$

It also allows reducing the computational cost and more importantly to give the possibility to sweep a wide range of potential involuntary pilot behaviors.

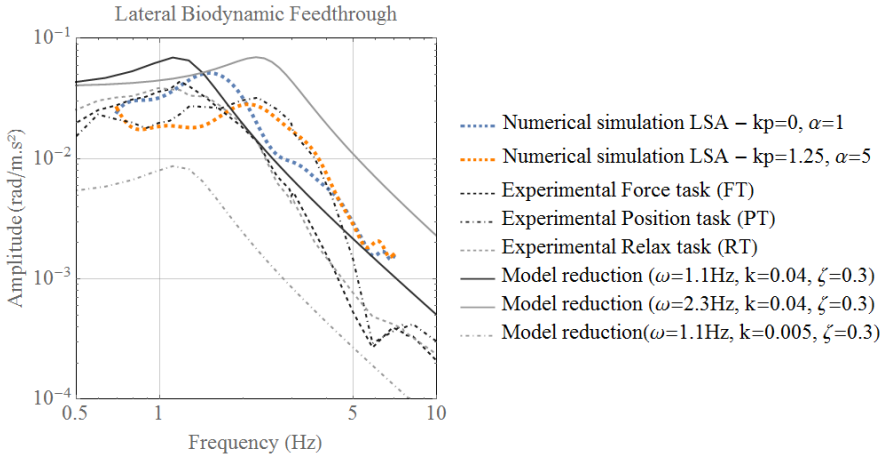

Figure 4-3. Biodynamic feedthrough envelop reduced models

[17] Campbell diagrams are especially used in the investigation of parametric instabilities that might occur in rotating systems. An application is given on Figure 4-6. A classic helicopter parametric instability known as ground resonance is detailed in the next chapter.

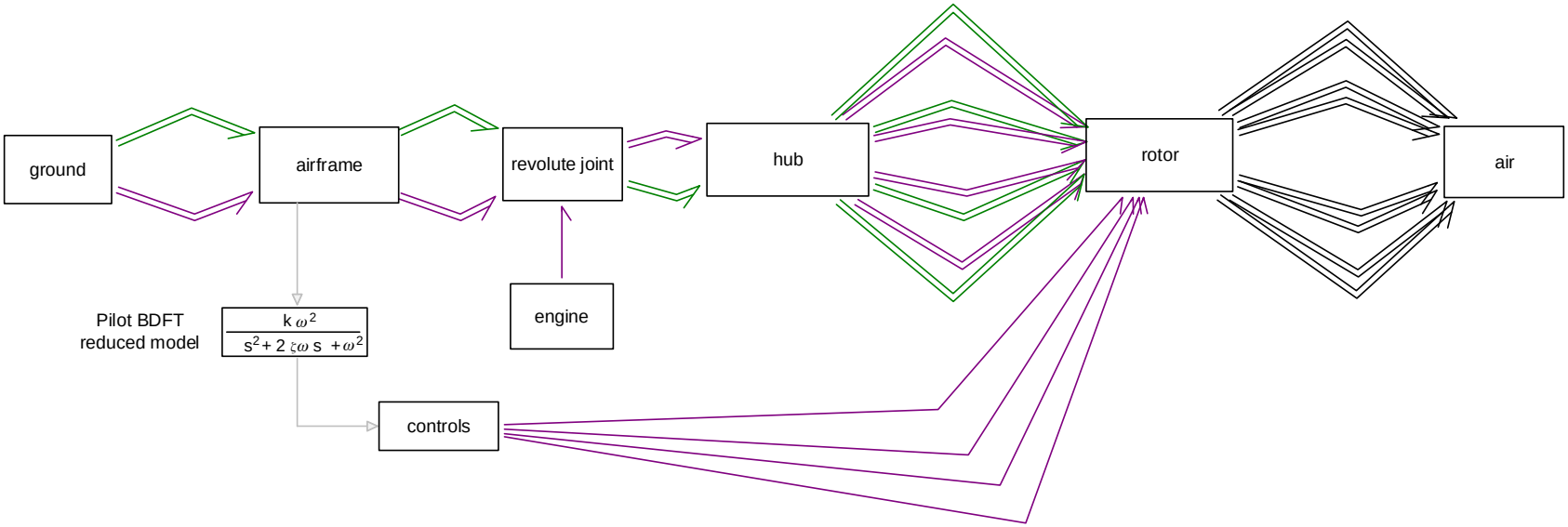

Figure 4-4. Bioaeroelastic system with a reduced BDFT pilot model

On Figure 4-3, the experimental results come from (Venrooij, et al., 2011) on the top of what, the numerical simulations results (LSA – least squares approximation) of the previous chapters have been superposed. The three model reductions presented on the same figure represent three different pilot neuromuscular model setups for which the gain *k* and the resonant frequency ω of the transfer function on equation (62) vary: the higher these parameters are, the 'stiffer' one could qualify the pilot involuntary behavior. These are the same quantities that are swept over a wide range of value on Figure 4-5.

4.2. Lateral-roll axis linear stability analysis and nonlinear time simulations

In this section, the models developed previously are analyzed, in particular on the lateral-roll axis of the helicopter. First a linear model is analyzed and then nonlinear time simulations are carried out.

4.2.1. Linear stability analysis results

The linearized equations from the vehicle model could have been obtained from the bond graph and would give the same results than the state space model that we have derived using Lagrange equations on section 2.2.3 *Lateral/roll dynamics validity of the model around hover*. The pilot model is concatenated to the helicopter model by first expressing the transfer function of equation (62) in the time domain, which becomes,

$$-G\omega^2\theta_{1c} - 2G\zeta\omega\dot{\theta}_{1c} + k\omega^2\ddot{x} - G\ddot{\theta}_{1c} = 0 \tag{63}$$

Where the parameter *G* corresponds to kinematic ratio between the maximum cyclic blade pitch angle and cyclic lever roll angle, $\theta_{lat} = G\theta_{1c}$. Then equation (63) is added to **M**, **C** and **K** matrices, see Appendix 2, with θ_{1c} as an additional state variable. The resulting system can put into the state space form,

$$\dot{\mathbf{x}} = \mathbf{A}\mathbf{x} \tag{64}$$

With the state vector $\mathbf{x} = [\dot{\mathbf{q}}, \mathbf{q}]^T$, and the generalized coordinates vector **q**,

$$\mathbf{q} = \left[x, z, \alpha_y, \beta_0, \beta_{1c}, \beta_{1s}, \delta_0, \delta_{1c}, \delta_{1s}, \theta_{1c} \right]^T$$

The stability of the equilibrium of the bioaeroelastic system can then be assessed by computing the real part of the eigenvalues of the state space matrix **A**. As mentioned previously, literature works (Muscarello, et al., 2015) have conjectured the potential mode that can be destabilized due to pilot BDFT is the regressing lag mode as in

ground resonance phenomena[18]. The approach presented here proposes a model that proves this conjecture. Furthermore, the results show that not only the regressing lag mode can be destabilized by the pilot involuntary behavior, but also the progressive lag mode, see Figure 4-5.
A set of parameters is fixed for the helicopter and the pilot, see Table 3. These parameters correspond to a medium weight helicopter; the individual blade lag motion natural frequency ω_δ is inferior to the rotor angular velocity,

$$\omega_\delta = \sqrt{\frac{k_\delta}{I_{bl}}} = 1.53\ Hz\ \left(\approx 0.33\Omega\right)$$

The positioning of ω_δ corresponds to a soft-in-plane rotor technology ($\omega_\delta < \Omega$) and has lightly damped in-plane rotor modes, see Figure 2-22. Actually there are two very important instabilities that can develop in soft-in-plane rotor technologies with lightly damped modes which are the ground and air resonance (Krysinski & Malburet, 2011). On Figure 4-5, the real part of the eigenvalues of both regressing and advancing lag modes have been computed for varying values of potential pilot neuromuscular system settings. On those figures it is interesting to notice that the instability domains do not have the same shape and in particular that for a pilot resonant frequency above around 3Hz (~ Ω-ω_δ) the regressing lag mode recovers more and more damping even if the pilot's neuromuscular system 'stiffens'.

[18] Developed in next chapter

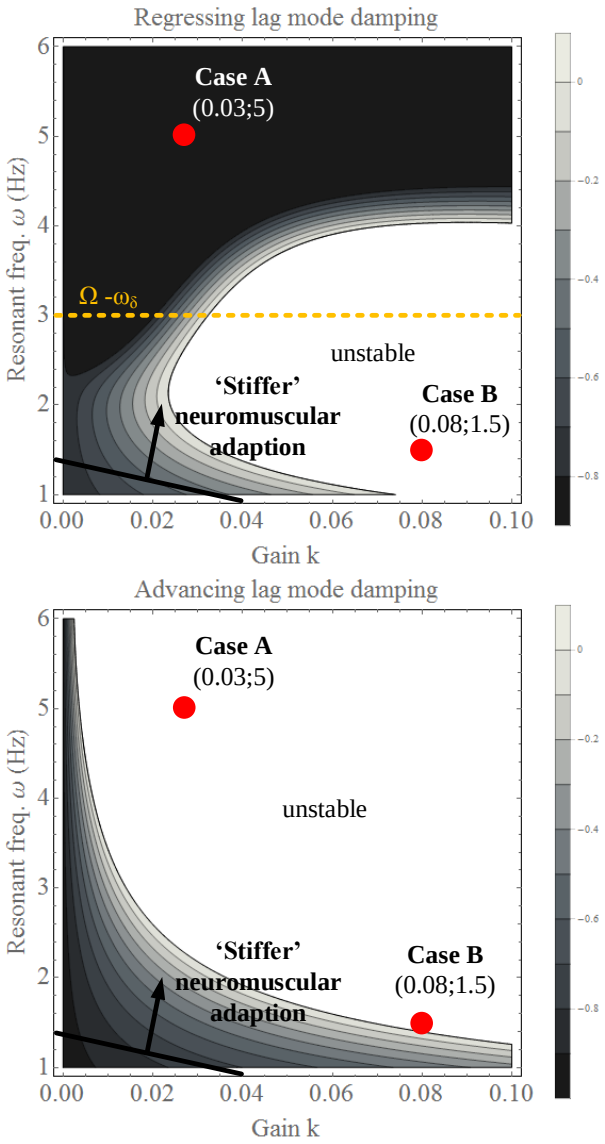

Figure 4-5. Lag modes damping for varying pilot neuromuscular system adaption

On the other side, the advancing lag mode seems to always be destabilized by any increase of pilot stiffness. In order to better understand why this might happen, the real and imaginary parts of the eigenvalues have been plotted for the case B pilot of Figure 4-5, while varying rotor angular velocities on the Campbell diagram on Figure 4-6.

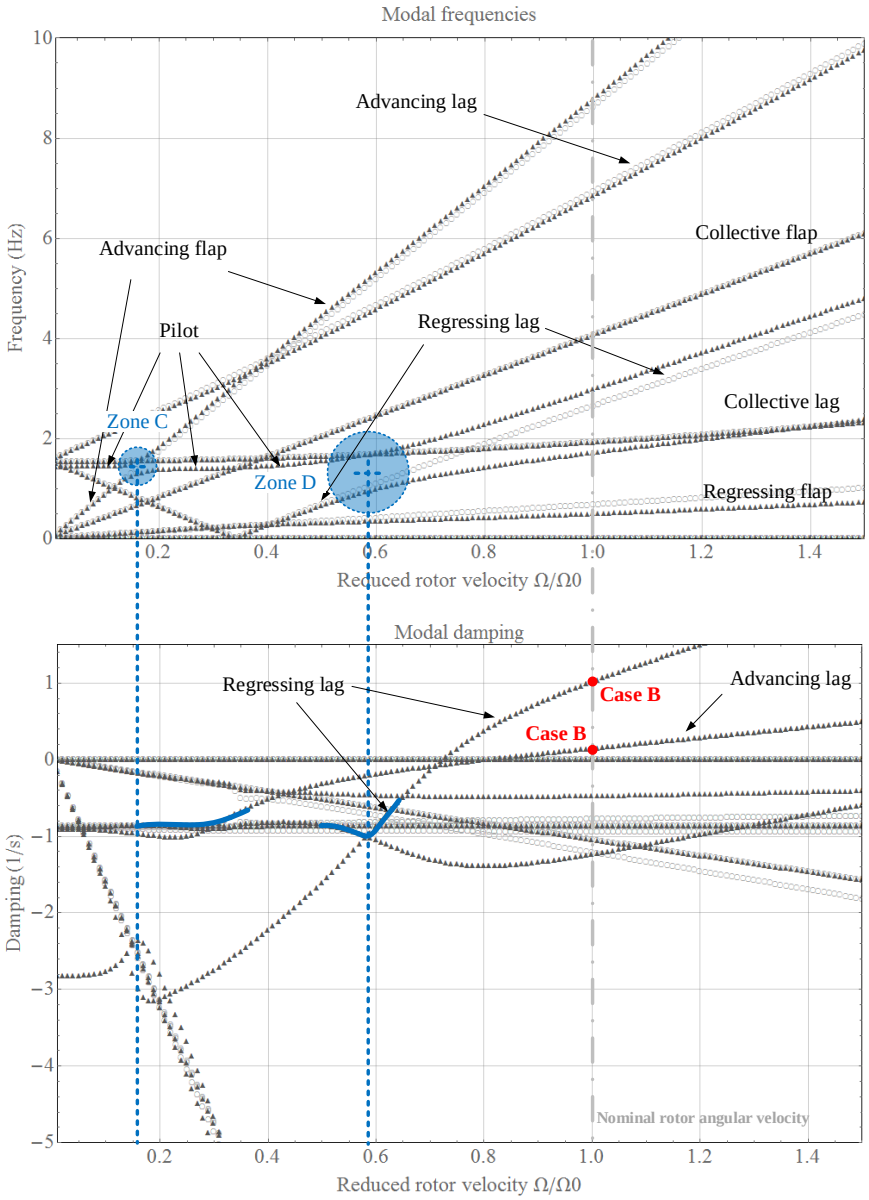

Figure 4-6. Campbell diagram, (○) no pilot biodynamics included, (▲) Case B - pilot (ω=1.5Hz, k=0.08, ζ=0.3)

The Campbell diagram of Figure 4-6 exhibits two modes that are clearly unstable when the rotor reduced velocity is higher than 1.2 which correspond to both regressing

and advancing lag modes. According to this figure, the advancing lag mode starts loosing damping at a very low reduced rotor velocity, when the pilot biodynamics mode crosses the advancing flap mode at around a reduced rotor velocity of 0.15 (Zone C). At this point, it can be conjectured that the advancing lag mode is destabilized due to the flap-lag coupling through the Coriolis effects.
On the other side, the regressing lag mode starts loosing damping when its frequency equals the pilot biodynamics mode at around a reduced rotor velocity of 0.6 (Zone D). The mechanism behind this destabilization seems to be very close to the one of ground resonance and confirms the conjecture found in literature (Muscarello, et al., 2015) "*predictions suggest that the roll/lateral PAO phenomena are more likely to occur (…) with pilots that are characterized by a natural frequency of the biodynamic poles that is close to the lightly damped in-plane rotor mode*".

4.2.2. Nonlinear time simulations

So far, the model that has been analyzed is a linear model. In this section, time simulations are performed directly from the nonlinear mathematical model obtained from the bond graph presented on Figure 4-4. Once a causal bond graph such as the one on Figure 4-4 is constructed, the most general form of mathematical model that is behind is a set of differential algebraic equations DAEs (Borutzky, 2009), with **y**(t) the state variables vector and *f* a nonlinear vector-valued function of the corresponding dimension,

$$f(\dot{\mathbf{y}}, \mathbf{y}, t) = \mathbf{0} \tag{65}$$

This equation can be obtained in a systematic manner (Borutzky, 2009) by hand or when the system becomes too large with a bond graph preprocessor such as 20-sim® software. For a reasonable DAE index[19] value, equation (65) can be numerically integrated with an adapted numerical method such as Backward Differences or Implicit Runge-Kutta, (Cuadrado, Cardenal, & Bayo, 1997), (Pennestri & Vita, 2004), (Mantegazza & Masarati, 2012). In our case a Backward Differentiation Formula (BDF) method is used, available in 20-sim®. To give an order of magnitude, there are 1600 equations to be processed by the software for the bond graph on Figure 4-4.

In order to compute the free response of the bioaeroelastic system, a perturbation is applied on the cyclic stick of the helicopter as it can be seen on the green curve of Figure 4-7. The free response on the lateral and roll axes of the helicopter in terms of velocities and rotor states using Coleman variables (beta 1s and delta 1c) are plotted. For the two pilot neuromuscular system setups, cases A and B described on Figure 4-5, the time simulation results show that the airframe oscillates respectively mainly at 7Hz and 3Hz, corresponding with the advancing and regressing lag mode frequencies, see Figure 4-8.

[19] Index: number of times the constraint equation has to be differentiated to obtain a system of ODEs (Van Dijk & Breedveld, Simulation of system models containing zero-order causal paths—I. Classification of zero-order causal paths, 1991)

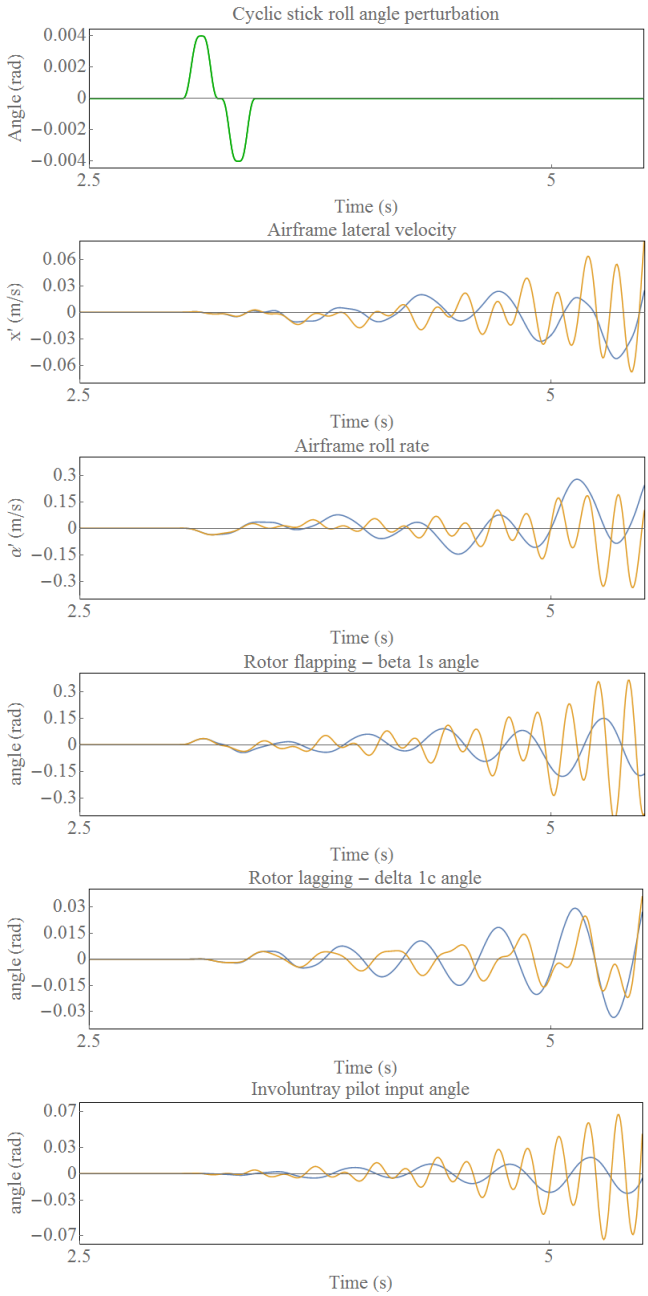

Figure 4-7. Time simulation results of the free response of the bioaeroelastic system for two pilot cases A (orange) and B (blue)

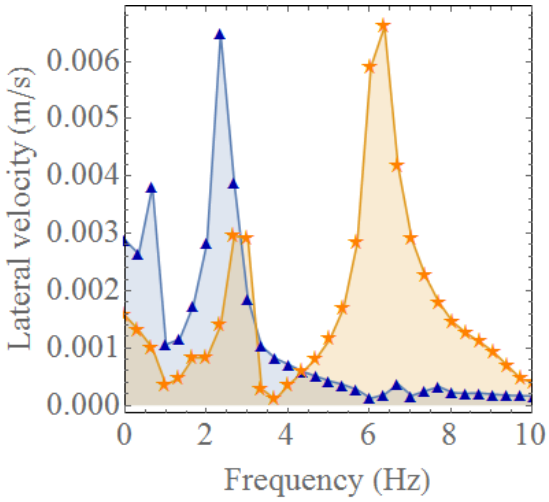

Figure 4-8. Discrete Fourier Transforms of the airframe lateral velocity free responses - case A (orange) and B (blue)

Screen captures of the 3D visualization of the simulation results have been synchronized and are presented on Appendix 5. The reader can have an appreciation of the evolution of the phenomena in a Cartesian space.

4.3. Conclusion

The first objective of this chapter, is to illustrate the *modular* or *structural approach* that is provided by the bond graph method. This was done by showing how the frontiers between subsystems of a physical system are materialized at the graphical level of a BG. This is illustrated by coupling both vehicle and pilot models developed in the previous chapters.

The human-machine model obtained represents a bioaeroelastic behavior that is then investigated more into detail; more precisely lateral-roll aeroelastic RPCs are investigated. A linear stability analysis confirms what has been conjectured in literature concerning the role played by the regressing lag mode in the phenomenon. Furthermore, the results show that for higher neuromuscular pilot stiffness's, the higher frequencies of the advancing lag mode could also excite the airframe. This last result needs to be confirmed by some experiments. It should be kept in mind that some of the assumptions taken here are reductive; especially concerning the quasi-steady aerodynamics, the flight configuration and the dry friction[20]-less cyclic lever. However, even if the predicted instability domains will move with more detailed physics, the kind of models used here will help understand the physical mechanisms behind the phenomena and could help explaining damping drops observed in real flights. Flight test results seem to be necessary here to go further.

[20] Viscous friction is taken into account

The theory of stability of equilibrium […] attracts and captivates people working in structural engineering nearly in the way ancient mythological sirens used to do with mariners, and hardly ever allows them to escape that enchanting problems.

(Perelmuter & Slivker, 2013)

Chapter 5
Towards design stability margins estimations using Chetaev functions

Résumé long du chapitre 5

Dans le chapitre précédent, un modèle de l'ensemble pilote-véhicule a été développé à l'aide d'une approche par bond graphs afin d'étudier les RPCs aéroélastiques sur les axes latéral et de roulis. Cet outil a permis d'avoir une approche système de la modélisation qui est cruciale pour l'étude de systèmes dynamiques complexes. Avoir la possibilité de modéliser et de simuler le comportement d'un système physique est important lorsqu'il s'agit de valider un modèle vis-à-vis d'essais expérimentaux. Néanmoins, plus que le modèle par lui-même, c'est son analyse qui permettra d'améliorer la conception des hélicoptères. Presque par nature, un comportement aéroélastique émerge des aéronefs à voilure tournante, et celui-ci doit être pris en compte par les concepteurs qui doivent définir un domaine de vol stable dans lequel est incluse, avec des marges, l'enveloppe de vol de l'aéronef. Le développement de méthodes de calcul efficaces afin de s'assurer de la stabilité des aéronefs permettra d'explorer plus en profondeur l'espace de conception. Ceci permettra également de réduire le nombre d'essais en vol et les solutions curatives développées, par définition, tardivement dans le processus de conception. Ce chapitre pose les premières pierres de ce qui pourrait devenir une méthode d'analyse de la stabilité directement à partir d'un modèle non linéaire à l'aide de fonctions de Chetaev, à un coût de calcul potentiellement intéressant.

Formellement, la stabilité est un concept qui caractérise les positions d'équilibres d'un système dynamique. La Figure 5-1 montre des exemples d'équilibres d'une particule de masse m en présence uniquement de la gravité. Afin de qualifier la nature de l'équilibre, stable ou non, il faut imaginer le mouvement de la particule si on lui appliquait une force aussi faible que l'on peut le souhaiter. Si après perturbation, la particule revient à sa position d'équilibre, alors on peut dire que cet équilibre est stable. Mathématiquement, la définition proposée par (Perelmuter & Slivker, 2013) *est rappelée, voir développement sous la Figure 5-1.*

Par abus de langage et afin d'alléger l'écriture, on parlera souvent de « la stabilité du système » pour parler de la stabilité d'un équilibre donnée du système en question.

La théorie la plus générale pour étudier la stabilité de l'équilibre d'un système dynamique, décrit par des équations différentielles ordinaires, est la théorie d'Aleksandr Mikhailovich Lyapunov datant de la fin du XIX^{ème} siècle. Les méthodes de Lyapunov peuvent être appliquées à des systèmes d'équations non linéaires. Ces méthodes sont souvent classées dans deux catégories : les méthodes dites directe et indirecte. La méthode indirecte est appelée ainsi car elle demande une première étape de linéarisation autour d'un équilibre. Ensuite, le calcul des parties réelles des valeurs propres donnent l'information de la stabilité ou non de l'équilibre : si

toutes ces parties réelles sont strictement négatives alors l'équilibre est asymptotiquement stable. Par contre, si au moins une de ces parties réelles est strictement positive alors l'équilibre est instable. Le dernier cas possible est celui où toutes les parties réelles sont strictement négatives, sauf une qui est nulle. Dans ce cas, il n'est pas possible de conclure sur la nature de l'équilibre, des termes de plus haut degré sont nécessaires pour conclure.

Dans le cas où le système est non-autonome, c'est-à-dire que le temps apparaît explicitement dans les équations, la méthode précédente n'est pas directement applicable puisque le temps n'est a priori pas une variable d'état en mécanique classique.

Le cas particulier des équations linéaires à coefficients périodiques, voir équation (66), peut néanmoins être traité à l'aide de la théorie de Floquet (Bielawa, 2006). *Le traitement de ce type d'équations est intéressant dans le monde de l'hélicoptère, puisque même le modèle le plus simple de système rotor-fuselage mène à des équations différentielles à coefficients périodiques. De manière très synthétique, il peut être retenu que la méthode de Floquet demande de calculer la norme des valeurs propres d'une matrice intermédiaire, appelée matrice de monodromie. Les vecteurs colonnes de celle-ci sont des solutions indépendantes obtenues numériquement par un nombre d'intégration égal à la dimension du vecteur d'état et sur un temps égal à la période des équations. Si la plus grande norme des valeurs propres est strictement inférieure à 1 alors l'équilibre est asymptotiquement stable. Si la plus grande norme des valeurs propres est strictement supérieure à 1 alors l'équilibre est instable, voir équation (67).*

Afin de traiter le cas le plus général des systèmes non-autonomes, une méthode existe : il s'agit du calcul des exposants de Lyapunov (LCEs). (Bielawa, 2006) *pensait, que les outils de la théorie du chaos pourraient être utiles dans l'analyse de la dynamique des hélicoptères. Les exposants de Lyapunov sont des grandeurs utilisées dans littérature afin de mesurer la sensibilité aux conditions initiales, sensibilité qui caractérise les systèmes chaotiques. Très récemment* (Tamer & Masarati, 2015) *propose d'appliquer cette méthode à des modèles utiles dans le monde de l'hélicoptère. L'exemple de l'équation d'une pale qui bat et qui en même temps possède une vitesse d'avancement est reproduit, voir l'équation (68). Celle-ci est linéaire à coefficients périodiques et donc peut-être étudiée à l'aide de la théorie de Floquet, comme à l'aide des exposants caractéristiques de Lyapunov, voir Figure 5-2. Il faut noter que cette méthode peut aussi bien s'appliquer à des trajectoires obtenues par simulation numérique qu'à des résultats expérimentaux, voir* (Wolf, Swift, Swinney, & Vastano, 1985).

Cette méthode, bien que générale, ne possède pas de lien explicite avec l'énergie. D'autres méthodes de la littérature applicables aux systèmes mécaniques ont, elles, un lien bien plus fort avec l'énergie, voir les théorèmes 1 à 3 sous la Figure 5-2. Le théorème le plus connu parmi ceux-ci est celui de Lagrange-Dirichlet : ***si l'énergie potentielle d'un système conservatif est strictement minimale au voisinage d'un équilibre alors cet équilibre est stable****. Un rotor dont la vitesse angulaire est maintenue constante par une source extérieure est par définition non conservatif. Ce théorème trouvera donc peu d'applications à l'étude de la dynamique de l'hélicoptère. Mais comme dans toute histoire moderne liée à la stabilité, Lyapunov doit apparaître quelque part. Une généralisation du théorème de Lagrange-Dirichlet a été proposée dans ce que l'on appelle la méthode directe*

de Lyapunov (Marquez, 2003). *Cette méthode consiste à trouver une fonction appelée fonction candidate de Lyapunov qui vérifierait les 3 propriétés du théorème 5. Si l'on est capable de trouver une fonction qui vérifie ces propriétés alors ce théorème donne des conditions suffisantes de stabilité de l'équilibre autour duquel la fonction vérifie les propriétés. En conséquence, si l'on n'est pas capable de trouver une fonction de Lyapunov, on ne peut tout simplement pas conclure sur la stabilité ou non d'un équilibre. En 1961, Nikolai Gur'evich Cheatev* (Marquez, 2003) *proposa des conditions suffisantes d'instabilité que doivent vérifier une fonction candidate, voir théorème 6.*

Afin d'illustrer l'intérêt que peut représenter l'application d'une telle approche à des problèmes plus complexes, il est proposé de commencer par traiter l'exemple classique du pendule simple. Ce système possède deux équilibres, l'un est stable, l'autre instable. Mais comment aurait-on pu le savoir sans faire aucune expérience ? Eh bien ceci aurait pu être conclu en prenant la fonction énergie totale ou Hamiltonien comme fonction candidate, voir équation (69) et Figure 5-3. Plaçons-nous, mentalement, au voisinage de l'équilibre inférieur du pendule simple, $\alpha=0$ et à l'équilibre $\dot{\alpha}=0$, donc $H(0)=0$. En choisissant le domaine D, tel que $D=\{\{-\pi/2; \pi/2\},R\}$, dans $D - \{0\}$, $1-\cos\alpha>0$. De plus, $\dot{\alpha}^2 \geq 0$. Donc, dans $D - \{0\}$, $H(x)>0$. Finalement, $\dot{H}(x)$ est la puissance dissipée par le système. Dans ce cas, elle est nulle donc $\dot{H}(x) \leq 0$ dans $D - \{0\}$. Le théorème 5 permet donc de conclure que H est une fonction de Lyapunov sur D et que l'équilibre inférieur du pendule simple est une position d'équilibre stable.

Plaçons-nous maintenant au voisinage de la position d'équilibre supérieure, $\alpha=\pi$. Par définition, à l'équilibre, $\dot{\alpha}=0$, donc $H(\pi)-2mgl=0$. En posant comme fonction V candidate, non plus exactement H, mais H décalé d'une valeur statique, $V=H-2mgl$, on a bien $V=0$ à l'équilibre. Afin de pouvoir appliquer le théorème de Chetaev théorème 6, l'existence de deux conditions doit être prouvée. C'est ici que nous postulons que cette méthode à un intérêt en termes de puissance de calcul. En effet, les deux conditions d'existence qui doivent être vérifiée n'ont pas besoin d'être vérifiée tout autour de l'équilibre, comme pour une fonction de Lyapunov, mais sur n'importe quelle portion, de l'espace des phases, aussi petite soit-elle. Afin de montrer l'existence d'une solution x_0 et d'un domaine U comme l'exige le théorème, il est proposé de faire cela visuellement, voir Figure 5-4, bien que cela puisse aussi être démontré analytiquement. Afin de construire la Figure 5-4 (a), il faut imaginer la projection des lignes de niveaux (iso-énergie) de la Figure 5-3 (b). La partie (b) de la Figure 5-4, permet de distinguer un domaine gris, où V est strictement positive ; et un domaine blanc, où V est strictement négative. On ajoute alors une hypothèse : du frottement visqueux autour du pivot du pendule. La dérivée totale par rapport au temps de V est la puissance dissipée, $\dot{V}=\dot{H}=P_{dissipated} < 0$ dans $R^2-\{R, \{0\}\}$ (ce domaine correspond à l'espace des phases auquel on retire la droite bleue en pointillés). Le signe de $\dot{V}$ est alors strictement négatif sur le domaine défini précédemment. Dès lors, en choisissant un des domaines U_i, de couleur orange, V et $\dot{V}$ sont de même signe et non nulles. De plus les domaines U_i ont un sommet qui part de l'équilibre, il existe donc un point x_0 dans le domaine U_i aussi proche que l'on peut le souhaiter de l'équilibre. Par conséquent, V est une fonction de Chetaev, ce qui nous permet de conclure que la position d'équilibre supérieure est instable.

Une synthèse *des points évoqués jusqu'à maintenant s'impose. Les méthodes actuelles utilisées dans la communauté consistent à analyser la stabilité de systèmes uniquement à partir de modèles linéaires. Cette approche, limite de fait la prise en compte de non linéarités. Cela supprime aussi la possibilité de conclure sur la stabilité de l'équilibre d'un système, directement à partir d'un modèle non linéaire. Des méthodes permettant de s'affranchir de ces limites existent, comme le calcul des exposants de Lyapunov (LCEs). Mais cette méthode, bien que très générale n'a aucun lien explicite avec l'énergie, contrairement à la méthode directe de Lyapunov pour laquelle les fonctions de Lyapunov et de Chetaev sont souvent associés à des fonctions basées sur l'énergie. De plus, cette méthode n'a pas encore été appliquée à des problèmes associés aux hélicoptères, et permet, comme les LCEs, de conclure sur la stabilité d'un équilibre directement à partir d'un modèle non linéaire. Mais cette méthode possède deux désavantages non négligeables. Le premier est que cette méthode ne donne que des conditions suffisantes de stabilité ou d'instabilité. Donc si l'on n'est pas capable de trouver une fonction de Lyapunov ou Chetaev, rien ne peut être conclu en termes de stabilité. Le deuxième désavantage est qu'il n'existe pas de méthode systématique pour trouver une fonction de Lyapunov ou Chetaev. Une personne censée se serait probablement arrêtée là et aurait passé son chemin. Mais l'application du théorème de Chetaev à l'exemple du pendule simple montre qu'une fonction candidate de Chetaev ne doit vérifier des propriétés que sur une portion de l'espace des phases autour d'un équilibre. Si l'on devait reconstruire la surface (b) de la* Figure 5-3 *numériquement, la reconstruction d'une portion de cette surface aurait déjà suffi à conclure sur l'instabilité de l'équilibre, voir (b) de la* Figure 5-6.

La synthèse du paragraphe précédent nous permet donc de formuler plus précisément notre ***proposition de méthode****. Dans le cas du pendule simple, l'utilisation d'une simulation temporelle afin de reconstruire l'allure de l'énergie totale au voisinage d'un équilibre n'est pas la méthode la plus efficace pour arriver à conclure sur la stabilité. Mais déterminer le signe d'une fonction comme l'énergie totale dans le cas d'un système non linéaire de grande dimension peut se révéler impossible de manière analytique. Dès lors, une simulation temporelle peut s'avérer indispensable pour apporter une réponse aux questions de stabilité.*

1. *La première proposition consiste à vérifier le signe d'une éventuelle fonction candidate à l'aide d'une simulation temporelle.*

Une fois qu'une fonction de Chetaev est trouvée, le temps de calcul peut être réduit au temps minimal d'apparition du domaine U au sens du théorème 6. Etant donné que les systèmes physiques que nous étudions présentent des instabilités paramétriques (voir chapitre précédent),

2. *La deuxième proposition consiste à réaliser des balayages paramétriques du modèle du système physique, pour des paramètres qui sont en général des paramètres de conception de l'hélicoptère, et de vérifier à chaque fois le signe de la fonction candidate et de sa dérivée à l'aide d'une simulation numérique.*

a. *Si le domaine U peut encore être trouvé, la fonction candidate est une fonction de Chetaev.*
b. *Sinon, rien ne peut être conclu quant à l'équilibre du système dynamique.*

Le problème de trouver un moyen systématique d'obtenir l'expression d'une fonction de Chetaev n'est pas résolu. Néanmoins, des fonctions candidates peuvent être proposées selon le problème à traiter. Par exemple, comme illustré dans la suite du chapitre, une fonction construite à partir de l'énergie totale, ou Hamiltonien, semble une bonne fonction candidate dans le cas du phénomène de « résonance sol ».
L'approche proposée ici peut bien évidemment être appliquée à d'autres représentations du système que le bond graphs. Néanmoins, l'idée proposée ici est née en construisant des bond graphs, avec lesquels finalement, des flux d'énergies sont tracés. De plus, cette idée a été inspirée par les travaux de (Junco, 1993) *qui propose d'extraire des fonctions de Lyapunov directement à partir des bond graphs. Il est donc revendiqué ici que, même si l'approche peut être appliquée à un autre type de représentation du système, les bond graphs ont constitué une étape intellectuelle nécessaire à l'émergence de cette idée.*
Le reste du chapitre est consacré à l'illustration de la proposition en application au cas de la résonance sol, un phénomène dynamique important dans le monde de l'hélicoptère. Le point de départ de cette dernière partie est l'approche classique que l'on utilise, depuis 40 ans maintenant, afin de prédire le phénomène. Le modèle possède 3 degrés de libertés après application du changement de variable de Coleman, voir Figure 5-7 *et les 3 équations du mouvement (77). La résonance sol, est une instabilité paramétrique, bien qu'elle soit appelé « résonance », voir le diagramme de Campbell en Appendix 6 (la perte d'amortissement du mode régressif de traînée autour de la vitesse nominale du rotor ; c'est-à-dire une vitesse réduite égale à 1 sur le diagramme). Pour le jeu de données présenté en* Table 5*, le mode régressif de traînée est instable, voir* Figure 5-8.
La méthode développée ici, propose de retrouver ces zones d'instabilités paramétriques à partir de la représentation bond graph du système et de résultats de simulations dans le domaine temporel au voisinage de l'équilibre de ce modèle non linéaire. Dans un premier temps, il est justifié pourquoi le Hamiltonien, somme de l'énergie cinétique et potentielle du système en question, est une fonction candidate intéressante dans le cas de la résonance sol. En effet, dans (Oberinger & Hajek, 2013)*, il est affirmé que « la condition de la présence d'une instabilité dynamique dans un système mécanique, c'est-à-dire l'apparition d'oscillations divergentes, est une augmentation de l'énergie interne du système ». L'énergie interne est dans ce cas l'énergie totale ou Hamiltonien. Afin de mieux comprendre cette affirmation, deux résultats de simulation sont présentés* Figure 5-9. *En bleu, ce sont les résultats lorsque le système est paramétré selon les valeurs nominales ; on constate, comme on peut s'y attendre, que la réponse libre du système est divergente après une petite perturbation appliquée sur la masse représentant le fuselage. En effet pour ces paramètres, l'équilibre est prédit instable par le modèle linéaire. En orange, voir* Figure 5-9*, l'amortissement des amortisseurs de torsions, voir* Figure 5-7 *est multiplié par 3 afin d'éviter le phénomène de résonance sol : après perturbation le système revient à sa position d'équilibre. La dernière figure*

de Figure 5-9*, montre l'évolution du Hamiltonien. Dans le cas stable, le Hamiltonien est décroissant alors qu'il est croissant dans le cas instable. Pour* (Oberinger & Hajek, 2013) *cette croissance est une condition suffisante d'instabilité. Ceci est très intéressant puisque si le Hamiltonien était strictement croissant, ce serait automatiquement une fonction de Chetaev. Mais le Hamiltonien n'est pas strictement croissant, voir* Figure 5-10*, ce n'est donc pas une fonction de Chetaev et on ne peut pas l'utiliser en l'état pour conclure sur l'instabilité de l'équilibre. Afin de rendre cette fonction monotone, il est proposé de calculer sa régression linéaire sur 4 périodes de rotor, après avoir attendu 6 périodes de rotor de régime transitoire, voir* Figure 5-10 *et équation (80). De cette manière, et sur la portion longue de 4 périodes de rotor, ce qui semblerait être une fonction de Chetaev est obtenue. Il est proposé, comme pour l'exemple du pendule simple en (b)* Figure 5-6*, d'observer H et sa dérivée totale par rapport au temps, dans le plan* (*V*, *V*)*, voir* Figure 5-11*. Dans le cas 2, en orange, il doit être noté, que la fonction ainsi construite n'est ni Chetaev, ni Lyapunov et que rien ne peut être conclu quant à la stabilité de cet équilibre. Pour être rigoureux il faut noter que la construction de la fonction de Chetaev proposée ici est incomplète puisqu'elle devrait être continue jusqu'à l'équilibre. Ceci reste donc en suspens et devra être abordé dans le futur. Néanmoins afin de vérifier le potentiel de l'approche proposée, la méthode a été appliquée sur un balayage plus important de paramètres, voir* Figure 5-12*. Afin d'estimer le domaine d'instabilité, il faut ne conserver que les points pour lesquels β est positif, ce qui permet d'obtenir le domaine d'instabilité en blanc de la* Figure 5-13*. Sur la même figure, ce domaine est comparé au domaine que l'on aurait obtenu à l'aide du modèle linéaire et d'un calcul de valeurs propres. On peut constater que les résultats sont très proches. Les points qui ne coïncident pas sont uniquement à la frontière du domaine. Sur cette frontière la méthode linéaire n'est plus valable. Mais la méthode proposée ici utilise une méthode numérique (BDF) qui elle-même possède des limites de stabilité et de précision dont il faudrait, dans le futur, quantifier l'impact.*

Finalement, les équations (83) à (86) donnent l'expression analytique du Hamiltonien à partir des variables d'état qui sont utilisées en bond graph. Le modèle bond graph du système rotor-fuselage est complétement développé Figure 5-14*. On peut notamment observer que des capteurs d'énergie ont été placés au pied des éléments de stockage I et C et des capteurs de puissance au pied des éléments de dissipation R et de la source d'énergie MSf, qui maintient le rotor à vitesse constante. La somme des valeurs indiquées par les capteurs d'énergie donne la valeur du Hamiltonien, et la somme des valeurs indiquées par les capteurs de puissance donne la dérivée totale par rapport au temps du Hamiltonien, qui n'est autre que la différence entre la puissance fournie par le moteur et la puissance dissipée par les amortisseurs de traînée et du train d'atterrissage. De ce point de vue, les résultats numériques montrent que, lorsque l'instabilité apparaît, le système se réorganise de telles manières qu'il tente de tirer de plus en plus d'énergie de la source, c'est-à-dire du moteur, afin de stocker celle-ci sous forme d'énergies cinétique et potentielle. Sur un système réel, les pièces mécaniques sont capables de stocker une quantité finie d'énergie après quoi leur rupture est inévitable, d'où l'intérêt des concepteurs d'éviter ce type de phénomènes.*

In the previous chapter, in order to investigate lateral-roll aeroelastic RPCs, a pilot-vehicle model has been proposed using bond graphs. This approach has allowed to have a system approach of modeling which is crucial when investigating complex dynamic systems. Having the possibility to model and simulate a model is important especially to validate models against experiments. However, more important than the model itself it is its analysis that will help designers improving rotorcraft designs. More than fifty years ago, (Chetaev, 1960)[21] already stated "*In modern engineering there arise new and increasingly more complex problems concerning the stability of motion. Looking at the past and anticipating the future, one can see that in order to keep up with technological progress it will be necessary to develop more and more precise methods for the investigation of these stability problems*". By nature rotorcraft exhibit an aeroelastic behavior for which designers need to define its stability domain that contains the rotorcraft flight envelop with some margins. The development of computationally efficient methods to investigate the stability of rotorcrafts will allow a deeper exploration of the design space in order to reduce flight tests costs and curative solutions costs that are by definition developed too late in the design process.

5.1. Definition

Formally, stability is a concept that characterizes the equilibrium positions of a system[22]. Imagine what would be the motion of the particles of mass *m* if they were slightly deviated from their equilibrium,

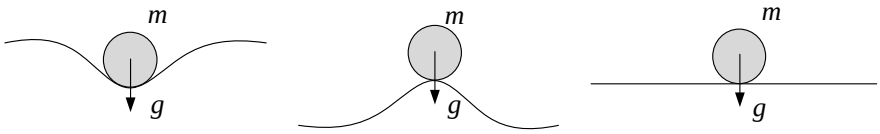

(a) stable (b) unstable, case 1 (c) unstable, case 2

Figure 5-1. Simple examples of stable and unstable equilibriums

A definition of the equilibrium stability concept "*is connected with motions which a system is capable of making after it is moved from its equilibrium by having its points receive very small initial deviations from the equilibrium position and very small initial velocities. If, after this violation of equilibrium, the system will deviate very little in its subsequent motion from the equilibrium position of interest, then this position of equilibrium is said to be stable*", (Perelmuter & Slivker, 2013).

---

[21] Nikolai Gur'evich Chetaev was a professor of Mechanics between 1930 and 1940, and gave among others, lectures on aircraft stability (Chetaev, 1960) at the University of Kazan; major city of the Russian helicopter industry.

[22] For simplicity we will very often speak about *the system's stability*, but one should keep in mind we refer to *the stability of a specific equilibrium of the system*.

Mathematically speaking, following (Perelmuter & Slivker, 2013): let $\mathbf{q}_0$ be the vector of a system's generalized coordinates for a given equilibrium. This state is said to be stable if for any small number ε there exists a respectively small number δ such that for any perturbations of the generalized coordinates, $\delta\mathbf{q}_0$, and initial velocities $\delta\dot{\mathbf{q}}_0$ which satisfy the conditions,

$$\left\|\delta\mathbf{q}_0\right\| < \delta, \quad \left\|\delta\dot{\mathbf{q}}_0\right\| < \delta$$

The following inequalities will hold at any time t,

$$\left\|\mathbf{q}(t) - \mathbf{q}_0\right\| < \varepsilon, \quad \left\|\dot{\mathbf{q}}(t)\right\| < \varepsilon$$

In other words, for an equilibrium to be stable, the generalized coordinates should not go beyond the ε neighborhood of the initial equilibrium state in the course of the system's subsequent motion. The same neighborhood should contain also the generalized velocities of the system which were zero in the initial state of equilibrium.

An equilibrium is said to be unstable if it is not stable.

It is critical to be able to determine as soon as possible in the design process whether a rotorcraft design is prone to any dynamic instability. Ideally, this should be assessed based on a model that represents the rotorcraft with the highest physical fidelity in terms of subsystems behaviors (structural mechanics, aerodynamics, hydraulics, pilot biodynamics, etc.) and independently from the linearity or nonlinearity of their associated mathematical models (due to geometry, large displacements or material behavior) at the lowest computational cost. In the rotorcraft community, stability studies usually limit to the investigation of linear models.

5.2. State-of-the art

The most general theory to investigate the stability of equilibriums of ordinary differential equations has been introduced by Aleksandr Mikhailovich Lyapunov at the end of the 19th century. Lyapunov's methods have the power of being applicable to nonlinear systems. His methods are usually classified in the direct and the indirect categories.

5.2.1. Lyapunov's indirect method

The indirect method allows to conclude on the local stability of an equilibrium of a nonlinear system $\dot{x}=f(x)$ by considering its linearization $\dot{x}=A.x$ around the equilibrium (Perelmuter & Slivker, 2013), A being the classic state-space matrix.

i. *If the real parts in all roots of the characteristic equation of the linearized system are negative, then the equilibrium of the nonlinear system is asymptotically stable*

ii. *If the real part in at least one root of the characteristic equation of the linearized system is positive, then the equilibrium of the nonlinear system is unstable*

However, one should keep in mind, that in the case the roots of the characteristic equation of the linearized system contain some purely imaginary ones, while all the others have negative real parts, the first approximation equations are not enough to decide whether the equilibrium is stable or not. In this case, higher order terms are necessary to conclude.

5.2.2. Periodic systems

Historically (Peters, Lieb, & Ahaus, 2011), back at the end of the 19th century, scientists investigated the stability of natural satellites' orbits around a planet under periodic variation in gravitational force. The problem can be casted in its simplest form in the following periodic differential equation, known as Mathieu equation,

$$\ddot{x}(t)+\left[\omega^2+\varepsilon\sin(t)\right]x=0 \tag{66}$$

It has a period of 2π and for $\varepsilon=0$ becomes aperiodic or constant. This kind of time periodic equations arise in rotating systems and especially in helicopter systems. The behavior of time periodic equations is particular in the sense it can lead to *parametric resonance* or *parametric instabilities*; this will be illustrated later with ground resonance.

To study the stability of periodic systems, many approaches exist (Peters, Lieb, & Ahaus, 2011). In the case of a rotor-airframe system, if the rotor is not isotropic and the equilibrium of the aircraft is far from hover flight or cannot be considered at low advancing speeds, the rotorcraft mathematical model takes after linearization the shape of a state-space system $\dot{x}=A(t).x$, with a time-periodic state space matrix, with $A(t+T)=A(t)$ where $T=2\pi/\Omega$ and Ω is the rotor angular velocity (Bielawa, 2006). In the rotorcraft and wind turbines community, the most popular method to investigate the stability of such systems was proposed by Gaston Floquet in 1883.

Floquet theory and linear time periodic systems

In this section, the Floquet method is presented (Bielawa, 2006), (Coisnon, 2014).
Let be a linear time periodic (LTP) system $\dot{x}=A(t).x,$ with $A(t+T)=A(t)$ and $x \in R^n$.

When the system is linear-time invariant (LTI), time does not appear explicitly in *A* and a stability analysis can be resumed to an eigenvalue resolution. In the case of an LTP this is not possible anymore. Floquet solves the problem by introducing a matrix **B**, called monodromy matrix that can be constructed by concatenating *n* independent solutions of the system at time T. The monodromy matrix characterizes the system state over 1 period. The *n* independent solutions are *n* vectors that can be obtained numerically by integrating *n* times for *n* different initial conditions, over a time interval between *0* and *T* with the help of a numerical method. The determination of the stability of an equilibrium can be assessed by computing the absolute value of the eigenvalues λ_i of matrix **B**,

$$\begin{cases} \max(|\lambda_i|) > 1 \Rightarrow \text{unstable} \\ \max(|\lambda_i|) < 1 \Rightarrow \text{asymptotically stable} \end{cases} \tag{67}$$

Computationally speaking one should note this method demands to compute *n* numerical solutions of the system over one period *T* of the system, and then run an eigenvalue analysis of the monodromy matrix. When the number of degrees of freedom of the system rises, the computational cost might become excessive.

5.2.3. Lyapunov Characteristic Exponents

As imagined by (Bielawa, 2006) chaos theory tools are progressively emerging in the field of rotorcraft dynamics field: "*the engineering application of chaos theory are […] in their infancy*", "*For most applications the existence of chaotic motion in a system would be, like vibrations and aeroelastic instability, a response condition to be avoided and/or designed out of the system*". It is the case, very recently in (Tamer & Masarati, 2015), in which Lyapunov Characteristic Exponents (LCEs) are proposed and applied to the investigation of stability of helicopter problems such as ground resonance with the inclusion of nonlinearities. LCEs are also used in literature to measure the sensitivity of solutions of dynamical systems to small perturbations which characterize chaotic systems. This method can be applied directly to: dynamic systems which are non-autonomous[23], time simulation results or time series from experiments (Wolf, Swift, Swinney, & Vastano, 1985). Stability estimation using LCEs can be seen as a generalization of conventional stability analysis of linear time invariant (LTI) or linear time periodic systems (LTP).
This is illustrated in particular in (Tamer & Masarati, 2015), in which a rigid blade flapping motion stability is investigated for varying values of advancing ratio μ,

$$\ddot{\beta} + \frac{\gamma}{8}\left(1 + \frac{4}{3}\mu\sin(t)\right)\dot{\beta} + \left(\nu_\beta^2 + \frac{\gamma}{8}\left(\frac{4}{3}\mu\cos(t) + \mu^2\sin(2t)\right)\right)\beta = 0 \tag{68}$$

[23] A non-autonomous dynamic system is system where the time *t* appears explicitly in the equations of motion, $\dot{x}=f(x,t)$.

The Figure 5-2 shows that the Floquet theory method and the estimation of LCEs give the same quantitative results.

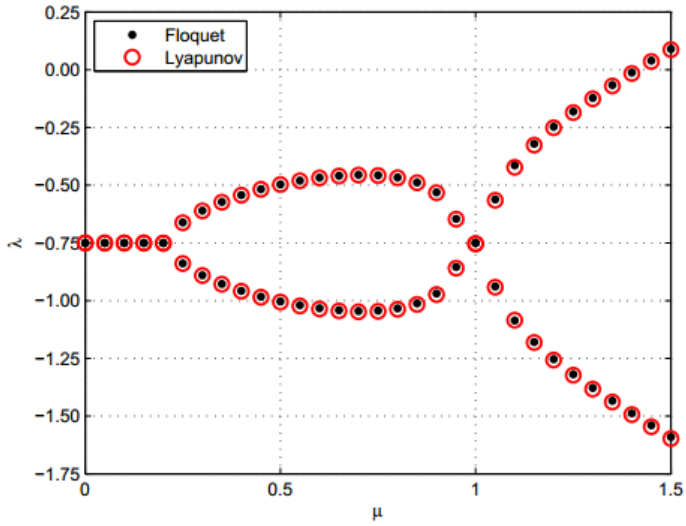

Figure 5-2. Lyapunov Characteristic Exponents and Floquet multipliers logarithm estimations for varying advancing ratios μ from (Tamer & Masarati, 2015)

5.2.4. Potential energy theorems

There exists in literature potential energy based theorems that give sufficient conditions of stability and instability (Perelmuter & Slivker, 2013). The most famous one is the Lagrange-Dirichlet[24] theorem that can be applied to conservative systems.

Theorem 1 - Lagrange-Dirichlet

If the potential energy of a system takes a strictly minimal value in the vicinity of an equilibrium state of interest, then this state of equilibrium of the conservative mechanical system is stable.

Remark
The potential energy has to be strictly minimal and not just minimal. An example of minimal potential energy that leads to an unstable equilibrium is the case 2 of Figure 5-1.

[24] The theorem was first proposed and demonstrated by Lagrange (1788) by neglecting higher order terms and later demonstrated for any order by Lejeune-Dirichlet (1846).

Theorem 2 - Lyapunov

The equilibrium is unstable if the absence of a potential energy minimum can be recognized by second-order terms in the expression of the potential energy, without the need to consider higher-order terms, (Perelmuter & Slivker, 2013).

Theorem 3 - Lyapunov

The equilibrium is unstable if the potential energy takes a maximum value, and the presence of this maximum can be found out from the lowest-order terms in the expansion of the potential energy into a power series, (Perelmuter & Slivker, 2013).

Theorem 4 –Chetaev's instability criterion generalization

If the potential energy of a non-conservative system does not have its minimum in a state of equilibrium, and this follows from considering lowest-order terms of the energy expansion, then this state of equilibrium is unstable, (Perelmuter & Slivker, 2013).

5.2.5. Lyapunov's direct method

Lyapunov's direct method consists in finding a candidate function that verifies three simple properties, see Theorem 5 (Marquez, 2003). If one is able to find such a function, then it is a sufficient condition for the stability of the equilibrium. Since this method gives only sufficient conditions of stability, as it is, not finding a Lyapunov function does not mean the equilibrium is unstable. In 1961, Chetaev proposed converse properties for candidate functions that give sufficient conditions of instability (Marquez, 2003).
A major barrier for the use in practical problems is there is no systematic method to find Lyapunov or Chetaev functions. Computationally speaking a major advantage of the method is there is no need to linearize the equations or compute eigenvalues and no time simulations need to be performed.

Theorem 5- Lyapunov functions

Let $x=0$ be an equilibrium point of the dynamic system described by $\dot{x}=f(x)$, and let be a function $V: D \rightarrow R$, where D is a region of R^n around 0 such that,

i. $V(0) = 0$
ii. $V(x) > 0 \text{ in } D - \{0\}$
iii. $\dot{V}(x) \leq 0 \text{ in } D - \{0\}$

Thus $x = 0$ is stable.
Furthermore if $\dot{V}(x) < 0 \text{ in } D - \{0\}$, then the equilibrium is asymptotically stable.

Theorem 6 – Chetaev functions

Let $x=0$ be an equilibrium point of the dynamic system described by $\dot{x}=f(x)$, and let be a function $V: D \rightarrow R$, where D is a region of R^n around 0 such that,

i. $V(0) = 0$

ii. $\exists\, x_0 \in R^n$, *arbitrarily close to* $x=0$ *such that* $V(x_0)>0$

iii. $\dot{V} > 0$ *for all* $x \in U$, *where* $U=\{x \in D: \|x\| \leq \varepsilon$, *and* $V(x) > 0\}$

Under these conditions, $x = 0$ is unstable.

Example of application, the simple pendulum equilibriums

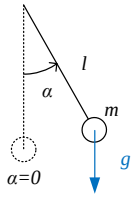

Let us imagine a simple pendulum of mass m parameterized by an angle α in the gravity field in the absence of friction. The total energy of the system, sum of kinetic and potential energy is its Hamiltonian H,

$$H = \frac{1}{2} m \left(l\dot{\alpha} \right)^2 + mgl\left(1 - \cos\alpha\right) \tag{69}$$

The nonlinear equation of motion of the system can be put in the form,

$$ml^2\ddot{\alpha} + mgl\sin\alpha = 0 \tag{70}$$

And in the form of an autonomous system,

$$\dot{\mathbf{x}} = f(\mathbf{x}) \text{ with, } \mathbf{x} = \begin{Bmatrix} x_1 \\ x_2 \end{Bmatrix} = \begin{Bmatrix} \alpha \\ \dot{\alpha} \end{Bmatrix} \text{ and } f \text{ such that } \begin{cases} \dot{x}_1 = \alpha \\ \dot{x}_2 = -\dfrac{g}{l}\sin x_1 \end{cases} \tag{71}$$

Lower equilibrium, $\alpha=0$

By definition at equilibrium $\dot{\alpha}=0$, therefore $H(0)=0$. By choosing $D=\{\{-\pi/2;\ \pi/2\},R\}$, in $D - \{0\}$, $1-\cos\alpha>0$. In addition $\dot{\alpha}^2 \geq 0$. Therefore, in $D - \{0\}$, $H(x)>0$. Finally, $\dot{H}(x)$ is the power dissipated by the system which in this case is null, therefore $\dot{H}(x) \leq 0$ *in* $D - \{0\}$. Theorem 5 allows to conclude that H is a Lyapunov function on D and that the lower equilibrium position of the system is stable.

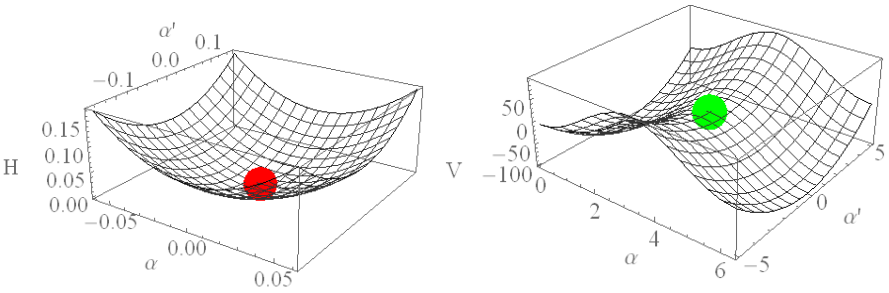

(a) Lower equilibrium, $\alpha=0$ (b) Upper equilibrium, $\alpha=\pi$

Figure 5-3. Hamiltonian in phase space around equilibriums of simple pendulum

Upper equilibrium, $\alpha=\pi$

By definition at equilibrium $\dot{\alpha}=0$, therefore $H(\pi)-2mgl=0$. By choosing $V=H-2mgl$, $V=0$ at equilibrium. In order to be able to apply Chetaev's theorem, the two existence conditions on x_0 and U need to be proved. This could be done analytically, however an explanation through figures is proposes, see Figure 5-4.

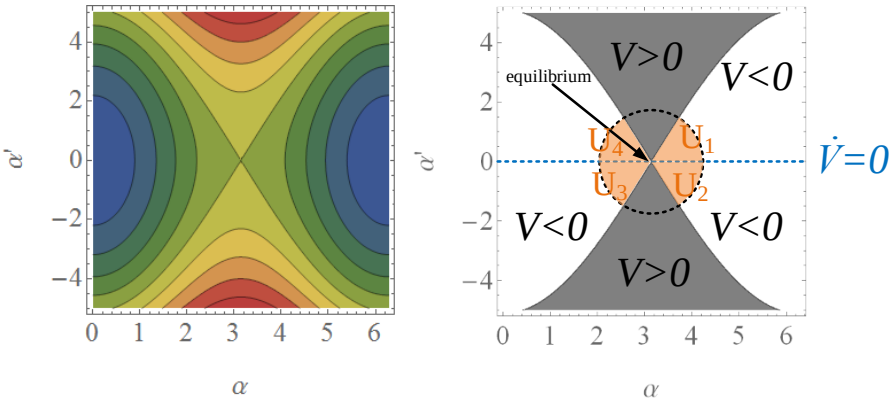

(a) Iso-V around $\alpha=\pi$ in phase space (b) Existence of at least one cone U in phase space

Figure 5-4. Geometric interpretation of Chetaev's theorem

To construct Figure 5-4 (a), one needs to imagine the isocurves of Figure 5-3 (b) projected on the phase space: in blue the energy is minimal and corresponds to the lower equilibrium points. On Figure 5-4 (b), colors distinguish two important domains: when Chetaev's candidate function is positive and negative definite. On the frontiers of Figure 5-4 (b), $V=0$. Since the orange domain takes its origin at the equilibrium, one can choose a point in the orange domain where $V<0$ as close as one can imagine close to the equilibrium: x_0 therefore exists.

Let us add some friction proportional to angular velocity to the system; the total time derivative of V is the power dissipated by friction: $\dot{V}=\dot{H}=P_{dissipated} < 0$ for $x \in R^2-\{R, \{0\}\}$[25]. The sign of $\dot{V}$ is therefore fixed. By choosing U equal to one of the orange domains U_i is sufficient to find a domain where V and $\dot{V}$ have the same sign and are not null. V is therefore a Chetaev function and the equilibrium is unstable.

5.3. Synthesis

5.3.1. Challenges

Actual methods in the rotorcraft community consist in investigating the stability of linear systems. This approach limits the nonlinearities that can be taken into account. It also demands to actually linearize a model suppressing the possibility to conclude on the stability without manipulating extensively its mathematical model when possible. To unlock these limits as imagined by (Bielawa, 2006) chaos theory tools are progressively emerging in rotorcraft dynamics field: "*the engineering application of chaos theory are […] in their infancy*", "*For most applications the existence of chaotic motion in a system would be, like vibrations and aeroelastic instability, a response condition to be avoided and/or designed out of the system*". It is the case, very recently in (Tamer & Masarati, 2015), in which Lyapunov Characteristic Exponents (LCEs) are proposed and applied to the investigation of stability of helicopter problems such as ground resonance with the inclusion of nonlinearities. This method can be applied directly to time simulation results or time series from experiments. However, this very general method is not explicitly related to the energy relations of a given physical system.
Another method that has not been applied yet to the investigation of rotorcraft dynamics and that we propose to apply is the use of Lyapunov's direct method for which usually the candidate Lyapunov and Chetaev functions are energy-based functions. This method allows to conclude on the stability of equilibriums from a nonlinear set of ordinary differential equations. However, it gives sufficient conditions of stability and can therefore only generate conservative results. Furthermore, there is no systematic method for finding Lyapunov or Chetaev functions, the method is therefore not systematic.

[25] This domain corresponds to the plane without the blue dashed line on Figure 5-4 where the power dissipated is null.

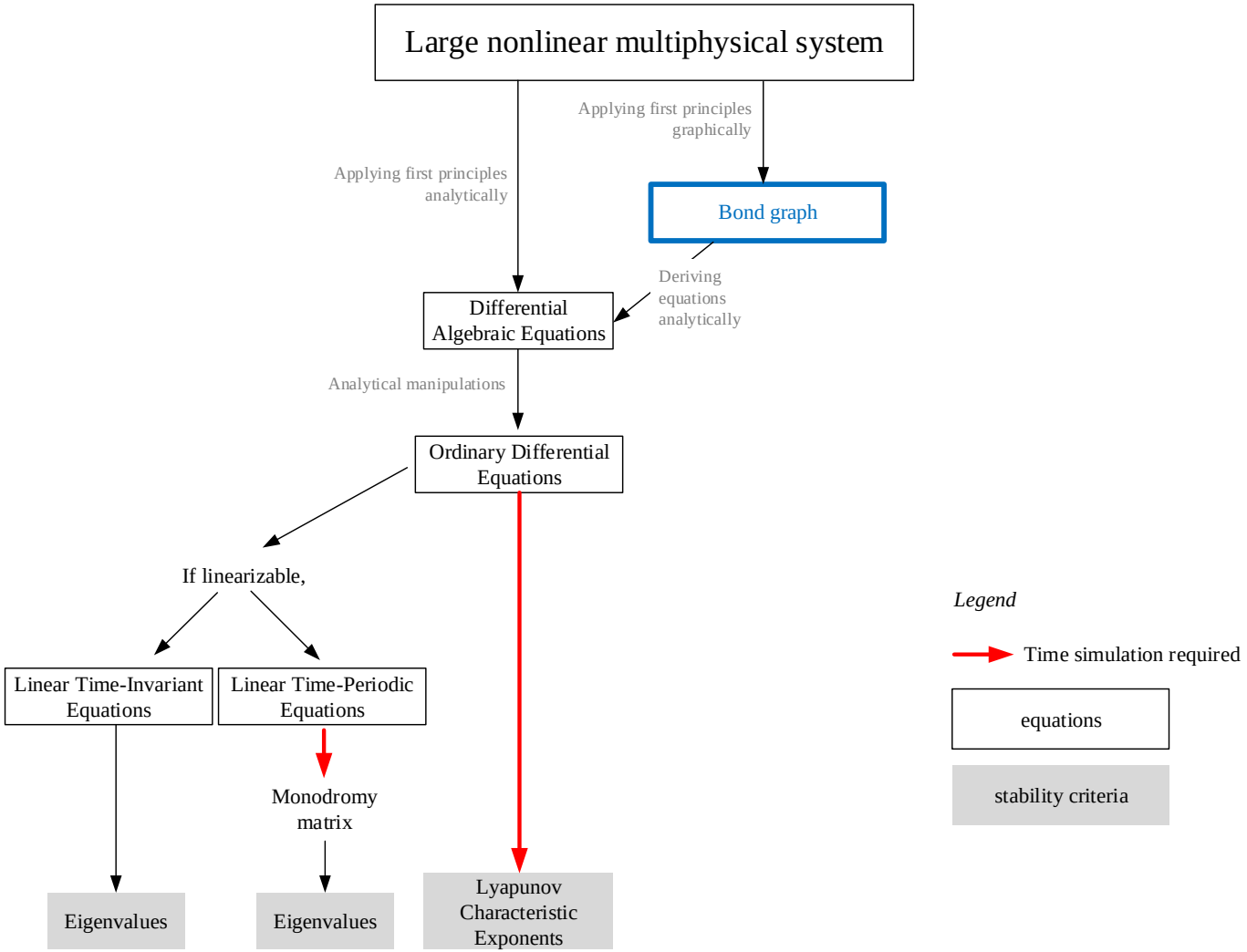

Figure 5-5. Synthesis of methods to evaluate the stability/instability of equilibriums

5.3.2. Proposal

An analysis of Chetaev's theorem proposed in the next lines reveals that proving the instability of an equilibrium using his theorem can be done with the help of a numerical simulation at a potentially interesting computational cost compared to other methods.

The justification of stability using Lyapunov candidate functions is more demanding in the sense the conditions need to be proved in every point of a domain *D-{0}* (which is the domain of stability). Whereas justifying the instability of an equilibrium demands to prove the existence of a small "cone" of vertex the equilibrium (Shnol, 2007) where V and $\dot{V}$ have the same sign and are not null.

The potential computational usefulness of this remark is proposed to be used and can be understood geometrically from Figure 5-3. Let us suppose the total time derivative of the candidate function is fixed. If we were to reconstruct the surfaces around equilibrium point by point to prove stability we would need to obtain points everywhere around the equilibrium to make sure its shape is a paraboloid of revolution (Figure 5-3 (a)) and not a hyperbolic paraboloid (Figure 5-3 (b)). While finding a domain U where V and $\dot{V}$ have the same sign and are not null is sufficient to prove instability.

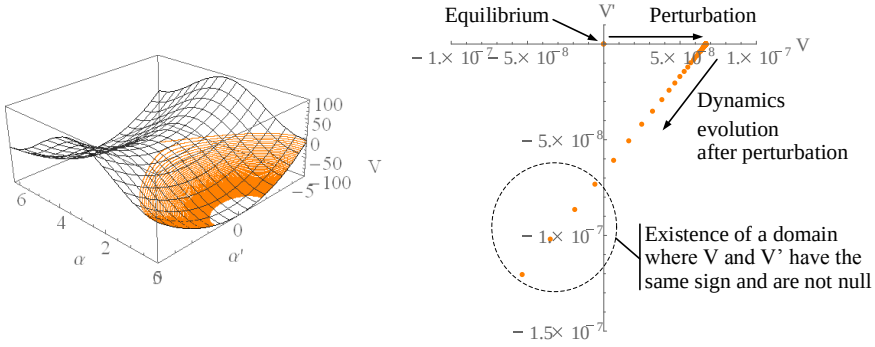

(a) Candidate function in phase space after a small perturbation

(b) Existence of a domain U around equilibrium, 1.5s after a small perturbation, 0.011s of computation time

Figure 5-6. Sign of Chetaev candidate function determination using a numerical simulation

In the case of the pendulum, the use of a numerical simulation to prove the existence of a domain U is not necessary because it could have been done more efficiently analytically. However when it comes to large nonlinear systems, trying to find analytically the sign of a candidate function and its total time derivative, V and $\dot{V}$, around equilibrium might become impossible.

1. The first proposal consists in checking the sign of eventual candidate functions with the help of a numerical simulation around equilibrium

Once a suitable Chetaev candidate function is found, the computation time[26] can be reduced to a minimal time where the existence of the domain U appears. Since the physical systems that we are interested in present parametric instabilities,

2. The second proposal consists in performing parametric sweeps of the physical system model, which are usually helicopter design parameters, and verifying each time the behavior of the candidate function using numerical simulations.
    a. If a domain U can be found, the candidate function is a Chetaev function. Quantitative information about the instability of the equilibrium can be obtained by memorizing the value of $\dot{V}$. If one chooses V as H, the Hamiltonian, or total energy, sum of kinetic and potential energies, $\dot{V}$ is the difference between the power input and power output of the system through its boundaries.

    b. If a domain U cannot be found, one should keep in mind one cannot, theoretically speaking, conclude whereas the equilibrium is stable or not.

The weakness of Lyapunov's direct method for which there is no systematic method to find such a function is not solved. However, problem dependent candidate functions can be proposed. A candidate function is proposed for the special problem of 'helicopter ground resonance' in this chapter.

The approach proposed here can obviously be applied to other representations than bond graphs. However, this idea emerged while mapping energy flows in bond graphs and reading (Junco, 1993) in which Lyapunov functions are proposed to be extracted from BGs. It is therefore claimed that even if the approach can be applied to other representations, bond graphs were a necessary intellectual step to arrive to this idea.

[26] The computation time of this method still needs to be compared to the computation time needed by other methods such as Lyapunov Characteristic Exponents, in order to better position it

5.4. Illustration, 'helicopter ground resonance' instability

The rest of this chapter is devoted to an application of the method proposed in the previous section. The application concerns helicopter ground resonance, which is a major dynamic phenomena of interest in rotorcraft dynamics. The starting point of this section dedicated to the ones that do not work on helicopters is the most classic ground resonance 3 degrees of freedom analytical model and its parametric instability analysis using a Campbell diagram known for more than 40 years now. Then the choice of a Hamiltonian based function of the system is discussed to be an interesting Chetaev candidate function. Time simulations of H for different parameter sets are computed around equilibrium and the soundness of the approach is illustrated.

5.4.1. A mechanical parametric instability

The simplest example consists in deriving the equations of a rotor on moving base in the absence of aerodynamic forces, see (Krysinski & Malburet, 2011).

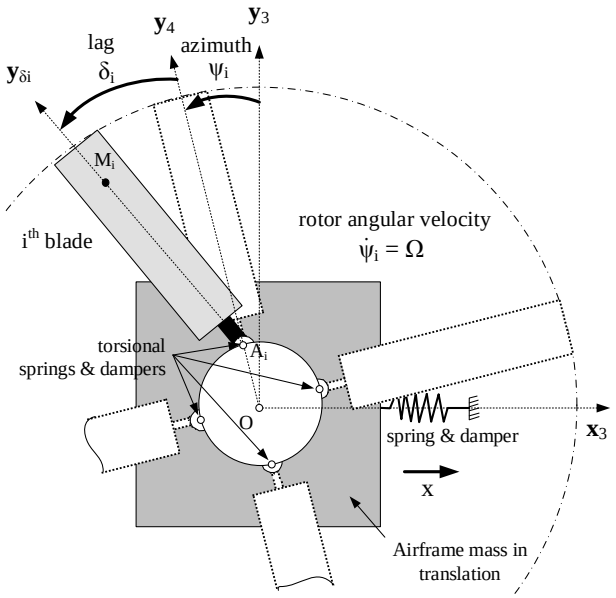

Figure 5-7. Simplified rotor-airframe model for ground resonance, 1 lag dof per blade, 1 translation dof for the airframe

Supposing the rotor has b blades, a massless hub-mast and a constant rotor angular velocity. By expressing the potential energy of the system, which is the sum of the contributions of the energy stored in the airframe landing gear represented by the spring & damper of characteristics k_f and c_x and the so-called rotor lag dampers represented by equivalent torsional springs & dampers of characteristics k_δ and c_δ,

$$V = \frac{1}{2}k_f x^2 + \sum_i^b \frac{1}{2}k_\delta \delta_i^2 \tag{72}$$

By expressing the dissipation energy of the system,

$$D = \frac{1}{2}c_x \dot{x}^2 + \sum_i^b \frac{1}{2}c_\delta \dot{\delta}_i^2 \tag{73}$$

Its kinetic energy,

$$T = \frac{1}{2}M_f \mathbf{V}^2{}_{G\in airframe/Rg} + \sum_i \frac{1}{2}\int_{blade_i} \mathbf{V}^2{}_{M\in blade_i/Rg}\, dm \tag{74}$$

The derivation of Lagrange equations and a linearization around small lag angles gives, for the airframe lateral motion,

$$\begin{aligned} &m_f \ddot{x} + bm_{bl}\ddot{x} + c_x \dot{x} + k_f x + m_s \Omega^2 \sum_{i=1}^b \cos(\Omega t + \frac{2\pi(i-1)}{b})\delta_i \\ &+2m_s \Omega \sum_{i=1}^b \sin(\Omega t + \frac{2\pi(i-1)}{b})\dot{\delta}_i - m_s \sum_{i=1}^b \cos(\Omega t + \frac{2\pi(i-1)}{b})\ddot{\delta}_i = 0 \end{aligned} \tag{75}$$

And for each i^{th} blade lag motion,

$$I_{bl}\ddot{\delta}_i + c_\delta \dot{\delta}_i + k_\delta \delta_i + em_s \Omega^2 \delta_i - m_s \cos(\Omega t + \frac{2\pi(i-1)}{b})\ddot{x} = 0 \tag{76}$$

In which one can see the time periodic coefficients in front of airframe generalized coordinates in blade equations and vice versa, the system of equations is a Linear Time Periodic one. Under the conditions of an isotropic rotor, hover flight or low advancing speeds, rotorcraft mathematical systems can be in addition put in the form of a linear time invariant (LTI) systems by using the multiblade coordinate transformation Appendix 2, and keep only the coupled equations,

$$\begin{cases} \left(bm_{bl} + m_f x\right)\ddot{x} + \frac{1}{2}bm_s \ddot{\delta}_{1s} + c_x \dot{x} + k_f x = 0 \\ \frac{1}{2}bI_{bl}\ddot{\delta}_{1c} + \frac{1}{2}bc_\delta \dot{\delta}_{1c} + bI_{bl}\Omega\dot{\delta}_{1s} + \frac{1}{2}bI_{bl}\left(-1+\nu^2\right)\Omega^2\delta_{1c} + \frac{1}{2}bc_\delta \Omega \delta_{1s} = 0 \\ \frac{1}{2}bm_s \ddot{x} + \frac{1}{2}bI_{bl}\ddot{\delta}_{1s} - bI_{bl}\Omega\dot{\delta}_{1c} + \frac{1}{2}bc_\delta \dot{\delta}_{1s} - \frac{1}{2}bc_\delta \Omega \delta_{1c} + \frac{1}{2}bI_{bl}\left(-1+\nu^2\right)\Omega^2\delta_{1s} = 0 \end{cases} \tag{77}$$

With,

$$\nu = \sqrt{\frac{k_\delta}{\Omega^2 I_{bl}} + \frac{em_s}{I_{bl}}} \text{ and } m_s = \int_0^L \rho.r.dr \tag{78}$$

The set of equations can be then casted into **M**, **C** and **K** matrices and set of equations is set into state space form with a state vector being $\mathbf{x}= [\mathbf{q},\dot{\mathbf{q}}]^T$ and $\mathbf{q}= [x,\delta_{1c}, \delta_{1s}]^T$,

$$\dot{\mathbf{x}} = \mathbf{A}\mathbf{x} \text{ with } \mathbf{A} = \begin{bmatrix} -\mathbf{M}^{-1}\mathbf{C} & -\mathbf{M}^{-1}\mathbf{K} \\ \mathbf{I} & [\mathbf{0}] \end{bmatrix} \tag{79}$$

A classic eigenvalue analysis of matrix **A** allows to conclude on the stability of the equilibrium. The equilibrium position of the system presented above is known to be potentially unstable due to a parametric instability when the undamped frequencies of each blade lag motion in the fixed frame equals the airframe undamped frequency lateral motion,

Table 5. Helicopter data

Main rotor		
Number of blades	b	4
Blade root eccentricity	e (m)	0.198
Blade length	L (m)	5.50
Angular velocity	Ω (rad/s)	38.7
Individual blade		
Static moment	m_s (m.kg)	102
Inertia	I_{bl} (m².kg)	373
Mass	m_{bl} (kg)	37
Equivalent angular lag damper stiffness	k_δ (N.m/rad)	100 000
Equivalent angular lag damper damping	c_δ (N.m.s/rad)	2500
Airframe		
Mass	m_f (kg)	2000
Landing gear		
Equivalent stiffness	k_f (N.m/rad)	808 520
Equivalent damping	c_x (N.m/rad)	1300

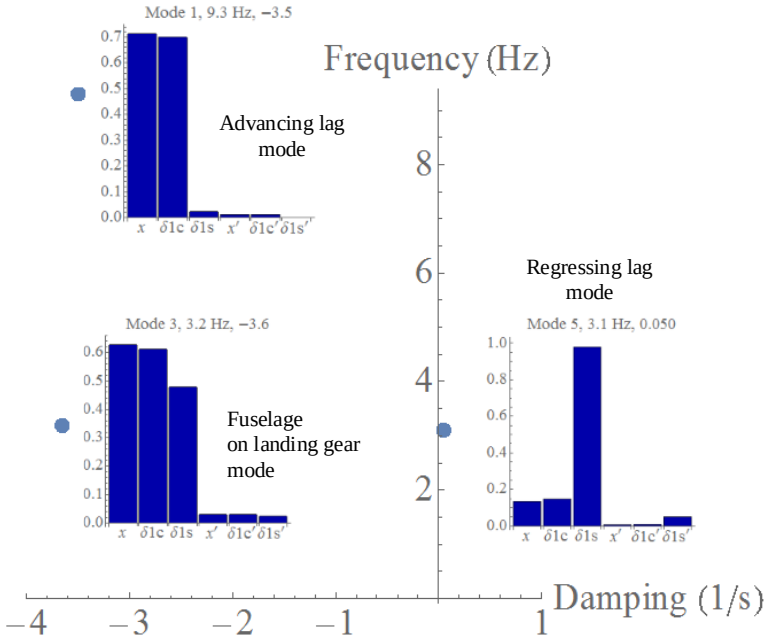

Figure 5-8. Modes and shapes in the complex plane at rotor nominal angular velocity

5.4.2. Average of the Hamiltonian function as a Chetaev candidate function

In (Oberinger & Hajek, 2013), the authors state that "*the condition for the presence of a dynamical instability of a mechanical system, i.e. divergent oscillations, is an increase of the system's internal energy*. Internal energy is defined in this case as the sum of kinetic and potential energies of the system and it is therefore the sum of total energy of the system, let us also call it the Hamiltonian. In that same paper the authors use this condition to trace the energy contributions of helicopter physical system's degrees of freedom to the increase of internal energy. They apply this to helicopter ground resonance and to more complex rotor-airframe couplings.

A numerical simulation of the response to a small force perturbation on the airframe of the idealized rotor-airframe physical system presented on Figure 5-7, is plotted below and illustrates what states Oberinger: in the blue case, nominal values of Table 5, according to Campbell diagram the system is unstable. Numerically the states appear to diverge and the Hamiltonian appears to grow. The system enters in a regime in which it demands power to the source. The model from which the results are obtained is a bond graph model that is presented in the next section.

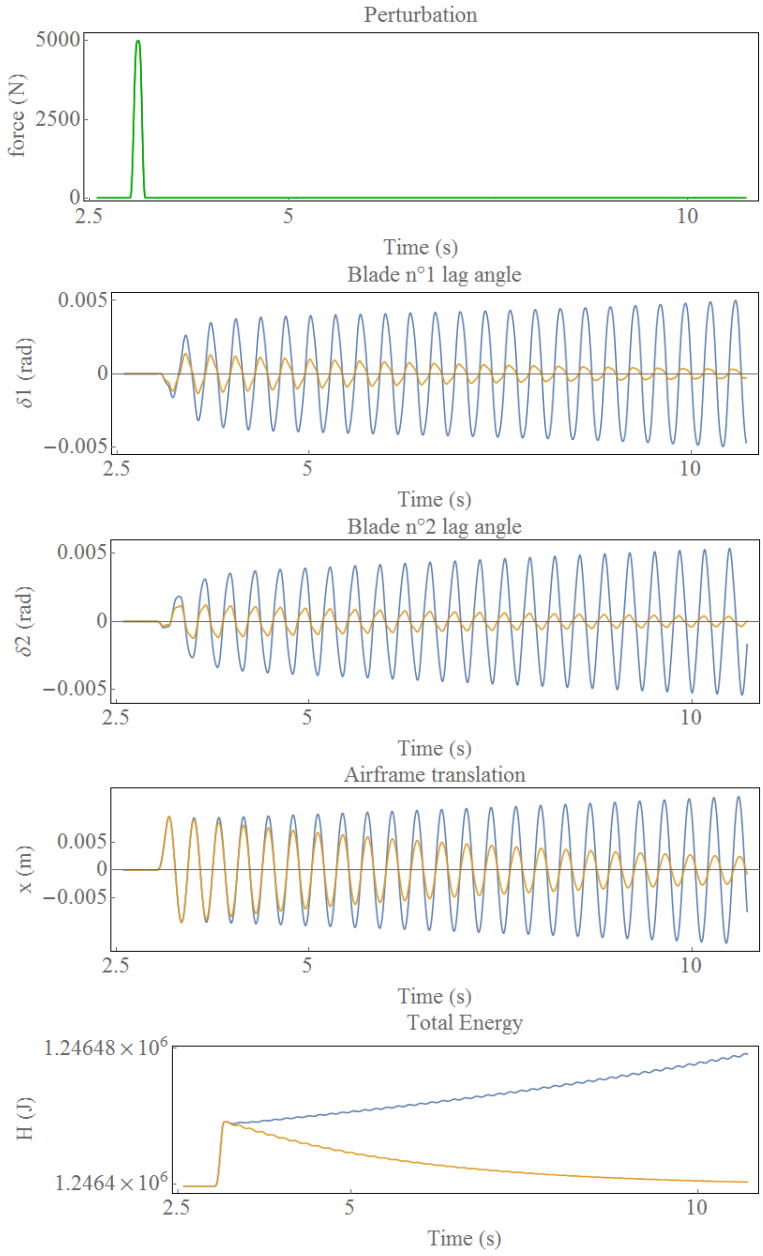

Figure 5-9. Free response of rotor-airframe for nominal parameters (blue) and three times higher damping in lag dampers (orange)

Stating that the internal energy increases is mathematically vague. As a matter of fact if the Hamiltonian would strictly increase in time around equilibrium, its total time

derivative would have the same sign as its Hamiltonian, and the function would immediately be a Chetaev function. However, a closer look to the Hamiltonian plotted before[27] shows H tends to increase with time but *not strictly*: it oscillates while increasing, therefore its total time derivative changes sign around the equilibrium and it is not a Chetaev function.
However, in the particular case of ground resonance parametric instability, it appears numerically, that a linear regression of the Hamiltonian around the equilibrium over a few rotor periods, defined as $\hat{H}$, could be a Chetaev function, see Figure 5-10.

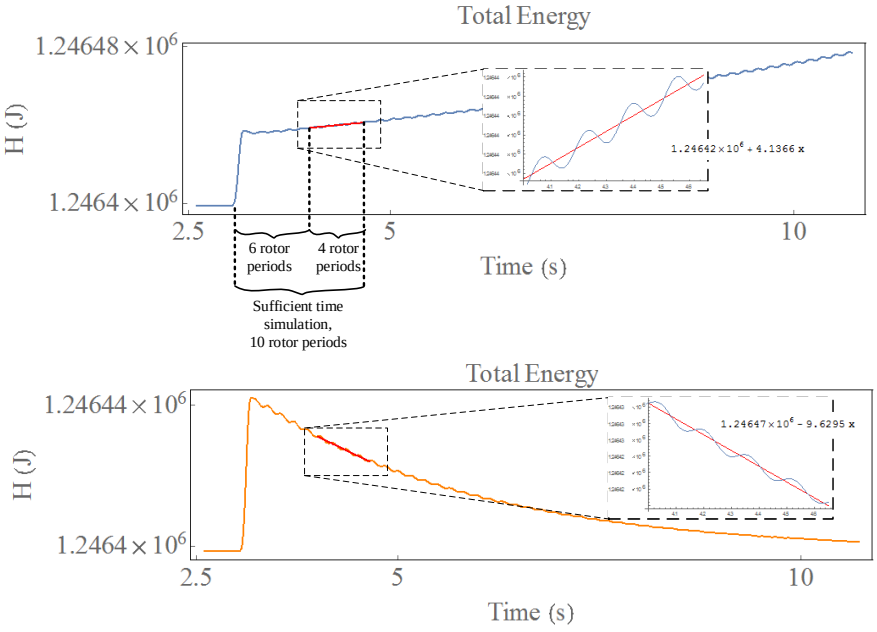

Figure 5-10. Computation of $\hat{H}$, a linear regression of total energy over a few rotor periods

Based on the numerical simulation results a least-squares fit is employed to find β and γ such that,

$$\hat{H}(t) = \beta.t + \gamma \tag{80}$$

This can be represented in the ($\dot{V}$, V) plane, see Figure 5-11; the reader should also come back to (b) Figure 5-6, to see the analogy between the simple pendulum and this more complex system by relating these two figures. A physical meaning can be given to the Chetaev function,

[27] (Oberinger & Hajek, 2013) numerical simulation results of ground resonance exhibit similar oscillations.

$$\frac{d\hat{H}}{dt} = \beta = \hat{P}_{engine} - \hat{P}_{dissipated} > 0 \tag{81}$$

In other words, when the system becomes unstable, it reorganizes itself in such a way it demands more energy to sources outside its boundaries than it is able to dissipate. This surplus of energy is in return stored in potential and kinetic energies.

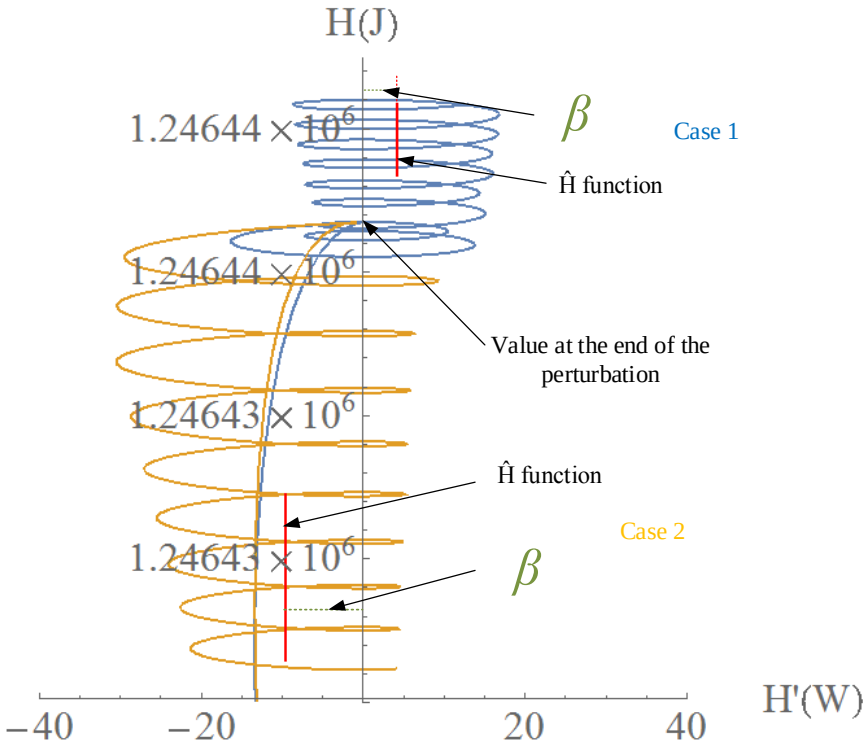

Figure 5-11. Projection in the ($\dot{V}$, V) plane after perturbation of equilibrium

5.4.3. Hamiltonian expression from a bond graph model of the physical system

The objective of this section is twofold, first to give an explicit graph that represents the physical system described before and secondly to explain how energy-based Chetaev candidate functions can be expressed.

Bong graph model of the physical system

Based on the rotor-airframe model using multibody dynamics developed in chapter 2, one can simplify it to obtain the bond graph presented on Figure 5-14. The first

simplification consists in modifying the equations of motion of the airframe: here it is considered as a rigid body in translation, as a result the superior part of the graph that accounts for Euler equations has been removed. The rest of the simplifications consist in modifying the parameters of the R and C elements to enforce constraints in joints between rigid bodies. The airframe is constrained in such a way it can only translate in the x direction and each one of the blades can lag but not flap or pitch. It can also be remarked that the hub inertia and mass have not been taken into account by just removing the inertial elements on its graph; the resulting equations behind it, represent therefore pure kinematic relations. In order, to show all the bonds and causal strokes, the full graph is presented on Figure 5-14.

In addition, to implement the constraints on the degrees of freedom that cannot move, parasitic elements are introduced. As already discussed in the first chapters of this work, this approach has advantages and disadvantages. This choice is motivated by the need to keep as many elements as possible in integral causality. However, the inertial elements that represent the mass matrices of each blade are still in derivative causality. Therefore, the system of equations is a set of DAEs. Rigorously speaking Chetaev functions apply only to ODEs. It is conjectured here, they can still be applied directly to the underlying proposed set of DAEs. A transformation to a set of ODEs would consist in adding R and C to all the revolute joints.
Furthermore, the set of ODEs one would obtain would be non-autonomous; the time *t* would appear explicitly in the equations. A supplementary step would be needed to make the system autonomous and apply the proposed Chetaev theorem by for example invoking the periodicity of the equations and adding the time *t* as a state variable as proposed in (Masarati, Quaranta, Lanz, & Mantegazza, 2003). Another option would be to see to what extent the non-autonomous version of Chetaev theorem can be applied. These two options need in any case further investigations.

Hamiltonian function expression from the bond graph

Interestingly, a bond graph such as the one presented next page can be seen as structured around the total energy of the system or Hamiltonian in our case. The physical system on Figure 5-7 is modeled as containing:

1. **5 linear springs** for which their potential energies are proportional to the square of the associated generalized position by their stiffness characteristic.

2. **5 rigid bodies** that are characterized by 5 kinetic energy terms: one associated to the airframe and 4 for each blade rotor. Each one of this blade kinetic energies can be decomposed into two terms: one associated with the rotation of the rigid body and one associated to its translation. In our approach these terms are therefore decomposed into 2 terms, as a remainder of the equation (16) given in Chapter 1,

$$T_i = \frac{1}{2} m_i \mathbf{V}^0_{G_i,i/0}{}^T . \mathbf{V}^0_{G_i,i/0} + \frac{1}{2} \boldsymbol{\Omega}^i_{i/0}{}^T . \mathbf{I}_{G,i} . \boldsymbol{\Omega}^i_{i/0} \tag{82}$$

Finally, the bond graph of our system contains 5 potential energy terms and 10 kinetic energy terms. The expression of each of these terms is then decomposed in the bond graph into the three directions of the Cartesian space and their sum give the expressions of kinetic and potential energy, in other words total energy or the Hamiltonian of the system,

$$\begin{aligned} H(\mathbf{p},\mathbf{q}) &= T(\mathbf{p}) + V(\mathbf{q}) \\ &= \sum \frac{p_i^2}{2I_i} + \sum \frac{q_j^2}{2C_j} \end{aligned} \tag{83}$$

Where, p_i are the generalized momenta and q_i are the generalized coordinates,

$$\mathbf{p} = {}^{T}\left[m\dot{x}, \left\{ I(\dot{\Psi} + \dot{\delta}_k), m\mathbf{V}^0_{G_k,k/0}.\mathbf{x}_3, m\mathbf{V}^0_{G_k,k/0}.\mathbf{y}_3, \text{ for each blade } k \right\} \right] \tag{84}$$

$$\mathbf{q} = {}^{T}\left[x, \delta_1, \delta_2, \delta_3, \delta_4 \right] \tag{85}$$

And the bond graph storage elements contain linear constitutive laws,

$$I_i = m_i \text{ and } C_j = \frac{1}{k_j} \tag{86}$$

As described in vector **p**, the rotor angular velocity is a state variable using this approach. To keep the hypothesis of constant rotor angular velocity, a perfect source of flow, an MSf bond graph element, is introduced in the graph: it represents the engine and keeps this state variable at the desired value at any time *t*. Compared to the classic formulation of the problem using Lagrange equations, at this stage, the kinetic energy of the system has a very compact form and does not contain itself the nonlinearities due to kinematic transformations from rigid body frames to the inertial reference frame. These nonlinearities are outside *H* and but are of course still present at the level of transformation elements.
Under these hypotheses the first principle of thermodynamics gives,

$$H(\mathbf{p},\mathbf{q}) = W_{engine}(\mathbf{p},\mathbf{q}) - W_{dissipations}(\mathbf{p}) \tag{87}$$

Each of the energy terms $p_i^2/2I_i$ and $q_j^2/2C_j$ of $H(\mathbf{p},\mathbf{q})$ can be computed from the graph by the energy sensors that have been placed at the root of the bond graph I and C elements see Figure 5-14. Additional power sensors have also been placed on R and the MSf elements to capture the total time derivative of *H*. Interestingly, under this form, see equation (83), *H* is a quadratic form of the states of the system with positive coefficients I_i and C_j; which means it is a positive definite function. At equilibrium the rotor angular velocity is constant and therefore the rotor kinetic energy is not null. On the other side, the potential energy of the system is null at equilibrium and since it is a quadratic form of states with positive coefficients C_j it is strictly minimal at the equilibrium.

5.4.4. Estimating the instability domain by parametric sweep

In the previous sections, it has been explained how the total energy of the system as well as its time derivative could be expressed from the bond graph. In this section, the computation of β, for system parameter variations, gives the sign of the proposed Chetaev function. The computation is done directly from the set of nonlinear DAEs and with the help of a Backward Differentiation Formula (BDF) method available in the bond graph preprocessor 20-sim®.
Relevant parameters of interest for the ground resonance phenomenon are the rotor angular velocity and the damping of the regressing lag mode, see Appendix 6. The damping of this mode is modified by varying the characteristic of the lag dampers damping. The results are presented on Figure 5-12, in which an increase of β becomes obvious around the nominal rotor angular velocity and decreases with an increase of lag damping. The determination of the necessary damping on a rotor is a major concern for rotorcraft designers. In fact over sizing the dampers will mean a heavier damper. In addition to the mass of the damper, which is a penalty by itself, the dampers rotate and will therefore generate higher centrifugal forces on other rotor parts. In return these parts will probably become heavier in other to substantiate static and fatigue strength criteria. Downsizing the lag damping degrades the stability of the rotor-airframe system and leads to aircrafts prone to *ground resonance*, *air resonance* or *lateral-roll aeroelastic RPCs*. However it should be noticed that other solutions exist to improve the damping of the regressing lag mode, such as the implementation of active controls (Takahashi & Friedmann, 1991), (Krysinski & Malburet, 2011).

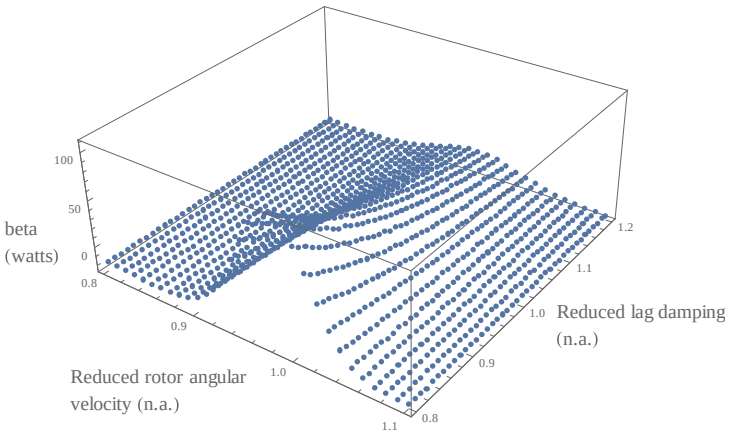

Figure 5-12. β for varying reduced rotor angular velocity and lag damping

To illustrate the soundness of the proposed approach, the results are compared to the linear stability results of the same physical system, see Figure 5-13. In orange, if the real part of all eigenvalues is strictly negative, an orange point is plotted. In blue, the criteria is on the sign of β: if beta is strictly negative, a blue point is plotted. A good agreement is found for the estimated instability domain between the two methods, see Figure 5-13. The minimal time computation to get this results have been of 10 rotor periods, as with Floquet theory. A higher number of periods converges to these results, but of course at an increased cost.

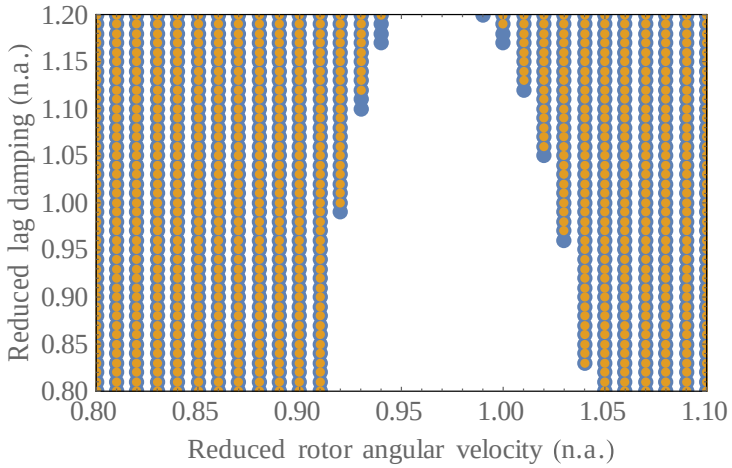

Figure 5-13. Instability domain estimations, negative real parts of the eigenvalues (orange) and negative beta (blue)

5.5. Conclusion

This chapter has presented and proposed an approach using Chetaev functions in order to determine if the equilibrium of a dynamic system is unstable directly from a nonlinear model. The use of this approach has a major limitations: there is no systematic method to find a Chetaev function and finding a Chetaev function gives only a sufficient condition of instability. As a result, if a Chetaev function is not found one cannot say the equilibrium is stable.
However, in the case where:

- There is a need to perform a parametric sweeps on a set of equations. It is in particular the case when investigating *parametric instabilities*.
- For one set of parameters, one has at disposal a Chetaev function. This would need to be proved analytically for that set.
- Then the method might have an interest in terms of computation time: indeed it is proposed to verify whether the Chetaev function candidate of the previous point is still Chetaev which demands a very short computation time.

This is illustrated on the ground resonance case for which total energy average seems to be an interesting Chetaev function candidate; an analytical proof still needs to be done for at least one case. It is shown that the computation time is in this case is around the same as what would be needed by applying the Floquet theory to the equivalent linear time periodic (LTP) system, which is 10 rotor periods for a system with 5 degrees of freedom. This computation time should be benchmarked to the time needed to compute the largest Lyapunov Characteristic Exponent. The approach proposed here can obviously be applied to other representations than bond graphs. However, this idea emerged while mapping energy flows in bond graphs and reading (Junco, 1993) in which Lyapunov functions are proposed to be extracted from BGs. It is therefore claimed that even if the approach can be applied to other representations, bond graphs were a necessary intellectual step to arrive to this idea.

Furthermore, extensive analytical work is still to be done. In particular the total energy average function proposed is not continuous till the equilibrium; to be rigorous it has to be continuous, so the connecting function expression needs to be found. The Chetaev theorem used in this chapter is the one that can be applied to autonomous systems; the transition from the nonlinear periodic equations to the nonlinear time invariant one needs to be justified more rigorously.

Finally, the algorithmic implications have not been discussed. As a matter of fact, *algebraic* instead of *ordinary* differential equations are numerically solved; but the Backward Differentiation Formula (BDF) method used here has its own stability and accuracy limitations that need to be taken into account to distinguish *physical instabilities* from *numerical* ones.

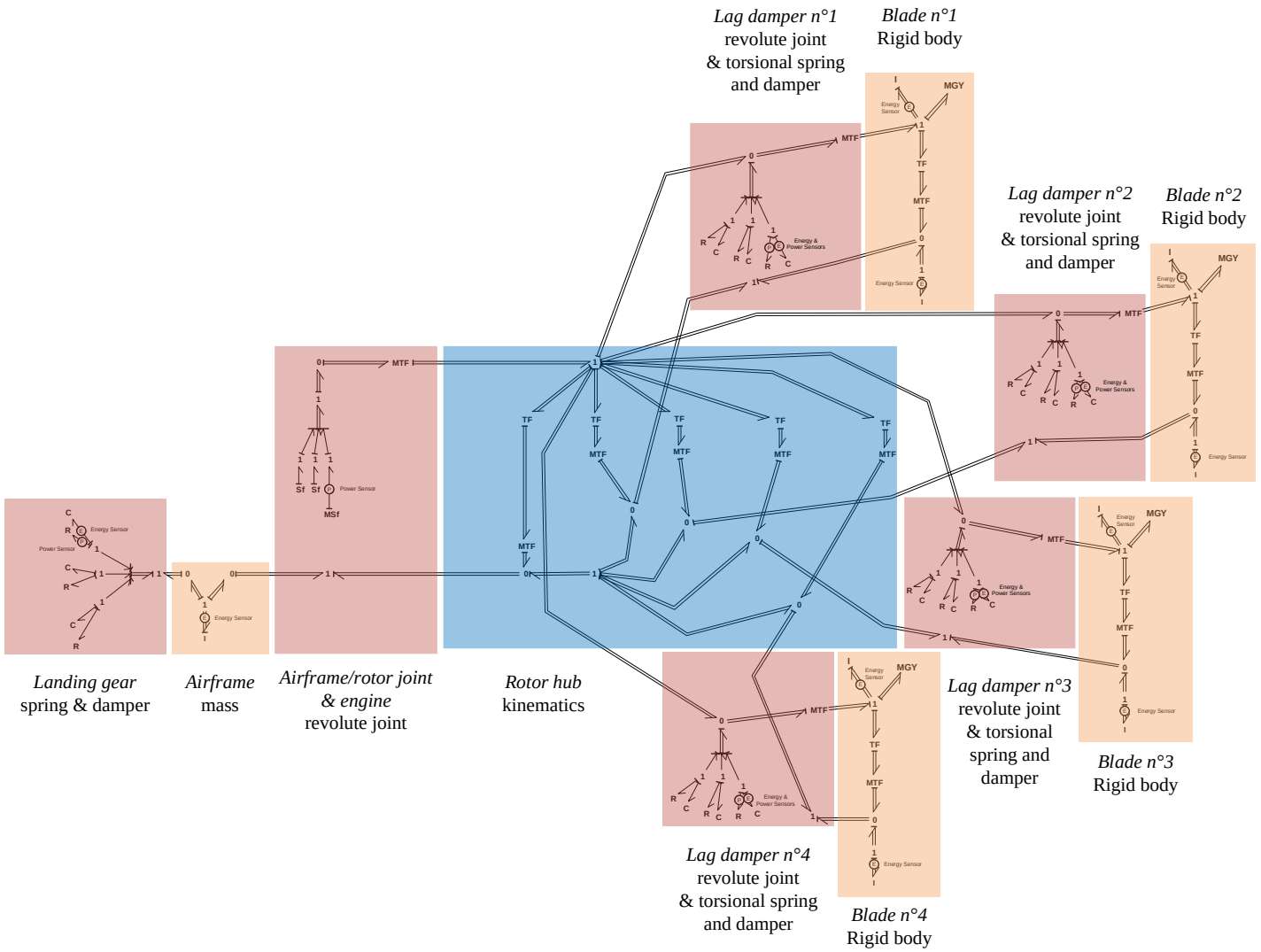

Figure 5-14. Rotor-airframe bond graph for ground resonance study using a multibody approach

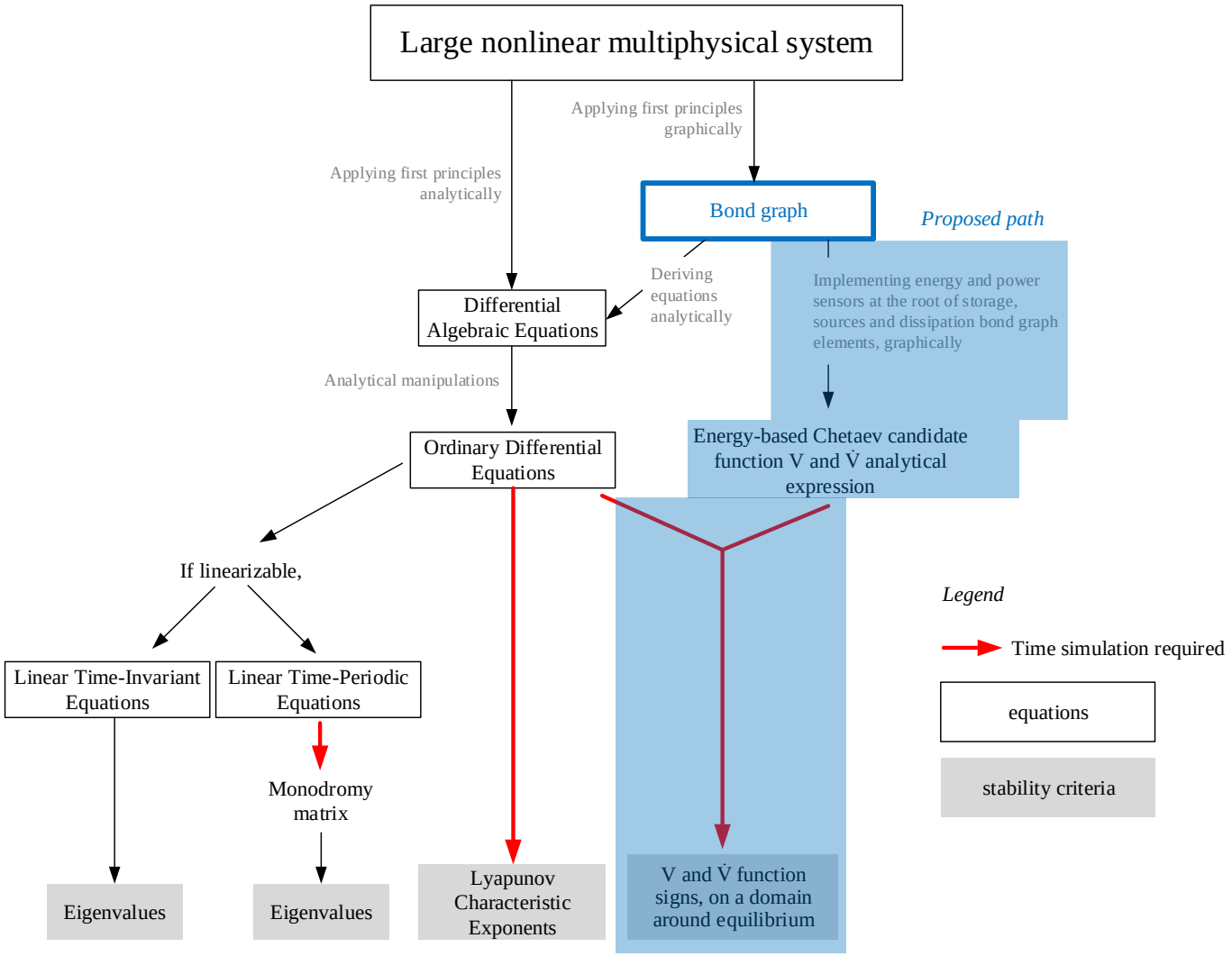

Figure 5-15. Path proposal, in the context of methods to evaluate the stability/instability of equilibriums

Conclusion

This thesis focuses on the modeling & analysis of complex dynamic systems using bond graphs. The modeling approach is in particular applied to the investigation of a dynamic phenomenon that appears on helicopters known as lateral-roll axes aeroelastic Rotorcraft-Pilot Couplings (RPCs). In this synthesis, three topics are put into perspective namely, the modeling method, the analysis of the resulting models and finally the application to RPCs themselves.

Concerning the modeling method

On the road towards a global energetic approach of helicopters in which as many subsystems and as physically detailed as necessary could be modeled, this investigation has illustrated two main advantages of the bond graph approach.
Modularity has been first illustrated when modeling multibody systems on chapters 2 & 3 using the bond graph pattern of a rigid body without manipulating equations. In fact, when modeled with such procedure, the equations of motion can be obtained relatively easily. However, as often in mechanics, the easier the equations of motion are obtained, the more complex the mathematical models are: not only Ordinary Differential Equations (ODEs) appear but also Differential Algebraic Equations (DAEs). The approach has of course the advantage of being applicable to a large class of problems but the drawback of probably not being the most computationally efficient for a particular problem. In addition in chapter 4, modularity was illustrated by showing how the frontiers between subsystems of a physical system are materialized at the graphical level of a BG.
A second advantage of BGs is that the form of their underlying mathematical models can be manipulated from the graphical level: "*An essential consequence of augmenting the bond graph with causal strokes is that the form of the mathematical model can be determined without formulating and manipulating any equation*", (Borutzky, 2009). This appears particularly useful to alleviate the level of complexity of the mathematical model prior to its resolution by a numerical method. This has been illustrated on chapter 2 when implementing the constraints between rigid bodies in a multibody system and in chapter 3 for systems that contain a closed kinematic chain (CKC). Furthermore an original bond graph has been proposed to model the concatenation of three revolute joints as needed when modeling the joint between articulated rotor blades and the rotor hub. The proposed bond graph allows to locally remove the algebraic constraints between blade and rotor hub joints at the graphical level.
It should be kept in mind that bond graphs represent naturally differential equations and not partial differential equations. If the need is such, for example to model complex aerodynamics, a more adapted energetic method could be used such as *Port-Hamiltonian Systems*, an evolution of bond graphs (Schaft, 2006).

Concerning the stability analysis of the resulting models

The last chapter presents and proposes the first blocks of an approach using Chetaev functions in order to determine if the equilibrium of a dynamic system is unstable directly from a nonlinear model. The approach proposed here can obviously be applied to other representations than bond graphs. However, this idea emerged while mapping energy flows in bond graphs and reading (Junco, 1993) in which energy based Lyapunov functions are proposed to be extracted from BGs. It is therefore claimed that even if the approach can be applied to other representations, bond graphs were a necessary intellectual step to arrive to this idea. The use of this approach has major limitations: there is no systematic method to find a Chetaev function and finding a Chetaev function gives only a sufficient condition of instability. As a result, if a Chetaev function is not found one cannot say the equilibrium is stable. However, the method might have an interest in terms of computation time in particular cases such as the investigation of *parametric instabilities.*

Concerning the application to lateral-roll aeroelastic RPCs

The development of an aeromechanical rotor-airframe model is proposed in chapter 2 to be representative of helicopter dynamics around hover at low frequencies. The aerodynamic model is a quasi-steady one for which the bond graph is considered to be an original contribution. It both allows to take into account for variable aerodynamic properties along blade spans and can be used without any modification to represent hover or forward flight configurations.
A pilot model has been developed in chapter 3. It consists in a neuromusculoskeletal model of pilot's left upper limb. The individual subsystems that compose this model have been translated into bond graphs from literature. However, multibond graph representations are proposed for the first time to model individual neuromuscular forces between bones that have spatial motion. This model is applied for the first time for the prediction of BDFT on the lateral axis of a helicopter. The BDFT of a given human being depends on the settings of his neuromuscular system; for example whether he/she is stressed or not. It is known that the computation of the motion of human movement or posture leads to a mathematical indeterminacy because the human body possesses less degrees of freedom than muscles that act as actuators. As proposed in literature, the addition of an energetic principle can solve the indeterminacy problem. Postulating that the human body minimizes metabolic cost during motion allows to compute muscle activation unknowns. From a computational point of view an optimization algorithm is used to minimize muscle forces work, an energetic quantity that can be computed naturally from the bond graph representation. Numerical simulations are performed to compute pilot's biodynamic feedthrough (BDFT). The results are quite encouraging: the task dependency of helicopter pilots BDFT can be predicted to a certain extent. An iterative procedure has allowed to find a set of parameters that have a physical meaning to reproduce what has been seen in experiments.
In chapter 4 the human-machine model obtained represents a bioaeroelastic behavior that is then analyzed more into detail; more precisely lateral-roll aeroelastic RPCs are investigated. A linear stability analysis confirms what has been conjectured in literature concerning the role played by the regressing lag mode in the phenomenon.

Furthermore, the results show that for higher neuromuscular pilot stiffness's, the higher frequencies of the advancing lag mode could also excite the airframe. This last result needs to be confirmed by some experiments. It should kept in mind that some of the assumptions taken in the full bioaeroelastic system are reductive; especially concerning the flight configuration and friction assumptions of the cyclic lever. However, even if the predicted instability domains will move with more detailed physics, the linear models used in chapter 4 will help understand the physical mechanisms behind the phenomena that could help explaining damping drops in real flights.

Future research

In the short term, the vehicle aeromechanical model needs to be further compared to flight tests to be considered as fully valid. One of the first improvements that will need to be done on the modeling hypothesis concerns the necessity to take into account rotor inflow velocity in the aerodynamic model. The implementation of unsteady aerodynamic models should also be investigated. The model prediction in terms of the pilot model kinematics should be compared to other literature models and supplementary experiments. More flight configurations should also be investigated and in particular forward flight.
In the long term, the next step would be to find an explicit mathematical relation between task and neuromuscular system parameters. This would allow obtaining a useful quantity for rotorcraft designers which would be BDFT maximal envelops rather than precise BDFT pilot behaviors.
Concerning the instability analysis using Chetaev functions an extensive analytical work is still to be done. In particular the total energy average function proposed is not continuous till the equilibrium; to be rigorous it has to be continuous, so the connecting expression needs to be found. The Chetaev theorem used in this chapter is the one that can be applied to autonomous systems; the transition from the nonlinear time periodic equations to the nonlinear time invariant ones needs to be justified more rigorously. In terms of computation time, the method should be benchmarked to the time needed to compute the largest Lyapunov Characteristic Exponent. Finally, the algorithmic implications have not been discussed. As a matter of fact, algebraic instead of ordinary differential equations are numerically solved; but the Backward Differentiation Formula (BDF) method used here has its own stability and accuracy limitations that need to be taken into account to distinguish physical instability estimation from numerical instabilities.

The models and the method employed to develop these models could be used in a wider range of applications, for example in the automotive industry, to investigate pilot-vehicle interactions. The neuromusculoskeletal model could be used in clinical applications to develop for example prosthesis based on muscle force estimations using non-invasive methods.

Finally, a characteristic of bond graphs that is probably underexploited is that not only the *equations of motion* can be obtained from the graphs, but at the same time, all the quantities necessary to compute the *conservation of energy* are represented.

References

Aponso, B., Johnston, D., Johnson, W., & Magdaleno, R. E. (1994). Identification of Higher Order Helicopter Dynamics using Linear Modeling Methods. *Journal of the American Helicopter Society*.

Bielawa, R. (2006). *Rotary Wing Structural Dynamics and Aeroelasticity*. AIAA Education Series.

Borutzky, W. (2009). *Bond graph methodology: development and analysis of multidisciplinary dynamic system models.* Springer.

Boudon, B. (2014). *Méthodologie de modélisation des systèmes mécatroniques complexes à partir du multi-bond graph: application à la liaison BTP-fuselage d'un hélicoptère.* Thèse de doctorat, ENSAM.

Brouwn, G. G. (2000). *Postural control of the human arm.* PhD Thesis, TU Delft, Delft University of Technology.

Chetaev, N. G. (1960). On certain questions related to the problem of the stability of unsteady motion. *Journal of Applied Mathematics and Mechanics*.

Chikhaoui, Z. (2013). *Contribution à la modélisation énergétique des hélicoptères en vue de la maîtrise de leurs comportements dynamiques.* Thèse de doctorat, ENSAM.

Coisnon, R. (2014). *Floquet.* Airbus Helicopters Note.

Cuadrado, J., Cardenal, J., & Bayo, E. (1997). Modeling and solution methods for efficient real-time simulation of multibody dynamics. *Multibody System Dynamics*.

Dabney, J. B. (2002). Modeling closed kinematic chains via singular perturbations. *American Control Conference.* IEEE.

Dauphin-Tanguy, G. (2000). *Les bond graphs.* Paris: Hermès Science Publication.

DefenceVideos. (2013, May 25). V-22 Osprey crash during testing. Retrieved from https://www.youtube.com/watch?v=n7Eao18qHVM.

Donham, R. E. (1969). Ground and Air Resonance Characteristics of a Soft In-Plane Rigid-Rotor System. *Journal of the American Helicopter Society*.

Dryfoos, J. B., Kothmann, B. D., & Mayo, J. (1999). An approach to reducing rotor-body coupled roll oscillations on the RAH-66 comanche using modified roll rate feedback. *AHS Forum Proceedings.* Montreal, Canada.

Eberhard, P., & Schiehlen, W. (2006). Computational dynamics of multibody systems: history, formalisms, and applications. *Journal of computational and nonlinear dynamics*.

Erdemir, A., McLean, S., Herzog, W., & van den Bogert, A. J. (2007). Model-based estimation of muscle forces exerted during movements. *Clinical Biomechanics*.

Favre, W. (1997). *Contribution à la représentation bond graph des systèmes mécaniques multicorps.* Thèse de doctorat, INSA Lyon.

Friedmann, P. (2004). Rotary-wing aeroelasticity: Current status and future trends. *AIAA journal*.

Garner, B. A., & Pandy, M. G. (2001). Musculoskeletal model of the upper limb based on the visible human male dataset. *Computer methods in biomechanics and biomedical engineering*.

Gennaretti, M., Collela, M. M., Serafini, J., Vu, B. D., Masarati, P., Quaranta, . . . Stefan, R. (2013). Anatomy, modelling and prediction of aeroservoelastic rotorcraft-pilot-coupling. *European Rotorcraft Forum.*

Hasenstaub, A., Otte, S., Callaway, E., & Sejnowski, T. J. (2010). Metabolic cost as a unifying principle governing neuronal biophysics. *Proceedings of the National Academy of Sciences*.

Hernani, R., Romero, G., & Jazmati, R. (2011). An Alternative for Human Gait Modeling Using the Bondgraph Technique. *Interdisciplinary Applications of Kinematics*.

Hess, R. A. (1998). Theory for roll-ratchet phenomenon in high-performance aircraft. *Journal of guidance, control, and dynamics*.

Höhne, G. (2000). Computer aided development of biomechanical pilot models. *Aerospace science and technology*.

Jex, Henry R., & Magdaleno, Raymond E. (1978). Biomechanical Models for Vibration Feedthrough to Hands and Head for a Semisupine Pilot. *Aviation, Space, and Environmental Medicine*.

Johnson, W. (1980). Helicopter theory.

Johnson, W. (2013). A history of rotorcraft comprehensive analyses. *In American Helicopter Society 69th Annual Forum.*

Junco, S. (1993). Stability analysis and stabilizing control synthesis via Lyapunov's second method directly on bond graphs of nonlinear systems. *Proceedings of the IECON.*

Karnopp, D. (1977). Lagrange's equations for complex bond graph systems. *Journal of Dynamic Systems, Measurement and Control*.

Karnopp, D. C., Margolis, D. L., & Rosenberg, R. C. (2012). *System Dynamics: Modeling, Simulation, and Control of Mechatronic Systems: Modeling, Simulation, and Control of Mechatronic Systems.* John Wiley & Sons.

Kiss, F., & Szentágothai, J. (1966). *Atlas anatomiae corporis humani.* Budapest: Akadémiai kiadó : Medicina könyvkiadó.

Krysinski, T., & Malburet, F. (2011). *Mechanical Instability.* Wiley-Iste.

Laffisse, J., & Zoppitelli, E. (1993). *Stabilité du mode de traînée régressif sur NH90.* Eurocopter France.

Lamoureux, L. (1992). *Cinématique et dynamique des solides.* Traité des nouvelles technologies.

Lantzsch, R., Hamers, M., & Wolfram, J. (2014). Flight Control and Handling Qualities Evaluations Considering Air Resonance. *Journal of the American Helicopter Society*.

Lee, S. H., & Terzopoulos, D. (2006). Heads up!: biomechanical modeling and neuromuscular control of the neck. *ACM Transactions on Graphics (TOG)*.

Lone, M. M., & Cooke, A. K. (2010). Review of Pilot Modelling Techniques. *48th AIAA Aerospace Sciences Meeting*(AIAA-2010-297).

Lone, M. M., & Cooke, A. K. (2014). Review of pilot models used in aircraft flight dynamics. *Aerospace Science and Technology*.

Mantegazza, P., & Masarati, P. (2012). *Analysis of Systems of Differential-Algebraic Equations (DAE).* Graduate Course on "Multibody System Dynamics", Politecnico di Milano.

Marquez, H. J. (2003). *Nonlinear control systems: analysis and design.* John Wiley.

Martin, M. (2013). *Contribution à l'intégration d'un actionneur intelligent à retour d'effort au sein d'un système complexe–Application aux commandes de vol d'hélicoptères.* Thèse de doctorat, ENSAM.

Martinez, L., Vera, C., & Félez, J. (1997). Bond graph model for the analysis of the dynamic behavior of the human body. *International Conference on Bond Graph Modeling and Simulation (ICBGM).*

Masarati, P., & Quaranta, G. (2014). Bioaeroservoelastic Analysis of Involuntary Rotorcraft-Pilot Interaction. *Journal of Computational and Nonlinear Dynamics*.

Masarati, P., Quaranta, G., Lanz, M., & Mantegazza, P. (2003). Dynamic characterization and stability of a large size multibody tiltrotor model by pod analysis. *International Design Engineering Technical Conferences and Computers and Information in Engineering Conference*. ASME.

Maschke, B. (1990). *Contribution à une approche par bond-graph de l'étude et la conception de lois de commande de robots contenant des segments flexibles.* Thèse de doctorat, Paris 11.

Mattaboni, M., Fumagalli, A., Quaranta, G., & al. (2009). Identification of the biomechanical behavior of a rotorcraft pilot arm. *XX AIDAA Congress, Milano, Italy*.

Maurel, W. (1999). *3D modeling of the human upper limb including the biomechanics of joints, muscles and soft tissues.* Doctoral dissertation, Ecole Polytechnique Federale de Lausanne.

Mayo, J. (1989). The Involuntary Participation of a Human Pilot in a Helicopter Collective Control Loop. *European Rotorcraft Forum.* Amsterdam, Netherlands.

McRuer, D. T. (1980). Human dynamics in man-machine systems. *Automatica*.

McRuer, D. T. (1995). *Pilot-Induced Oscillations and Human Dynamic Behavior.* NASA Report.

McRuer, D. T., & Jex, H. R. (1967). A review of quasi-linear pilot models. *Human Factors in Electronics, IEEE Transactions on*.

Montgomery, R. C., & Granda, J. J. (2003). Using Bond Graphs for Articulated, Flexible Multi-bodies, Sensors, Actuators, and Controllers with Application to the International Space Station. *Simulation Series*.

Muscarello, V., Quaranta, G., & Masarati, P. (2014). The role of rotor coning in helicopter proneness to collective bounce. *Aerospace Science and Technology*.

Muscarello, V., Quaranta, G., Masarati, P., Lu, L., Jones, M., & Jump, M. (2015). Prediction and Simulator Verification of Roll/Lateral Adverse Aeroservoelastic Rotorcraft-Pilot Couplings. *Journal of Guidance, Control, and Dynamics*.

Ng-Thow-Hing, V. (2001). *Anatomically-based models for physical and geometric reconstruction of humans and other animals.* Doctoral Thesis, University of Toronto.

Oberinger, O., & Hajek, M. (2013). Analysis of complex rotor-airframe coupled instabilities by energy flow considerations. *American Helicopter Society Conference Proceedings.*

Orlita, M. (2015). *Collective bounce estimation - tool development.* Master of Science internship final report, Arts et Metiers ParisTech.

Pandy, M. G. (2001). Computer modeling and simulation of human movement. *Annual review of biomedical engineering*.

Pandy, M. G., & Barr, R. E. (2003). Biomechanics of the musculoskeletal system. In M. Kutz, *Standard Handbook of Biomedical Engineering & Design.* McGRAW-HILL.

Parham, T., Popelka, D., Miller, D., & Froebel, A. (1991). V-22 pilot-in-the-loop aeroelastic stability analysis. *AHS Forum Proceedings.* Phoeniz, AZ.

Pavel, M. (2010). Modeling Lead-Lag Dynamics for Rotorcraft-Pilot-Couplings Investigation. *AHS Forum Proceedings.* Phoenix, AZ.

Pavel, M. D., Jump, M., Dang-Vu, B., Masarati, P., Gennaretti, M., Ionita, A., . . . Malecki, J. (2013). Adverse rotorcraft pilot couplings—past, present and future challenges. *Progress in Aerospace Sciences*.

Pavel, M., & Padfield, G. (2008). Understanding the Peculiarities of Rotorcraft-Pilot-Couplings. *AHS Forum Proceedings.*

Pennestri, E., & Vita, L. (2004). Strategies for the numerical integration of DAE systems in multibody dynamics. *Computer Applications in Engineering Education*.

Pennestri, E., Stefanelli, R., Valentini, P. P., & Vita, L. (2007). Virtual musculo-skeletal model for the biomechanical analysis of the upper limb. *Journal of biomechanics*.

Perelmuter, A. V., & Slivker, V. (2013). *Handbook of Mechanical Stability in Engineering.* World Scientific.

Peters, D. A., Lieb, S. M., & Ahaus, L. A. (2011). Interpretation of Floquet eigenvalues and eigenvectors for periodic systems. *Journal of the American Helicopter Society*.

Preumont, A. (2013). *Twelve Lectures on Structural Dynamics.* Université Libre de Bruxelles.

Rezgui, D., Lowenberg, M. H., Jones, M., & Monteggia, C. (2014). Continuation and Bifurcation Analysis in Helicopter Aeroelastic Stability Problems. *Journal of Guidance, Control, and Dynamics*.

Schaft, A. (2006). Port-Hamiltonian systems: an introductory survey.

Schiehlen, W. (2006). Computational dynamics: theory and applications of multibody systems. *European Journal of Mechanics-A/Solids*.

Serafini, J. G. (2008). Aeroelastic and biodynamic modeling for stability analysis of rotorcraft-pilot coupling phenomena. *In Proceedings of the 34th European Rotorcraft Forum.*

Shnol, E. E. (2007). Chetaev function. *Scholarpedia*, 2(9):4672., revision #91127.

Stroeve, S. (1999). Impedance characteristics of a neuromusculoskeletal model of the human arm I. Posture control. *Biological cybernetics*.

Takahashi, M. D., & Friedmann, P. (1991). Helicopter Air Resonance Modeling And Suppression Using Active Control. *Journal of Guidance, Control, and Dynamics*.

Tamer, A., & Masarati, P. (2015). Do We Really Need To Study Rotorcraft as Linear Periodic Systems? *American Helicopter Society Conference Proceedings.*

Tiernego, M. J., & Bos, A. M. (1985). Modelling the dynamics and kinematics of mechanical systems with multibond graphs. *Journal of the Franklin Institute*.

Tod, G., Malburet, F., Gomand, J., & Barre, P.-J. (2013). Modeling Flexibility in Rotational Degrees of Freedom using Multibond Graphs. *iNaCoMM*. Roorkee, India.

Tod, G., Malburet, F., Gomand, J., & Barre, P.-J. (2014). An upper limb musculoskeletal model using bond graphs for rotorcraft-pilot couplings analysis. *Simbio-M Conference.* Marseille, France.

Tod, G., Malburet, F., Gomand, J., Barre, P.-J., & al. (2013). An Energetic Approach to Aeroelastic Rotorcraft-Pilot Couplings Analysis. *European Rotorcraft Forum.*

Van Dijk, J., & Breedveld, P. C. (1991). Simulation of system models containing zero-order causal paths—I. Classification of zero-order causal paths. *Journal of the Franklin Institute*.

Van Dijk, J., & Breedveld, P. C. (1991). Simulation of system models containing zero-order causal paths—II Numerical implications of class 1 zero-order causal paths. *Journal of the Franklin Institute*.

Venrooij, J. (2014). *Measuring, modeling and mitigating biodynamic feedthrough.* Doctoral dissertation, TU Delft, Delft University of Technology.

Venrooij, J., Yilmaz, D., Pavel, M. D., Quaranta, G., Jump, M., & Mulder, M. (2011). Measuring Biodynamic Feedthrough in Helicopters. *European Rotorcraft Forum.* Italy.

Walden, R. B. (2007). A Retrospective Survey of Pilot-Structural Coupling Instabilities in Naval Rotorcraft. *AHS Forum Proceedings.*

Wang, J., Shan, W., Bin, W., & Bauchau, O. (2015). Time domain approaches to the stability analysis of flexible dynamical systems. *Journal of Computational and Nonlinear Dynamics*.

Wojcik, L. (2003). Modeling of musculoskeletal structure and function using a modular bond graph approach. *Journal of the Franklin Institute*.

Wolf, A., Swift, J. B., Swinney, H. L., & Vastano, J. A. (1985). Determining Lyapunov exponents from a time series. *Physica D: Nonlinear Phenomena*.

Zajac, F. E. (1988). Muscle and tendon: properties, models, scaling, and application to biomechanics and motor control. *Critical reviews in biomedical engineering*.

Zarrugh, M. Y., Todd, F. N., & Ralston, H. J. (1974). Optimization of energy expenditure during level walking. *European Journal of Applied Physiology and Occupational Physiology*.

Zeid, A. (1989). Some bond graph structural properties: eigen spectra and stability. *Journal of dynamic systems, measurement, and control*.

Zeid, A., & Chung, C.-H. (1992). Bond graph modeling of multibody systems: a library of three-dimensional joints. *Journal of the Franklin Institute*.

Zeid, A., & Overholt, J. L. (1995). Singularly Perturbed Formulation: Explicit Modeling Of Multibody Systems. *Journal of the Franklin Institute*.

Appendix 1
Some bond graph basics

A bond graph is at the visual level the interconnection of elements that can either be sources (or sinks), dissipators or energy stores, see Fig. 1. Once the elements are connected through a junction structure, one obtains an acausal bond graph. For a general introduction and also specialist topics, the reader can refer to the available books in literature, one in French (Dauphin-Tanguy, 2000) and two in English (Karnopp, Margolis, & Rosenberg, 2012) and (Borutzky, 2009). It is proposed here, to illustrate through a simple classic example how the equations can be obtained from a bond graph through the concept of causality.

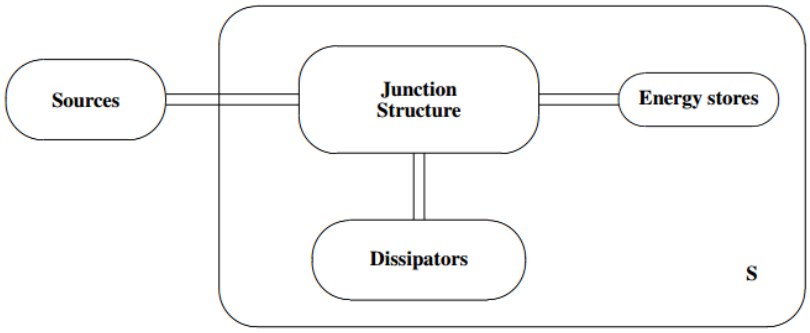

Fig. 1. General structure of a bond graph from (Borutzky, 2009)

In bond graphs, an analogy between physical domains can be made in terms of efforts and flows, see Fig. 2. The generalized *momentum p(t)* and *displacements q(t)* can be defined in terms of efforts and flows,

$$p(t) = \int e(t)dt$$
$$q(t) = \int f(t)dt$$

From those notations, the energy can be expressed as a function of time,

$$E(t) = \int e(t).f(t)dt$$

With the above definitions of p and q, the energy can also be expressed as a function of p or q energy variables,

$$E(p) = \int f(p)dp$$
$$E(q) = \int e(q)dq$$

Energy domain	Effort e	Flow f	Generalised momentum p	Generalised displacement q
Translational mechanics	Force F [N]	Velocity v [m/s]	Momentum p [Ns]	Displacement x [m]
Rotational mechanics	Angular moment M [Nm]	Angular velocity ω [rad/s]	Angular momentum p_ω [Nms]	Angle θ [rad]
Electro-	Voltage u [V]	Current i [A]	Linkage flux λ [Vs]	Charge q [As]
magnetic domain	Magnetomotive force V [A]	Magnetic flux rate $\dot{\Phi}$ [Wb/s]	–	Magnetic flux Φ [Wb]
Hydraulic domain	Total pressure p [N/m^2]	Volume flow Q [m^3/s]	Pressure momentum p_p [N/m^2 s]	Volume V_c [m^3]
Thermo-dynamic	Temperature T [K]	Entropy flow $\dot{S}$ [J/K/s]	–	Entropy S [J/K]
Chemical domain	Chemical potential μ [J/mole]	Molar flow $\dot{N}$ [mole/s]	–	Molar mass N [mole]

Fig. 2. Analogy between physical domain in terms of efforts and flows

Element	Acausal Form	Causal Form	Causal Relation
Effort source	$S_e \rightharpoonup$	$S_e \dashv$	$e(t) = E(t)$
Flow source	$S_f \rightharpoonup$	$S_f \vdash$	$f(t) = F(t)$
Resistor	$R \leftharpoonup$	$R \vdash$	$e = \Phi_R(f)$
		$R \vdash$	$f = \Phi_R^{-1}(e)$
Capacitor	$C \leftharpoonup$	$C \dashv$	$e = \Phi_C^{-1}\left(\int^t f\, dt\right)$
		$C \vdash$	$f = \frac{d}{dt}\Phi_C(e)$
Inertia	$I \leftharpoonup$	$I \vdash$	$f = \Phi_I^{-1}\left(\int^t e\, dt\right)$
		$I \dashv$	$e = \frac{d}{dt}\Phi_I(f)$

Fig. 3. Bond graph elements from (Karnopp, Margolis, & Rosenberg, 2012)

Flow junction, or 0-junction	$\overset{e_1}{\rightharpoonup}_{f_1}\ 0\ \overset{e_3}{\leftharpoonup}_{f_3}$ $e_2 \downarrow f_2$	$e_1 = e_2 = e_3,$ $f_1 + f_2 + f_3 = 0$
Effort junction, or 1-junction	$\overset{e_1}{\rightharpoonup}_{f_1}\ 1\ \overset{e_3}{\leftharpoonup}_{f_3}$ $e_2 \downarrow f_2$	$f_1 = f_2 = f_3,$ $e_1 + e_2 + e_3 = 0$

Fig. 4. Two basic junctions from (Karnopp, Margolis, & Rosenberg, 2012)

If one projects the bond graph of the complete physical system, it would consist in a network of storage elements (inertial, capacitance), dissipative elements and sources of energy, see Fig. 5. Let us imagine the spring damper mass system,

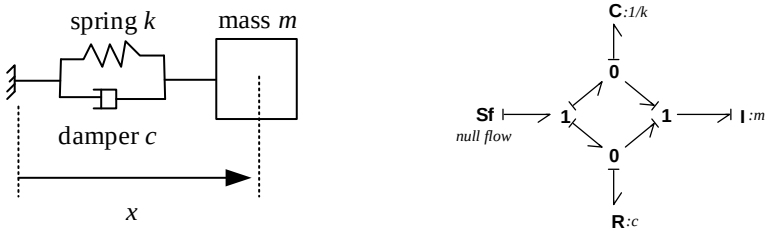

(a). classic representation (b). equivalent bond graph

Fig. 5. Spring-damper mass system

The graph on (b) of Fig. 5 represents the system on the left without any simplifications. The first thing that can be seen is that if one superposes the BG on the classic representation, the graph bonds could be stretched in such a way it matches the *structure* of the physical system. The zeros and ones are the *junction structure* of Fig. 1. The strokes on the top or the bottom of the bonds are *causal* strokes. Without

them the BG is *acausal*. There are rules of attribution of these causalities that can be discovered in (Borutzky, 2009). The causalities fix what is imposed to a given element. For example as such, the *I* kinetic energy storage element, on the right, receives an imposed **flow** from the *1 junction* and sends in return its mass *m* times its acceleration as an **effort**.

At the same time, "*an essential consequence of augmenting the bond graph with causal strokes is that the form of the mathematical model can be determined without formulating and manipulating any equation*", (Borutzky, 2009). Let us illustrate this very important point in two steps. First, let us propose a simplification of the BG (b) of Fig. 5,

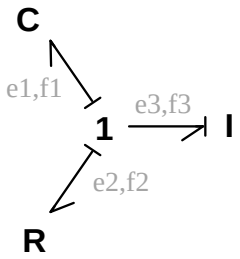

Fig. 6. Simplified bond graph of the spring mass damper system, with defined efforts and flows on each bond

Now, a systematic way to obtain the equations of a given system from a BG consists in writing the equations at each junction of the graph using the rules, (Borutzky, 2009). In the case of Fig. 6, there is a 1 junction, which means that all the surrounding flows are equal. A 0 junction would have meant all the surrounding efforts are equal; when thinking bond graphs, one should always think about the effort-flow *duality*. Coming back to our case,

$$f1 = f2 = f3 = \dot{x}$$

The second rule around the 1 junction is about the efforts. The sum of entering efforts equals the sum of existing efforts. As a result,

$$e1 + e2 + e3 = 0$$

Now the expression of each element effort expression depends on the law it contains and the nature of the element. Let us suppose the internal laws in this example are linear, in that case,

$$k.\int f1.dt + c.f2 + m.\frac{d(f3)}{dt} = 0$$

Which leads, by replacing the flow expression and reordering the terms, to the classic equation of motion,

$$m\ddot{x} + c\dot{x} + kx = 0$$

Something important needs to be pointed out here. The equation obtained here is an ordinary differential equation (ODE). This could have been claimed, by verifying, that all the bonds of the graph, on Fig. 6, are in what is called *integral causality*, see Fig. 7. If at least one of the bonds is not in integral, but in *derivative causality*, the underlying mathematical model will be a *differential algebraic equation* (DAE).

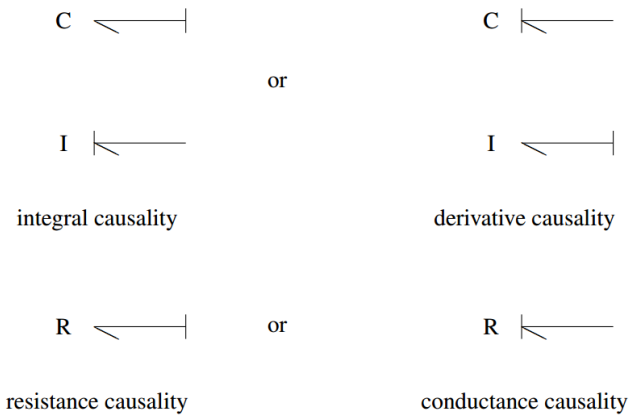

Fig. 7. Causalities at the port of basic elements from (Borutzky, 2009)

The one mass spring damper system can be seen as a multibody system with a single rigid body of mass m. Let us add a second rigid body attached to the first mass,

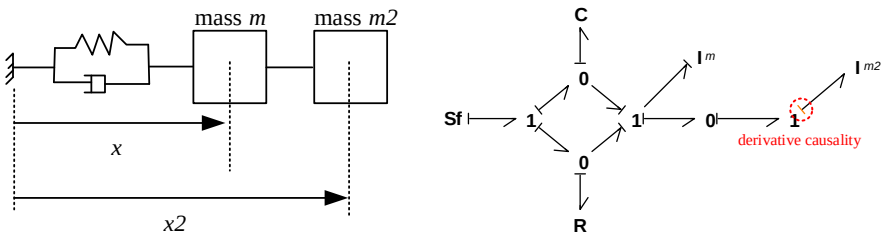

(a). adding a mass (b). a derivative causality appears

Fig. 8. The two mass problem

On Fig. 8 (a), once the mass is rigidly attached to the previous system, the application of the causality rules would lead a bond graph that contains a derivative causality (b); as a result the mathematical model will be a DAE. Let us explicit the DAE, by first simplifying the bond graph of Fig. 8.

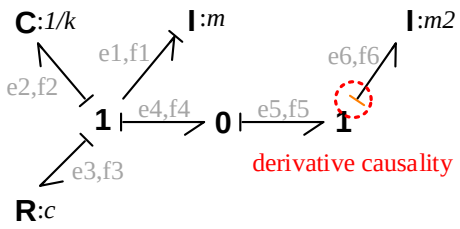

Fig. 9. Simplified two mass system bond graph

Let us derive methodically the equations from Fig. 9,

1. Expressing the equations at each junction taking causality into account
2. Expressing the physical laws of each element taking causality into account
3. Expressing the equations in terms of independent state space variables and their total time derivative
4. For our particular case of storage elements with derivative causality, include the constraint equations between storage elements

These steps are illustrated in the following paragraph,

Junctions

$$\begin{aligned} 1&:\begin{cases} e1 = -(e2+e3+e4) \\ f1 = f2 = f3 = f4 \end{cases} \\ 0&:\begin{cases} e4 = e5 \\ f4 = f5 \end{cases} \\ 1&:\begin{cases} e5 = e6 \\ f5 = f6 \end{cases} \end{aligned} \tag{A1.1}$$

Elements laws

$$\begin{aligned} f1 &= \frac{1}{m}\int e1.dt \\ e2 &= k.\int f2.dt \\ e3 &= c.f3 \\ e6 &= m2.\frac{d(f6)}{dt} \end{aligned} \tag{A1.2}$$

The dimension of the state vector is given by the number of storage elements in integral causality: in our case there are two, a generalized momentum and a generalized position,

$$\begin{pmatrix} p_{I1} \\ q_C \end{pmatrix} = \begin{pmatrix} m.f1 \\ \int f3.dt \end{pmatrix} \tag{A1.3}$$

By using the equations (A1.1), (A1.2) and (A1.3), the total time derivative of the state vector can be expressed,

$$\begin{pmatrix} \dot{p}_{I1} \\ \dot{q}_C \end{pmatrix} = \begin{pmatrix} -\frac{c}{m} p_{I1} - k.q_c - \frac{m2}{m} \dot{p}_{I1} \\ \frac{1}{m} p_{I1} \end{pmatrix} \tag{A1.4}$$

Which becomes in matrix form,

$$\begin{pmatrix} 1+\frac{m2}{m} & 0 \\ 0 & 1 \end{pmatrix} . \begin{pmatrix} \dot{p}_{I1} \\ \dot{q}_C \end{pmatrix} = \begin{pmatrix} -\frac{c}{m} & -k \\ \frac{1}{m} & 0 \end{pmatrix} . \begin{pmatrix} p_{I1} \\ q_C \end{pmatrix} \tag{A1.5}$$

Now the second inertial element is in derivative causality, its state is dependent to the first inertial element state, therefore,

$$p_{I2} = \frac{m2}{m} p_{I1} \tag{A1.6}$$

And by combining (A1.5) and (A1.6) in matrix form,

$$\begin{pmatrix} 1+\frac{m2}{m} & 0 & 0 \\ 0 & 1 & 0 \\ 0 & 0 & 0 \end{pmatrix} . \begin{pmatrix} \dot{p}_{I1} \\ \dot{q}_C \\ \dot{p}_{I2} \end{pmatrix} = \begin{pmatrix} -\frac{c}{m} & -k & 0 \\ \frac{1}{m} & 0 & 0 \\ -\frac{m2}{m} & 0 & 1 \end{pmatrix} . \begin{pmatrix} p_{I1} \\ q_C \\ p_{I2} \end{pmatrix} \tag{A1.5}$$

Or by introducing **E** and **A** matrices and the state vector **x**,

$$\mathbf{E\dot{x} = Ax} \tag{A1.6}$$

The reason why the problem is *algebraic* and not *ordinary* lies in the singularity of matrix **E**. As a matter of fact, the matrix **E** contains a last column made of zeros; its determinant is therefore null and the matrix is not invertible. It is not possible to multiply each left side by the inverse of **E**. The equation (A1.6) is a particular form of DAEs, more generally expressed by,

$$f(\dot{\mathbf{y}},\mathbf{y},t)=\mathbf{0} \tag{A1.7}$$

In such a simple problem, one could assume there is only one mass instead of two. Or one could change the modeling hypothesis and take into account the rigidity of the connection between the two masses; this would introduce a C element between the two I elements and lead back to integral causality of the graph, (Borutzky, 2009), (Karnopp, Margolis, & Rosenberg, 2012), see Fig. 10. This will also have the consequence of adding an additional state variable.

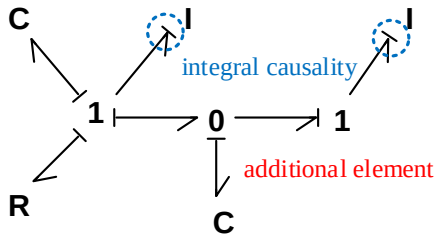

Fig. 10. Taking into account the elasticity between the two masses

Appendix 2
Linear lateral-roll aeromechanical model using Lagrange equations

This appendix is based on chapter 2 assumptions and Figure 2-2 for airframe axis definitions, Figure 2-3 for rotor blade axis definitions and Figure 2-10 for blade section definitions. The generalized coordinates of the system are,

$$\left[x, z, \alpha_y, \beta_1, \beta_2, \beta_3, \beta_4, \delta_1, \delta_2, \delta_3, \delta_4\right]^T$$

One can therefore express the kinetic *T*, potential *V* and dissipation *D* energies of the system that will be used in Lagrange equations,

$$\begin{cases} T = T_{blades} + T_{fuselage} \\ V = V_{lag\_dampers} \\ D = D_{lag\_dampers} \end{cases}$$

Which becomes,

$$\begin{cases} T_{blades} = \sum_i \frac{1}{2} \int_{blade_i} \mathbf{V}^2{}_{M \in blade_i / Rg} dm \\ T_{fuselage} = \frac{1}{2} M_f \mathbf{V}^2{}_{G \in fuselage/Rg} + \frac{1}{2} I_{yy} \boldsymbol{\Omega}^2{}_{fuselage/Rg} \\ V_{lag\_dampers} = \sum_i \frac{1}{2} k_\delta \delta_i^2 \\ D_{lag\_dampers} = \sum_i \frac{1}{2} c_\delta \dot{\delta}_i^2 \end{cases}$$

The aerodynamic forces can be considered in a first approach in the investigation of low frequency phenomena by considering the lifting-line theory with quasi-steady aerodynamics. The local lift forces expression on each M point by considering small angles is,

$$\mathbf{dF}_{air,blade} = \frac{\gamma I_{bl}}{2R^4} \left(\theta_i . U_T - U_p . U_T \right) \mathbf{z}_\beta$$

Which once integrated along the blade length lead to a resultant force and moment at each blade root A,

$$\begin{cases} \mathbf{F}_{air\to blade} = \int\limits_{blade_i} dF_{air\to blade}\mathbf{z}_\beta \\ \mathbf{M}_{A,air\to blade} = \int\limits_{blade_i} \mathbf{AM}\wedge\mathbf{dF}_{air\to blade} = \int\limits_{blade_i} r.\mathbf{y}_\beta \wedge \mathbf{dF}_{air\to blade} \end{cases}$$

Generalized aerodynamic forces can therefore be expressed as,

$$Q_i = \mathbf{F}_{air\to blade}.\frac{\partial \mathbf{V}_{A\in fuselage/Rg}}{\partial \dot{q}_i} + \mathbf{M}_{A,air\to blade}.\frac{\partial \mathbf{\Omega}_{fuselage/Rg}}{\partial \dot{q}_i}$$

With the expressions of kinetic, potential, dissipation and generalized forces, the Lagrangians associated with each one of the generalized coordinates can be obtained,

$$\frac{d}{dt}\left(\frac{\partial T}{\partial \dot{q}_i}\right) - \left(\frac{\partial T}{\partial q_i}\right) + \left(\frac{\partial V}{\partial q_i}\right) + \left(\frac{\partial D}{\partial \dot{q}_i}\right) = Q_i$$

Once each one of the Lagrangians is obtained, the equations are linearized around a steady state $\mathbf{q_{ss}}$,

$$\begin{aligned} \mathbf{q_{ss}} &= \left[x_{ss}, z_{ss}, \alpha_{yss}, \beta_{1ss}, \beta_{2ss}, \beta_{3ss}, \beta_{4ss}, \delta_{1ss}, \delta_{2ss}, \delta_{3ss}, \delta_{4ss}\right]^T \\ &= \left[0,0,0,\beta_{0ss},\beta_{0ss},\beta_{0ss},\beta_{0ss},0,0,0,0\right]^T \end{aligned}$$

At this point the equations of motion obtained are linear time periodic of period $T=2\pi/\Omega$,

$$\dot{\mathbf{x}} = \mathbf{A}(t).\mathbf{x} \text{ with } \mathbf{A}(t+T) = \mathbf{A}(t)$$

The rotor considered in this study is isotropic and therefore *the multiblade transformation* (Bielawa, 2006) can be used to transform the time periodic into a time invariant system. The transformation consists in introducing a change a variables that is chosen in this work as,

$$x_i = x_0 + x_{1c}\cos(\Psi_i) + x_{1s}\sin(\Psi_i)$$

$$\text{with } \Psi_i = \Omega t + 2\pi\frac{i-1}{n_{blades}} \text{ and } x_i = \left\{\beta_i, \delta_i, \theta_i, 1\le i\le n_{blades}\right\}$$

The new state variable vector becomes,

$$\mathbf{x} = (\dot{\mathbf{q}}, \mathbf{q})^T \text{ with } \mathbf{q} = \left[x, z, \alpha_y, \beta_0, \beta_{1c}, \beta_{1s}, \delta_0, \delta_{1c}, \delta_{1s}\right]^T$$

And the input vector $\left[\theta_{1c}, \theta_{1s}\right]^T$.

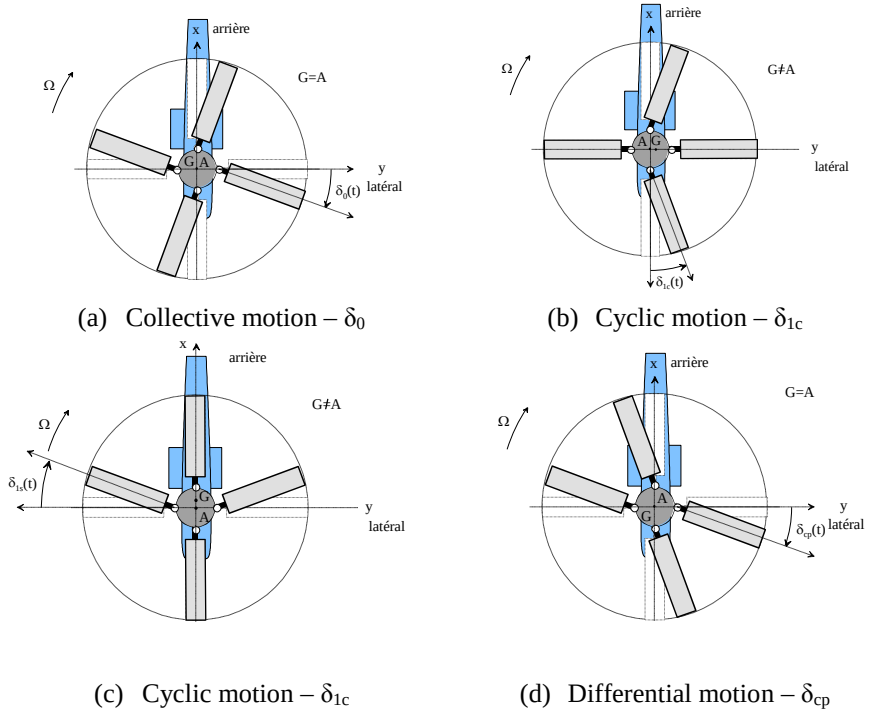

(a) Collective motion – δ_0 (b) Cyclic motion – δ_{1c}

(c) Cyclic motion – δ_{1c} (d) Differential motion – δ_{cp}

Fig. 11. Physical interpretation of multiblade coordinates from (Krysinski & Malburet, 2011)

The simplification of the equations of motion of such systems by hand is tedious and the use of formal computer algebra software such as Mathematica® is necessary. The results are presented in matrix form and equations on the next pages.

With our choice of axis definitions, the angle that controls the vehicle roll is $\theta 1c$ as illustrated in the time simulation results of the integration of the vehicle model for the given input, see Fig. 12. The result allows verifying that a positive input angle generates a positive roll angle.

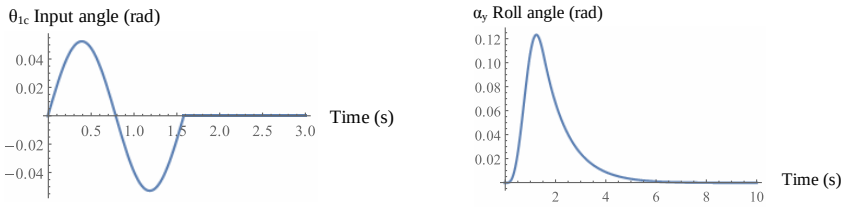

(a). Cyclic pitch angle θ_{1c} input (b). Roll angle α_y output

Fig. 12. Roll attitude verification

The vehicle aeromechanical model coupled with the pilot biodynamics model under matrix form is,

$$\mathbf{q} = \left[x, z, \alpha_y, \beta_0, \beta_{1c}, \beta_{1s}, \delta_0, \delta_{1c}, \delta_{1s}, \theta_{1c} \right]^T$$

$$\mathbf{M} = \begin{bmatrix}
M_f + 4M_{bl} & 0 & 4\left(hM_{bl} + m_s\beta_{0ss}\right) & 0 & 0 & 2m_s\beta_{0ss} & 0 & -2m_s & 0 & 0 \\
0 & M_f + 4M_{bl} & 0 & 4m_s & 0 & 0 & 0 & 0 & 0 & 0 \\
4\left(hM_{bl} + m_s\beta_{0ss}\right) & 0 & 2I_{bl} + I_{yy} + 2e^2M_{bl} + 4h^2M_{bl} + 4em_s + 8hm_s\beta_{0ss} & 0 & 0 & 2\left(I_{bl} + m_s\left(e + h\beta_{0ss}\right)\right) & 0 & -2\left(hm_s + I_{bl}\beta_{0ss}\right) & 0 & 0 \\
0 & 4ms & 0 & 4I_{bl} & 0 & 0 & 0 & 0 & 0 & 0 \\
2m_s\beta_{0ss} & 0 & 2\left(I_{bl} + m_s\left(e + h\beta_{0ss}\right)\right) & 0 & 0 & 2I_{bl} & 0 & 0 & 0 & 0 \\
0 & 0 & 0 & 0 & -2I_{bl} & 0 & 0 & 0 & 0 & 0 \\
0 & 0 & 0 & 0 & 0 & 0 & 4I_{bl} & 0 & 0 & 0 \\
0 & 0 & 0 & 0 & 0 & 0 & 0 & 2I_{bl} & 0 & 0 \\
2m_s & 0 & 2\left(hm_s + I_{bl}\beta_{0ss}\right) & 0 & 0 & 0 & 0 & -2I_{bl} & 0 & 0 \\
k\omega^2 & 0 & 0 & 0 & 0 & 0 & 0 & 0 & 0 & -G
\end{bmatrix}$$

$$\mathbf{C} = \begin{bmatrix}
0 & 0 & \frac{I_{bl}\left(3e+2R\right)\beta_{0ss}\gamma\Omega}{6R^2} & 0 & 0 & \frac{I_{bl}\beta_{0ss}\gamma\Omega}{3R} & 0 & 0 & 0 & 0 \\
0 & \frac{I_{bl}\gamma\Omega}{R^2} & 0 & \frac{2I_{bl}\gamma\Omega}{3R} & 0 & 0 & 0 & 0 & 0 & 0 \\
\frac{I_{bl}\left(3e+2R\right)\beta_{0ss}\gamma\Omega}{6R^2} & 0 & \frac{I_{bl}\left(6e^2+8eR+3R^2+12eh\beta_{0ss}+8hR\beta_{0ss}\right)\gamma\Omega}{12R^2} & 0 & -4\left(I_{bl}+em_s\right)\Omega & \frac{I_{bl}\left(4e+3R+4h\beta_{0ss}\right)\gamma\Omega}{12R} & 0 & 0 & 0 & 0 \\
0 & \frac{2I_{bl}\gamma\Omega}{3R} & 0 & \frac{I_{bl}\gamma\Omega}{2} & 0 & 0 & 8I_{bl}\beta_{0ss}\Omega & 0 & 0 & 0 \\
\frac{I_{bl}\beta_{0ss}\gamma\Omega}{3R} & 0 & \frac{I_{bl}\left(4e+3R+4h\beta_{0ss}\right)\gamma\Omega}{12R} & 0 & -4I_{bl}\Omega & \frac{I_{bl}\gamma\Omega}{4} & 0 & 0 & 4I_{bl}\beta_{0ss}\Omega & 0 \\
0 & 0 & -4\left(I_{bl}+em_s\right)\Omega & 0 & -\frac{1}{4}I_{bl}\gamma\Omega & -4I_{bl}\Omega & 0 & -4I_{bl}\beta_{0ss}\Omega & 0 & 0 \\
0 & 0 & 0 & -8I_{bl}\beta_{0ss}\Omega & 0 & 0 & 4c_\delta & 0 & 0 & 0 \\
0 & 0 & 0 & 0 & 0 & -4I_{bl}\beta_{0ss}\Omega & 0 & -4I_{bl}\Omega & 2c_\delta & 0 \\
0 & 0 & 0 & 0 & 4I_{bl}\beta_{0ss}\Omega & 0 & 0 & -2c_\delta & -4I_{bl}\Omega & 0 \\
0 & 0 & 0 & 0 & 0 & 0 & 0 & 0 & 0 & -2G\zeta\omega
\end{bmatrix}$$

$$\mathbf{K} = \begin{bmatrix}
0 & 0 & 0 & 0 & -\frac{I_{bl}\beta_{0ss}\gamma\Omega^2}{3R} & 0 & 0 & 0 & 0 & 0 \\
0 & 0 & 0 & 0 & 0 & 0 & -\frac{eI_{bl}\beta_{0ss}\gamma\Omega^2}{R^2} & 0 & 0 & 0 \\
0 & 0 & 0 & 0 & -\frac{I_{bl}\left(4e+3R+4h\beta_{0ss}\right)\gamma\Omega^2}{12R} & 0 & 0 & 0 & -\frac{eI_{bl}\left(3e+2R\right)\beta_{0ss}\gamma\Omega^2}{6R^2} & 0 \\
0 & 0 & 0 & 4\left(I_{bl}+em_s\right)\Omega^2 & 0 & 0 & -\frac{2eI_{bl}\beta_{0ss}\gamma\Omega^2}{3R} & 0 & 0 & 0 \\
0 & 0 & 0 & 0 & -\frac{1}{4}I_{bl}\gamma\Omega^2 & 2em_s\Omega^2 & 0 & -4I_{bl}\beta_{0ss}\Omega^2 & -\frac{eI_{bl}\beta_{0ss}\gamma\Omega^2}{3R} & 0 \\
0 & 0 & 0 & 0 & -2em_s\Omega^2 & -\frac{1}{4}I_{bl}\gamma\Omega^2 & 0 & \frac{eI_{bl}\beta_{0ss}\gamma\Omega^2}{3R} & -4I_{bl}\beta_{0ss}\Omega^2 & \frac{1}{4}I_{bl}\gamma\Omega^2 \\
0 & 0 & 0 & 0 & 0 & 0 & 4\left(k_\delta+em_s\Omega^2\right) & 0 & 0 & 0 \\
0 & 0 & 0 & 0 & 4I_{bl}\beta_{0ss}\Omega^2 & 0 & 0 & -2c_\delta\Omega & 2\left(k_\delta+\left(-I_{bl}+em_s\right)\Omega^2\right) & 0 \\
0 & 0 & 0 & 0 & 0 & 4I_{bl}\beta_{0ss}\Omega^2 & 0 & -2\left(k_\delta+\left(-I_{bl}+em_s\right)\Omega^2\right) & -2c_\delta\Omega & 0 \\
0 & 0 & 0 & 0 & 0 & 0 & 0 & 0 & 0 & -G\omega^2
\end{bmatrix}$$

Equations of motion,

x	$-\frac{I_{bl}\beta_{0ss}\gamma\Omega^2\beta_{1c}}{3R}-\frac{I_{bl}\beta_{0ss}\gamma\Omega^2\theta_{1s}}{3R}+\frac{eI_{bl}\beta_{0ss}\gamma\Omega\alpha_y'}{2R^2}+\frac{I_{bl}\beta_{0ss}\gamma\Omega\alpha_y'}{3R}+\frac{I_{bl}\beta_{0ss}\gamma\Omega\beta_{1s}'}{3R}+M_f x''+4M_{bl}x''+4hM_{bl}\alpha_y''+4m_s\beta_{0ss}\alpha_y''+2m_s\beta_{0ss}\beta_{1s}''-2m_s\delta_{1c}''=0$	(A2.1)
z	$-\frac{eI_{bl}\beta_{0ss}\gamma\Omega^2\delta_0}{R^2}-\frac{2I_{bl}\gamma\Omega^2\theta_0}{3R}+\frac{I_{bl}\gamma\Omega z'}{R^2}+\frac{2I_{bl}\gamma\Omega\beta_0'}{3R}+M_f z''+4M_{bl}z''+4m_s\beta_0''=0$	(A2.2)
α_y	$-\frac{1}{4}I_{bl}\gamma\Omega^2\beta_{1c}-\frac{eI_{bl}\gamma\Omega^2\beta_{1c}}{3R}-\frac{hI_{bl}\beta_{0ss}\gamma\Omega^2\beta_{1c}}{3R}-\frac{e^2I_{bl}\beta_{0ss}\gamma\Omega^2\delta_{1s}}{2R^2}-\frac{eI_{bl}\beta_{0ss}\gamma\Omega^2\delta_{1s}}{3R}-\frac{1}{4}I_{bl}\gamma\Omega^2\theta_{1s}-\frac{eI_{bl}\gamma\Omega^2\theta_{1s}}{3R}-\frac{hI_{bl}\beta_{0ss}\gamma\Omega^2\theta_{1s}}{3R}+\frac{eI_{bl}\beta_{0ss}\gamma\Omega x'}{2R^2}+\frac{I_{bl}\beta_{0ss}\gamma\Omega x'}{3R}+\frac{1}{4}I_{bl}\gamma\Omega\alpha_y'$ $+\frac{e^2I_{bl}\gamma\Omega\alpha_y'}{2R^2}+\frac{2eI_{bl}\gamma\Omega\alpha_y'}{3R}+\frac{ehI_{bl}\beta_{0ss}\gamma\Omega\alpha_y'}{R^2}+\frac{2hI_{bl}\beta_{0ss}\gamma\Omega\alpha_y'}{3R}-4I_{bl}\Omega\beta_{1c}'-4em_s\Omega\beta_{1c}'+\frac{1}{4}I_{bl}\gamma\Omega\beta_{1s}'+\frac{eI_{bl}\gamma\Omega\beta_{1s}'}{3R}+\frac{hI_{bl}\beta_{0ss}\gamma\Omega\beta_{1s}'}{3R}+4hM_{bl}x''+4m_s\beta_{0ss}x''+2I_{bl}\alpha_y''$ $+I_{yy}\alpha_y''+2e^2M_{bl}\alpha_y''+4h^2M_{bl}\alpha_y''+4em_s\alpha_y''+8hm_s\beta_{0ss}\alpha_y''+2I_{bl}\beta_{1s}''+2em_s\beta_{1s}''+2hm_s\beta_{0ss}\beta_{1s}''-2hm_s\delta_{1c}''-2I_{bl}\beta_{0ss}\delta_{1c}''=0$	(A2.3)
β_0	$4I_{bl}\Omega^2\beta_0+4em_s\Omega^2\beta_0-\frac{2eI_{bl}\beta_{0ss}\gamma\Omega^2\delta_0}{3R}-\frac{1}{2}I_{bl}\gamma\Omega^2\theta_0+\frac{2I_{bl}\gamma\Omega z'}{3R}+\frac{1}{2}I_{bl}\gamma\Omega\beta_0'+8I_{bl}\beta_{0ss}\Omega\delta_0'+4m_s z''+4I_{bl}\beta_0''=0$	(A2.4)
β_{1c}	$-\frac{1}{4}I_{bl}\gamma\Omega^2\beta_{1c}+2em_s\Omega^2\beta_{1s}-4I_{bl}\beta_{0ss}\Omega^2\delta_{1c}-\frac{eI_{bl}\beta_{0ss}\gamma\Omega^2\delta_{1s}}{3R}-\frac{1}{4}I_{bl}\gamma\Omega^2\theta_{1s}+\frac{I_{bl}\beta_{0ss}\gamma\Omega x'}{3R}+\frac{1}{4}I_{bl}\gamma\Omega\alpha_y'+\frac{eI_{bl}\gamma\Omega\alpha_y'}{3R}+\frac{hI_{bl}\beta_{0ss}\gamma\Omega\alpha_y'}{3R}-4I_{bl}\Omega\beta_{1c}'+\frac{1}{4}I_{bl}\gamma\Omega\beta_{1s}'$ $+4I_{bl}\beta_{0ss}\Omega\delta_{1s}'+2m_s\beta_{0ss}x''+2I_{bl}\alpha_y''+2em_s\alpha_y''+2hm_s\beta_{0ss}\alpha_y''+2I_{bl}\beta_{1s}''=0$	(A2.5)
β_{1s}	$-2em_s\Omega^2\beta_{1c}-\frac{1}{4}I_{bl}\gamma\Omega^2\beta_{1s}+\frac{eI_{bl}\beta_{0ss}\gamma\Omega^2\delta_{1c}}{3R}-4I_{bl}\beta_{0ss}\Omega^2\delta_{1s}+\frac{1}{4}I_{bl}\gamma\Omega^2\theta_{1c}-4I_{bl}\Omega\alpha_y'-4em_s\Omega\alpha_y'-\frac{1}{4}I_{bl}\gamma\Omega\beta_{1c}'-4I_{bl}\Omega\beta_{1s}'-4I_{bl}\beta_{0ss}\Omega\delta_{1c}'-2I_{bl}\beta_{1c}''=0$	(A2.6)
δ_0	$4k_\delta\delta_0+4em_s\Omega^2\delta_0-8I_{bl}\beta_{0ss}\Omega\beta_0'+4c_\delta\delta_0'+4I_{bl}\delta_0''=0$	(A2.7)
δ_{1c}	$4I_{bl}\beta_{0ss}\Omega^2\beta_{1c}-2c_\delta\Omega\delta_{1c}+2k_\delta\delta 1s-2I_{bl}\Omega^2\delta_{1s}+2em_s\Omega^2\delta_{1s}-4I_{bl}\beta_{0ss}\Omega\beta_{1s}'-4I_{bl}\Omega\delta_{1c}'+2c_\delta\delta_{1s}'+2I_{bl}\delta_{1s}''=0$	(A2.8)
δ_{1s}	$4I_{bl}\beta_{0ss}\Omega^2\beta_{1s}-2k_\delta\delta_{1c}+2I_{bl}\Omega^2\delta_{1c}-2em_s\Omega^2\delta_{1c}-2c_\delta\Omega\delta_{1s}+4I_{bl}\beta_{0ss}\Omega\beta_{1c}'-2c_\delta\delta_{1c}'-4I_{bl}\Omega\delta_{1s}'+2m_s x''+2hm_s\alpha_y''+2I_{bl}\beta_{0ss}\alpha_y''-2I_{bl}\delta_{1c}''=0$	(A2.9)

Appendix 3
Modal analysis results

The results presented here the results of a modal analysis performed on the aeromechanical model presented in chapter 2, and in particular in the section in which the validity of the model is discussed. The bars correspond to the eigenvector component along a given state variable. In the title of each mode shape representation, the frequency and damping obtained from the associated eigenvalue are provided, see Fig. 13 and Fig. 14.

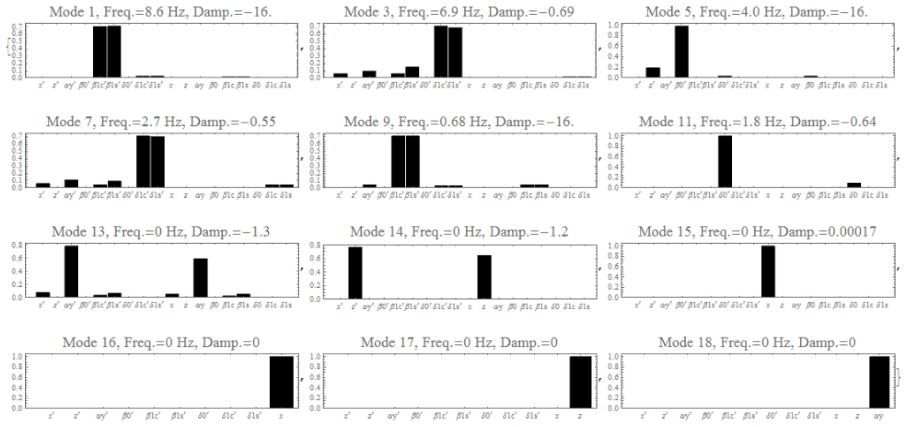

Fig. 13. Without the stabilizing elements

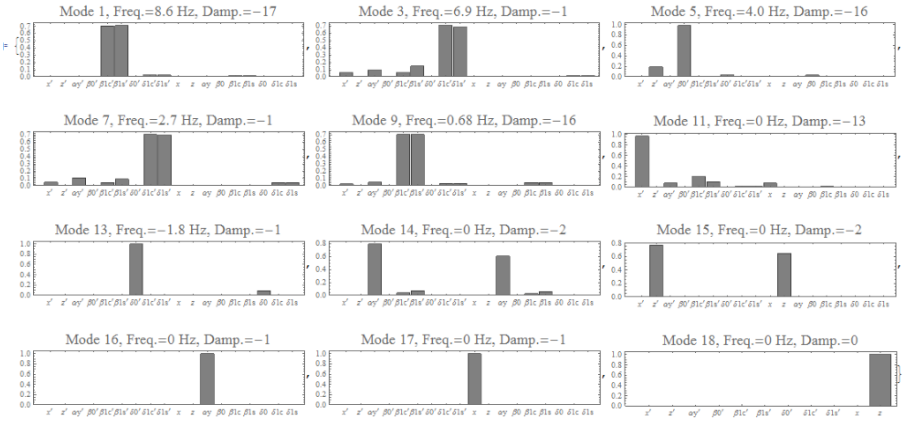

Fig. 14. With the additional stabilizing elements

Appendix 4
Neuromusculoskeletal model parameters

In this appendix, the parameters of both pilot arm model and cyclic lever model are given as well as the axis definitions and the reference frames.
Concerning the upper limb multibody model on Fig. 15, the pilot is in a position such that it looks that he is pitching the lever: the $\boldsymbol{x_i}$ vectors are collinear with the airframe vector $\boldsymbol{x}$ of Figure 2-2. The reference frame #103, see top right of Fig. 15, is a fixed frame in the reference frame #3 of the airframe; for a visual purpose it is not on the top of the frame #10 but both of them have the same center and initial position.
Concerning the positioning of the muscles of Figure 3-7, they can be found on Fig. 17. The last columns of the last figure provide the initial muscle lengths (l_0) and maximal muscle forces (f_0) from (Masarati & Quaranta, 2014). The general characteristic data of both arm and cyclic lever will be found in Table 6 and Table 7.
Finally a sample of the responses of the full arm model are provided on Fig. 16, exhibiting how the multiple frequencies that appear when neuromuscular feedback coefficients are not null, yellow response case.

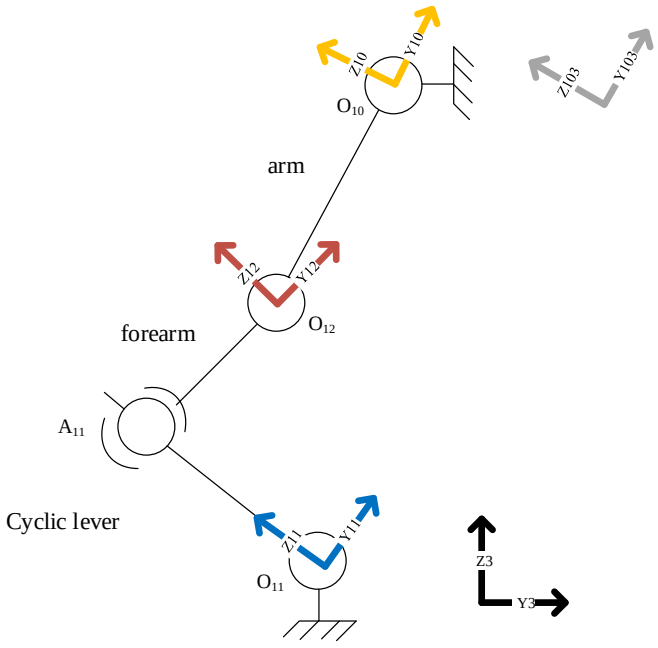

Fig. 15. Axes definitions of the upper limb multibody system

Table 6. Cyclic lever characteristics data from (Venrooij, et al., 2011)

		unit
Length	0.413	m
Inertia (around CG)	0.098	kg.m²
Mass	7	kg
Stiffness	38	Nm/rad
Damping	3.6	Nms/rad

Table 7. Upper limb multibody system data

Skeleton	**Inertia - around CG (kg.m²)**	**Mass (m)**	**Source**
Arm (humerus)	0.015	2.0	(Jex, Henry R. & Magdaleno, Raymond E., 1978)
Forearm (radius+ulna)	0.007	1.2	
Articulations	**Stiffness (Nm/rad)**	**Damping (Nms/rad)**	**Source**
Shoulder	5	0.04	(Mattaboni, Fumagalli, Quaranta, & al., 2009)
Elbow	0.3	0.035	
Wrist	100	1	(Mattaboni, Fumagalli, Quaranta, & al., 2009)

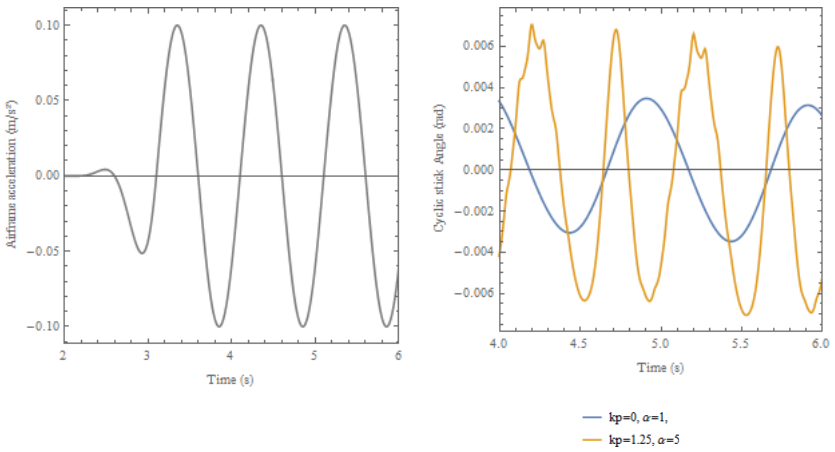

(a). cockpit lateral acceleration input (b). cyclic stick angle response

Fig. 16. Sample of the neuromusculoskeletal model responses in the time domain

		abrev													source polimi	
			points d'attache					p2						l0	f0	
			p1													
	mm		dans R103			dans R0					dans R0					newton
	humerus shoulder		d			x	y	z			x	y	z			
1	pectoralis major (stern)	pm1	80			-573	-1615	548			-411	-1585	535	166	423	
2	pectoralis major (clav)	pm2	125			-564	-1644	515			-503	-1559	612	143	423	
3	pectoralis major (ribs)	pm3	47,5			-580	-1594,5	572			-407	-1627	452	213,5	423	
4	latissimus dorsi (thoracic)	ltdt	125								-421	-1533	375	228	175	
5	latissimus dorsi (lumbar)	ltdtl	80								-418	-1553	336	270	175	
6	latissimus dorsi (illiac)	ltdti	47,5								-415	-1574	293	325	125	
										p2				l0	f0	
	usi		dans R103			dans R0			dans R11		dans R0					newton
	humerus hand		x	y	z	x	y	z	x	y	z	x	y	z			
7	flexor carpi radialis	fcr	0,011	-0,328	-0,015	-0,517	-1,760	0,353	-0,037	0,047	0,409	-0,452	-2,046	0,327	0,294	74
8	flexor carpi ulnaris	fcu	idem	idem	idem	idem	idem	idem	-0,014	0,050	0,387	-0,432	-2,035	0,306	0,291	128,9
9	extensor carpi radialis	ecr	-0,024	-0,320	-0,005	-0,548	-1,775	0,369	-0,064	0,016	0,413	-0,465	-2,085	0,331	0,323	405,4
10	extensor carpi ulnaris	ecu	-0,017	-0,334	-0,021	-0,544	-1,771	0,348	-0,054	0,022	0,373	-0,458	-2,076	0,291	0,322	93,2
			p1								p2			l0	f0	
	usi		dans R12			dans R0					dans R0					newton
	radius shoulder		x	y	z	x	y	z			x	y	z			
11	bicep brachii caput l/b	bic	0,000	-0,030	0,001	-0,514	-1,794	0,371			-0,555	-1,534	0,619	0,362	137	
			p1								p2			l0	f0	
	usi		dans R12			dans R0					dans R0					newton
	ulna shoulder		x	y	z	x	y	z			x	y	z			
12	triceps brachii caput longus	ticl	-0,003	-0,030	-0,035	-0,521	-1,792	0,335			-0,536	-1,534	0,582	0,357	135	
									p2							
	usi		dans R103			dans R0			dans R12		dans R0					newton
	humerus ulna		x	y	z	x	y	z	x	y	z	x	y	z			
13	triceps brachii caput l/m	ticlm	0,007	-0,154	-0,024	-0,560	-1,644	0,476	-0,003	-0,030	-0,035	-0,521	-1,792	0,335	0,208	108
14	brachialis	bra	-0,010	-0,249	0,011	-0,544	-1,734	0,431	0,000	-0,030	0,001	-0,514	-1,794	0,371	0,090	167
									p2					l0	f0	
	usi		dans R103			dans R0			dans R12		dans R0					newton
	humerus radius		x	y	z	x	y	z	x	y	z	x	y	z			
15	brachioradialis	brd	0,000	-0,266	0,000	-0,535	-1,734	0,411	-0,056	-0,260	0,006	-0,479	-2,027	0,350	0,305	45
16	pronator teres	prnt	0,014	-0,316	-0,001	-0,512	-1,761	0,372	-0,024	-0,080	0,001	-0,517	-1,849	0,366	0,089	54

Fig. 17. Positions of the extremities of the muscles, initial muscle length (l_0) and maximal muscle force (f_0)

Appendix 5
Lateral-roll time simulation results

Three dimensional visualization results of time simulation results presented in chapter 4 are reported here on Fig. 18, Fig. 19 and Fig. 20. These captures represent simulations results from 5s after the perturbation until 15s after the perturbation, see Figure 4-7; they give an idea of what could be experienced by a pilot during a lateral-roll aeroelastic RPC. These visualizations are simulated and captured using the bond graph preprocessor 20-sim ®.
On Fig. 18 and Fig. 19, the camera was fixed in the inertial frame. One can see that the main rotor blades motion amplitudes are larger than the fuselage motion amplitude. On Fig. 20, the camera is fixed on the hub and points from the sky to the ground the rotor blades; in this frame there is no azimuthal motion of the blades. They can only flap, lag and pitch. One can observe progressive emergence of a combination in the motion of the lag modes.

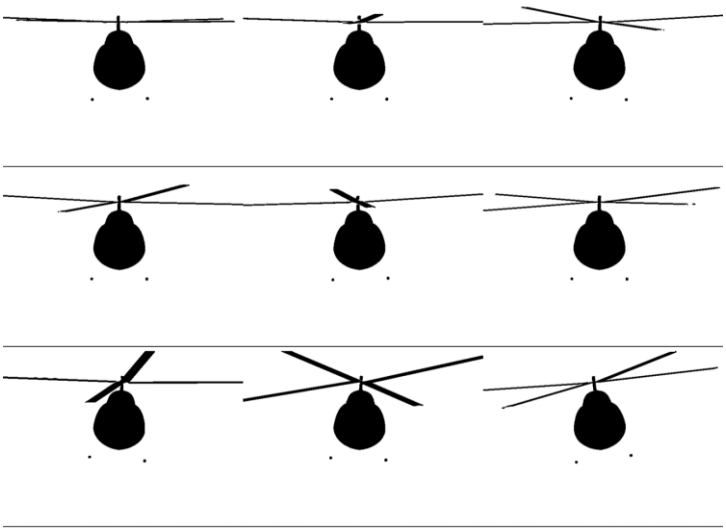

Fig. 18. Front view in the inertial frame

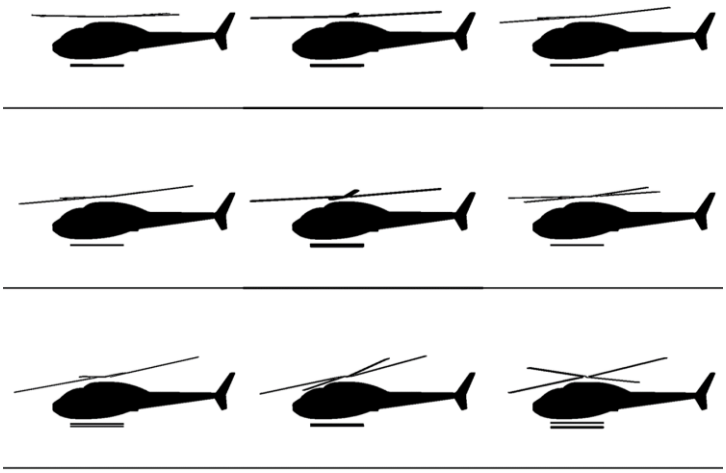

Fig. 19. Lateral view in the inertial frame

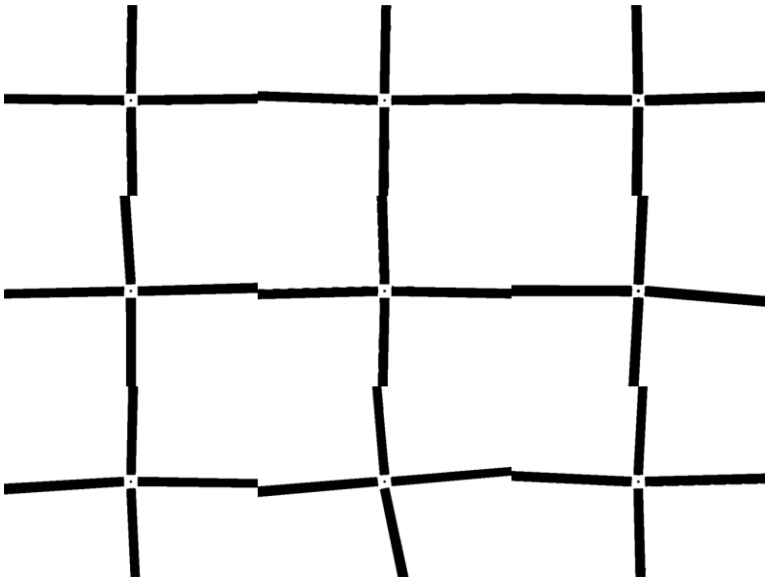

Fig. 20. Top view in rotor reference frame

Appendix 6
Ground resonance parametric instability Campbell diagram

An eigenvalue analysis of the 3 degrees of freedom ground resonance model of equation (77) is presented here for varying rotor angular velocities. When the fuselage on its landing gear mode frequency equals the regressing lag mode frequency, this last mode loses damping resulting in the *parametric instability* known as 'ground resonance'.

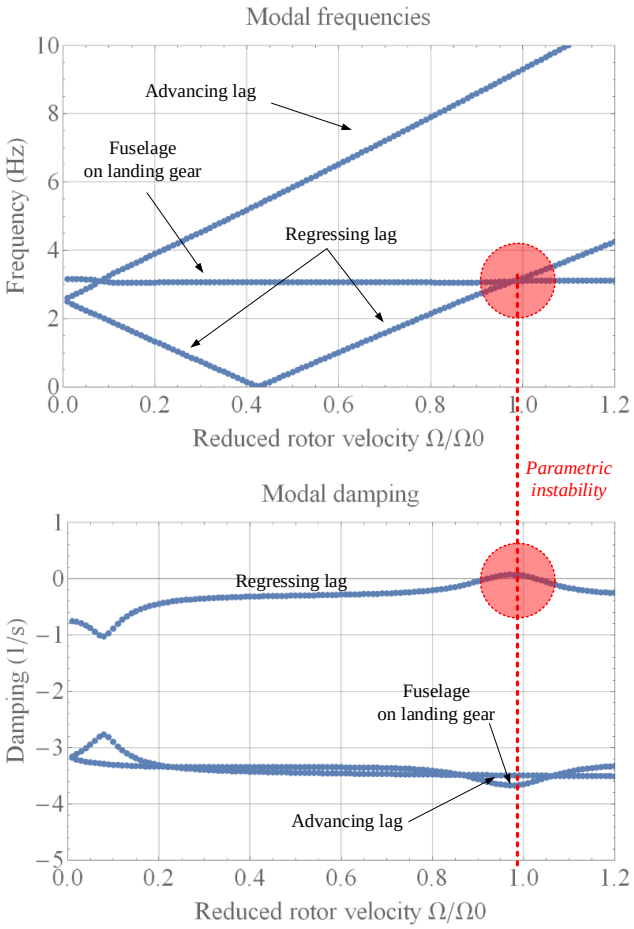

Fig. 21. Frequency coalescence and regressing lag mode damping loss

BIOAEROELASTICITE D'AERONEFS A VOILURE TOURNANTE PAR BOND GRAPHS

RESUME : Dans certaines conditions de vol, les aéronefs à voilure tournante souffrent parfois de l'émergence d'oscillations indésirables, phénomènes potentiellement instables connus sous le nom de Couplages Pilote-Aéronef aéroélastiques (CPA). Ces phénomènes affectent de manière critique la sécurité et la performance des aéronefs. Par conséquent, il est important d'être capable de prédire l'émergence de tels phénomènes dynamiques, le plus tôt possible dans le processus de conception des hélicoptères. Une revue de la littérature révèle que ces phénomènes sont le résultat d'interactions entre les comportements biodynamique du pilote et aéroélastique des hélicoptères. Afin d'avoir une plus grande modularité et granularité dans le processus de modélisation de systèmes complexes, une approche par bond graphs est adoptée. Un modèle aéromécanique d'hélicoptère et un modèle neuro-musculo-squelettique d'un des membres supérieurs du pilote sont développés en bond graphs. Parmi les représentations proposées, trois sont originales, notamment afin de modéliser : des efforts aérodynamiques quasi-statiques, la liaison traînée-battement-pas entre pale et moyeu rotor, et les efforts musculaires à partir d'un modèle de Hill qui tient compte d'une boucle de rétroaction neuromusculaire. Des résultats encourageants sont obtenus lorsque l'on compare la transmissibilité, entre l'angle de manche de pas cyclique imposé par le pilote et des accélérations latérales de la cabine, calculée à partir du modèle biodynamique, et à partir des résultats expérimentaux tirés de la littérature. Un modèle du système bioaéroélastique homme-machine est linéarisé, au voisinage d'un vol stationnaire, et analysé en termes de stabilité. L'étude révèle, comme conjecturé dans la littérature, que le mode régressif de traînée peut être déstabilisé. De plus, il apparaît que le mode progressif de traînée peut également être déstabilisé lors d'un CPA sur l'axe latéral-roulis. Un critère d'analyse de la stabilité d'un équilibre d'un système dynamique à partir d'un modèle linéaire limite la possibilité de prendre en compte certains comportements non-linéaires et donc réduit l'espace de conception. Les premières pierres vers une méthode basée sur des fonctions de Chetaev sont posées, afin de déterminer si l'équilibre d'un système dynamique est instable, directement à partir d'un modèle mathématique non-linéaire de grande dimension, à un coût de calcul potentiellement intéressant. Afin d'illustrer la pertinence de la proposition, le cas de la résonance sol d'un hélicoptère est présentée.

Mots clés : bond graphs, couplage pilote-aéronef, aéroélasticité, modèle neuro-musculo-squelettique, systèmes multicorps, fonctions de Chetaev, hélicoptères

ROTORCRAFT BIOAEROELASTICITY USING BOND GRAPHS

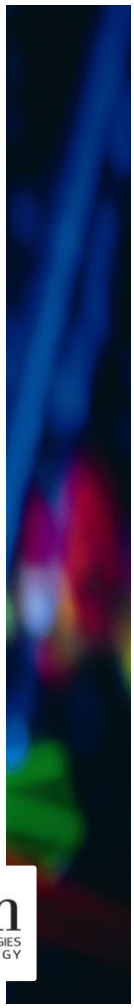

ABSTRACT: Under certain flight conditions, rotorcrafts might suffer from the emergence of undesirable oscillations, potentially unstable phenomena, known as aeroelastic Rotorcraft-Pilot Couplings (RPCs). These phenomena critically affect the safety and performance of rotorcraft designs. Therefore, there is an important interest in being able to predict the emergence of such dynamic phenomena, as soon as possible during the design process of helicopters. A review of the state-of-the-art reveals that these phenomena are the result of interactions between pilots' biodynamics and helicopters' aeroelastic behaviors. In order to provide more modularity and granularity in the modeling of complex systems, a bond graph based approach is used. A helicopter aeromechanical model and a pilot upper limb neuromusculoskeletal model are developed using bond graphs. Three original bond graph representations are proposed, to model: quasi-steady aerodynamic forces, lag-flap-pitch joint at blades' roots, and a Hill-type muscle force model that accounts for muscle reflexive feedback. Encouraging results are found when comparing the pilot biodynamic model transmissibility cyclic lever angle to lateral cockpit accelerations computations to literature experimental results. A linear model of the coupled human-machine bioaeroelastic system around hover is analyzed in terms of stability. It reveals not only the regressing lag mode, as conjectured in literature, but also the advancing lag mode can be destabilized during a lateral-roll aeroelastic RPC. Furthermore, a criterion to assess the stability of the equilibrium of a dynamic system from a linear model limits the possibility to take into account nonlinear physical behaviors, reducing the design space. The first blocks towards a method based on Chetaev functions is proposed, to determine if an equilibrium is unstable, directly from its large nonlinear mathematical model, at a potentially interesting computational cost. The helicopter 'ground resonance' case illustrates the soundness of the proposal.

Keywords : bond graphs, Rotorcraft-Pilot Couplings, aeroelasticity, neuromusculoskeletal system, multibody systems, Chetaev functions, helicopters

ARTS ET MÉTIERS ParisTech

ParisTech
INSTITUT DES SCIENCES ET TECHNOLOGIES
PARIS INSTITUTE OF TECHNOLOGY